THE SIGNIFICANCE OF VORTEX RING FORMATION AND NOZZLE EXIT OVER-PRESSURE TO PULSATILE JET PROPULSION

Thesis by
Paul Samuel Krueger

In Partial Fulfillment of the Requirements for the Degree of
Doctor of Philosophy

California Institute of Technology
Pasadena, California

2001

(Defended May 4, 2001)

Acknowledgements

I would first like to thank and acknowledge all of the instructors with which I have had the privilege of working over the years. I especially want to thank my 7th grade teacher, Craig Stowers, who recognized and encouraged my potential in math and science. I also wish to acknowledge my high school Chemistry teacher and advisor, Robert Boekelheide, who presented the fundamental principles of science to me as well as any of my instructors at institutions of higher education. Special thanks also to Professors Dennis Lieu and Benson Tongue at the University of California at Berkeley. Their advice and encouragement was invaluable during my undergraduate studies. Finally, I am grateful to my thesis advisor, Professor Mory Gharib. Without his patience and insight, this work would not have been possible.

Among my colleagues here at GALCIT, I would like to especially thank Dr. Dana Dabiri for his assistance with DPIV, as well as many helpful discussions concerning this work. Dr. David Jeon also deserves special recognition for his assistance with the DPIV processing software. Many others have contributed insight and support, both in the lab and in life. In this group are Dr. Jerry Shan, Jimmy Fung, Dr. Michael Ol, Sanjeev Malhotra, Theodore Tuttle, and Christopher Adams, to name a few.

Finally, I would like to thank my thesis committee, Professors Mory Gharib, Hans Hornung, Anthony Leonard, and Joseph Shepherd for their careful evaluation of this work.

This work is dedicated to:

My family and friends for their love and support over the years;

My wife for her unfathomable patience and understanding;

and

The I AM, through whom all things were made and without whom nothing was made that has been made.

Abstract

The Significance of Vortex Ring Formation and Nozzle Exit Over-Pressure to Pulsatile Jet Propulsion

by
Paul Samuel Krueger

Pulsatile jet propulsion can be accomplished using a fully-pulsed jet (i.e., a periodic series of starting jets or pulses), the unsteady nature of which engenders vortex ring formation. The significance of vortex ring formation for this type of propulsion is studied experimentally using a piston-cylinder mechanism to generate starting and fully-pulsed, round jets of water into water at a maximum jet Reynolds number of 13,000. Starting jets are considered separately since they are the limiting case of a fully-pulsed jet at zero pulsing frequency. Direct measurements of the total impulse per pulse (starting jets) and time-averaged thrust (fully-pulsed jets) are made using a force balance. Hotfilm anemometry is used to measure the jet velocity and Digital Particle Image Velocimetry (DPIV) is used to measure vortex ring position, vorticity, energy, circulation, and impulse.

The pulses for both types of jets are generated using piston stroke to diameter ratios (L/D) in the range 2 to 8 for piston velocity programs in a generally positive-sloping (PS) or negative-sloping (NS) family. The range of L/D considered brackets the transition between the case where an individual vortex ring is produced with each pulse (small L/D) and the case where the vortex ring stops growing and pinches off from its generating jet, producing a trailing jet (large L/D). This transition occurs at a higher L/D for the PS ramps, allowing the effects of vortex ring formation and pinch off to be illuminated by comparison of the results for the NS and PS ramps.

The significance of vortex ring formation is first analyzed for starting jets. Measurements of the total impulse per pulse as a function of L/D show that a leading vortex ring adds more impulse per unit L/D than a trailing jet. This leads to a maximum in the average thrust during a pulse at the L/D s just before vortex ring pinch off is observed for both the PS and NS ramps. The propulsive benefit provided by a leading vortex ring over a trailing jet is connected to over-pressure at the nozzle exit plane during vortex ring formation. DPIV measurements demonstrate that nozzle exit over-pressure also makes an important contribution to energy and circulation. It is shown that this over-pressure can be related to the momentum that must be supplied by the forming vortex ring to ambient fluid in the form of added and entrained mass. A model is proposed for nozzle exit over-pressure near the initiation of an impulsive velocity program where entrainment can be ignored. The model readily accounts for the pressure contribution to circulation in the NS ramps, but modeling of entrainment is required to properly determine impulse and energy.

For the fully-pulsed jet experiments, a normalized thrust, F_{IJ}, is introduced to characterize the pressure effects associated with vortex ring formation. The pulsing frequency is expressed in dimensionless form as St_L, which is between 0 and 1 for all fully-pulsed jets. A propulsive benefit from pressure ($F_{IJ} > 1$) is observed for all L/D and St_L considered. At low St_L, the results are similar to those for the starting jets. At higher St_L, F_{IJ} decreases with L/D as with the starting jets, which is related to the existence of vortex ring pinch off for all observed St_L. At a fixed L/D, two dominant decreasing trends in F_{IJ} with St_L appear and seem to be related to the effects of previously ejected pulses on forming vortex rings. No dramatic increase in F_{IJ} with St_L (associated with the increased con-

vective velocity of multiple coaxial vortex rings over that of individual vortex rings) is observed since (a) the ring separation is never reduced low enough to see an increase in the ring velocity (even for $St_L \rightarrow 1$), and (b) the vortex rings don't remain coaxial or coherent as $St_L \rightarrow 1$.

Table of Contents

List of Figures

List of Tables

Nomenclature

General Fluid Mechanics

g	Gravitational constant [9.81 m/s^2]	
$\mathbf{I}$	Hydrodynamic impulse [Ns] (see also $I(t)$, below)	(D.5), p. 163
p	Absolute pressure [Pa]	
t	Time [s]	
$\mathbf{u}$	Velocity vector [m/s]	
u, v, w	Velocity components in the axial, radial, and azimuthal directions, respectively [m/s]	
S	Control surface	
C	Boundary of control surface	
ϕ	Velocity potential [m^2/s]	p. 64
ν	Kinematic viscosity [$9.60\times10^{-7}\ m^2/s$ for water]	
ψ	Stokes stream function [m^3/s]	(3.24), p. 71
ρ	Fluid density [1000 kg/m^3 for water]	
τ	Shear stress tensor [N/m^2]	
ω	$= \nabla\times\mathbf{u}$; vorticity vector [1/s]	(D.6), p. 163
ω_x, ω_r, ω_θ	Axial, radial, and azimuthal components of vorticity, respectively [1/s]	
Ω, Ω_0	Control volume	
$\partial\Omega$, $\partial\Omega_0$	Boundary of corresponding control volume	

Coordinate Systems

x, r, θ	Coordinates of a cylindrical coordinate system with the origin at the nozzle center line and nozzle exit plane [m, m, radians]	Figure 2.1, p. 14
$\hat{\mathbf{x}}$, $\hat{\mathbf{r}}$, $\hat{\theta}$	Unit vectors of the cylindrical coordinate system in the axial, radial, and azimuthal directions respectively	
$\mathbf{x}$	$= x\hat{\mathbf{x}} + r\hat{\mathbf{r}} + \theta\hat{\theta}$	
$\hat{\mathbf{n}}$	Unit outward normal to a control surface or a control volume, as implied by the context	

Other Symbols

a	Vortex ring separation in the axial direction [m]	§4.5, p. 117
f	$= 1/T$; Pulsing frequency (Hz)	p. 14
h	Vertical height above the nozzle center line (positive when opposite the direction of gravity) [m]	p. 162
p_h	$= p_\infty - \rho g h$; ambient fluid pressure [Pa]	(D.2), p. 162
p_∞	Ambient pressure on the nozzle center line, i.e., the pressure at $(x, r) \rightarrow (\infty, 0)$ [Pa]	p. 40, p. 162
r_v	$= u_{cl}/U_J$; Center-line velocity ratio	(2.6), p. 27
t_F	Time during a pulse after which the SG model predicts no additional circulation (or impulse or energy) ejected by the jet will be entrained into the leading vortex ring [s]	(C.7), p. 153
t_p	Pulse duration [s]	Figure 2.1, p. 14
$u_{cl}(t)$	Jet velocity at the nozzle center line, i.e., at $(x, r) = (0, 0)$ [m/s]	p. 27
$u_J(r, t)$	Jet velocity (x-component) at the nozzle exit plane $[m/s]$	Figure 2.1, p. 14
x_i	Axial distance from nozzle inlet [m]	p. 34
x_N	Axial distance from nozzle inlet to nozzle exit plane $[6.125D]$	p. 28
A	Nozzle cross-sectional area at the nozzle exit plane $(x = 0)$ [m^2]	p. 14
D	Nozzle diameter [1.27 cm]	Figure 2.1, p. 14
D_p	Piston diameter [11.43 cm]	
$E(t)$	Total energy (kinetic) energy added to the flow by a piston-cylinder mechanism[a] [J]	(D.16), p. 166; and (D.17),p. 166
$E_p(t)$	Pressure work done on the flow at the nozzle exit plane[a] [J]	(D.19), p. 167
E_{ring}	Kinetic energy of the leading vortex ring [J]	(3.23), p. 71
$E_{sm}(t)$	$E(t)$ determined using the slug model[a] [J]	(C.3), p. 152
$E_U(t)$	Kinetic energy added to flow by energy flux from the jet[a] [J]	(2.16), p. 35; and (D.18), p. 166
$E_{U,ring}$	$= E_U(t_F)$ [J]	p. 72
$E_{U,TJ}$	$= E_U(t_p) - E_U(t_F)$ [J]	p. 72

$E_U^u(t)$	$E_U(t)$ evaluated assuming $u_J(r, t) = U_J(t)$ [J]	(2.20), p. 37
$E_U^P(t)$	$E_U(t)$ evaluated assuming $u_J(r, t)$ has a radial dependence as shown in Figure 2.6 [J]	(2.21), p. 38
F	Formation number	§1.2.1.1, p. 4; and (C.8), p. 153
$F_{FB}(t)$	Force (thrust) on the jet section measured by the force balance [N]	p. 40
F_{IJ}	Intermittent jet normalized thrust	(4.2), p. 101
$\bar{F}_p$	Average thrust during a pulse [$= I/t_p$ where I is given by equation (3.2)] [N]	(3.3), p. 53
$\bar{F}_T$	Time-averaged thrust [i.e., time average of $F_{FB}(t)$] [N]	p. 41
$I(t)$	Impulse added to the flow by a piston-cylinder mechanism[a], or, equivalently, magnitude of the hydrodynamic impulse (see **I** above) [Ns]	(D.9), p. 164 [see also (3.2)]
I_{nd}	Non-dimensional impulse	(3.4), p. 55
$I_p(t)$	Impulse added to the flow by nozzle exit over-pressure[a] [Ns]	(D.11), p. 164 [see also (3.5)]
I_{ring}	Hydrodynamic impulse of the leading vortex ring [Ns]	(3.6), p. 61
$I_{sm}(t)$	$I(t)$ determined using the slug model[a] [Ns]	(C.2), p. 152
I_{TJ}	Portion of the total impulse of a pulse contributed by the trailing jet [Ns]	p. 61
$I_U(t)$	Impulse added to the flow by momentum flux from the jet[a] [Ns]	(2.15), p. 35; and (D.10), p. 164
$I_U^u(t)$	$I_U(t)$ evaluated assuming $u_J(r, t) = U_J(t)$ [Ns]	(2.17), p. 36
$I_U^P(t)$	$I_U(t)$ evaluated assuming $u_J(r, t)$ has a radial dependence as shown in Figure 2.6 [Ns]	(2.18), p. 36
L	$= X(t_p)$; Total length of an ejected pulse [m]	(2.1), p. 13
L_p	Piston stroke corresponding to L [m]	p. 19
R	$= D/2$ [m]	
Re_a	$= \frac{U_J D}{\nu}$; Reynolds number based on U_J for steady commanded U_p	(2.7), p. 27
Re_m	$= \frac{U_{max} D}{\nu}$; Reynolds number based on U_{max}	(3.1), p. 47

Re_R	$= \frac{U_J R}{\nu}$; Reynolds number based on R and U_J for steady commanded U_p	(2.9), p. 28
Re_{x_N}	$= \frac{U_J x_N}{\nu}$; Reynolds number based on x_N and U_J for steady commanded U_p	(2.12), p. 29
Re_0	$= \frac{U_0 R}{\nu}$; Reynolds number based on R and U_0	(2.23), p. 38
Re_Γ	$= \frac{\Gamma}{\nu}$; Reynolds number based on circulation	§3.5.4, p. 76
R_r	Vortex ring radius [m]	§4.5, p. 117; and p. 153
St_L	Non-dimensional pulsing frequency	(4.1), p. 98
T	Pulse period [s]	Figure 2.1, p. 14
U_{cal}	Jet velocity as determined from hotfilm measurements using a calibration based on U_J for steady commanded U_p [m/s]	(2.5), p. 23
$U_J(t)$	Spatially averaged jet velocity (x-component) at the nozzle exit plane [m/s]	(2.3), p. 13
U_{max}	Maximum of $U_J(t)$ over the interval $[0, t_p]$ [m/s]	p. 47
U_p	Driver piston velocity (commanded) [m/s or in/s]	p. 26
U_0	Time averaged U_J [m/s]	p. 38
W	Translational velocity of a vortex ring [m/s]	Figure 3.9, p. 67 and p. 153
$X(t)$	Length of an ejected slug of fluid at time t [m]	(2.2), p. 13
α	Non-dimensional energy used to predict pinch off	(3.43), p. 88
δ	Thickness of a parabolic approximation of the boundary layer at the nozzle exit plane [m]	Figure 2.6, p. 28
ϕ_g	Gravitational potential per unit volume [N/m^2]	(D.2), p. 162
$\Gamma(t)$	Circulation added to the flow by a piston-cylinder mechanism[a] [m^2/s]	(D.33), p. 171
$\Gamma_p(t)$	Circulation added to the flow by nozzle exit overpressure[a] [m^2/s]	(D.33), p. 171
Γ_{ring}	Circulation of the leading vortex ring [m^2/s]	(3.27), p. 76
$\Gamma_{sm}(t)$	$\Gamma(t)$ determined using the slug model[a] [m^2/s]	(C.1), p. 152

$\Gamma_U(t)$	Circulation added to the flow by vorticity flux from the jet[a] [m^2/s]	(D.33), p. 171
$\Gamma_{U,ring}$	$= \Gamma_U(t_F)$ [m^2/s]	p. 76 and p. 77
$\Gamma_{U,TJ}$	$= \Gamma_U(t_p) - \Gamma_U(t_F)$ [m^2/s]	p. 77

a. The notation in chapters 3 and 4 is such that reference to this quantity without any explicit time dependence refers to the value of the quantity at the completion of a pulse. For example, $E_U = E_U(t_p)$ and I is the total impulse measured during a pulse as defined by equation (3.2).

Common Subscripts

cl	Nozzle center line (at $x = 0$)
J	Jet
p	Pressure term (or pulse, or piston)
ring	Refers to the leading vortex ring
SG	SG model
sm	Slug model
TJ	Trailing jet
U	Velocity/flux term

Abbreviations

GRS	Gharib, Rambod, and Shariff (refers to Gharib *et al.* [12])	
SG	Shusser and Gharib (refers to the model proposed by Shusser *et al.* [36] for vortex ring pinch off)	Appendix C

CHAPTER 1

Introduction and Background

1.1 Introduction: Jet Propulsion and Vortex Rings

Since the advent of the turbojet in the mid-20th century, jet propulsion has been commonly associated with aeronautics. The concept of jet propulsion, however, was pioneered not in aviation, but in the ocean by aquatic creatures, such as cephalopods (e.g., squid), salps, and jellyfish. Significantly, jet propulsion in this venue is highly unsteady, consisting of bursts of fluid issuing from an orifice or tube. A single burst or pulse of fluid issuing from a nozzle into quiescent fluid is often referred to as a starting jet and has long been associated with vortex ring formation. A multiplicity of such pulses is dubbed a fully-pulsed jet and can lead to a multiplicity of vortex rings in the resulting flow. Given the preference in nature for *unsteady* jet propulsion, it is relevant to consider the role vortex ring formation plays in this form of locomotion. Specifically, is there any propulsive benefit from vortex ring formation by a single pulse (in terms thrust, impulse, and/or energy)? If there is a benefit, is there a way to optimize whatever is gained? And finally, in the case of a multiplicity of pulses, is there any effect, beneficial or detrimental, from

the presence of multiple vortex rings in the flow? These issues are the primary focus of this investigation.

1.2 Background

Given the central role of vortex ring formation and pulsed jets to this investigation, a brief account of relevant material in these two broad subject areas is presented here.

1.2.1 Vortex Ring Formation

The recent reviews of Shariff and Leonard [33] and Lim and Nickels [16] discuss much of the current understanding of vortex ring formation as well as other issues related to the dynamics of laminar and turbulent vortex rings. In the laboratory, vortex rings are most commonly formed using a piston-cylinder mechanism where a piston initially at rest in a cylinder of diameter D moves through a length L ejecting fluid into ambient fluid of similar density, thereby creating a starting jet of characteristic stroke ratio L/D. The vorticity generated by this jet principally through the boundary layer at the inner surface of the nozzle then rolls up into an initially axisymmetric vortex ring. The evolution of the size, position, and circulation of vortex rings generated in this manner have been studied experimentally by numerous researchers, such as Maxworthy [18], Didden [10], and Glezer [14]. Models of the roll-up process have also been considered analytically by Saffman [29], who considered the roll-up of a cylindrical vortex sheet, and Saffman [30] and Pullin [26], who modeled the initial roll-up using planar similarity theory. Nitsche [23] was able to show numerically that planar similarity theory correctly predicts the *initial*

motion of a rolling-up vortex sheet issuing from a circular tube. At later times, however, the results of planar similarity theory do not agree with investigations of vortex ring formation (see for example Didden [10] and Nitsche and Krasny [22]). At present, a precise theoretical account of the observed motion of the core of a forming vortex ring is lacking, and the exact nature of vortex ring roll-up is still not completely understood.

Most of the work in vortex ring formation ignores the issue of the roll-up of a vortex sheet altogether and focuses on the amount of the dynamic quantities (circulation, impulse, and energy) ejected by the piston-cylinder mechanism generating the ring. Assuming whatever is ejected from the cylinder is eventually entrained by the forming vortex ring, its final bulk properties can then be determined. In nearly every case, the amount of each dynamic quantity generated by the piston-cylinder mechanism is modeled using a fluid "slug" model where the ejected fluid is viewed as having a uniform velocity equal to the piston velocity and pressure equal to the ambient pressure. This model is most commonly used to estimate the circulation of the resulting vortex ring by considering the flux of vorticity due to this slug flow. Glezer ([13] and [14]) also uses it to determine vortex ring impulse. Despite the obvious oversimplifications of this model and the fact that its deficiencies in determining vortex ring circulation have been demonstrated by Didden [10], its simplicity is appealing and it is still widely used in vortex ring research.

The apparently reasonable assumption that all (or nearly all) of the circulation, impulse, and energy ejected by a piston-cylinder mechanism eventually ends up in the vortex ring, independent of stroke ratio, is actually *not* trivial. Since most vortex ring research focuses on $L/D < 3$, this assumption was not fully addressed until the recent

work of Gharib, Rambod, and Shariff [12] (referred to as GRS herein). GRS considered large stroke ratios and introduced the important concept of vortex ring pinch off.

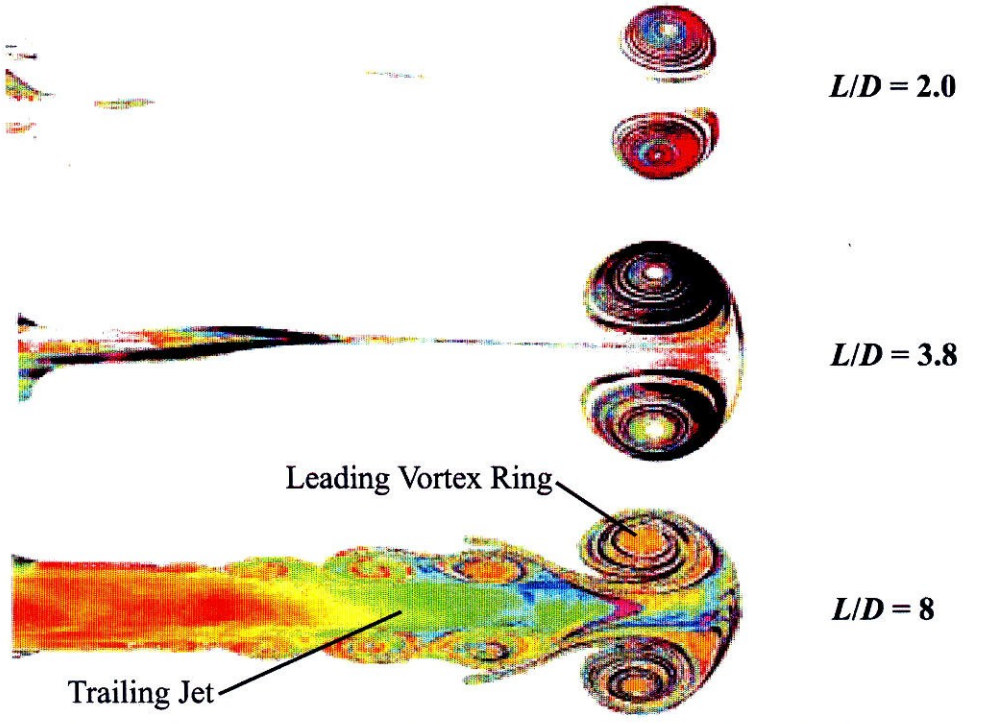

FIGURE 1.1 Illustration of Vortex Ring Pinch Off (GRS [12]).

1.2.1.1 Vortex Ring Pinch Off

On investigating vortex ring formation from a piston-cylinder mechanism for large stroke ratios ($L/D > 4$), GRS discovered that after the non-dimensional, time-dependent piston displacement $X(t)/D$ had passed a certain value[1], no additional energy or circulation entered the forming vortex ring and the remaining fluid in the pulse was simply ejected as a "trailing jet." After this point the vortex ring is said to have "pinched off" from the generating jet. This situation is illustrated by the planar laser induced fluorescence (PLIF) flow visualization for three cases with different L/D shown in Figure 1.1

1. GRS considered $X(t)/D$ to be a non-dimensional time given by $t\overline{U}_p(t)/D$ where $\overline{U}_p(t)$ is the running average of the piston velocity. At the end of a pulse, $X(t)/D = L/D$.

(reproduced from GRS). In the first two instances (L/D = 2.0 and 3.8), only an isolated vortex ring is formed, but for the last case (L/D = 8), the stroke ratio is sufficiently large for the leading vortex ring to have pinched off from the generating jet and it is no longer growing.

GRS defined the value of $X(t)/D$ at which pinch off occurred as the "formation number," F. The value of F was determined for several piston velocity programs and nozzle geometries by finding the value of $X(t)/D$ at which the circulation in the pinched off vortex ring equaled the total circulation ejected from the nozzle. For all of the cases tested, F was found to be between 3.6 and 4.5.

The narrow range for F observed by GRS led them to conclude that the formation number had a relatively universal value for vortex rings. Subsequent work has revealed that F can be significantly manipulated by adjusting at least three properties of the jet used to generate a vortex ring. The first property of the generating jet that affects the formation number was discovered by Rosenfeld, *et al.* [28] through a series of numerical experiments simulating a piston-cylinder mechanism. In attempting to numerically replicate the results of GRS, Rosenfeld, *et al.* also studied the effect of varying the velocity profile of the jet at the nozzle exit. Varying the jet profile away from a nearly uniform profile was found to reduce the formation number. When the jet velocity profile was blunted to the limiting case of parabolic, F was reduced to 1.0. Rosenfeld, *et al.* explained this by noting that the normalized vortex ring circulation [$\Gamma_{ring}/(U_{max}D)$, where U_{max} is the maximum piston velocity during the pulse] appears to universally fall between 1.8 and 2.6, while the vorticity flux from the nozzle for the parabolic profile increases by approximately a factor

of four over the uniform profile. Thus, the pinch off should occur at a value of X/D four times smaller than for the case of a uniform profile.

The second jet property affecting the formation number is the form of the velocity program (i.e., the piston velocity as a function of time) used to generate the pulse. This was briefly discussed by Rosenfeld, *et al.*, who showed that the formation number could be increased to 5.22 for a linearly increasing velocity program (with a nearly uniform velocity profile). The suggestion that increasing the velocity during a pulse ejection can increase the formation number was also confirmed numerically by Mohseni *et al.* [21] who simulated the compressible Navier-Stokes equations with a time-varying non-conservative force as the vortex generating mechanism. Mohseni, *et al.* reasoned that increasing the jet velocity during a pulse increases the formation number because it forces the shear layer of the following jet to keep up with the leading vortex (which continues to gain velocity as its circulation increases), thereby allowing vorticity to be added to the ring for a longer period of time[2].

The final property of the generating jet known to affect the formation number is the time dependent behavior of its diameter. Mohseni, *et al.* [21] numerically simulated a case analogous to a piston-cylinder mechanism with a time varying diameter. By effectively increasing the diameter during the generation of the vortex ring, they were able to achieve a leading vortex very near to the limiting case of Hill's spherical vortex (i.e., large formation number). The explanation given by Mohseni *et al.* for this effect was that increasing the diameter counteracted the tendency of the velocity field induced by the vor-

2. The suggestion that the relative velocity of the forming vortex ring and the shear layer of its generating jet is a critical parameter determining vortex ring pinch off was actually first proposed by Shusser and Gharib [34], as will be discussed later.

tex ring to push the shear layer feeding the ring toward the symmetry axis where its strength is reduced.

1.2.1.2 Models of Vortex Ring Pinch Off

The interesting nature of vortex ring pinch off and its recognized importance as a maximization principle for vortex ring formation has led to many efforts to model vortex ring pinch off and predict the formation number. The first model was proposed by GRS. Using the Kelvin-Benjamin variational principle for steadily translating vortex rings, GRS hypothesized that vortex ring pinch off occurs when the generating jet is no longer able to supply energy at a rate compatible with the requirement that a steadily translating vortex ring have maximum energy with respect to impulse-preserving, iso-vortical perturbations. Using the slug model to calculate the value of the non-dimensional energy supplied by the jet, they obtained good agreement between formation numbers observed experimentally and those predicted by this model, but were forced to rely on experimental results to determine the limiting value of the non-dimensional energy for vortex rings. Mohseni and Gharib [20] were able to predict this limiting value to within reasonable accuracy by assuming that the fluid discharge from the cylinder nozzle can be described by the slug model and that the vortex ring at the moment of pinch off can be approximated as a member of the Norbury [24] family of vortices.

While the model based on the Kelvin-Benjamin variational principle is functional, it gives little insight into the physical mechanism leading to vortex ring pinch off. This realization led Shusser and Gharib [34] to consider a kinematic model of the formation process based on the assumption that pinch off occurs when the ever-increasing velocity

of the ring becomes equal to the velocity of the jet immediately behind the ring, causing the ring to physically separate from the generating jet. Shusser and Gharib [35] were able to show that this model also predicts the limiting value of the non-dimensional energy used in the model based on the Kelvin-Benjamin variational principle. In a more recent paper, Shusser *et al.* [36] have extended the model to cases of time varying piston velocity programs and have clearly demonstrated the mechanism that increases formation number when the piston velocity increases with time.

A final model for vortex ring pinch off was proposed by Linden and Turner [17]. Here the slug model and Norbury family of vortex rings is employed as in Mohseni and Gharib [20], but the equations are closed by imposing the additional constraint that the volume of fluid emitted by the jet and that in the pinched off vortex ring are the same. This leads to a formation number of 3.5 for piston velocity programs with uniform velocity, but, as shown by Shusser *et al.* [36], the model incorrectly predicts the formation number for time varying velocity programs.

1.2.2 Pulsed Jets

Pulsed jets have an imposed unsteady component to the jet velocity at the nozzle exit plane. The most common case is where the unsteady component is a small fraction (a few percent) of the mean jet velocity, which is often referred to as a forced jet. The limiting case where the jet velocity returns to zero between pulses (possibly for finite time) is referred to as a fully-pulsed jet. The literature on fully-pulsed jets is sparse, but extensive information exists for forced jets.

Most of the literature on forced jets is concerned with the mean and fluctuating velocities in the flow (near or far field) and the enhanced entrainment and mixing effects achieved through forcing. Attention has also been given to the dynamics of "coherent structures" produced in the near jet region (e.g., Crow and Champagne [9], and Broze and Hussain [6] and [7]), which are sometimes referred to as "puffs" or even vortex rings, where the interest has been in transition to turbulence. In these studies it is difficult to know to what extent the results are related to vortex ring formation as described previously since forced jets enhance a Kelvin-Helmholtz type instability in the jet shear layer while the vortex rings are associated with the roll-up of a half-infinite vortex sheet. Nevertheless, it is interesting to note that Vermeulen *et al.* [38] directly measured the entrainment of an acoustically forced axisymmetric jet and found a maximum entrainment rate at a Strouhal number, *St*, of approximately 0.24. Given that $St = fD/\bar{U} = D/(T\bar{U})$ where $\bar{U}$ is the average jet velocity and $f = 1/T$ is the pulsing frequency, *St* can be interpreted as the inverse stroke ratio for a pulse (see footnote 1). This seems to imply that the maximum entrainment rate occurs for $L/D \approx 4$, which suggests that vortex ring pinch off may play a role in the entrainment process for forced jets and, conversely, that vortex ring formation in starting jets or fully-pulsed jets could be a powerful entrainment mechanism.

The experimental work on fully-pulsed jets, on the other hand, is due primarily to Bremhorst, *et al.* (e.g., Bremhorst and Hollis [4] and Bremhorst and Gehrke [5]). While Bremhorst and Gehrke [5] were interested in measurements of Reynolds stress and energy budgets in the downstream region (greater than 50 diameters from the nozzle) for the purpose of modeling turbulence, Bremhorst and Hollis [4] considered behavior in the near jet as well. They noted that the ordered nature of the leading vortex produced by each pulse

yielded a region of "pulse dominated" flow that extended to 50 diameters downstream and it was not until after this point that the center line velocity decay and center line turbulence intensities approached those expected for steady jets. Bremhorst and Hollis also reported entrainment twice that of an equivalent steady jet and they attributed the increase to the vortex ring formed by each pulse, in qualitative agreement with above speculation based on the results of Vermeulen *et al.* [38]. No information was given about the effect of vortex ring formation on impulse or thrust since this study was primarily concerned with the development of the flow field. Furthermore, these results were for stroke ratios of greater than 140 and an on-to-off ratio of 1:2, which suggests each pulse had a very long trailing jet associated its the leading vortex ring and was greatly separated from the preceding pulse.

Theoretical work on fully-pulsed jets has been done by Siekmann [37] (2D) and Weihs [39] (axisymmetric) in the context of aquatic propulsion. In both cases, the analysis is based on an assumed flow structure for the jet [vortex rings (Weihs) or vortex pairs (Siekmann)], but this flow is taken as the result of a fully-pulsed jet. Since Weihs considers the axisymmetric case, only his analysis will be discussed.

Weihs considers the case where a propeller has been emitting pulses for a long time, yielding an infinite train of vortex rings. In a control volume analysis, the vortex rings are treated as particles with a (constant) associated mass and a velocity determined by the structure of the vortex train. Then the thrust is proportional to the rate at which vortex rings leave the control volume, which is determined by their velocity. Appealing to the result that the velocity of rings in an infinite train increases as their separation decreases, he reasons that substantial (several tens of percent) propulsive benefits could be

obtained by aquatic creatures if their pulsing frequency was sufficiently high to take advantage of this mutual effect of vortex rings on one another. The limiting value of the ratio of ring separation to ring radius above which little or no velocity/thrust increase is expected is about 3 to 4.

1.3 Objectives

The potential significance of vortex ring pinch off for pulsatile propulsion was first conjectured by GRS. This conjecture is scrutinized by this investigation in the context of starting and fully-pulsed jets. Special emphasis is placed on determining whether or not vortex ring pinch off represents a maximization principle for propulsion in that pulses with stroke ratios giving vortex rings of maximal circulation (i.e., on the verge of pinching off) maximize some dynamic quantity (e.g., impulse or thrust). If so, it is of interest to determine what fluid mechanical mechanisms related to the formation of vortex rings (e.g., entrainment) are responsible for this maximization. Stated differently, the goal is to determine the relative importance of the leading vortex ring and trailing jet on the dynamic quantities (e.g., impulse, energy, and circulation) generated by individual pulses issuing from a piston cylinder mechanism. Motivated by Weihs' result, it is also of interest to determine the effect of the spacing of successive pulses in a fully-pulsed jet to see if propulsive benefits can be obtained by packing vortex rings sufficiently close together and whether or not close-packing of pulses affects vortex ring formation and/or pinch off. Whereas the interest in vortex ring pinch off is concerned with determining an optimal stroke ratio for pulsatile propulsion, the interest in pulse spacing is related to finding an optimal pulsing frequency.

These objectives are addressed by direct measurement of the total impulse associated with starting jets of varying stroke ratio and the time averaged thrust of fully-pulsed jets with varying stroke ratios and pulsing frequencies. The measurements for the fully-pulsed jets are related to the structure of the jets using Digital Particle Image Velocimetry (DPIV), which is also used to determine the energy and circulation associated with the starting jets. The apparatus used for these experiments is described in chapter 2. Chapter 3 discusses the measurements of the dynamic quantities impulse, energy, and circulation of individual starting jets while chapter 4 presents the time averaged thrust measurements of several fully-pulsed jets along with DPIV measurements of the associated jet structure. The results are summarized and recommendations for future work are given in chapter 5.

CHAPTER 2

Experimental Apparatus and Setup: Design, Operation, and Characterization

2.1 General Description of the Experiment

This investigation studies the dynamic properties (specifically the impulse or time averaged thrust) of starting and fully-pulsed jets and how these properties are related to the formation and structure of the jet. Generation of a fully-pulsed jet is illustrated schematically in Figure 2.1 where a periodic series of finite-duration, round water jets with diameter D are ejected into quiescent water. The length of the ejected pulses L is defined by

$$L = X(t_p) \tag{2.1}$$

where

$$X(t) \equiv \int_0^t U_J(\tau)d\tau\,, \tag{2.2}$$

$$U_J(t) \equiv \frac{1}{A}\int_A u_J(r, t)dS\,, \tag{2.3}$$

u_J is the jet velocity at the nozzle exit plane ($x = 0$), A is the cross-sectional area of the nozzle at $x = 0$, and t_p is the pulse duration. The ejection rate of the pulses (pulsing frequency) is $f = 1/T$, where $f < 1/t_p$ since a fully-pulsed jet requires that the flow between pulses return to zero. By specifying $U_J(t)$, f and L can be varied independently and the velocity program (defined as the time dependence of $U_J(t)$ between $t = 0$ and t_p) can be altered, all of which can affect properties of the resulting jet. The flow reduces to a starting jet in the limit $f \rightarrow 0$.

Given this general setting, thrust or impulse measurements were obtained by direct measurement of the force on the apparatus generating the jet. The flow was evaluated at the nozzle using hotfilm anemometry and in the bulk using digital particle image velocimetry (DPIV). Finally, limited flow visualization was performed using planar laser induced fluorescence (PLIF).

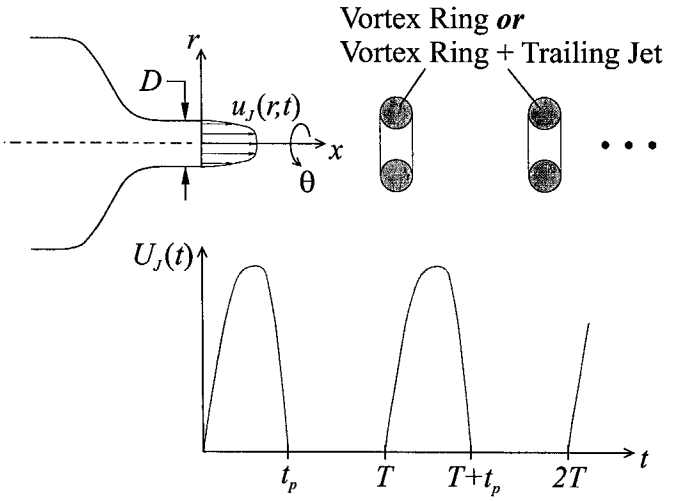

FIGURE 2.1 General Schematic of the Experiment.

2.2 General Description of the Experimental Apparatus and Its Operation

A layout schematic of the relevant features of the apparatus used to generate the fully-pulsed jet for this experiment is shown in Figure 2.2. The basic system consists of two piston-cylinder arrangements (one oriented vertically and the other oriented horizontally) connected by a combination of PVC piping and a flexible hose. Because of the incompressibility of water, the floating piston in the horizontal cylinder follows the motion of the driver piston (actuated by the servo motor), as indicated by the gray arrows in the figure. Most of the cylinder pieces were made from Plexiglas. The pistons were made from Ultra-High Molecular Weight (UHMW) plastic. Other pieces were made from anodized aluminum, stainless steel, or other corrosion-resistant materials.

The entire apparatus was mounted in a tank facility with dimensions of 37 3/4 in. (95.9 cm) by 33 3/4 in. (85.7 cm) by approximately 12 ft. 31 in. (444.5 cm). The tank frame was steel and the walls were 3/4 in. glass for flow visualization purposes. The apparatus was rigidly fixed to the top of the tank with steel fixtures. The hatch marks in Figure 2.2 indicate the portions of the apparatus that were, in some way, rigidly fixed to the tank. The entire apparatus was mounted at one end of the tank, making the minimum separation of the nozzle from any of the boundaries that of the distance between the nozzle center line and the free surface, namely 12.45 in. (31.6 cm = 24.9D where D is the nozzle diameter).

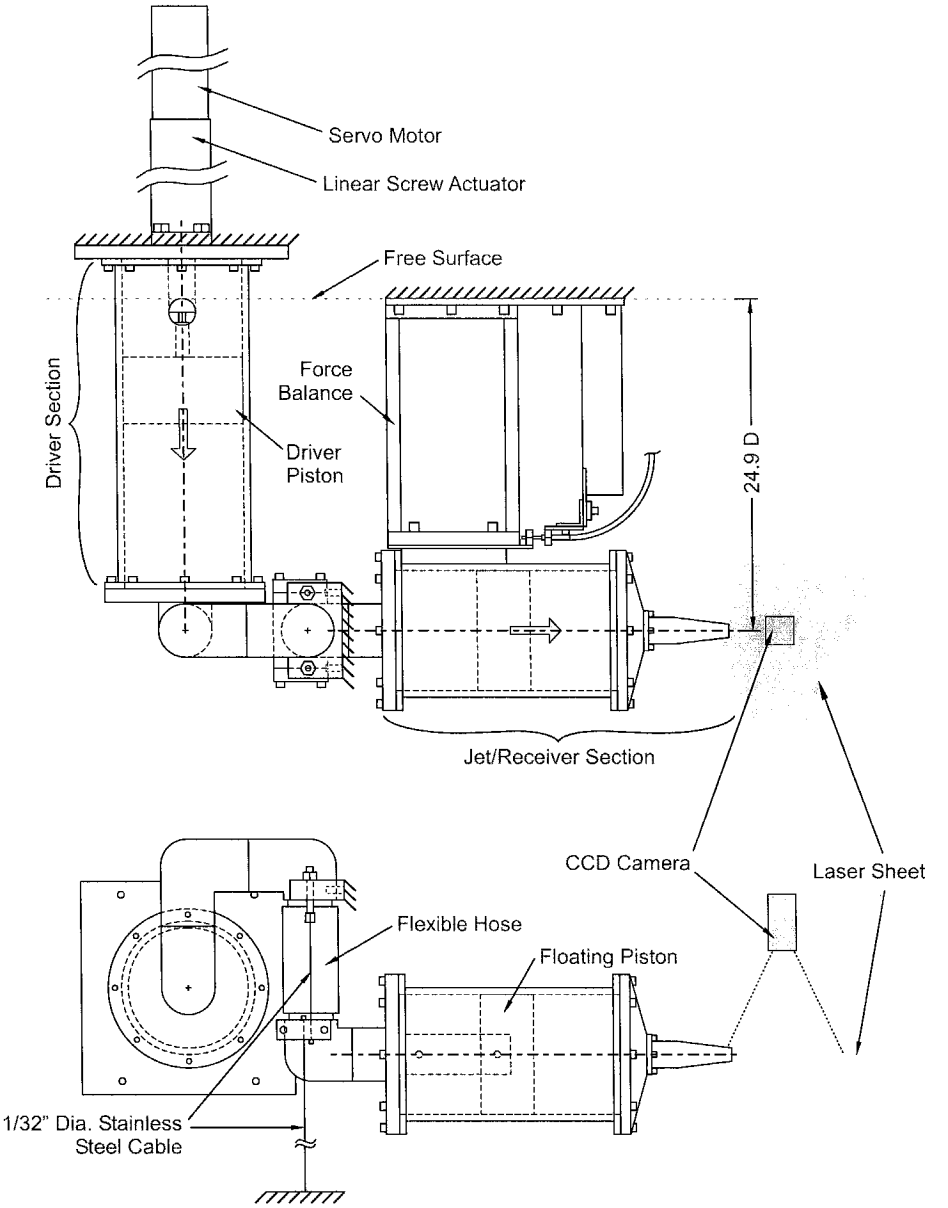

FIGURE 2.2 Schematic of the Apparatus Used to Generate a Fully-Pulsed Jet. Only those hidden features necessary to illustrate the operation of the device are shown. Hatch marks indicate those features which have been rigidly attached to the tank.

2.2.1 Driver Section Details and Operation

The driver section consists of a (nominal) 4.5 in. inner diameter (5.0 in. out diameter) Plexiglas cylinder with a UHMW piston, Plexiglas base plate and associated plumb-

ing, and a computer controlled servomotor/actuator combination. The diameter of the piston was machined to within 0.002" of the inner diameter of the cylinder to provide a nearly water tight seal without the use of O-rings or other gaskets. Although it was observed that the Plexiglas swelled slightly with prolonged exposure to water while the piston geometry appeared relatively stable, an acceptable seal between the piston and cylinder was maintained throughout the experiment, providing no discernible leakage past the cylinder during operation.

To achieve zero backlash between the driver piston and the actuating mechanics, the piston was connected to the linear actuator via a direct, bolted connection. The actuator itself was a Dynact "Pulse Power II" in-line linear actuator [Dynact designation CU/PP1-B5(DN)-D1-XX-12-FLF-TSF(1/4-28)-MS(3)-ES] with a 0.20" lead on the drive screw (accurate to within 0.015 in. per foot), a zero backlash nut ("double-nut" configuration), and a 7 in. useful stroke length. The actuator was coupled to the servomotor with a Helical XCA25-9mm-8mm flexible coupling with a torsional stiffness of 4.55 Nm/degree. This configuration provided an extremely stiff connection between the servomotor and the driver piston with zero backlash, which was necessary for precise positioning and actuation of the driver piston.

The servomotor used to drive the system was an Indramat MKD025B-144-GP1-KN servomotor with an available torque of 2.4 Nm and a maximum revolution rate of 8400 rpm. The motor was driven by an Indramat DKC01.1-030-3 drive. The drive provided the signal to operate the motor and closed the velocity loop for control of the motor. The actual motor operation and position loop closure was controlled via PC using a Delta-Tau Mini-PMAC multi-axis programmable controller. Through software provided by

Delta-Tau, the controller was able to command the actuator to move through virtually any specified path, whether the path is specified as position or velocity as a function of time.

The following error between the commanded and actual position of the motor was minimized by proportional-integral-derivative (PID) control with velocity and acceleration feed-forward gains, where the actual motor position was taken from the output of the internal angular position encoder on the motor. The encoder output was calibrated to 25,000 counts per inch of linear motion. This calibration was found to be accurate to within 0.0005 in. (the resolution of the measuring device).

Overall, the motor was found to have sufficient torque to give the desired piston accelerations for the experiment, despite the large inertia between driver piston and the nozzle exit, while the versatility provided by computer control was a luxury that later proved essential to the operation of the experiment (see section 2.4.2.1).

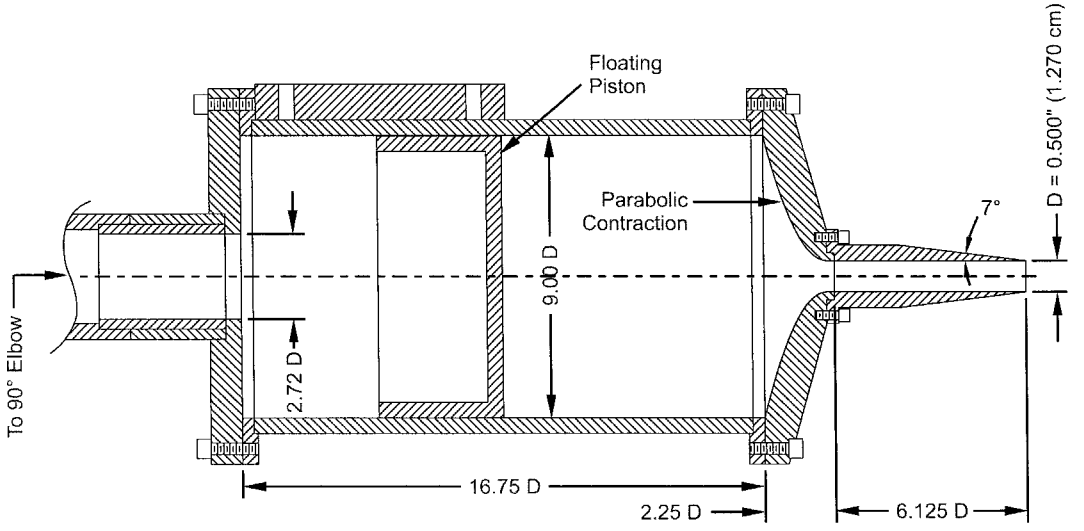

FIGURE 2.3 Cross Section of the Jet/Receiver Section.

2.2.2 The Jet Section

A cross section view of the jet section is shown in Figure 2.3. The flow from the piping connecting the jet and driver sections enters from the left where it encounters the floating piston. The floating piston ensures that the flow out of the nozzle is free from any disturbances introduced after passing through the plumbing connecting the two cylinders. At the exit of the jet section, the flow is contracted from a diameter of 4.5 in. to a diameter of 0.5 in. using a parabolic contraction to provide smooth, attached flow at the entrance of the nozzle. The nozzle had a diameter of D = 0.5 in (1.27 cm) with a length of $6.125D$ (i.e., > $6D$) and a tip angle of 7° so that vortex rings formed by the ejection of fluid pulses during the experiment experience only minimal interaction with the surfaces behind the nozzle exit plane.

Although this design is slightly more complicated than the standard configuration for a piston cylinder mechanism used for generating vortex rings and ejecting fluid pulses, it fit the requirements of this experiment nicely. First, the large contraction between the piston diameter and the nozzle diameter allows large flow rates through the nozzle (U_J), and hence large (i.e., easily measurable) thrust values, to be obtained with only moderate piston velocities. Furthermore, since the fluid is incompressible, the piston displacement, L_p, for a single pulse is related to the length of the fluid "slug" ejected from the nozzle, L, through continuity by

$$\frac{L_p}{L} = \left(\frac{D}{D_p}\right)^2 \tag{2.4}$$

where D_p is the piston diameter (4.5 in.). The large contraction ratio therefore allows for a large number of pulses of moderate L/D (i.e., $2 < L/D < 10$) without requiring a large accumulated displacement of the piston. Second, by isolating the jet section from the drive mechanics, the overall mass of this component was substantially reduced. Since the flexible force balance and the attached jet section comprise a resonant mass-spring system, reducing the mass of the jet section gave a much higher resonant frequency of the system without compromising the sensitivity of the force balance. The resonant frequency of the system was a critical design factor since some experimental conditions required pulsing the jet up to 22 Hz.

2.2.3 The Connecting Plumbing

The piping between the jet and driver sections was made primarily of 1 1/4 in. PVC pipe with the exception of a small (~ 3 in.) section of flexible hose that connects to the jet section at a right angle to the sensing axis of the force balance. The section of flexible hose was necessary since one objective of the experiment was to measure the force on the jet section. The stainless steel cables shown in the bottom view in Figure 2.2 constrain the length of the flexible hose, making the volume of fluid between the driver and floating pistons constant. Since the cables were 1/32 in. in diameter and greater than 6 in. in length, they were unable to support loads aligned with the axis of the force balance and, therefore, did not significantly affect the sensitivity of the force balance. Finally, in order to prevent extraneous forces generated by the operation of the driver section from being transmitted to the jet section, the point where the PVC pipe from the driver section enters the flexible hose was rigidly fixed in place by an attachment mounted to the tank.

2.3 Measurement Techniques

The measurements of interest for this experiment were the force on the jet section in the direction of the nozzle axis (i.e., thrust), the time-varying average and center-line jet velocities at the nozzle exit plane [$U_J(t)$ and $u_{cl}(t)$ respectively], and full field velocity measurements near the nozzle exit (i.e., $0 < x < 10D$). These measurements were obtained using a custom-made force balance, hotfilm anemometry of the center line velocity at $x = 0$, and digital particle image velocimetry (DPIV) measurements of the near-field jet.

2.3.1 The Force Balance

A schematic of the force balance used to measure the thrust produced by the jet section is shown in Figure 2.4. Figure 2.2 illustrates how it is mounted to the jet section. The top of the force balance is bolted into steel fixtures, providing rigid support for the device and a direct connection to the top of the tank, as represented by the cross hatching in Figure 2.2. All of the components except the displacement transducer and its mounting brackets were made from anodized aluminum.

The configuration of the force balance is basically a parallel bending beam design where the force is determined by direct measurement of the displacement of the beam when a force is applied. Then, as long as the forces remain primarily in the elastic regime of the beam, Hook's law applies and the measured beam displacement is linearly proportional to the applied force.

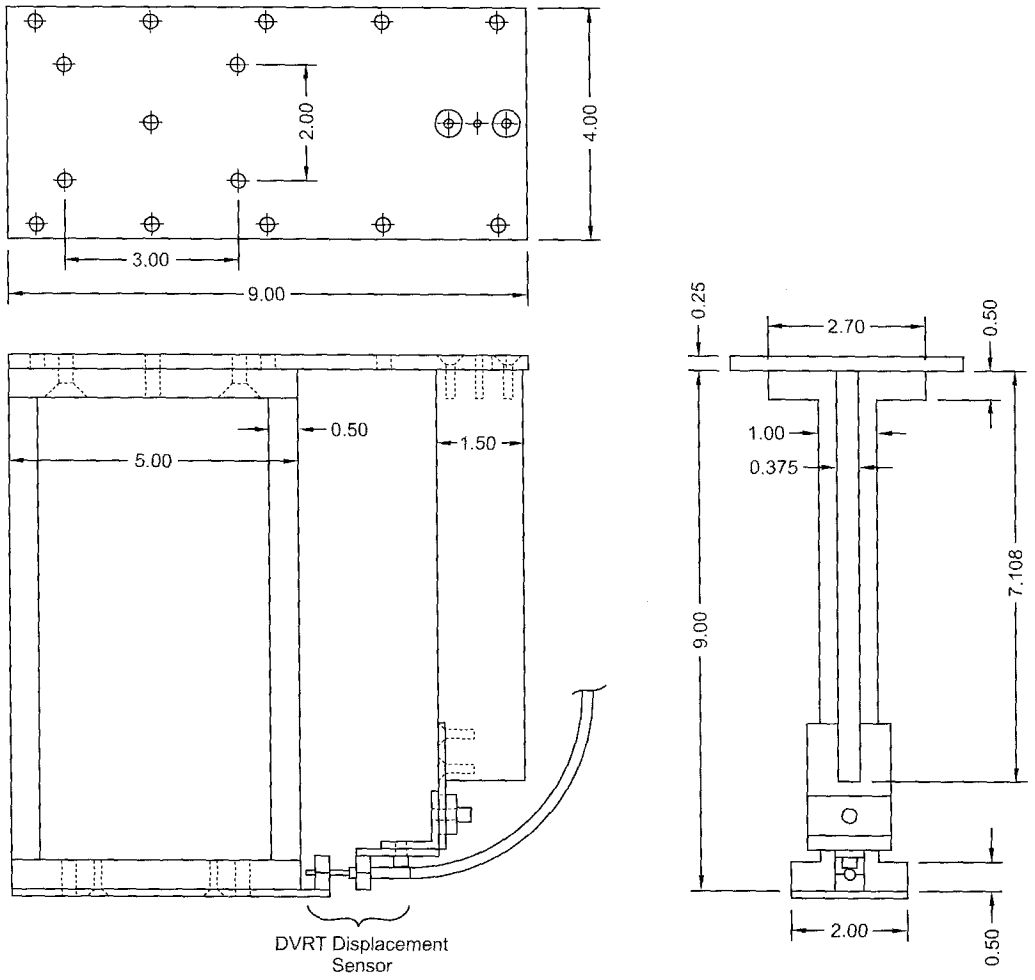

FIGURE 2.4 Schematic of the Force Balance Used for Force Measurements. Only those hidden lines necessary to illustrate the assembly of the device are shown. All dimensions are in inches.

To prevent significant motion of the jet section during pulsed operation, the force balance beam was designed with a stiffness in the direction of the jet axis of $5.07\times10^{5} N/m$. To provide the desired force sensitivity, a MicroStrain Super High Resolution Differential Variable Reluctance Transducer (DVRT) was used to measure the displacement. The sensitivity of the DVRT was 13.067 V/mm and the device was linear to within 0.2% over its 0.5 mm stroke length. Given these specifications, the force balance

was easily able to resolve forces smaller than 1 gram (0.0098 N), *without* any signal conditioning, and its overall response was linear.

During actual experiments, the force data was collected by a personal computer using LabView and a National Instruments PCI-1200 12-bit A/D converter with a -5 V to + 5V range. To achieve sufficient resolution of the input signal after A/D conversion and to prevent aliasing, the signal from the DVRT was conditioned by a x50 pre-amp with a low pass filter. The force signals were typically sampled at > 400 Hz.

2.3.2 Hotfilm Measurements

Hotfilm measurements of the jet velocity at the nozzle exit plane ($x = 0$) were accomplished with a TSI 1231W hotfilm probe using a TSI IFA-100 flow analyzer and a Model 150 anemometer. After filtering with a low pass filter (1 kHz cutoff frequency), the signal was sampled at 1 kHz (using a the same A/D converter that sampled the force balance signal) and saved to disk following processing by LabView.

To obtain the desired measurements of the jet velocity, the probe was positioned at the nozzle exit plane and on the nozzle center line to within 1 mm (0.078D) in all three dimensions. The desired accuracy in the measurements was ensured by repeated calibrations using the flow produced by steady (commanded) piston motion over flow rates U_J ranging from 20 cm/s to 144 cm/s and fitting the results to a curve of the form

$$U_{cal} = aS^n \tag{2.5}$$

where S is the signal from the probe in volts and $n \approx 4$. The fit for a and n was done to minimize the sum of the percent errors between U_{cal} and the reference velocity deter-

mined from the known piston velocity and the known contraction ratio between the piston and nozzle diameters. The resulting calibration was accurate to within 2% over the range of velocities observed in the investigation. The calibration expressed by equation (2.5) is not exactly correct in that the hotfilm is measuring the center-line velocity and not the mean flow rate through the nozzle U_J (i.e., $U_{cal} = U_J$ only for steady cases), which is an issue addressed in section 2.4.

Finally, since the presence of the hotfilm probe disturbs the flow outside of the nozzle, experiments to measure the thrust and jet velocity were done separately.

2.3.3 DPIV Measurements

The DPIV technique for flow field measurement is described in detail by Willert and Gharib [41] and Raffel, *et al.* [27], so only a general description of the technique and details relevant to the measurements in this investigation will be described.

In DPIV, two digital images of a particle-seeded flow illuminated by a thin laser sheet are used to determine the displacement field of the particles in the field of view. By cross-correlating pixels in a subsection of the two images (sampling window), the average displacement of the particles in the sampling window can be determined. Applying this procedure repeatedly to windows spanning the two images generates the flow displacement field at the instant midway between the time at which the images were taken. Dividing by the time difference between the two images yields the velocity field of the flow in the plane of the laser sheet used to illuminate the flow.

The technique can be further refined if the images are processed twice: once using the method above and a second time using the displacement field just determined to guide

which pixels (of the size of the sampling window) in the second image should be cross-correlated with the sampling window at a given location in the first image. This refinement, known as "window shifting," substantially reduces errors in DPIV vector fields by accounting for particles that have convected out of the sampling window between the time the two images were taken. A detailed analysis of the effect of window shifting on the accuracy of DPIV results is presented by Westerweel *et al.* [40].

The particles used to seed the flow in this experiment were neutrally buoyant, silver coated hollow glass spheres with diameters in the range of 40 - 60 μm. The particles were illuminated with an Nd:YAG laser with a power rating of 50 mJ per pulse. A cylindrical lens was used to form a laser sheet, which was positioned relative to the nozzle as indicated schematically in Figure 2.2. The laser was slaved to a Pulnix CCD camera (model TM-9701) with a frame size of 480 x 768 pixels, an 8-bit intensity resolution per pixel, and a 30 Hz frame rate. At two images per vector field this gave a data rate of 15 Hz. Various lenses were used with the camera, depending on the size of the desired field of view.

Processing of the PIV images was accomplished using in-house code. Generally two approaches were taken depending on the field of view. For the starting jet ($f = 0$) experiments discussed in chapter 3, the sampling window was 32x32 pixels with a 16 pixel offset (giving a spacial resolution of $0.099D$ in x and $0.12D$ in r). For improved accuracy, the images were processed a second time with a window shifting algorithm using the same sampling window size and window offset. This produced very accurate vector fields with few or no errant vectors per image. For the fully-pulsed jet experiments in chapter 4, the focus was more on the overall structure of the jet, so the field of view was

enlarged and more importance was placed on spacial resolution than on vector accuracy. As such, the images were first processed with 32x32 pixel sampling windows with 8 pixel offset and then reprocessed with a window shifting algorithm using sampling windows of 16x16 pixels and 8 pixel offset. This resulted in slightly more errant vectors (mostly near the cores of the vortex rings) but doubled the spatial resolution. (At the magnification used for these cases the spacial resolution was $0.097D$ in x and $0.11D$ in r.) The effect of the increase in errant vectors on determination of vortex ring circulation and locations of the vortex ring centroids or vorticity peaks was observed to be minimal.

2.4 Flow and System Characterization

Before any actual investigations of vortex rings or fully-pulsed jets were initiated, several simple experiments were performed to determine if the system was behaving according to design. These experiments involved measurements of the jet velocity and thrust for constant commanded piston velocities, U_p, and measurements of the time varying jet velocity U_J for a few pulsed cases.

2.4.1 PIV Measurements of the Steady Jet

To address the hotfilm calibration issue noted in section 2.3.2, PIV measurements of the (time averaged) jet velocity at the nozzle exit plane, $\overline{u_J}(r)$, were performed for steady commanded piston velocities in the range 0.1 in/s to 1.0 in/s in increments of 0.1 in /s. This range represents twice the desired piston velocity range for the starting jet and fully-pulsed jet experiments. Extracting the results near the center line ($r = 0$) gives a cal-

ibration curve for $r_v \equiv u_{cl}/U_J$ where u_{cl} is the center line velocity. This calibration curve is shown in Figure 2.5. A least squares fit of this data (accurate to within 2%) gives

$$r_v = \frac{u_{cl}}{U_J} = 16.100 Re_a^{-0.5244} + 1 \tag{2.6}$$

where

$$Re_a \equiv \frac{U_J D}{\nu} \tag{2.7}$$

and ν is $9.60\times10^{-7}\ m^2/s$ for water. Equation (2.6) can also be expressed as

$$u_{cl} = 0.111 U_J^{0.4756} + U_J. \tag{2.8}$$

Therefore, since $U_{cal} = U_J$ under the conditions for which equation (2.8) is valid, combining equations (2.8) and (2.5) gives a hotfilm calibration for u_{cl} that is accurate to within 3%, *independent of the unsteadiness of the measured flow* since it involves no assumptions about the velocity profile $u_J(r, t)$.

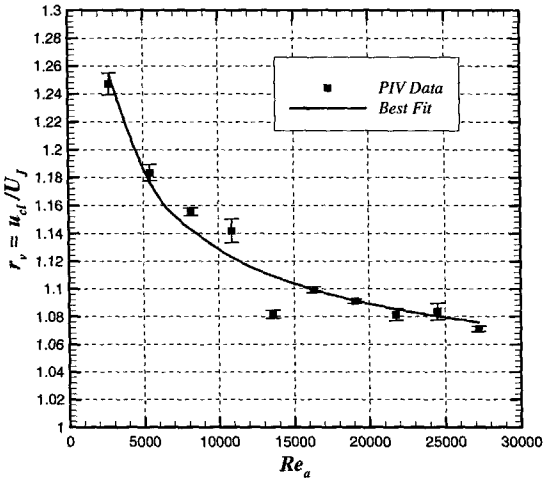

FIGURE 2.5 Calibration Curve of r_v vs. Re_a from PIV Measurements of the Nozzle Flow at $x = 0$.

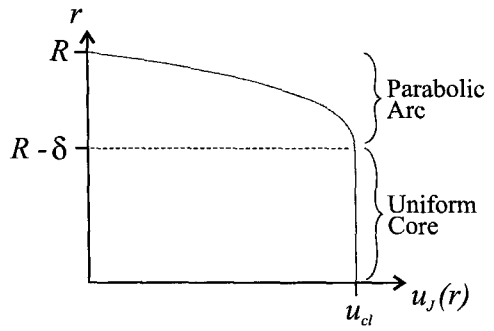

FIGURE 2.6 Illustration of Assumed Velocity Profile at Nozzle Exit Plane.

It is also interesting to consider these results from the standpoint of steady state entrance pipe flow. In this case the abscissa of interest is $\frac{x_N}{R \cdot Re_R}$ where $x_N = 6.125D$ is the distance from the nozzle/pipe entrance to the nozzle exit plane, R is the nozzle radius and

$$Re_R = \frac{U_J R}{\nu}. \tag{2.9}$$

Applying this equation to the results of Figure 2.5 shows that $0.009 < \frac{x_N}{R \cdot Re_R} < 0.0009$ for the cases studied here. Since the entrance length for steady pipe flow is $\frac{x_N}{R \cdot Re_R} = 0.26$ (Prandtl and Tietjens [25]), it follows that the flow is well within the realm of entrance pipe flow for nearly all jet velocities of interest in this experiment. Following L. Prandtl [25] it can therefore be assumed that the velocity profile at the nozzle $\overline{u_J}(r)$ is flat near the center and tapers off parabolically to zero at the wall between $r = \delta$ and $r = R$, as illustrated in Figure 2.6. Using this assumed profile, conservation of mass gives

$$\frac{\delta}{R} = 2 - \sqrt{\frac{6}{r_v} - 2}. \tag{2.10}$$

Re-plotting Figure 2.5 in coordinates of $\frac{\delta}{R}$ vs. $\frac{x_N}{R \cdot Re_R}$ gives Figure 2.7, which indicates that

$$\frac{\delta}{R} = 3.78\left(\frac{x_N}{R \cdot Re_R}\right)^{0.51}. \tag{2.11}$$

Finally, defining

$$Re_{x_N} \equiv \frac{U_J x_N}{\nu} \tag{2.12}$$

and substituting into equation (2.11) gives

$$\frac{\delta}{R} = 3.78 Re_{x_N}^{-0.51} \approx 3.78 Re_{x_N}^{-1/2}. \tag{2.13}$$

The nozzle flow for this apparatus, therefore, follows the expected trend that the normalized boundary layer thickness (represented by δ/R in this case) decays like $Re^{-1/2}$.

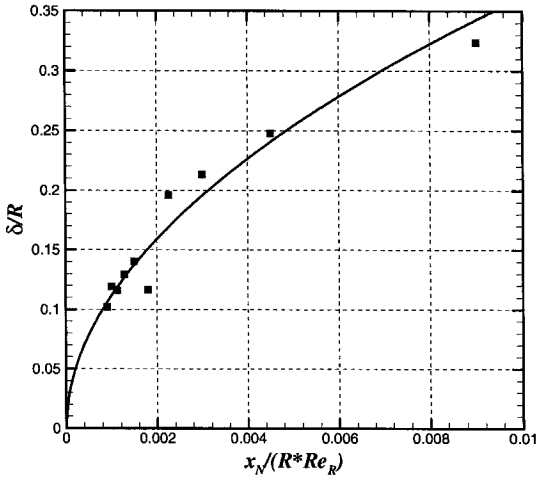

FIGURE 2.7 Data of Figure 2.5 Plotted in Re-normalized Coordinates.

2.4.2 Hotfilm Measurements of "Steady" Jets

To achieve better time resolution of the jet flow, the steady jet experiments of section 2.4.1 were repeated and the jet velocity U_J (actually, U_{cal}) was measured for U_p between 0.1 in/s and 0.7 in/s. The results for 0.1 in/s < U_p < 0.5 in/s are plotted in Figure 2.8 (a). Clearly the jet flow is anything but steady, despite the fact the commanded piston velocity is steady[1]. This is a very undesirable result, but because the experiment is not concerned with *steady* jets, all is not lost. The question now remains if this problem can be avoided for jet pulses of finite duration t_p by appropriately shaping the commanded piston motion during a pulse. This possibility is first considered by looking at the frequency response of the data in Figure 2.8 (a).

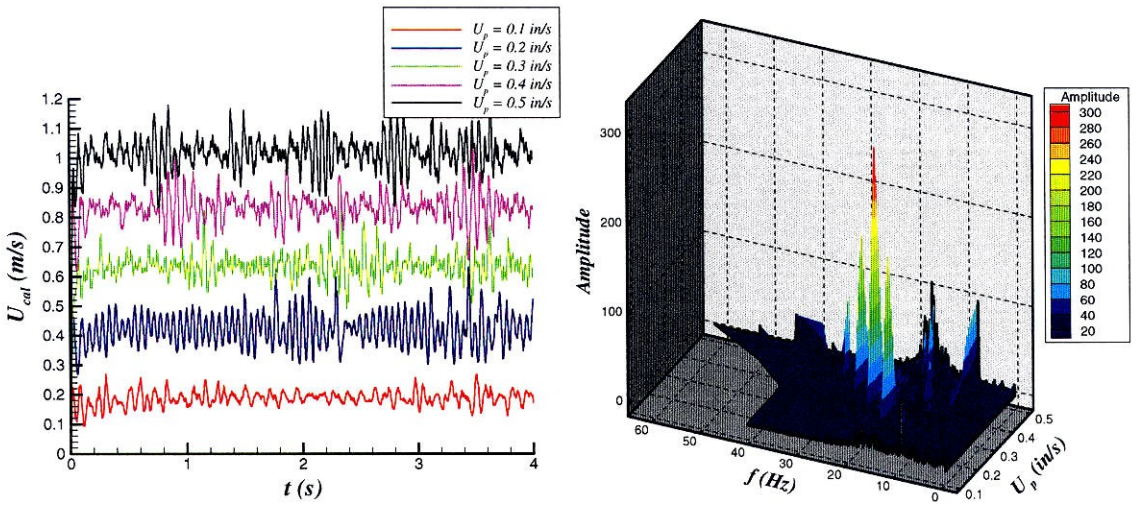

(a) (b)

FIGURE 2.8 Results of the Hotfilm Measurements of the Jet Velocity at the Nozzle Exit Plane for Steady Commanded Piston Motion: (a) Velocity measurements as a function of time, (b) frequency response of the data in (a).

1. Because of this phenomenon, the "steady" PIV results and hotfilm calibration scheme described earlier are based on the *time averaged* jet flow $\overline{U_J(t)}$ and $\overline{u_J(r,t)}$ for steady commanded piston velocities.

2.4.2.1 Frequency Response of the "Steady" Jet Velocity as a Function of Piston Speed

The frequency response of the jet velocity data in Figure 2.8 (a) is shown in Figure 2.8 (b). From this figure, a series of peaks that appears to dominate the dynamics is seen to appear around 10 Hz at $U_p = 0.1$ in/s and steadily increase with U_p until reaching about 30 Hz for $U_p = 0.4$ in/s. This response is most likely due to friction between the piston and cylinder in the driver section since its effects were dramatically reduced when an unnecessary rubber piston seal was removed early in the testing of the apparatus. Given this observation, appendix A gives a simple model of the phenomenon based on frictional effects. The model suggests that the jet velocity for steady piston motion is unstable to small disturbances, which implies that these peaks in the frequency response would be difficult to completely eliminate. On the positive side, this analysis suggests these dynamics will primarily affect the initial portion of finite-duration pulses since the frictional effect would be most pronounced during initiation of piston motion. Thus, by tailoring the commanded piston motion during pulse initiation, it should be possible to diminish the effects of this frictional response on the jet velocity.

For larger piston velocities, Figure 2.8 (a) indicates that two more peaks begin to appear. The first starts around 5 Hz and grows to around 8 Hz at $U_p = 0.5$ in/s. The effect of this peak, however, is very isolated (i.e., the peak has zero width to within the frequency resolution of the discrete fourier transform used on the time signal), so it would be difficult for this peak to significantly affect the overall dynamics of the apparatus. The second peak, however, is much more broad. It begins around 10 Hz and grows in amplitude while its frequency increases, reaching nearly 17 Hz at $U_p = 0.5$ in/s. Since this peak

is so broad, it may pose a significant problem in the fully-pulsed jet experiments when the jet is pulsed above about 12 Hz for pulses with maximum velocities corresponding to U_p = 0.5 in/s. The exact nature of the dynamics generating this peak is unknown, but it may be related to the overall compliance of the plastic components (i.e., cylinders and piping) between the two pistons.

2.4.2.2 Comparison of Jet Velocity with Piston Velocity for Some Simple Time-Dependent Velocity Programs

Figure 2.9 shows some examples of measured jet velocity (U_{cal}) compared with the expected jet velocity based on the piston velocity program as determined from the velocity feedback of the motor encoder for a pulsing frequency of f = 2 Hz. As expected from the previous observations of the frequency response, the actual jet velocity initially undershoots and then overshoots the commanded velocity, but the jet velocity appears to be a smooth function of time during the pulse. After the pulse, a slight oscillation in jet velocity is sometimes observed, but this is easily reduced to nearly zero by appropriately shaping the commanded piston velocity program. It should also be noted that the integral of the actual and expected jet velocity with time (i.e., the pulse length L) is nearly the same, indicating the piston is very nearly moving the correct displacement at each pulse despite having to overcome friction. It is possible, therefore, to obtain jet pulses with time varying velocities appropriate for the goals of this investigation despite the fact that the apparatus cannot generate a steady jet.

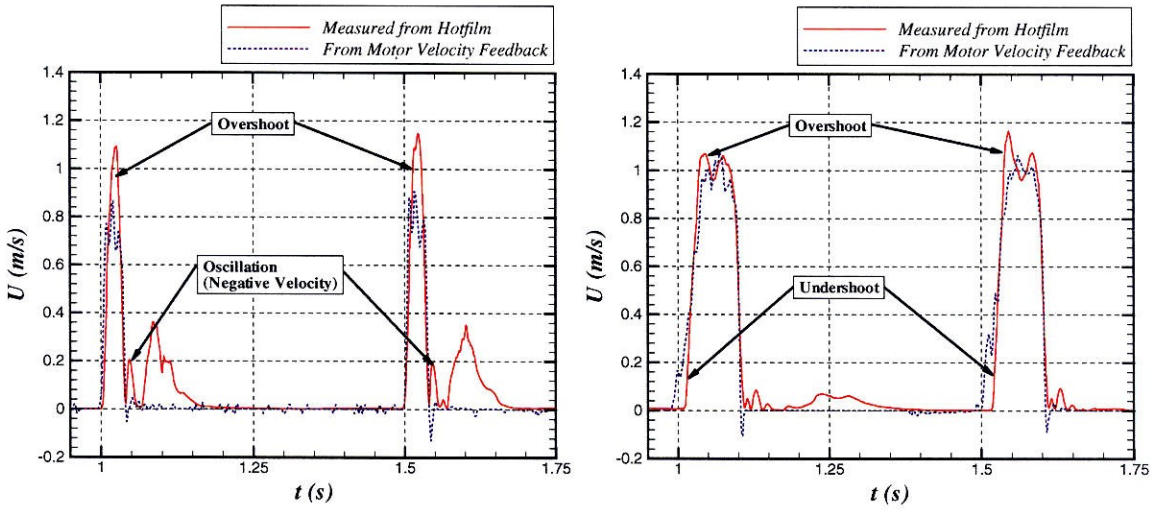

FIGURE 2.9 Comparison of Commanded and Actual Jet Velocities for a Few Simple Cases at f = 2 Hz: (a) L/D = 2.0, (b) L/D = 6.0.

2.4.2.3 Resolving the Discrepancy Between the Commanded and Actual Jet Velocity Programs

While section 2.4.2.2 indicates that pulses with time-varying jet velocity appropriate for this experiment can be generated with the apparatus described herein, it also reveals that the commanded piston velocity does not precisely describe the resulting jet velocity. This is a difficulty primarily because complete analysis of the thrust measurements requires knowledge of the time dependent jet velocities $U_J(t)$, $u_J(r, t)$, and $u_{cl}(t)$, which can no longer be estimated from $U_p(t)$. Measurements of $u_{cl}(t)$ are easily obtained from hotfilm measurements using the calibration scheme described above, but it remains to be seen if the other two quantities can be estimated from hotfilm measurements of the center-line velocity.

This problem is addressed using the analytical solution of Atabek and Chang [1]. Their analysis considers periodic inflow to a circular tube. The analysis is simplified by applying the boundary layer approximations to the flow and linearizing the equations by

assuming that the convective velocity at each downstream station is given by the flow rate at the inlet. This results in a closed-form expression for $u_J(x_i, r, t)$ that is exact at the inlet ($x_i = 0$) and far downstream (fully-developed flow), but is approximate in between. A more detailed description of this analysis and its results is given in appendix B.

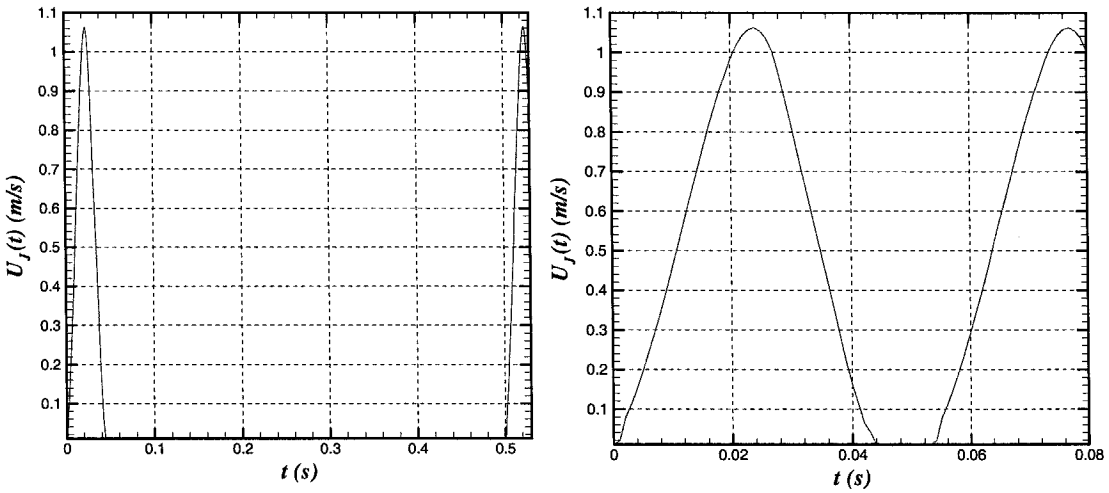

FIGURE 2.10 Specified Inlet Velocities $U_J(t)$ for the Application to the Results of Atabek and Chang, [1]: (a) $f = 2$ Hz, (b) $f = 18.9$ Hz.

The result of Atabek and Chang is applied to a simple $L/D = 2$ case used in this experiment [$L/D = 2$, PS Ramp (see chapter 3)] for two different pulsing frequencies. The prescribed inlet velocities for one period of the two frequencies considered are shown in Figure 2.10[2]. Using the calculated center-line velocities, the calibration equation (2.8) is used to determine what $U_J(t)$ the hotflim would actually measure (i.e., to determine $U_{cal}(t)$ given the known velocity at the nozzle exit plane). These values are compared with the specified $U_J(t)$ in Figure 2.11. From this figure it is clear that

2. The velocity between each pulse for these cases is a small, finite value (0.01 m/s) so that the analytical result (which requires the inlet velocity to be nonzero throughout the oscillation period) can be properly applied.

$$U_{cal}(t) \approx U_J(t) \tag{2.14}$$

to within a few percent, even for these highly unsteady cases. The accuracy of this approximation improves for f = 18.9 Hz.

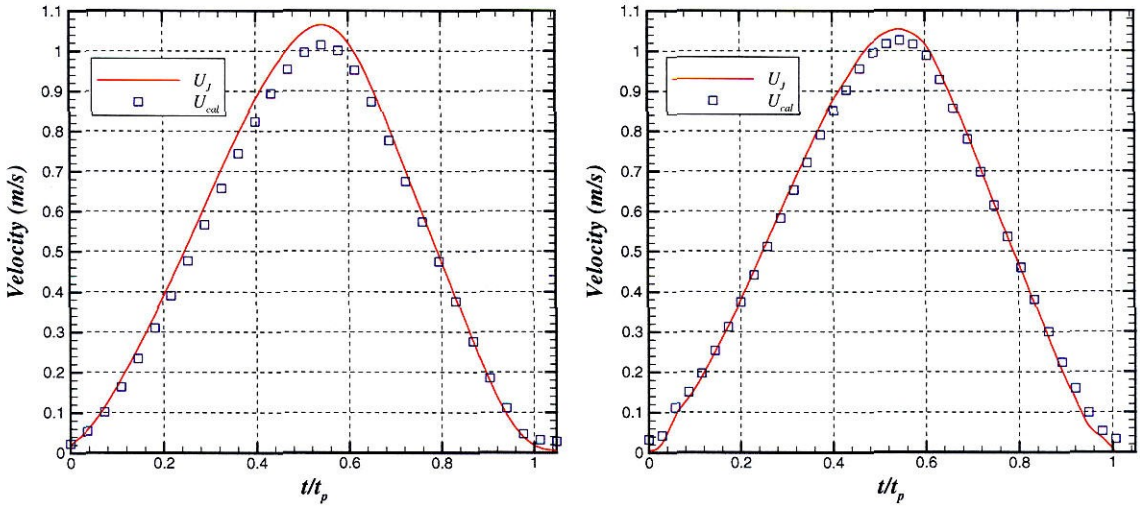

FIGURE 2.11 Comparison of Specified $U_J(t)$ with the $U_J(t)$ Expected From Measurements [$U_{cal}(t)$] for the Example Cases of Figure 2.10: (a) f = 2 Hz, (b) f = 18.9 Hz.

In regard to determining $u_J(r, t)$, what is actually of interest experimentally is

$$I_U(t) \equiv \rho \int_0^t \int_0^R \int_0^{2\pi} u_J^2(r, \tau)\, r\, d\theta\, dr\, d\tau \tag{2.15}$$

and

$$E_U(t) \equiv \frac{\rho}{2} \int_0^t \int_0^R \int_0^{2\pi} u_J^3(r, \tau)\, r\, d\theta\, dr\, d\tau \tag{2.16}$$

where ρ is the fluid density, u_J is the jet velocity at the nozzle exit plane, I_U will be referred to as the "velocity impulse," and E_U will be referred to as the "kinetic energy

term." Considering the impulse first, if one assumes that u_J is uniform in r for all t, equation (2.15) reduces to

$$I_U^u(t) = \rho A \int_0^t U_J^2(\tau) d\tau \tag{2.17}$$

where A is the nozzle cross-sectional area. If the slightly more reasonable assumption is made that the velocity profile at each time is as depicted in Figure 2.6, then the velocity impulse is

$$I_U^P(t) = \rho A \int_0^t \frac{r_v(\tau)}{15}\left(24 - r_v(\tau)\left\{5 + \sqrt{\frac{6}{r_v(\tau)} - 2}\right\}\right) U_J^2(\tau) d\tau . \tag{2.18}$$

For the test cases in Figure 2.10, $I_U(t)$ can be computed exactly and the values of $I_U^u(t)$ and $I_U^P(t)$ that would be determined from the hotfilm measurements can be evaluated using equation (2.8). These three quantities are compared in Figure 2.12, which shows good agreement between $I_U(t)$ and $I_U^P(t)$ for both cases, but $I_U^u(t)$ tends to significantly underestimate $I_U(t)$. Given these results, it is clear that

$$I_U^P(t) \approx I_U(t) , \tag{2.19}$$

to within a few percent, despite the highly unsteady nature of the inlet flow and the fact that the hotfilm calibration is based on steady piston motion.

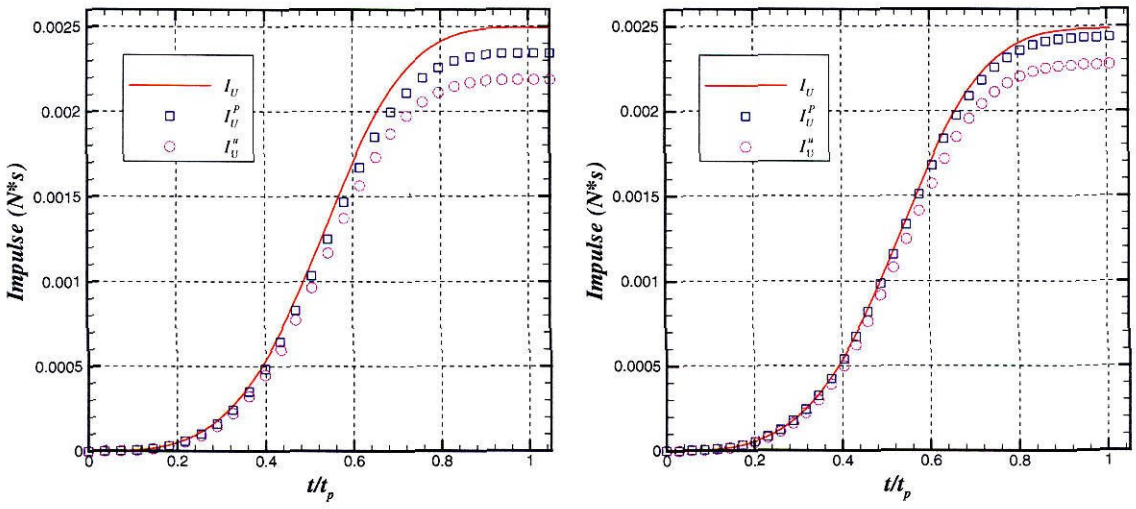

FIGURE 2.12 Comparison of the "Exact" and Experimentally Estimated Velocity Impulses for the Cases Depicted in Figure 2.10: (a) f = 2 Hz, (b) f = 18.9 Hz.

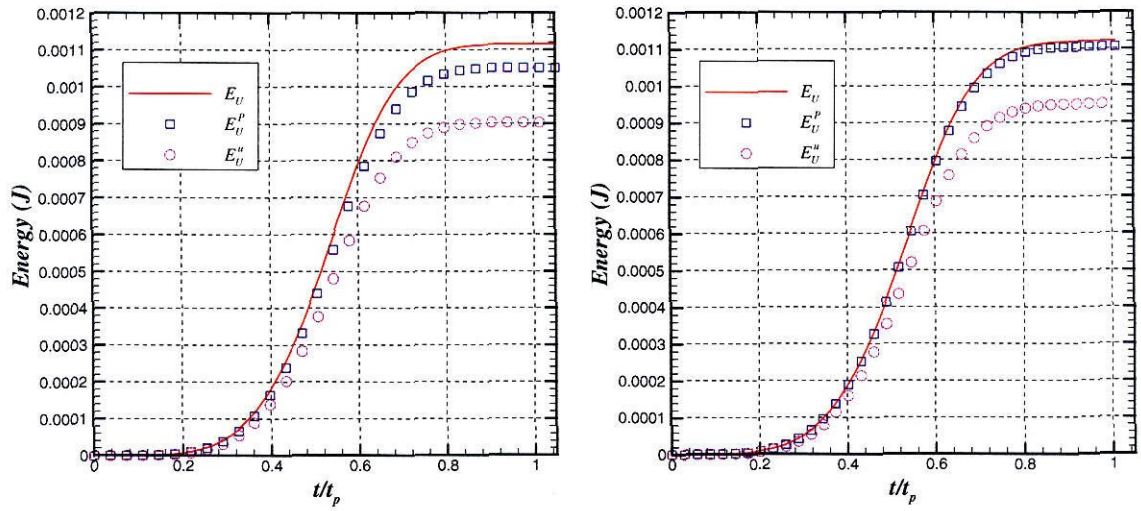

FIGURE 2.13 Comparison of the "Exact" and Experimentally Estimated Kinetic Energy Terms for the Cases Depicted in Figure 2.10: (a) f = 2 Hz, (b) f = 18.9 Hz.

A similar analysis can be performed for the kinetic energy term. In this case the equations analogous to equations (2.17) and (2.18) are

$$E_U^u(t) = \frac{\rho A}{2}\int_0^t U_J^3(\tau)d\tau \qquad (2.20)$$

and

$$E_U^P(t) = \frac{\rho A}{2}\int_0^t \frac{r_v^2(\tau)}{70}\left(141 - r_v(\tau)\left\{35 + 18\sqrt{\frac{6}{r_v(\tau)} - 2}\right\}\right)U_J^3(\tau)d\tau \qquad (2.21)$$

respectively. Following the approach used for the impulse analysis, these quantities are determined along with E_U for the test cases in Figure 2.10. The results are shown in Figure 2.13 and indicate that $E_U^u(t)$ underestimates $E_U(t)$ by a larger factor than $I_U^u(t)$ underestimates $I_U(t)$ while

$$E_U^P(t) \approx E_U(t) \qquad (2.22)$$

to within a few percent.

In evaluating these results, it should be noted that for $f = 2$ Hz, $\frac{x_N}{R \cdot Re_0}$ is approximately 0.037, where Re_0 is given by

$$Re_0 \equiv \frac{U_0 R}{\nu} \qquad (2.23)$$

and U_0 is the time averaged value of U_J. For the $f = 18.9$ Hz results, $\frac{x_N}{R \cdot Re_0} \approx 0.004$, indicating that the nozzle exit is much closer to the inlet in a non-dimensional sense for this case. Thus, the analytical results for $f = 18.9$ Hz are more accurate than the results for $f = 2$ Hz, which further supports the validity of the approximations indicated by equations (2.14), (2.19), and (2.22). Finally, Re_0 is lowest for the case of $L/D = 2.0$ (the lowest L/D considered in these experiments), so these ideas should be valid over the entire

parameter space of this experiment. The approximations expressed in equations (2.14), (2.19), and (2.22) are therefore considered to be "exact" for the purposes of this experiment.

Based on this analysis, hotfilm measurements were used to determine $U_J(t)$, $I_U(t)$, and $E_U(t)$ before (and sometimes after) a series of thrust measurements were made, giving complete knowledge of the thrust and jet velocity characteristics for a given point in the experimental parameter space.

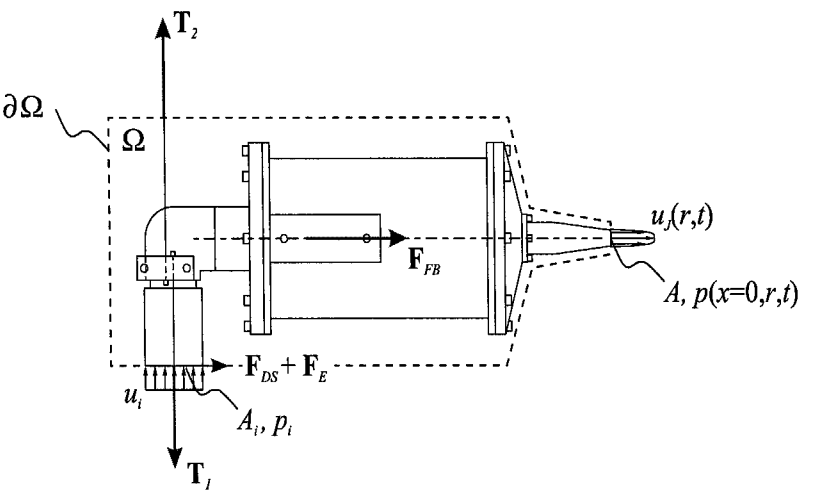

FIGURE 2.14 Control Volume Analysis of Forces on the Jet Section.

2.4.3 Force Measurements: Confirmation and Measurement Issues

2.4.3.1 Control Volume Analysis of Forces on the Jet Section

Since the force balance measures the forces on the entire jet section, it is necessary to analyze the forces applied to the jet section in order to understand the force balance measurements. Figure 2.14 shows a top view of the jet section with a control volume Ω suitable for this analysis. Ignoring the effect of gravity (since it simply leads to a linear

increase in the ambient pressure with depth) and viscosity (since the flow external to the device is quiescent), the momentum equation for Ω is

$$\frac{\partial}{\partial t}\int_{\Omega} \rho \mathbf{u} dV + \int_{\partial\Omega} \rho \mathbf{u}(\mathbf{u}\cdot\hat{\mathbf{n}}) dS = -\int_{\partial\Omega} p\,\hat{\mathbf{n}} dS + \mathbf{F}_{FB} + \mathbf{F}_{DS} + \mathbf{F}_{E} + \mathbf{T}_1 + \mathbf{T}_2 \qquad (2.24)$$

where $\mathbf{F}_{FB}$ is the force applied to the jet section by the force balance to hold it in place, $\mathbf{F}_{DS}$ is the force applied to the jet section by the driver section (through the hose), and $\mathbf{F}_{E}$ is the elastic force in the hose applied by deflection of the hose along the x direction. Since $\mathbf{F}_{FB} = F_{FB}\hat{\mathbf{x}}$, only the x-component of equation (2.24) is of interest. Assuming a constant density fluid (water) this gives

$$\rho\frac{\partial}{\partial t}\int_{JS} u dV + \rho\int_{A} u_j^2(r,t) dS + \int_{A} [\,p(x=0,r,t) - p_\infty] dS = F_{FB} + F_{DS} + F_{E} \qquad (2.25)$$

where A is the nozzle cross-sectional area (at $x = 0$), JS is the jet section volume, and it is understood that p_∞ is the average ambient pressure over the nozzle area (or equivalently, the ambient pressure at the nozzle center line[3]). Due to rigid support of the pipe leaving the driver section (see Figure 2.2), $F_{DS} = 0$. Furthermore, F_E is accounted for in the calibration of the force balance, so equation (2.25) reduces to

3. The ambient pressure p_∞ (that is, the pressure at $x \to \infty$) actually varies with depth h as $\rho g h$, but since the dependence on h is linear and the nozzle is circular, the average value of p_∞ is just its value at the depth of the nozzle center line.

$$\overbrace{\rho\frac{\partial}{\partial t}\int_{JS} u dV}^{\text{Acceleration}} + \overbrace{\underbrace{\rho\int_{A} u_J^2 dS}_{\text{Momentum Flux}} + \underbrace{\int_{A}(p-p_\infty)dS}_{\text{Nozzle Exit Over-Pressure}}}^{\text{Jet}} = F_{FB} \ . \qquad (2.26)$$

Equation (2.26) shows that the force balance measures an unsteady term associated with the acceleration and deceleration of the fluid in the jet section, whereas the quantities of interest are those associated with the jet only (i.e., momentum flux and nozzle exit over-pressure terms). However, the time integral of the acceleration term over the pulse period T is identically zero since for this experiment the jet velocity returns to the same value at the end of each pulse, namely zero. Thus, the experimental quantities of interest are the time averaged (jet) thrust $\overline{F_T} = \overline{F_{FB}}$ and the total (jet) impulse $I = T \cdot \overline{F_{FB}}$ [4].

2.4.3.2 Impulse Response of the Force Balance/Jet Section System

The impulse response of the force balance with the jet section and associated plumbing attached was obtained by applying an impulsive force (impact from a mallet) to the jet section along its axis. The response, shown in Figure 2.15, is essentially that of a single degree of freedom (SDOF) linear oscillator with a resonance peak at 44 Hz. The system response at 0 Hz is 1.0 indicating that the force balance dynamics do not affect measurements of the mean thrust or total impulse since these quantities are related to the zero frequency components of the measured signal. Furthermore, the response at 22 Hz (the maximum pulsing frequency used in this experiment) is about 1.2, so the deflection of

4. Since the fluid is incompressible, one could try to determine the unsteady term in equation (2.26) by measuring the velocity at the nozzle exit and multiplying by a constant factor to convert it to an integral over the volume. This was not attempted for this investigation.

the force balance is not appreciably affected by the pulsing of the jet and, therefore, does not affect the jet dynamics.

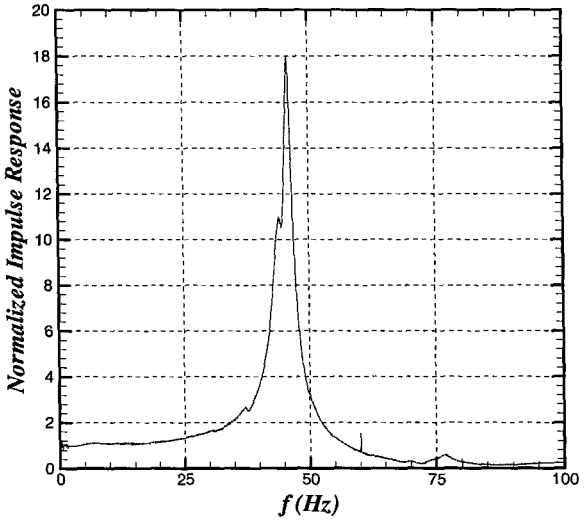

FIGURE 2.15 Impulse Response of the Force Balance/Jet Section System.

2.4.3.3 Zero-Point Drift in the Force Measurements

By performing several measurements of the thrust for steady commanded piston velocities, it was observed that the measured thrust decayed linearly with time and after the piston stopped, the zero point for the force balance was lower than when the test began. The total zero-point shift increased in proportion to the piston velocity for a constant test duration. The magnitude of the shift was in the range 0.03 N to 0.1 N for tests of 4 second duration and piston velocities in the range 0.3 to 0.7 in/s. This zero-drift phenomenon was attributed to two causes:

1. The floating piston in the jet section was actually slightly buoyant, so as it translated in the jet section it could apply a time-varying torque to the force balance and shift the zero point slightly; and
2. The force balance and hose attached to the jet section experienced a slight amount of hysteresis from the acceleration term in equation (2.26) and the unsteadiness of the jet velocity despite the fact that the commanded piston velocity was steady [see Figure 2.8 (a)]. This led to (relatively) large oscillations of the force balance coupled with a net mean force from the jet itself — a combination that can produce

zero-point drift for hysteretic systems. (Hysteresis from the hose was minimized by using a very flexible hose.)

Since the zero drift was linear in time, it was decided to subtract it out of all thrust measurements using the measured zero point after a test was completed and the specified test time. It was confirmed that this correction properly accounted for the drift by plotting the running average of the measured thrust, defined as

$$F_{ra}(t) = \frac{1}{t}\int_0^t F_{FB}(\tau)d\tau . \tag{2.27}$$

For runs where the running average was not sufficiently steady, the results were not recorded.

CHAPTER 3

Investigation of the Dynamic Properties of Individual Vortex Rings and Starting Jets

3.1 Introduction

For impulsively started jets, the vortex ring pinch off phenomenon introduced in chapter 1 represents a maximization principle for vortex ring formation in that for sufficiently large formation time $X(t)/D = [tU_J(t)]/D$, the leading vortex ring no longer entrains any energy or circulation from the generating jet giving the characteristic structure of a vortex ring followed by a trailing jet shown in Figure 1.1. The importance of this pinch off process as a thrust/impulse optimization mechanism was suggested by Gharib *et al.* [12] (referred to as GRS herein). Bartol [2] also makes reference to the apparent importance of vortex rings in the propulsion of squid. One proposed argument for why vortex ring pinch off might be important for propulsion begins with the observation that vortex rings entrain and convect ambient fluid in addition to the fluid ejected from the nozzle (Didden, [10]). As a ring increases in size (circulation), it entrains more fluid, so a maximum ring size implies maximum fluid entrainment per pulse. In addition to more entrained mass, larger rings (i.e., those that have more circulation but are generated from the same diameter tube) also have a larger translational velocity (Shusser and Gharib,

[35]). These last two points, taken together, imply larger transport of momentum downstream by larger vortex rings and hence, more thrust per pulse for larger rings. Thus, maximal vortex ring size (circulation) is taken to imply maximal thrust per pulse.

This reasoning, however, has several pitfalls. First, for a given jet exit velocity, a longer pulse is required to generate a larger ring. A simple control volume analysis [ignoring the nozzle exit over-pressure in equation (2.26)] indicates that a longer pulse should generate more thrust due simply to the longer duration of momentum flux from the nozzle (given a relatively constant average momentum flux). So, statements about maximum thrust per pulse should be made in reference to some normalized thrust where the pulse duration has been factored out. Second, the amount of fluid entrained during vortex ring formation is not well documented, so it is not known if this is a strong or weak effect (i.e., any maximum that exists may be too small to have any practical benefit). Third, even after the leading vortex pinches off for $L/D \gg F$, the remainder of the jet is ejected and contributes to the thrust. This portion of the pulse *also* entrains fluid through the Kelvin-Helmholtz instability at the interface between the jet and ambient fluid. It is not clear, therefore, that any propulsive benefit obtained by vortex ring formation will dominate the contribution of a trailing jet or even that fluid entrainment is the most important characteristic of vortex ring formation in terms of propulsion. These points, taken together, make it difficult to assess the importance of vortex ring pinch off for propulsion *a priori*.

The goal of this chapter is to address the above issues by investigating the potential benefit of vortex ring formation for propulsion. Of particular interest is determining whether or not vortex ring pinch off in starting jets represents a maximization principle for

propulsion in that some normalized thrust is optimized by the formation of vortex rings with maximum circulation and no trailing jet. If such a maximization principle exists, it is also of interest to determine the role played by entrainment of ambient fluid or other mechanisms in this optimization. More generally, it is of interest to determine the relative importance of the leading vortex ring and the trailing jet to the dynamic properties (impulse, energy, circulation) generated by a starting jet. These ideas are addressed by experimental measurement of the impulse, energy, and circulation generated by starting jets of water into water for a range of L/D that crosses the transition between the flow states characterized by an individual vortex ring and a vortex ring with a trailing jet for two different velocity programs. An analytical model for the flow near the initiation of an impulsively started jet is introduced to help clarify some of the physics.

3.2 Experimental Conditions

The strong dependence of the formation number on the overall slope of the velocity program, $U_J(t)$, used to generate a starting jet (as discussed in section 1.2.1.1) was used to advantage in these experiments. Specifically, the servomotor was programmed to execute two different classes of finite-duration starting jets (or pulses) for a range of L/D. The velocity program of the first class was primarily negative sloping (designated NS ramp) while the second class was primarily positive sloping (designated PS ramp). The flow rates as a function of time for each class (averaged over 20 pulses) for each L/D as determined from hotfilm anemometry at the nozzle exit are plotted in Figure 3.1. The coordinates of this figure are t/t_p and $U_J(t)/U$ where U is the *desired* peak velocity of

1.03 m/s. The Reynolds Number, Re_m, for these velocity programs is defined, following Rosenfeld *et al.* [28], as

$$Re_m \equiv \frac{U_{max} D}{\nu} \tag{3.1}$$

where U_{max} is the maximum U_J achieved during a pulse. The measurements in Figure 3.1 indicate that Re_m was 13,000 to within 10% for the NS and PS ramps.

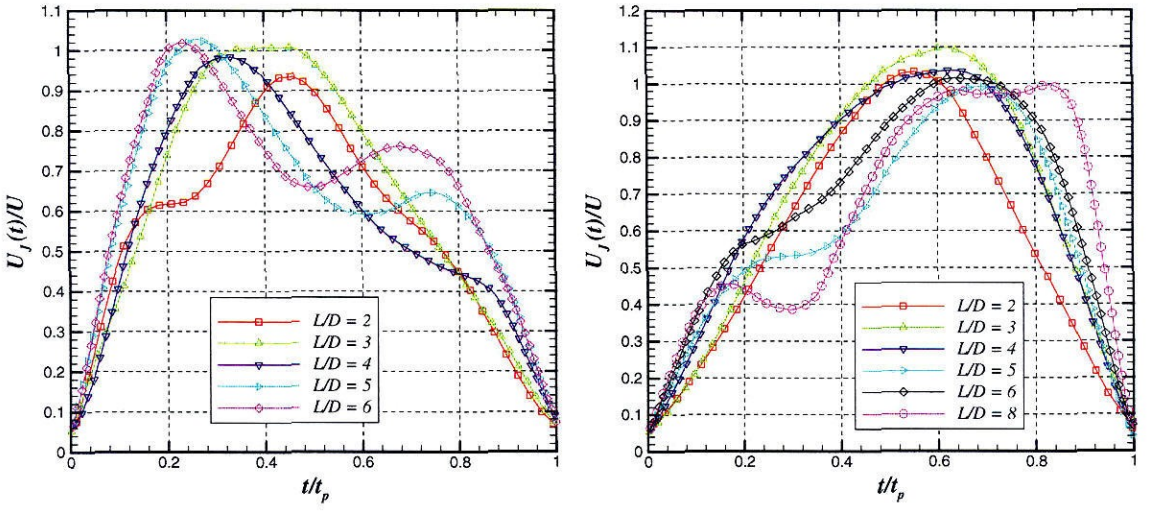

FIGURE 3.1 The Velocity Programs Used to Generate the Starting Jets for this Section: (a) Negative Sloping (NS) Ramps, (b) Positive Sloping (PS) Ramps.

Difficulties getting the flow rate $U_J(t)$ to follow the commanded piston motion $U_p(t)$ (see section 2.4.2.2) prevented the velocity programs from collapsing exactly in the normalized coordinates. Nevertheless, their overall form is the same for all L/D, i.e., generally positively or negatively sloping. The positive and negative sloping character of the velocity programs was introduced so that the L/D for which a significant trailing jet appeared would be higher for the PS ramps than the NS ramps. The subject of when vortex ring pinch off occurs for these velocity programs is investigated further in section 3.3.

For the velocity programs illustrated in Figure 3.1, the total impulse (time integral of the measured thrust) was measured for 25 pulses at each L/D. The velocity programs for the NS and PS ramps were measured using hotfilm anemometry for 20 pulses before and after the force measurements were taken. Finally, DPIV measurements of the pinched-off vortex rings were made for 10 pulses with $2 \leq L/D \leq 5$ (both NS and PS ramps) where the downstream viewing area of the camera was $0.45 < x/D < 5.25$. The relatively large number of trials for each measurement ensured repeatability of the measurements and allowed for ensemble averaging to reduce noise and other sources of uncertainty. The standard deviation of the measurements was used to generate the error bars in the following results, indicating the *precision* of the measurements.

3.3 Determining the Formation Number for the NS and PS Ramps

Because vortex ring pinch off plays a central role in the goals of this chapter, knowledge of the formation number is essential to interpret the results. For the purpose of measuring the thrust, however, large pulse velocities (~ 1 m/s) are desirable. This constraint combined with D = 1.27 cm dictated that the pulse times for the velocity programs in Figure 3.1 range between 0.04s and 0.1s. Since the data rate of DPIV is 15 Hz, vector fields can be obtained at a rate of only 1 every 0.067s, which is clearly insufficient to temporally resolve the formation process for the velocity programs used in this investigation. Thus, DPIV could not be used to determine the $X(t)/D$ corresponding to a pinched off vortex ring (and hence, the formation number) as was done in GRS. To circumvent this difficulty, the model of Shusser and Gharib [35] and [36] (referred to as the SG model

herein) was used to predict the formation number F from the measured velocity programs, $U_J(t)$.

Although the SG model was presented briefly in section 1.2.1.2, a detailed overview of this model as well as a justification for its use in these experiments is given in appendix C due to the central role it plays in this investigation. Two key observations in this overview are noteworthy. First, the model was shown in Shusser *et al.* [36] to predict the L/D at pinch off for the time-varying velocity programs investigated in Rosenfeld *et al.* [28] to within 4%. Its applicability to velocity programs similar to those shown in Figure 3.1 is demonstrated in section C.2 using PLIF flow visualization and a high-speed video camera to measure vortex ring velocity. Thus, the results of the model can be trusted to give an accurate account of vortex ring pinch off in this investigation. Second, it is noted that a key feature of the model is its generalization of the concept of formation number to pulses with small (< 5) stroke ratio. As expressed in GRS, the formation number corresponds to the non-dimensional time $[tU_J(t)]/D = X(t)/D$ when the total circulation ejected corresponds to the circulation in the pinched off vortex ring, so it requires a large enough L/D for pinch off to be observed in order to determine the formation number from this definition. In the SG model, on the other hand, the model returns $L/D \approx F$ for sufficiently short L/D, indicating that no pinch off has occurred and an isolated vortex ring is produced by the pulse. For large enough L/D, the model gives $L/D \gg F$, implying that the leading vortex ring has pinched off from the generating jet before the entire pulse is ejected. This motivates the definition of a non-dimensional trailing jet

length as $L/D - F$ where vortex ring pinch off has occurred for values of $L/D - F$ significantly different from zero.

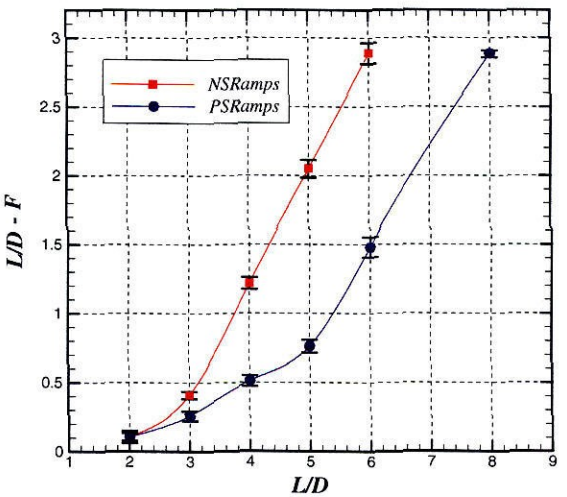

FIGURE 3.2 SG Model Predictions of the Non-dimensional Trailing Jet Length *L/D - F* for the Velocity Programs Used in this Experiment.

With this background on the SG model in place, the $L/D - F$ results for the velocity programs given in Figure 3.1 are shown in Figure 3.2[1]. The model shows that a significant trailing jet (as defined by $L/D - F > 0.5$) doesn't appear until $L/D > 2.0$ for both the NS and PS ramps. It also shows that the rate of growth of the trailing jet with L/D increases after $L/D = 3.0$ for the NS ramps, so a transition in the behavior of this family of velocity programs is expected here if vortex ring formation and pinch off plays a significant role in the dynamics of starting jets. The PS ramps show a similar increase at $L/D = 5.0$. By $L/D = 4.0$, however, the trailing jet is already becoming a significant

1. The L/D used in the calculation of $L/D - F$ in Figure 3.2 is $(L/D)_{measured}$ determined from the time integral of U_J over the pulse duration. This quantity is used instead of the nominal L/D specified by the commanded piston displacement since F is determined by a time integral of U_J up to the point where pinch off is predicted [see equation (C.10)]. The nominal L/D is plotted on the abscissa in this figure. Since $(L/D)_{measured} \approx (L/D)_{nominal}$, only the nominal stroke ratio is referenced in the remainder of the text.

part of the flow and may affect the results. Thus, a transition in the behavior of the PS ramps is expected between $L/D = 4.0$ and 5.0. This is a shift of at least $L/D = 1.0$ over the NS ramps, substantiating the use of two velocity programs in this investigation (as anticipated). That is, if vortex ring formation is critical to the impulse and thrust produced by starting jets, the measurements of these quantities should show a similar shift between the NS and PS cases.

3.4 Impulse and Thrust Measurements

Measurements of the total impulse per pulse were accomplished for each of the velocity programs depicted in Figure 3.1 by calculating

$$I = \int_0^\infty F_{FB}(\tau)\,d\tau \tag{3.2}$$

where F_{FB} is the force measured by the force balance[2]. The ensemble average of the measurements for each case are shown in Figure 3.3 where, as for all cases in this chapter, the error bars indicate the precision of the measurements. The solid reference lines in the figure are matched to the slopes of the first few points in each case ($L/D \leq 3$ for the NS ramps and $L/D \leq 4$ for the PS ramps). The dashed reference lines are matched to the *slopes* of the total impulse due to jet momentum flux, I_U, at $L/D \geq 4$ for the NS ramps and $L/D \geq 5$ for the PS ramps. [$I_U = I_U(t_p)$ where $I_U(t)$ is defined in equation (2.15).]

2. The convention used throughout this chapter is that I, E, and Γ (without reference to time dependence) refer to the *total* impulse, energy, and circulation per pulse, respectively.

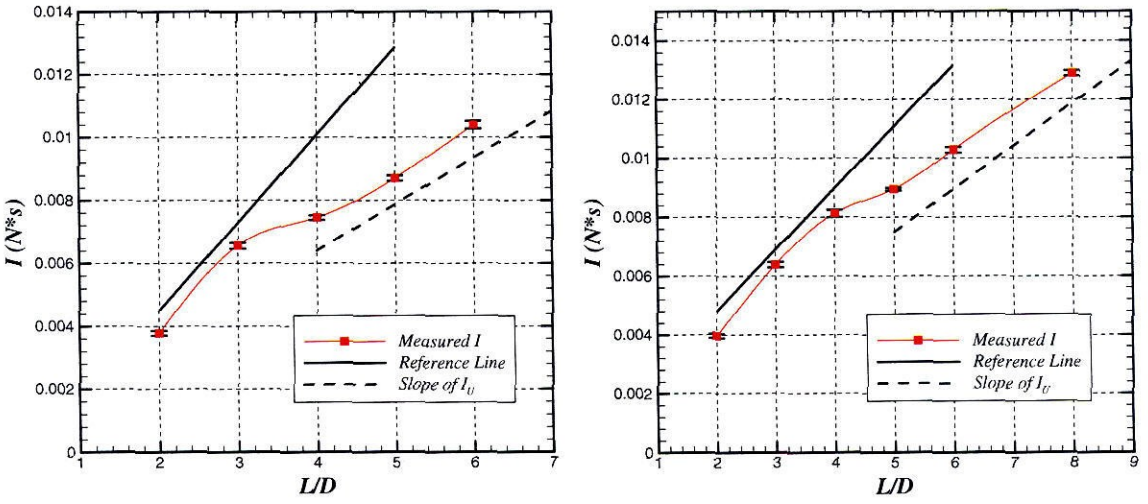

FIGURE 3.3 Total Impulse (per Pulse) for the Velocity Programs Depicted in Figure 3.1: (a) NS Ramps, (b) PS Ramps.

Comparison of the measured total impulse with the solid reference lines clearly shows a transition in behavior at $L/D = 3$ for the NS ramps and $L/D = 4$ for the PS ramps. Specifically, the impulse increases at a lower rate with increasing L/D for $L/D > 3$ in the NS case and $L/D > 4$ in the PS case. This represents a shift in the transition point of $L/D = 1$ between the NS and PS cases, following the observed shift in the trailing-jet growth seen in Figure 3.2. On closer comparison of Figure 3.3 with Figure 3.2, it also follows that the rate of increase of total impulse with L/D changes where $L/D - F$ becomes greater than 0.5, that is, where a trailing jet begins to become a significant part of the flow. This implies that vortex ring pinch off plays a significant role determining the impulse of a starting jet. Indeed, for $L/D > 3$ and $L/D > 4$ of the NS and PS ramps respectively, I increases at the same rate as the impulse from a steady jet (shown by the dashed reference line for the slope of I_U). The difference in slopes between the solid and dashed reference lines therefore indicates the difference between "ring-like" and

"jet-like" behavior, illustrating that a trailing jet contributes less to the total impulse per unit L/D than a comparable increase in the strength of a leading vortex ring.

While the total impulse measurements lend great insight into the relative importance of the leading vortex ring and trailing jet for generating impulse, it is necessary to make an attempt to account for the fact that the duration of the pulse increases with L/D to test the effectiveness of vortex ring formation for generating thrust. This is pursued by determining the average thrust during a pulse, $\overline{F_p}$, defined as

$$\overline{F_p} \equiv \frac{I}{t_p} \tag{3.3}$$

where t_p is the pulse duration.

Figure 3.4 (a) shows $\overline{F_p}$ as a function of L/D for the NS and PS ramps. A peak in $\overline{F_p}$ occurs around $L/D = 3$ for the NS case and around $L/D = 3.5$ for the PS case. These values are very close to the L/D values noted above where a significant trailing jet begins to appear and are shifted to higher L/D for the PS ramps as expected from Figure 3.2. This fact directly links a maximum in $\overline{F_p}$ with vortex ring pinch off. The trailing jet, therefore, adds less to the average thrust during a pulse than an equivalent increase in the leading vortex ring, indicating that $\overline{F_p}$ is maximized by pulses that generate vortex rings of maximum circulation without leaving a trailing jet. That is, once the L/D of a pulse is large enough that the leading vortex ring starts to pinch off and a trailing jet appears, any additional increase in L/D will give more impulse, but it takes proportionally more time to do it than if the additional fluid was actually added to the forming vortex ring.

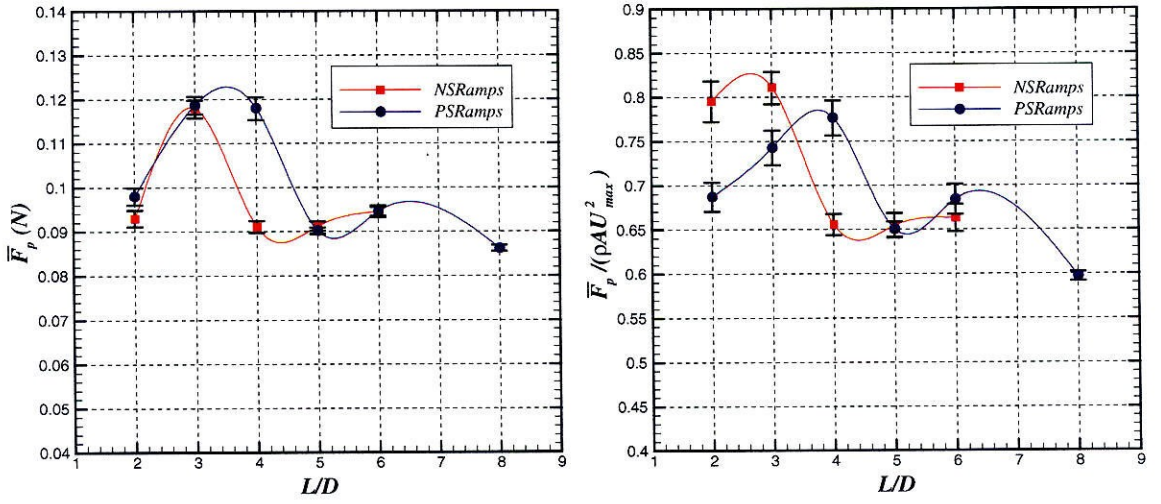

FIGURE 3.4 Average Thrust per Pulse Measurements: (a) Average Thrust per Pulse, (b) Normalized Average Thrust per Pulse.

These ideas are bolstered by considering $\overline{F_p}$ normalized by $\rho A U_{max}^2$. If all the velocity programs achieved the same maximum velocity (or more importantly, the same basic shape within their class), this normalization would not affect the trends observed in Figure 3.4 (a). Figure 3.1, however, indicates that there is some variation between pulses in the normalized coordinates, so this normalization of $\overline{F_p}$ makes an attempt to account for these variations. The normalized results are shown in Figure 3.4 (b) and indicate that the trends observed previously are still present. The peak for the NS case is not as sharp as in the $\overline{F_p}$ measurements, but the peak for the PS case has shifted to $L/D = 4.0$ in accordance with the observations based on the total impulse per pulse. This confirms and strengthens the conclusions based on the dimensional average thrust per pulse, underscoring the importance of $\overline{F_p}$ as the propulsive quantity maximized by pulses producing vortex rings of maximal circulation without a trailing jet.

While the normalized average thrust per pulse attempts to factor out variations in the measurements induced by differences between velocity programs in a given class, it only does so by considering differences at only one point in the velocity programs. A quantity that attempts to account for variations in the overall shape of velocity programs in a given class is a non-dimensional impulse, I_{nd}, defined as

$$I_{nd} \equiv \frac{I}{I_U} \tag{3.4}$$

where $I_U \equiv I_U(t_p)$ [determined from equation (2.18)]. This quantity also accounts for the increase in I with L/D since I_U increases with t_p. A plot of the non-dimensional impulse as a function of L/D for the NS and PS ramps is shown in Figure 3.5.

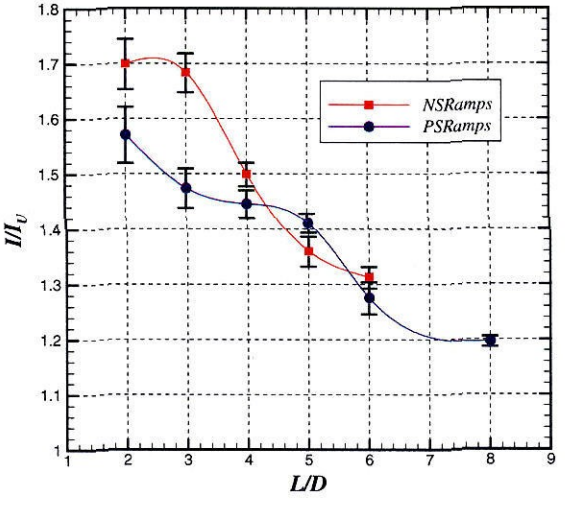

FIGURE 3.5 Non-Dimensional Impulse for the NS and PS Ramps.

The results for I_{nd} indicate that this quantity is greater than 1.0 for all cases tested. The significance of this observation is that it implies the impulse generated by a starting jet is greater than the impulse expected from the momentum flux of the jet velocity alone.

This is due to the nozzle exit over-pressure associated with starting jets as will be discussed in section 3.5.

Figure 3.5 also shows that I_{nd} for the NS ramps decreases significantly after $L/D = 3.0$, where the vortex rings have pinched off from the generating jet. This restates the previous observation that the contribution of the trailing jet to the total impulse is proportionally less significant than the leading vortex ring. The trend for the PS ramps allows a similar conclusion, although the initial drop in I_{nd} after $L/D = 4.0$ is less dramatic. This owes in part to the fact that the trailing jet has a larger velocity (i.e., is more significant) for this class of velocity programs. It is also partly due to the variation of the basic shape of the velocity program between $L/D = 4.0$ and 5.0 for the PS ramps, which is partially corrected for in this normalization giving a much less significant difference between $L/D = 4.0$ and 5.0 in I_{nd} than in $\overline{F_p}$. (This is in agreement with the assessment in section 3.3 that a transition in the behavior of the PS ramps is expected somewhere between $L/D = 4.0$ and 5.0.)

As a final observation, the PS ramps indicate an initial decrease in I_{nd} from $L/D = 2.0$ to 4.0. Because this trend is observed for $L/D < 4.0$, it is not associated with growth of a significant trailing jet. Rather, it is likely associated with the steady decrease in initial jet acceleration with L/D, which, as will be discussed in section 3.5, can be related to a decrease in the nozzle exit over-pressure associated with the acceleration of ambient fluid.

Overall the impulse and thrust measurements directly indicate the importance of the formation of a leading vortex ring in starting jets for impulse and thrust generation and

show that a trailing jet plays a less important role for these quantities. In particular, the average thrust per pulse measurements demonstrate that the propulsive quantity maximized by formation of a vortex ring of maximal circulation and a minimal trailing jet is $\overline{F_p}$.

3.5 The Contribution of Nozzle Exit Over-Pressure to the Dynamic Properties of Starting Jets

While the results of the previous section clearly answer the question of the importance of vortex ring formation and pinch off for the dynamic quantities I, $\overline{F_p}$, and I_{nd}, the source of the benefit provided by vortex ring formation is unclear. This can be illuminated by considering the pressure contribution to total impulse. To do this, it is necessary to first consider the generalized slug-flow equations, which express the impulse, energy, and circulation supplied to the flow by a piston-cylinder mechanism in terms of the velocity and pressure at the nozzle exit plane. From these equations it is apparent that pressure at the nozzle exit (i.e., nozzle exit over-pressure) plays an important role in the dynamic quantities of energy and circulation as well, showing that energy and circulation should also be considered to provide a complete picture of the physics of starting jets generated by a piston-cylinder arrangement. Thus, the following subsections begin with a presentation of the generalized slug-flow equations, followed by an evaluation of the pressure contribution to total impulse and the physics associated with this effect. The pressure contribution

to energy and circulation is then considered. A simple model of the pressure effects at the initiation of a starting jet concludes this section.

TABLE 3.1 Generalized Slug-Flow Equations and the Slug Model Equations.

Dynamic Quantity		Velocity/Flux Term		Pressure Term
Generalized Slug-Flow Equations				
I	=	$I_U(t) \equiv \rho \int_0^t \int_A u_j^2(r,\tau)\, dS d\tau$	+	$I_p(t) \equiv \int_0^t \int_A [p(r,\tau) - p_\infty] dS d\tau$
E	=	$E_U(t) \equiv \frac{\rho}{2} \int_0^t \int_A u_j^3(r,\tau)\, dS d\tau$	+	$E_p(t) \equiv \int_0^t \int_A [p(r,t) - p_\infty] u_j(r,t)\, dS d\tau$
Γ	=	$\Gamma_U(t) \equiv \frac{1}{2} \int_0^t u_{cl}^2(\tau) d\tau$	+	$\Gamma_p(t) \equiv \frac{1}{\rho} \int_0^t [p_{cl}(\tau) - p_\infty] d\tau$
Slug Model Equations				
I	=	$I_{sm}(t) = \rho A \int_0^t U_j^2(\tau) d\tau$		
E	=	$E_{sm}(t) = \frac{\rho A}{2} \int_0^t U_j^3(\tau) d\tau$		
Γ	=	$\Gamma_{sm}(t) = \frac{1}{2} \int_0^t U_j^2(\tau) d\tau$		

3.5.1 The Generalized Slug-Flow Equations

The generalized slug-flow equations for a piston-cylinder mechanism are derived in appendix D with the results given in equations (D.9), (D.10), (D.11), (D.17), (D.18), (D.19), and (D.33). For convenience, the equations are reiterated here in Table 3.1, which also includes the slug model equations for comparison. The basic motif of the generalized slug-flow equations is that the amount of each dynamic quantity (I, E, or Γ) supplied to a

flow by a piston-cylinder mechanism is determined by the sum of a velocity/flux term [denoted $(\ldots)_U$] and a pressure term [denoted $(\ldots)_p$]. The slug model, on the other hand, ignores any contribution from pressure at the nozzle and also assumes that the velocity profile at the nozzle is nearly uniform so that $u_J(r, t) \approx U_J(t)$ over the nozzle cross section. Since knowledge of u_J is obtained from hotfilm measurements of the jet velocity during a pulse, the generalized slug-flow equations provide a means of determining the contribution of nozzle exit pressure by comparing measured values of E, I, and Γ (from force or PIV measurements) with the values expected from velocity alone. As a practical point, Newton's third law guarantees that the total impulse measured by the force balance is equivalent to that determined by equation (D.9), even though this result refers to the impulse associated with the flow external to the jet mechanism.

3.5.2 The Contribution of Nozzle Exit Over-Pressure to Impulse

The generalized slug-flow equation for impulse [equation (D.9)] gives the pressure impulse as

$$I_p = I - I_U \tag{3.5}$$

where I is determined from the measurements of the total impulse and I_U can be determined from the measurements of the jet velocity during a pulse. For the NS and PS ramp classes studied here, this gives the results shown in Figure 3.6 (a). The significance of this contribution is illustrated in Figure 3.6 (b) where the fraction of I contributed by I_p is plotted. As before, the error bars represent the precision of the measurements.

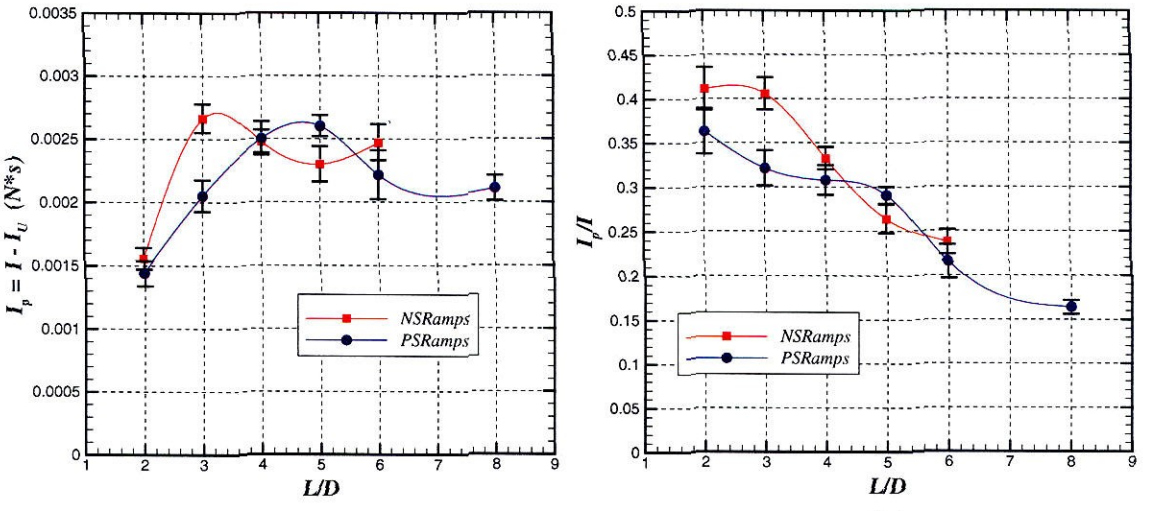

FIGURE 3.6 Pressure Contribution to Impulse for the NS and PS Ramps: (a) Pressure Impulse, (b) Normalized Pressure Impulse.

Figure 3.6 (a) demonstrates that the pressure impulse increases with L/D as long as the leading vortex ring continues to develop. As soon as a significant trailing jet begins to appear ($L/D > 3.0$ for the NS ramps and $L/D > 4.0$ for the PS ramps), however, this increase tapers off and starts a slight decline, but remains approximately constant. This motivates the approximation $I_p(t) \approx 0$ for $t > t_F$, or more boldly, $p(r, t) \approx p_\infty$ for $t > t_F$ where $t_F < t_p$ denotes the time where pinch off is predicted by the SG model (see appendix C). That is, nozzle exit over-pressure is ignored during the ejection of a trailing jet. This approximation also makes sense physically as long as there is no sudden acceleration of the jet for $t > t_F$ so that the trailing jet can be treated as a "steady" jet. Such appears to be the case for most of the velocity programs, except for the $L/D = 6.0$ of the NS ramp family where a second peak in the velocity program is observed around $t/t_p = 0.75$ [see Figure 3.1 (a)].

In addition to these observations, Figure 3.6 (b) also indicates that the pressure impulse makes a very significant contribution to the total impulse, reaching as much as 40% for the NS ramp at the lower L/D values. The slug model would, therefore, seriously underestimate the impulse, especially for small L/D.

Using the above approximation that $I_p(t) \approx 0$ for $t > t_F$ and the SG model to determine t_F, an approximation to the impulse due to the leading vortex ring alone is given by

$$I_{ring} = I - I_{TJ} \tag{3.6}$$

where I_{TJ} is the impulse due to the trailing jet and is approximated as

$$I_{TJ} \approx \rho \int_{t_F}^{t_p} \int_A u_J^2(r, \tau)\, dS d\tau . \tag{3.7}$$

Applying this approximation to the impulse measurements gives the results shown in Figure 3.7. This figure also gives the impulse of the leading vortex ring determined from PIV measurements of the vorticity field, where, for axisymmetric flow, the impulse of the ring is given by

$$I_{ring} = \pi\rho \int_{ring} \omega_\theta(r, x) r^2 dS \tag{3.8}$$

(see Lim and Nickels [16]).

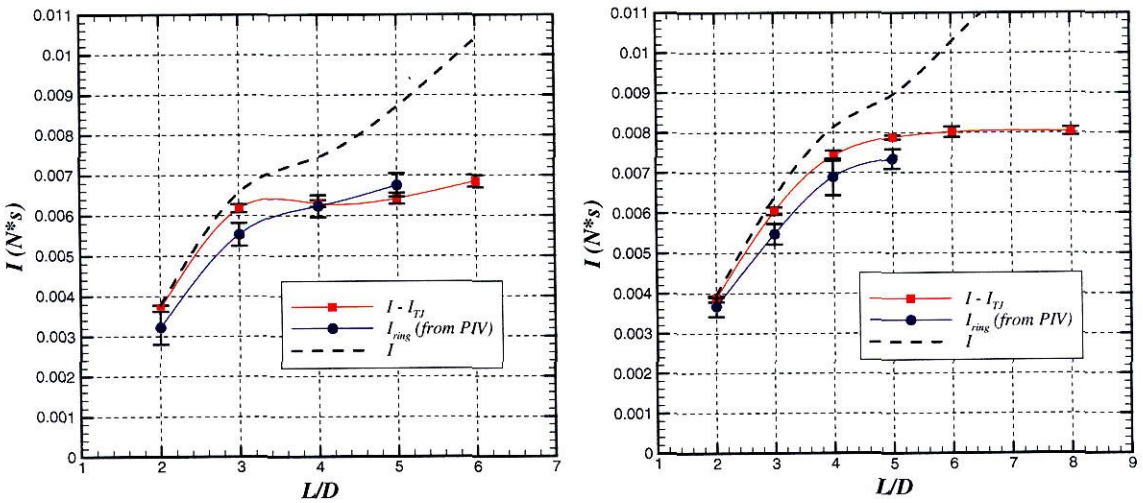

FIGURE 3.7 Measurements of the Ring Impulse Obtained from Total Impulse Measurements and PIV Vorticity Measurements: (a) NS Ramps, (b) PS Ramps.

Two conclusions follow from a comparison of the approximated ring impulse shown in Figure 3.7 with the total measured impulse I (plotted as the dashed reference line) and the ring impulse measured from PIV. First, the approximated ring impulse determined using equations (3.6) and (3.7) starts to level off for $L/D > 3.0$ for the NS ramps and $L/D > 4.0$ for the PS ramps, as expected from vortex ring pinch off. Second, the approximated ring impulse agrees with the measured ring impulse to within 10% in all cases (for $L/D < 5.0$) and 8% in most cases. The later result gives strong confirmation of the assumption that nozzle exit over-pressure adds a trivial amount of impulse after the vortex ring pinches off from the generating jet. Stated differently, there appears to be no significant over-pressure at the nozzle exit during the ejection of a trailing jet, allowing it to be approximated as a steady jet.

The apparent dearth of nozzle exit over-pressure during the ejection of a trailing jet and the significant over-pressure provided during vortex ring formation indicates that the

propulsive benefit provided by vortex ring formation is determined by nozzle exit over-pressure. The need for over-pressure is related to the acceleration of ambient fluid (i.e., the inertia of the ambient fluid) during the ejection of a starting jet. This will be illustrated in two ways, first by considering a control volume analysis of the fluid in front of the nozzle exit plane and then by analyzing the features of a completely developed vortex ring.

3.5.2.1 Control Volume Analysis for $x > 0$.

An axisymmetric, fixed control volume surrounding the jet flow in front of the nozzle exit plane ($x > 0$) is shown in Figure 3.8 and designated Ω_0. Considering this control volume allows the fluid external to the jet section to be considered as an entity separate from the jet mechanism, making it explicit that the pressure at the nozzle exit can be viewed as a reaction force between the jet mechanism and the ambient fluid. Stated differently, Newton's third law guarantees that any force (e.g., pressure) exerted on Ω_0 by the jet section is also exerted on the jet section by Ω_0 in an opposite sense, giving thrust.

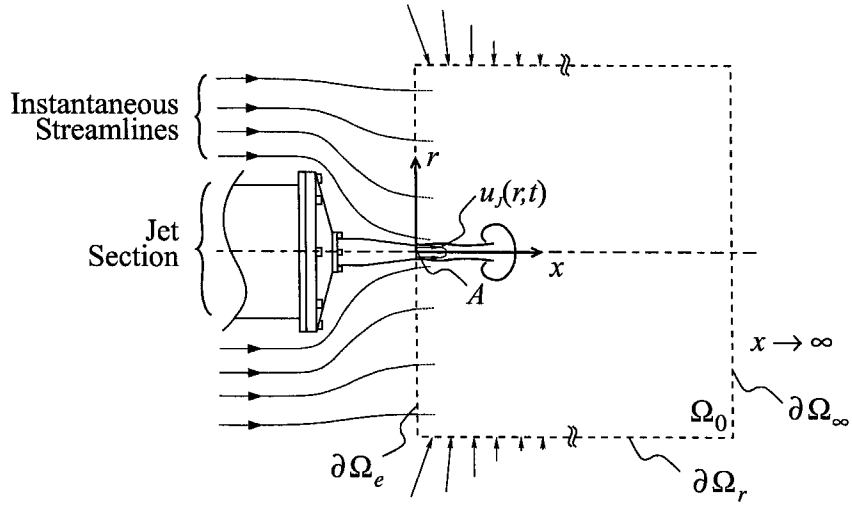

FIGURE 3.8 Axisymmetric Control Volume for Fluid in Front of Nozzle Exit Plane.

The physics behind these statements are illuminated by an analysis of the momentum equation for the control volume illustrated in Figure 3.8. Since no external forces are applied to this control volume, the momentum equation for Ω_0 is

$$\rho\frac{\partial}{\partial t}\int_{\Omega_0}\mathbf{u}dV+\rho\int_{\partial\Omega_0}\mathbf{u}(\mathbf{u}\cdot\hat{\mathbf{n}})dS=-\int_{\partial\Omega_0}(p-p_h)\hat{\mathbf{n}}dS \tag{3.9}$$

where p_h is the hydrostatic pressure field defined in equation (D.2) and Ω_0 is taken to be large enough that viscous effects are unimportant over its boundary. Enforcing axisymmetry eliminates the radial component of equation (3.9). Noting that $\int_{\partial\Omega_e}p_h dS=\int_{\partial\Omega_e}p_\infty dS$ (see footnote 3 in appendix D) and that $p-p_h\to 0$ as $x\to\infty$ (see Cantwell [8])[3] simplifies equation (3.9) further. The result is

$$\rho\frac{\partial}{\partial t}\int_{\Omega_0}u(r,x,t)dV-\rho\int_{\partial\Omega_e}u^2(r,t)dS=\int_{\partial\Omega_e}[p(r,t)-p_\infty]dS \tag{3.10}$$

where p_∞ is the ambient pressure at the nozzle center line [i.e., at $(x, r)\to(\infty, 0)$]. Assuming irrotational flow external to the nozzle and jet section for $x<0$, the flow in this region can be described by the unsteady Bernoulli equation, namely,

$$\rho\frac{\partial\phi}{\partial t}+\frac{1}{2}\rho|\mathbf{u}|^2+(p-p_h)=0 \tag{3.11}$$

---

3. What is actually required to get the result in equation (3.10) is that $\int_{\partial\Omega_\infty}(p-p_h)dS\to 0$ as $x\to\infty$. This is in fact the case and follows from the observation that $p-p_h\sim\frac{1}{x^2}$ (along the center line) as $x\to\infty$ (Cantwell [8]), while the area of $\partial\Omega_\infty$ remains constant and finite as $x\to\infty$.

where ϕ is the velocity potential satisfying $\mathbf{u} = \nabla\phi$ and $\phi \to 0$ as $|\mathbf{x}| \to \infty$. This result gives the pressure on $\partial\Omega_e$ external to the nozzle (i.e., on $\partial\Omega_e - A$) as a function of flow velocity and ϕ so that equation (3.10) can be written as

$$\int_A [p - p_\infty] dS \approx \rho \left[\left(\frac{\partial}{\partial t} \int_{\Omega_0} u dV - \int_{\partial\Omega_e} u^2 dS \right) + \frac{1}{2} \int_{\partial\Omega_e - A} |\mathbf{u}|_e^2 dS + \frac{\partial}{\partial t} \int_{\partial\Omega_e - A} \phi dS \right]. \qquad (3.12)$$

Equation (3.12) is only approximate because equation (3.11) is not exact near the outer annulus of the nozzle where viscosity becomes significant. Finally, integrating equation (3.12) in time gives the pressure impulse $I_p(t)$, namely,

$$_p(t) \approx \rho \int_0^t \left[\left(\frac{\partial}{\partial \tau} \int_{\Omega_0} u dV - \int_{\partial\Omega_e} u^2 dS \right) + \frac{1}{2} \int_{\partial\Omega_e - A} |\mathbf{u}|_e^2 dS + \frac{\partial}{\partial \tau} \int_{\partial\Omega_e - A} \phi dS \right] d\tau. \qquad (3.13)$$

For comparison with the measurements, the quantity of interest is the total pressure impulse $I_p = I_p(t \to \infty)$. From equation (3.13) this is given by

$$I_p \approx \rho \int_0^\infty \left[\underbrace{\left(\frac{\partial}{\partial \tau} \int_{\Omega_0} u dV - \int_{\partial\Omega_e} u^2 dS \right)}_{\text{Ambient Reaction}} + \underbrace{\frac{1}{2} \int_{\partial\Omega_e - A} |\mathbf{u}|_e^2 dS}_{\text{Co-flow}} \right] d\tau \qquad (3.14)$$

where the contribution from the potential term is zero in this limit since ϕ (for $x < 0$) is zero initially and after the flow convects down stream following the completion of the pulse.

The ambient reaction term in equation (3.14) is the rate of change of momentum of the fluid in front of the nozzle minus the contribution from the flux of momentum across

the plane at $x = 0$ (e.g., from the jet momentum flux). It therefore represents the rate of change of momentum of the *ambient* fluid initially in front of the nozzle, which is effected by the jet pushing this fluid out of the way as it is ejected. This indicates that part of the nozzle exit over-pressure is due to the inertia of the fluid initially anterior to the nozzle giving the jet something to "push off" of as it is ejected (as noted above). The co-flow term, on the other hand, represents the fluid accelerated across the nozzle exit plane to satisfy flow continuity and entrainment requirements as the vortex ring develops. The inertia related to this flow also contributes to the over-pressure as it must be accelerated from rest to non-zero velocity, but it is difficult to view the jet as directly "pushing off" of this fluid. (This term also suggests propulsive benefits could be obtained by placing a shroud around the nozzle to create a jet-pump.) Overall this analysis underscores the idea that the nozzle exit over-pressure derives from the inertia of the ambient fluid, which must be accelerated to non-zero velocity as a vortex ring is forming.

3.5.2.2 Relationship of Nozzle Exit Over-Pressure to Entrained and Added Mass

While the control volume analysis of the previous subsection demonstrates the connection between nozzle exit over-pressure and the acceleration of ambient fluid, consideration of the flow features generated by a starting jet unveils the physical mechanisms by which a starting jet can impart momentum to the ambient fluid. This is illustrated here by considering a developed vortex ring as shown on the right in Figure 3.9. The schematic of a developed vortex ring on the left in Figure 3.9 illustrates the two classes of ambient fluid accelerated by a starting jet. The first is ambient fluid entrained into the vortex ring bubble (defined by the ellipsoidal region containing dyed fluid) as the shear layer from the

nozzle boundary layer rolls up into a ring near the nozzle exit, as noted by Didden [10]. This can be seen in the PLIF image in Figure 3.9 where the dark bands in the ring indicate ambient fluid that is now moving downstream at the mean velocity of the ring. The second is an added mass effect, which occurs because some of the fluid in front of the jet must be accelerated out of the way when the starting jet is initiated and some ambient fluid must be brought in behind the ring to preserve continuity of the flow once it begins moving downstream. The illustration of this on the left in Figure 3.9 is meant to convey the added mass associated with the motion of a completely formed vortex ring[4],[5].

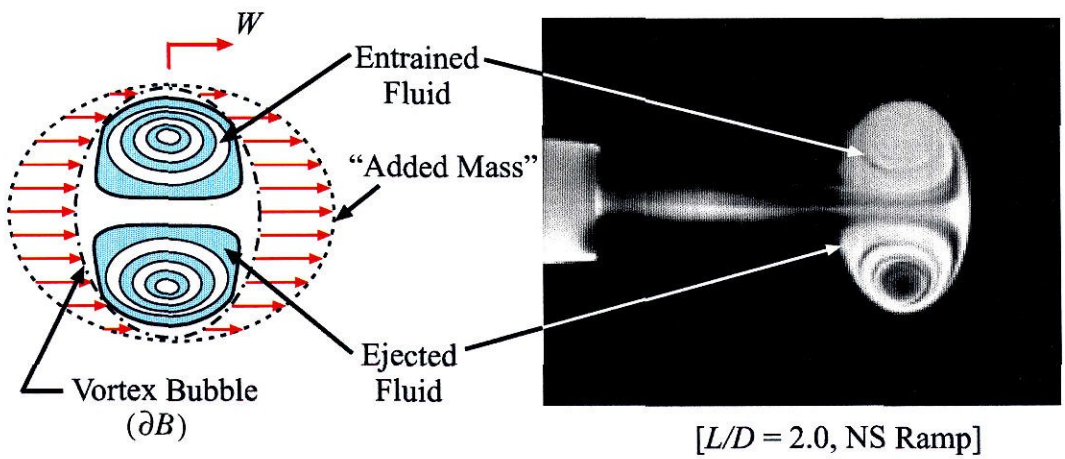

FIGURE 3.9 Illustration of the Two Classes of Ambient Fluid Accelerated by a Vortex Ring. (The image on the right is PLIF flow visualization for *L/D* = 2.0, NS ramp.)

4. The illustration of the added mass effect in Figure 3.9 suggests the added mass of the fluid external to the ring is actually convected with the ring in the sense that the same fluid particles are always in front of and behind the ring. Since the vorticity in the ring generates a velocity field that tends to sweep fluid around the boundary of the ring, this cannot be entirely true. Indeed, when a starting jet is initiated, this effect is manifested as ambient fluid getting pushed *out of the way*. It is therefore not possible to define this added mass as entrained mass in the traditional sense. The fluid inducted into to the body of the ring, however, can be considered entrained mass in that it is convected downstream with the ring.
5. Perhaps a term other than "added mass" should be used to describe the potential flow external to a completely formed vortex ring since it is associated with the steady motion of the ring while added mass is typically related to accelerating bodies. To avoid excessive terminology, however, added mass as used here also refers to the fluid motion external to a formed vortex ring.

A mathematical basis for these concepts as applied to vortex rings can be deduced from §4.2 of Saffman [32]. Here it is shown that the hydrodynamic impulse $\mathbf{I}_v$ of a vortex bound by a material surface ∂B can be expressed as

$$\mathbf{I}_v = \mathbf{P}_B + \mathbf{I}_a \tag{3.15}$$

where

$$\mathbf{P}_B \equiv \rho \int_B \mathbf{u} dV \tag{3.16}$$

and $\mathbf{I}_a$ is the virtual momentum of the material surface. The physical meaning of $\mathbf{I}_v$ is that it is the impulse that must be applied to the fluid to generate the flow [see equation (D.5)]. The virtual momentum, $\mathbf{I}_a$, is the impulse required to set a (massless) body in the shape of ∂B in motion against the inertia of the fluid.

For a vortex ring, ∂B is defined as the largest stream surface in the frame of reference moving with the ring velocity W that contains all of the ring vorticity. This is equivalent to the vortex bubble illustrated in Figure 3.9. Since the flow velocity on ∂B in the frame moving with the ring is tangential, it follows from the identity vector identity

$$\int_B \mathbf{u} dV = -\int_B \mathbf{x}(\nabla \bullet \mathbf{u}) dV + \int_{\partial B} \mathbf{x}(\mathbf{u} \cdot \hat{\mathbf{n}}) dS \tag{3.17}$$

and the incompressibility of the flow (i.e., $\nabla \bullet \mathbf{u} = 0$) that

$$\mathbf{P}_B = \rho V_B W \hat{\mathbf{x}} \tag{3.18}$$

where V_B is the volume of the vortex ring bubble and $\hat{\mathbf{x}}$ is aligned with the axis of the ring. If the ring is large enough so that B is simply connected, then $\mathbf{I}_a$ is given by

$$\mathbf{I}_a = \lambda \rho V_B W \hat{\mathbf{x}} \tag{3.19}$$

where $M = \lambda \rho V_B$ is the added mass of the vortex bubble[6]. That is, λ is given by

$$\lambda = \frac{1}{V_B} \int_{\partial B} \Phi \frac{\partial \Phi}{\partial n} \, dS \tag{3.20}$$

where $\phi = W\Phi$ satisfies $\nabla^2 \phi = 0$ and $\frac{\partial \phi}{\partial n} = W(\hat{\mathbf{x}} \cdot \hat{\mathbf{n}})$ on ∂B (see §5.1 of Saffman [32]). Given that $V_B = V_{ejected} + V_{entrained}$ as illustrated by Figure 3.9, it follows that

$$I_v = (m_{ejected} + m_{entrained} + M) W . \tag{3.21}$$

For L/D sufficiently small so that no trailing jet is formed, I_v represents the total impulse in the flow, I, which by equation (D.9) is equivalent to $I_U + I_p$ and by Newton's third law is equivalent to the total impulse measured by the force balance. Thus,

$$I = I_U + I_p = (m_{ejected} + m_{entrained} + M) W \tag{3.22}$$

for a vortex ring. From experiments, $I_U > m_{ejected} W$ for vortex rings with no trailing jet[7], so I_p is only associated with the acceleration of $m_{entrained}$ and M from rest to a

---

6. If the vortex ring is thin enough that the vortex "bubble" is actually a torus (as assumed by Weihs [39] and Miloh *et al.* [19]), then an extra term is required in equation (3.19) to correct for the fact that the "bubble" is not simply connected.

7. For example, the results for $L/D = 2$ of the NS ramps are $m_{ejected} W = 1.34 \times 10^{-3} \pm 0.09 \times 10^{-3} Ns$ and $I_U = 2.23 \times 10^{-3} \pm 0.04 \times 10^{-3} Ns$.

velocity of W. Because the contribution to I_p from a trailing jet is negligible, this conclusion also holds if a trailing jet is present (even though the calculation of M is complicated by the presence of the trailing jet). It therefore follows that I_p is associated with the acceleration of ambient fluid in the form of added and entrained mass from rest to a non-zero velocity (which is W in the case of an isolated vortex ring).

Taking these observations together with the previous discussion of the pressure impulse measurements demonstrates that the primary benefit of a leading vortex ring over a trailing jet for producing thrust is its mechanisms for moving and entraining ambient fluid. The contribution of this perspective is that it suggests ways for modeling the flow that would allow analytical evaluation of I_p. The added mass contribution holds the most promise since it is related to a potential flow problem. While the previous analysis dealt with the added mass for a developed ring, the idea could, in principle, be extended to a developing ring provided the shape of the ring could be approximated as it is forming. A rudimentary model along these lines will be presented in section 3.5.5. In any case, added mass effects should dominate at the initiation of a pulse since the jet must initially push ambient fluid out of the way as it is ejected. Entrainment, on the other hand, is related to the roll-up of the vortex sheet forming the ring. The non-linearity of this process and the ambiguity of the notion of a vortex bubble for a developing ring would make modeling entrainment more difficult, but a rudimentary model would still be worthwhile.

While the concepts of added and entrained mass add physical insight into the flow associated with the pressure impulse, there are a few caveats to this approach. First, the inequality $I_U > m_{ejected} W$ for vortex rings indicates that I_U is associated with $m_{entrained}$ and M as well. As a consequence conclusions about entrainment cannot be made directly

from I_p, so the question of the relative entrainment of a leading vortex ring and its trailing jet is not resolved by the data presented here. Second, the above analysis is for a developed ring, but what is actually of interest is how I_p evolves as a ring is forming. As noted above, this is an issue that must be addressed in formulating a model to predict I_p. Third, although related, the ambient reaction term in equation (3.14) is *not* equivalent to MW in equation (3.22). Similarly, the co-flow term in equation (3.14) and entrained mass term in equation (3.22) are related but not equivalent. Despite these caveats, the concepts of added and entrained mass clarify important issues and motivate further analysis/modeling.

3.5.3 The Contribution of Nozzle Exit Over-Pressure to Energy

Having explored the contribution of nozzle exit over-pressure to the total impulse of starting jets as well as the physics associated with this effect, the focus is now shifted to the pressure contribution to energy. To this end, measurements of the kinetic energy of the vortex rings only were extrapolated from PIV measurements for $L/D \leq 5.0$ using the relation

$$E_{ring} = \pi\rho \int_{ring} \omega_\theta(r,x)\psi(r,x)dS \tag{3.23}$$

where ψ is the Stokes stream function defined by

$$u = \frac{1}{r}\frac{\partial\psi}{\partial r} \qquad v = -\frac{1}{r}\frac{\partial\psi}{\partial x} \tag{3.24}$$

(see Lim and Nickels [16]) and the integration is over the extent of the vortex ring. Although no satisfactory method existed for *directly* determining the *total* energy, E,

injected into the flow by a pulse or the pressure work, E_p, done on the flow during a pulse, these quantities can be estimated using the assumption that $p(r, t) \approx p_\infty$ for $t > t_F$ justified in the previous section. This approximation states that the pressure work is only important for the formation of the vortex ring, so the total energy injected into the flow during a pulse is approximately

$$E \approx E_{ring} + E_{U,\,TJ} \tag{3.25}$$

and the pressure work is approximately

$$E_p \approx E_{ring} - E_{U,\,ring} \tag{3.26}$$

where E_{ring} is determined from PIV measurements using equation (3.23), $E_{U,ring}$ is $E_U(t_F)$, and $E_{U,TJ}$ is $E_U - E_U(t_F)$. [See equation (D.18) or Table 3.1 for a definition of $E_U(t)$ and appendix C for a definition of t_F.] The total energy determined this way is compared with the ring energy in Figure 3.10, where $E_{U,\,ring} = E_U(t_F)$ is also shown for comparison. The ratio of the pressure work and total energy determined by this analysis is shown in Figure 3.11.

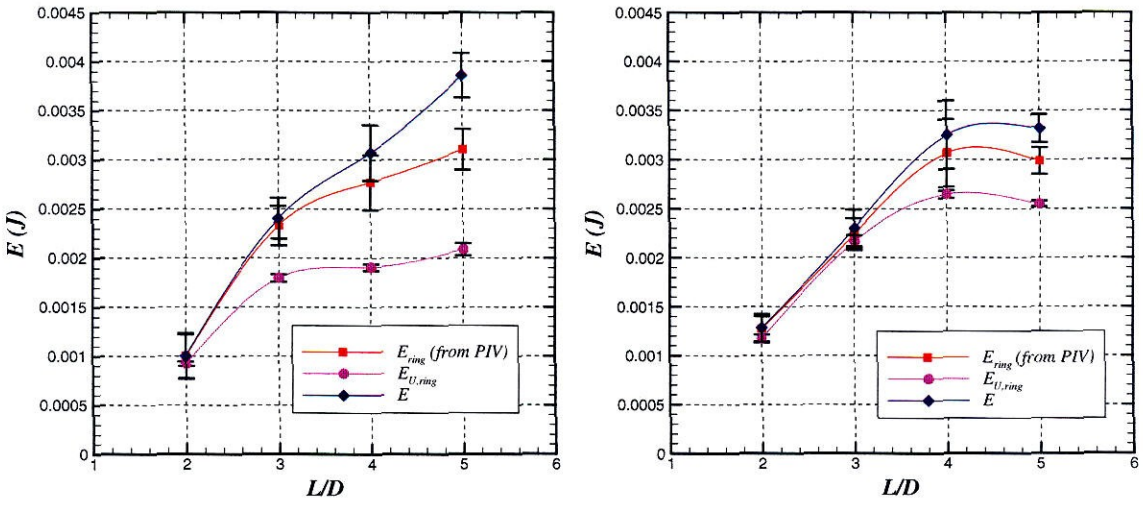

FIGURE 3.10 Vortex Ring Energy, Approximate Total Energy, and Energy from Velocity Flux Only: (a) NS Ramps, (b) PS Ramps.

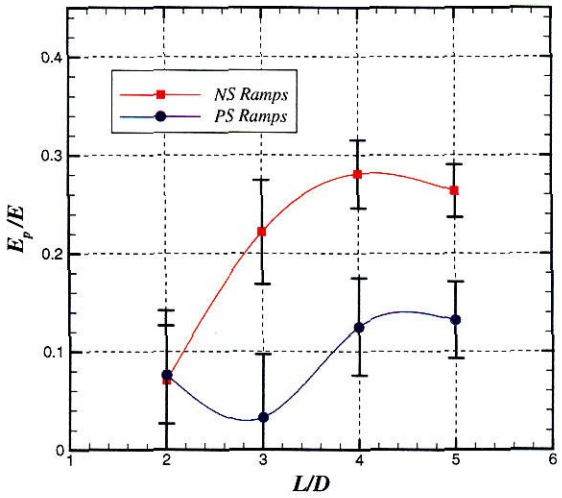

FIGURE 3.11 Ratio of Approximate Pressure Work to Approximate Total Energy for the NS and PS Ramps.

On comparing $E_{U,ring}$ with E_{ring}, it is apparent that the pressure work term makes a large contribution to the ring energy for the NS ramps and a smaller but significant contribution to the ring energy for the PS ramps. This checks with intuition since the pressure impulse for the two cases is comparable [see Figure 3.6 (a)], but the velocity increases much faster for $t < t_F$ with the NS ramps giving a larger contribution to E_p for these veloc-

ity programs since the pressure is weighted by u_J in the evaluation of E_p. The estimated total energy, on the other hand, is comparable to the ring energy for the cases tested, suggesting a relatively small contribution to the total energy from the trailing jet.

The results for E_p/E in Figure 3.11 show that the pressure work term can be as much as 28% of the total energy, as shown in the NS Ramp case for $L/D = 4.0$. More importantly, however, the overall trend of E_p/E (for the cases shown) is increasing with L/D, which is very different from the (generally) decreasing trend for I_p/I. While the magnitude of the error bars (indicating the precision of the measurements) makes it difficult to evaluate the strength of this trend, a reasonable hypothesis can be made about its source. Namely, an increasing trend could be explained by a large contribution to nozzle exit over-pressure late in a pulse where the jet velocity tends to be highest (especially for the PS ramps). Such a pressure contribution is most likely related to entrained mass effects since the shear layer roll-up is more advanced later in the pulse. This effect should increase with L/D, giving the observed trend. Added mass effects, on the other hand, likely dominate during the initiation of a pulse (as suggested in section 3.5.2.2) where the average jet velocity tends to be lower, making added mass an unlikely explanation for the trend in E_p/E at $L/D \geq 2.0$. For larger L/D (e.g., $L/D = 5.0$, NS Ramp), it appears that these considerations lose out in deference to the weak contribution to E_p from the trailing jet and E_p/E eventually starts to decrease.

Given the central role impulse plays in this study, it is also worthwhile to consider what impulse results for a given energy input to the flow, i.e., I/E. Using the measured total impulse and the estimated total energy determined above, this quantity is plotted in

Figure 3.12 along with I_U/E_U (the ratio considering only the velocity contribution to each quantity) for comparison. Although the error bars for I/E in Figure 3.12 are large, the general trend shows that I/E is greatest for smaller L/D and starts to level off after a significant trailing jet begins to appear for both the NS and PS cases. So, for a forming vortex ring, proportionally more energy than impulse is put into the flow to increase the size of the ring for the instances studied here. Due to the lack of nozzle exit over-pressure in the trailing jet, however, the impulse and energy increase roughly in proportion to each other when increasing the size of a trailing jet. Significantly, Figure 3.12 also shows that I_U/E_U is approximately constant for both the NS and PS cases, indicating these features would be missed if the pressure contributions were ignored.

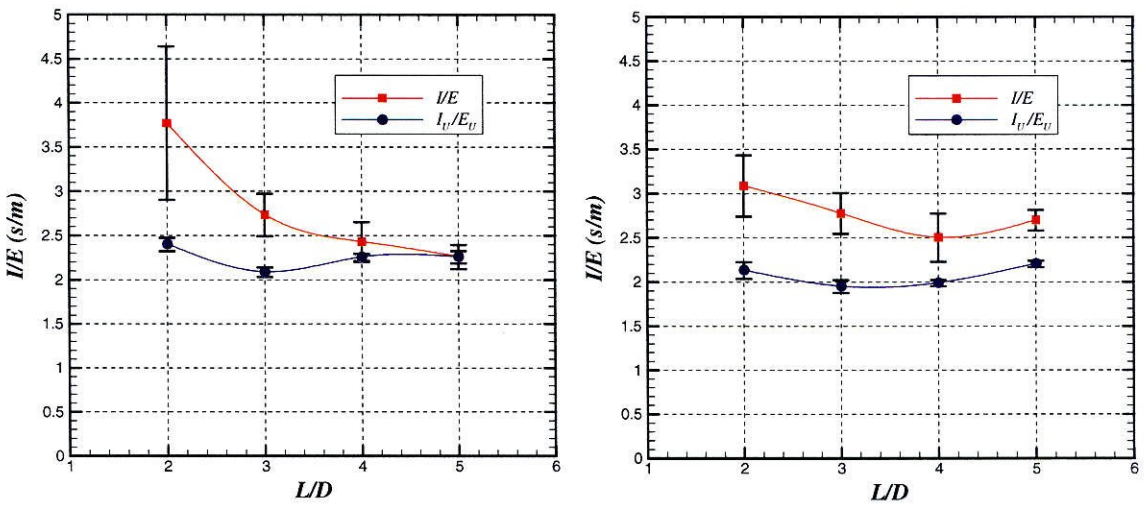

FIGURE 3.12 Estimates of the Impulse per Energy Inputs for the (a) NS Ramps, and (b) PS Ramps.

Overall the results of this section indicate the importance of nozzle exit over-pressure for correct evaluation of the energy input into the flow by starting jets, especially for the NS ramps. They also suggest that different sources of nozzle exit over-pressure during

the formation of a vortex ring (i.e., mass entrainment vs. added mass at pulse *initiation*) can effect E_p differently.

3.5.4 The Contribution of Nozzle Exit Over-Pressure to Circulation

Measurements of the actual ring circulation for $L/D \leq 5$ were obtained using PIV measurements of the vorticity field ω_θ and the result

$$\Gamma_{ring} = \int_{ring} \omega_\theta(r, x) dS \tag{3.27}$$

(see appendix D). Figure 3.13 compares these measurements with the ring circulation expected from the vorticity flux associated with the boundary layer of the jet, namely, $\Gamma_{U,\,ring} = \Gamma_U(t_F)$ where the definitions of $\Gamma_U(t)$ and t_F are given in equation (D.33) and appendix C respectively. Figure 3.13 also plots $Re_\Gamma \equiv \frac{\Gamma}{\nu}$ on the right-hand axis for comparison. From this figure it is clear that $\Gamma_{U,\,ring} < \Gamma_{ring}$ for all the cases tested. This result is not entirely surprising since $\Gamma_{U,ring}$ is essentially a boundary-layer corrected slug model for ring circulation and Didden [10] showed that the slug model significantly under estimates the circulation injected into the flow. The equation for total circulation in the generalized slug flow equations [see equation (D.33) or Table 3.1], on the other hand, indicates that the difference between $\Gamma_{U,ring}$ and Γ_{ring} is due to a contribution from nozzle exit over-pressure at the nozzle center line. Figure 3.13 shows that this contribution to the ring circulation is relatively constant with L/D for the NS ramps and steadily decreases

with L/D for the PS ramps. In both cases it accounts for as much as 30% of the ring circulation at $L/D = 2.0$.

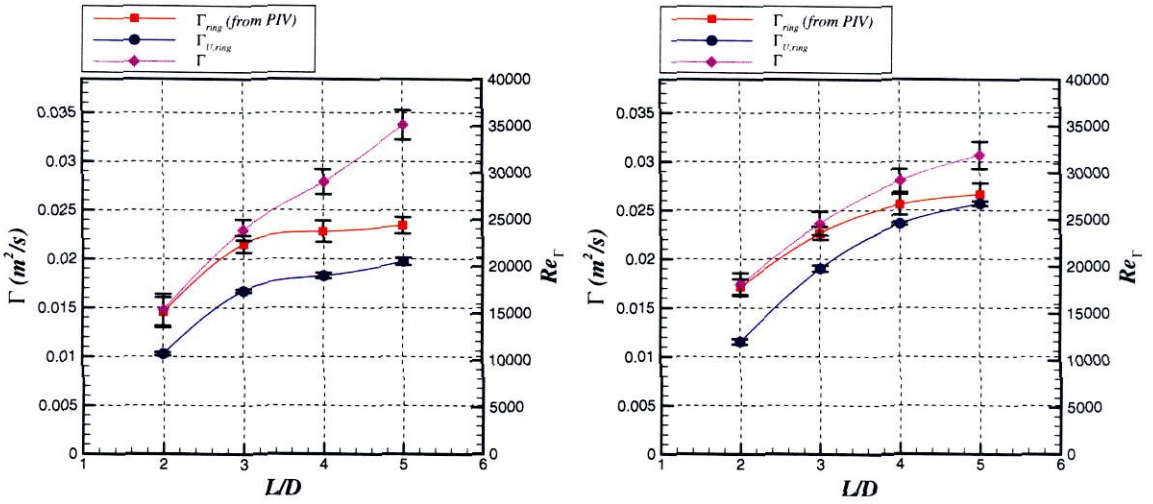

FIGURE 3.13 Circulation of the Ring and Total Circulation Ejected During a Pulse: (a) NS Ramps, and (b) PS Ramps.

The overall significance of the pressure contribution to circulation can be evaluated by approximating the total circulation ejected during a pulse, Γ, and the total pressure contribution to this circulation, Γ_p. This can be accomplished with the same approximations used to determine the total energy, E, and pressure work, E_p, in section 3.5.3. Accordingly, Γ is approximated by

$$\Gamma \approx \Gamma_{ring} + \Gamma_{U,TJ} \tag{3.28}$$

and Γ_p is approximated by

$$\Gamma_p \approx \Gamma_{ring} - \Gamma_{U,ring} \tag{3.29}$$

where $\Gamma_{U,\,ring} = \Gamma_U(t_F)$ (defined previously), $\Gamma_{U,\,TJ} = \Gamma_U - \Gamma_U(t_F)$ is the approximate contribution of the trailing jet to the total circulation in the flow, and $\Gamma_U = \Gamma_U(t_p)$. The results for Γ are plotted in Figure 3.13 and will be used in subsequent sections while the results for Γ_p are used to generate the plot of Γ_p/Γ shown in Figure 3.14.

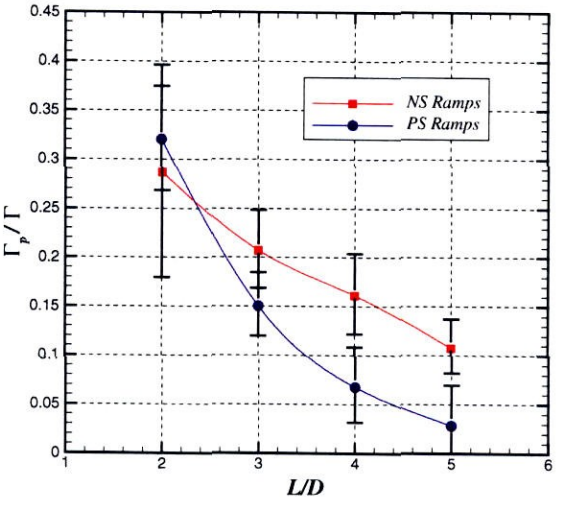

FIGURE 3.14 Ratio of Circulation Due to Nozzle Pressure and Total Circulation.

Figure 3.14 illustrates that, as noted earlier, Γ_p can be as much as 32% of the total circulation injected into the fluid for the cases studied. More importantly, Γ_p/Γ shows a generally decreasing trend, which, by analogy with the earlier discussion comparing E_p/E with I_p/I, suggests that over-pressure due to added mass effects at the *initiation* of a starting jet contribute significantly to (or dominate) Γ_p. This hypothesis is illuminated by the theoretical example considered in the next section.

3.5.5 Insight from a Model for an Impulsive Velocity Program

An impulsive velocity program is illustrated in Figure 3.15. The initially sharp increase in jet velocity means that the ambient fluid must be impulsively accelerated at the initiation of the pulse. The control volume analysis of section 3.5.2.1 indicates that the contribution from nozzle exit over-pressure will therefore be large (indeed, infinite) during the initiation of such a velocity program, making it a nice example to illustrate pressure phenomena at pulse initiation. It is also a reasonable approximation for the initiation of the NS ramps and may provide some insight to the results discussed previously for this class of velocity programs. In this section a model for the initial stages of such an impulsive velocity program is proposed and its relationship to the previous measurements is discussed.

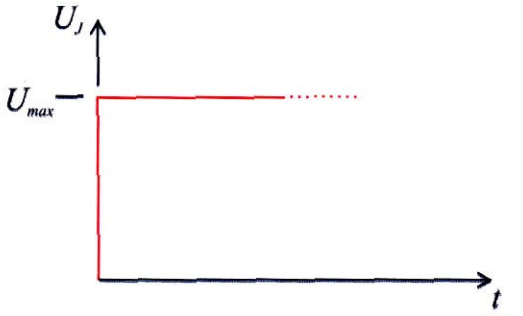

FIGURE 3.15 Illustration of an Initially Impulsive Velocity Program.

3.5.5.1 A Model for an Impulsive Velocity Program Near Pulse Initiation

Some insight into an appropriate model for the early stages of an impulsive velocity program can be gained by considering flow visualization near the initiation of nearly impulsive velocity programs, such as the NS Ramps. Figure 3.16 shows three instances near the initiation of a starting jet for $L/D = 5$ of the NS ramps. From these images it is

apparent that the flow exiting the nozzle is more cylinder-like than ring-like for $X/D \ll 1$ where $X(t)$ is defined in equation (2.2). This motivates a model for the *initial* stages of pulse ejection that ignores the roll-up of the vortex ring, as illustrated schematically for three successive instances in Figure 3.17.

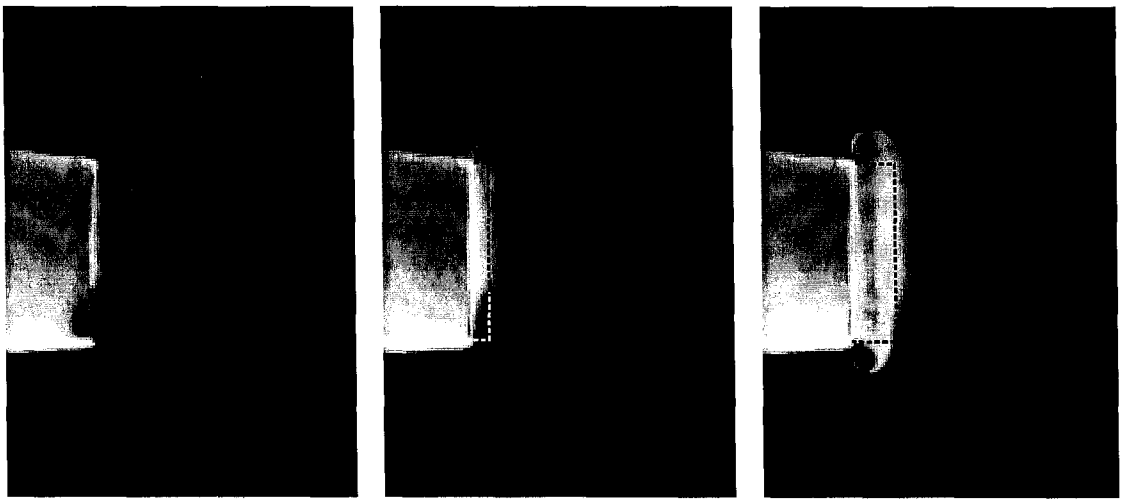

$t < 0$ | $t = 0.007$s, $X/D \ll 1$ | $t = 0.011$s, $X/D \ll 1$

Cylinder-like | **Approximately cylinder-like**

FIGURE 3.16 Illustration of the Cylinder-Like Nature of the Flow at Pulse Initiation for $L/D = 5$ of the NS Ramps.

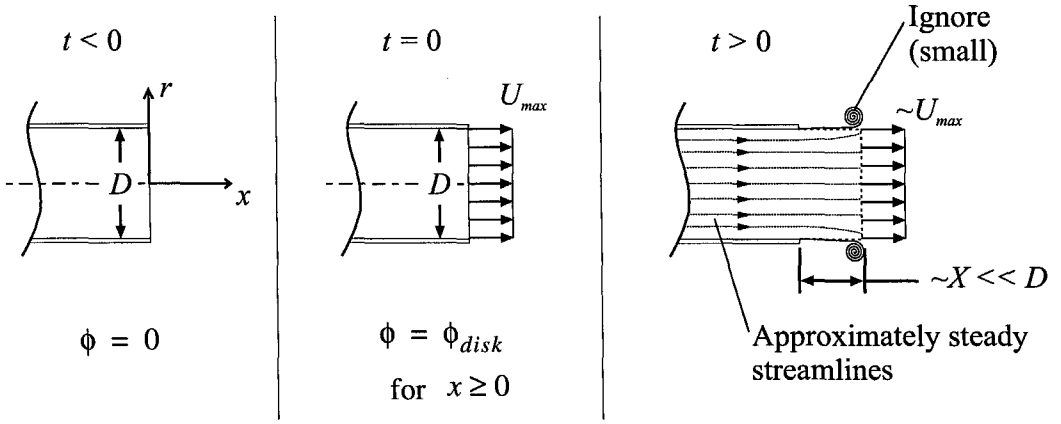

FIGURE 3.17 Model for the Initiation of an Impulsive Velocity Program.

By ignoring the ring formation in the range $0 < X/D \ll 1$, the model shown in Figure 3.17 assumes that the jet essentially behaves like a steady jet for $t > 0$ and all of the pressure effects are concentrated at the initiation of the jet (i.e., $t = 0$). The advantage of this approximation is that the flow is irrotational for $t \leq 0$, so the unsteady Bernoulli equation, given by equation (3.11), can be used to evaluate the pressure effects at the initiation of the jet. This is accomplished by evaluating equation (3.11) at $x = 0$ (the nozzle exit plane), integrating in time over an interval near $t = 0$, and integrating over the nozzle cross section when necessary. For impulse and circulation the results are

$$I_p(0) = -\rho \lim_{\varepsilon \to 0}\left[\frac{1}{2}\int_{-\varepsilon}^{\varepsilon}\int_A |\mathbf{u}(0, r, \tau)|^2 dS d\tau + \int_{-\varepsilon}^{\varepsilon} \frac{\partial}{\partial \tau}\left(\int_A \phi(0, r, t) dS\right) d\tau\right] = -\rho \int_A [\phi] dS \quad (3.30)$$

and

$$\Gamma_p(0) = -\lim_{\varepsilon \to 0}\left[\frac{1}{2}\int_{-\varepsilon}^{\varepsilon} |\mathbf{u}(0, 0, \tau)|^2 d\tau + \int_{-\varepsilon}^{\varepsilon} \left.\frac{\partial \phi}{\partial \tau}\right|_{r, x = 0} d\tau\right] = -[\phi]|_{r = 0} \quad (3.31)$$

where $[\phi]$ denotes the change in $\phi(0, t)$ at $t = 0$. The pressure work contributed at $t = 0$ is then given by

$$E_p(0) = U_{max} I_p(0) \quad (3.32)$$

because the jet velocity is constant at U_{max}. Finally, it follows from the model that $I_p \approx I_p(0)$, $\Gamma_p \approx \Gamma_p(0)$, and $E_p \approx E_p(0)$ since pressure contributions are ignored for $t > 0$ and $X/D \ll 1$.

The $[\phi]$ terms in equations (3.30) and (3.31) can be evaluated by noting that the jet velocity is uniform over the nozzle cross section at the initiation of the jet, as illustrated in

Figure 3.17. That is, the flow for $x > 0$ at $t = 0$ appears like the potential flow in front of a circular disk translating at a velocity U_{max} in the x direction. Combining this with the fact that $\phi = 0$ for $t < 0$ gives

$$[\phi] = -\frac{2U_{max}}{\pi}\sqrt{\left(\frac{D}{2}\right)^2 - r^2}. \tag{3.33}$$

(See §6.8 of Batchelor [3] or §6.4 of Saffman [32] for the potential flow solution over a circular disk.) Using this result in equations (3.30), (3.31), and (3.32) gives

$$I_p \approx \frac{1}{6}\rho D^3 U_{max}, \tag{3.34}$$

$$\Gamma_p \approx \frac{U_{max} D}{\pi}, \tag{3.35}$$

and

$$E_p \approx \frac{1}{6}\rho D^3 U_{max}^2. \tag{3.36}$$

Then, combining these results with the generalized slug flow equations (Table 3.1) gives

$$I(t) \approx \rho\int_0^t \int_A u_J^2(r,\tau)\,dS\,d\tau + \frac{1}{6}\rho D^3 U_{max}, \tag{3.37}$$

$$\Gamma(t) \approx \frac{1}{2}\int_0^t u_{cl}^2(\tau)\,d\tau + \frac{U_{max} D}{\pi}, \tag{3.38}$$

and

$$E(t) \approx \frac{\rho}{2}\int_0^t \int_A u_J^3(r,\tau)\,dS\,d\tau + \frac{1}{6}\rho D^3 U_{max}^2 \tag{3.39}$$

for an impulsive velocity program at $X/D \ll 1$.

The utility of this model is that is illustrates the origin of nozzle exit over-pressure at the initiation of a starting jet. Specifically, the pressure results given by equations (3.34), (3.35), and (3.36) are based on a potential flow solution for $x > 0$, indicating that by increasing the jet velocity at $x = 0$ from 0 to U_{max}, *all* of the fluid for $x > 0$ must also be imparted some momentum. The reaction force associated with this manifests itself as pressure at the nozzle exit. This idea also illustrates how added mass can provide an equivalent description of the pressure impulse at the initiation of a starting jet. That is, as noted before, the flow produced by the jet initially appears like that over the front half of a disk moving at U_{max}. The added mass associated with the flow in front of a circular disk, however, is $m_{a,\,half\text{–}disk} = \frac{1}{6}\rho D^3$ (see §6.10 of Batchelor [3]) so that the impulse required to initiate the flow is simply

$$m_{a,\,half\text{–}disk} U_{max} = \frac{1}{6}\rho D^3 U_{max} = I_p(0). \tag{3.40}$$

Thus, the initial pressure impulse can be related to the added mass associated with the initial acceleration of the jet (approximated as a cylindrical slug) into the ambient fluid.

This model does, however, over simplify the initial formation process. By neglecting the roll-up of the vortex sheet it ignores the unsteady component of the flow following the initiation of the jet. As a consequence, entrainment has been ignored as well as the fact that the effective diameter of the front of the slug is increasing in time rather than constant at D. The net effect of these approximations is that the model underestimates the contribution of pressure to I, Γ, and E for $t > 0$. At $X/D \ll 1$, however, the corrections

implied by these observations should be relatively minor, so the model still gives a nice illustration of the flow physics at the initiation of a starting jet.

3.5.5.2 Application of the Model for an Impulsive Velocity Program to the NS Ramps

As indicated by Figure 3.1 (a), the NS ramp velocity programs begin with a relatively impulsive ramp up to U_{max} at $t = t_{max}$ and then decelerate down to zero at $t = t_p$. The impulsive nature of the startup for these velocity programs suggests that the startup period (i.e., $t = 0$ to t_{max}) for the NS ramps could be modeled as in section 3.5.5.1. In particular, if the fluid entrainment into the ring during formation has negligible effect on the nozzle pressure at the center line (a reasonable assumption since the entrainment initially occurs away from the center line), then the pressure contribution to the circulation of the ring is due primarily to the acceleration ambient fluid in front of the ring as the jet is initiated. Further support for this idea is given by Figure 3.14, which shows that Γ_p/Γ decreases with increasing L/D. Since pulses with longer duration do not seem to increase the contribution of Γ_p it appears that Γ_p is determined principally at the initiation of the jet. Given this background, it seems reasonable to approximate the *total* pressure contribution to circulation for the NS ramps by equation (3.35), namely, $\Gamma_p \approx \frac{U_{max}D}{\pi}$. Implicit in this approximation is the assumption used in sections 3.5.3 and 3.5.4 that $p \approx p_\infty$ at the nozzle exit after the ring is formed.

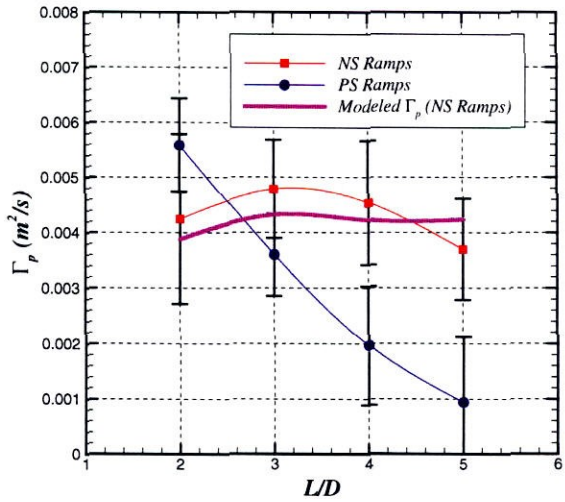

FIGURE 3.18 Comparison of the Measured Pressure Contribution to Circulation and the Model Based on an Impulsive Velocity Program.

This model for Γ_p can be compared directly with experimental measurements. Following section 3.5.4, Γ_p can be determined using equation (D.33) to give

$$\Gamma_p = \Gamma - \Gamma_U \approx \Gamma_{ring} - \Gamma_{U,\,ring} \tag{3.41}$$

where Γ_{ring} and $\Gamma_{U,ring}$ are defined following equation (3.29) and are determined directly from measurements. Measurements of Γ_p obtained this way for the NS and PS ramps are compared with the model value of $\Gamma_p \approx \dfrac{U_{max} D}{\pi}$ for the NS ramps in Figure 3.18. The results agree well for the NS ramps, but it is apparent that this model will not work for the PS ramps since it does not capture the steady decrease in Γ_p with L/D. This is to be expected since these velocity programs become less impulsive as L/D increases (i.e., the fluid in front of the jet is only accelerated to the velocity of the ring for larger L/D, which is smaller than the maximum jet velocity). At the very least, this analysis suggests a good

model for the circulation injected into the flow by *impulsive* velocity programs from a piston-cylinder mechanism is

$$\Gamma(t) \approx \frac{1}{2}\int_0^t u_{cl}^2(\tau)d\tau + \frac{U_{max}D}{\pi} \qquad t > t_{max}. \tag{3.42}$$

Significantly, equation (3.42) accounts for the relatively constant offset between actual measurements of circulation and the slug model predictions for nearly impulsive velocity programs (Didden [10]), placing this discrepancy squarely in the realm of pressure effects.

Based on the successful application of the model results of section 3.5.5.1 to Γ_p for the NS Ramps, it is tempting to also apply the model results for I_p to the measured results for this class of velocity programs. Using equation (3.34) with $U_{max} = U = 1.03 m/s$, however, gives I_p = 0.000352 Ns, which is about 22% of the actual I_p for the NS ramp at $L/D = 2$. Clearly this approximation cannot account for all of the measured I_p because it ignores any nozzle over pressure required to accelerate entrained fluid as the ring is forming. It also does not account for the added mass effects associated with the change in shape of the ring from a disc to an ellipsoid of larger diameter as it forms. Nevertheless, this result demonstrates that the added mass effect associated with the acceleration of ambient fluid at the initiation of a starting jet can supply a substantial fraction of the pressure impulse, especially for small L/D. It also suggests the generally higher values of I_p/I for the NS ramps over the PS ramps may be due to a larger contribution to nozzle over-pressure at the initiation of a pulse for the NS ramps since the initial jet velocity ramp is more impulsive for these velocity programs.

3.5.5.3 Some Comments on the Limit as *L/D* Goes to Zero

The model proposed above for the initiation of an impulsive velocity program is strictly valid only in the limit $X/D \rightarrow 0$. An analogous limit of some interest is the limit $L/D \rightarrow 0$ while U_{max} is kept constant. In this limit, both the NS and PS ramps approach the same limiting velocity program, namely that shown in Figure 3.19. Clearly the pulse initiation for this case can be modeled as in section 3.5.5.1, but the pulse termination poses a problem because it is nearly coincident with the pulse initiation. (That is, the limit $X/D \rightarrow 0$ for an impulsive velocity program and $L/D \rightarrow 0$ while U_{max} is kept constant are not equivalent.) Indeed, one could argue that for $L/D \rightarrow 0$, the effects at pulse initiation and termination nearly cancel. If, however, they do not precisely cancel, then it follows directly that $I_p/I = \Gamma_p/\Gamma = E_p/E = 1$ in the $L/D \rightarrow 0$ limit since the jet velocity is only finite for an infinitesimal amount of time. This result, if true, implies a minimum in E_p/E between $L/D = 4$ and 0 for both the NS and PS ramps. A trend of this nature could give insight into the development of nozzle exit over-pressure while a pulse is being ejected, motivating further investigation of cases with $L/D \ll 1$.

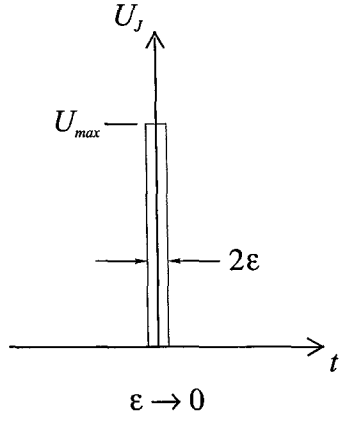

FIGURE 3.19 Velocity Program for the Limit of *L/D* Going to Zero.

3.6 Vortex Ring Pinch Off Models Revisited

All of the models for predicting vortex ring pinch off that presently exist employ the slug model approximations to estimate the energy, impulse, and circulation injected into the flow by a piston-cylinder mechanism. As noted in section 3.5.1, the slug model explicitly ignores the contribution of pressure to these quantities. The discussion to this point, however, has revealed the importance of including the contribution of nozzle exit over-pressure for a correct representation of the dynamics of starting jets. So, it is relevant to evaluate these models in light of this information.

3.6.1 The Dynamic Model Based on the Kelvin-Benjamin Variational Principle

The model proposed by GRS based on the Kelvin-Benjamin variational principle for steadily translating vortex rings (see section 1.2.1.2) considers the non-dimensional energy, α, defined as

$$\alpha \equiv \frac{E/\rho}{\sqrt{(I/\rho)\Gamma^3}}. \tag{3.43}$$

It then hypothesizes that as long as the α supplied by the generating device exceeds the α of a pinched off ring (denoted α_{lim}), ring formation continues. In their model, GRS estimated the α supplied to the flow by their piston-cylinder mechanism, α_{piston}, using the slug model, i.e., $\alpha_{piston} \approx \alpha_{sm}$, and showed that α_{piston} crossed α_{lim} approximately where vortex ring pinch off was observed in their experiments.

A similar analysis is applied to the results of this investigation, as shown in Figure 3.20. Here the α of the isolated vortex rings for each L/D (determined using PIV measurements of E, I, and Γ and denoted α_{ring}) are plotted instead of α_{lim}. The results for α_{ring} give approximately straight lines for both the NS and PS cases at levels similar to the value of $\alpha_{lim} = 0.31$ determined by GRS. Estimates for α_{piston} are made using the slug model, denoted α_{sm}, and using the velocity terms in the generalized slug flow equations, denoted α_U, which gives a boundary layer correction to the slug model. For both the NS and PS cases, Figure 3.20 shows that both α_{sm} and α_U intersect α_{ring} at a value of L/D larger than the point where a significant trailing jet begins to appear. The model, therefore, over predicts the value of L/D at which pinch off is observed for these velocity programs. Significantly, the model does a better job for the PS ramps, where the pressure contribution to circulation is less dramatic. Clearly, then, the pressure terms do make a difference in this model for the velocity programs considered here.

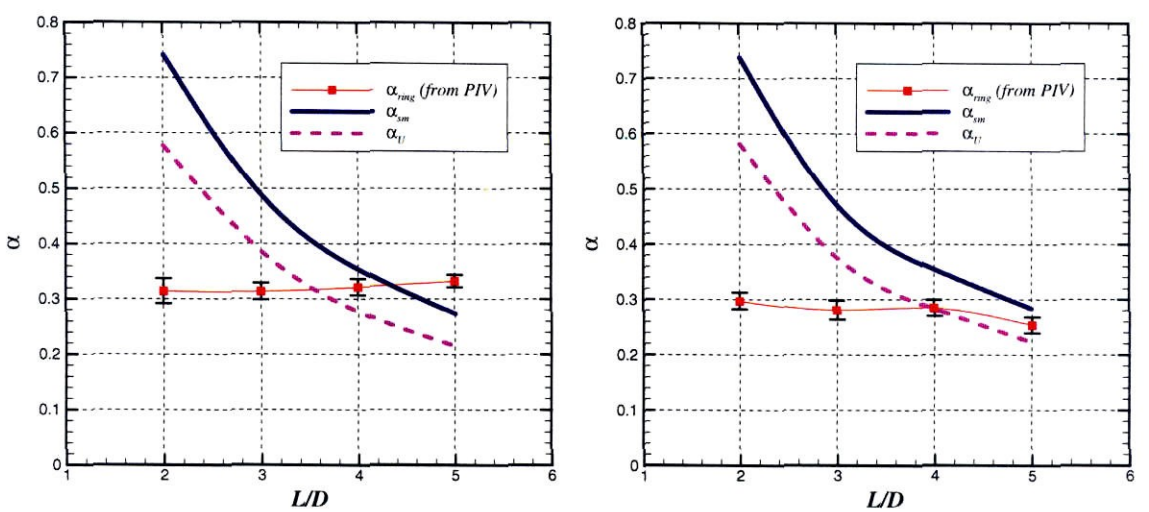

FIGURE 3.20 Applying the Kelvin-Benjamin Variational Principle to the Results of this Investigation: (a) NS Ramps, (b) PS Ramps.

The importance of the pressure terms is more apparent when it is realized that the α's calculated here refer to *completed* pulses (rather than developing rings/jets as in GRS). That is, for cases where only an isolated ring is formed, the energy, impulse, and circulation ejected by the piston-cylinder mechanism are completely entrained into ring, so α_{piston} and α_{ring} should be *equal* as long as the vortex ring has not pinched off from its generating jet. Based on this realization, α_{piston} is recalculated using the total measured impulse and the approximations of the total energy and circulation made in sections 3.5.3 and 3.5.4. Denoting the result as α_T, this estimate of α_{piston} is plotted with α_{ring} in Figure 3.21. The approximate values for α_T appear to always be below α_{ring}, but aren't significantly below α_{ring} until $L/D = 3$ is reached for the NS ramps and $L/D = 4$ is reached for the PS ramps. Furthermore, after these points the α's begin to diverge, as expected from the model proposed by GRS. These observations suggest the hypothesis based on the Kelvin-Benjamin variational principle given by GRS accurately describes vortex ring pinch off, but the slug model vastly over estimates α for small L/D. It is hypothesized that a proper determination of α_{piston} as a function of time should give α_{piston} greater than but approximately equal to α_{lim} while the vortex ring is forming (since not all of the fluid ejected has actually rolled up into the ring during formation), but indicate that it drops below α_{lim} once the leading vortex ring has pinched off.

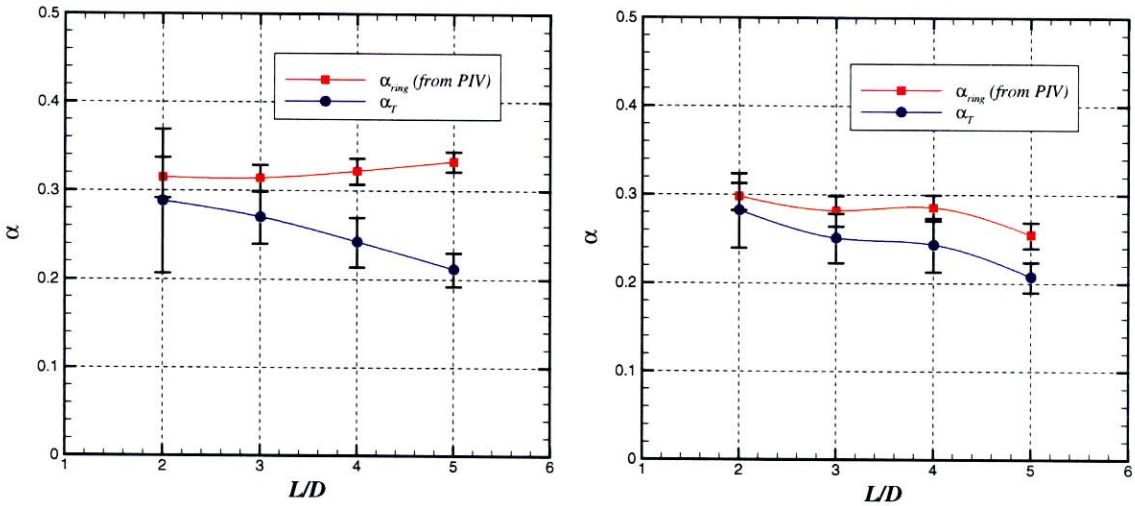

FIGURE 3.21 Comparison of α_{ring} with Estimates of α_T: (a) NS Ramps, (b) PS Ramps.

3.6.2 The SG Model

The predictions of vortex ring pinch off in this investigation were based primarily on the SG model discussed earlier, which also relied on the slug model approximations. A detailed analysis of the implications of the slug model for the SG model will not be given here, except to note that the slug model does not affect the SG model as seriously as the model based on the Kelvin-Benjamin variational principle for three reasons. First, the results of the SG model only apply near vortex ring pinch off. As seen in the previous sections, the amount by which the slug model differs from the expected result is much less here than for smaller L/D. Second, the dependence of the SG model on the dynamic quantities of the jet goes as $\sqrt{I\Gamma}$ [see equation (C.9)], so the dependence on Γ is much less pronounced in this model (α depends on $\Gamma^{-3/2}$). As a result, errors in the determination of Γ do not affect this model as severely. Finally, Shusser *et al.* [36] indicate that the

predictions of the model depend strongly on the value chosen for ε, but note that over the wide variety of time-varying velocity programs studied, ε = 0.4 always gave the best result. This suggests that a proper choice of ε has "tuned out" some of the deficiencies of the slug model.

3.7 Conclusions

The dynamic properties of starting jets are investigated using two classes of velocity programs (NS and PS), where the SG model for vortex ring pinch off demonstrates that a trailing jet does not become a significant part of the flow until $L/D > 3.0$ for the NS case and $L/D \geq 4.0$ for the PS case. Measurements of the total impulse for these velocity programs show a significant decrease in the growth rate of total impulse with L/D once the starting jets reach stroke ratios of 3.0 and 4.0 for the NS and PS cases respectively. From this it is concluded that the trailing jet contributes proportionately less to the total impulse than the leading vortex ring. Additionally, the average thrust during a pulse is maximal near L/D = 3.0 and 4.0 for the NS and PS cases respectively. This confirms the original hypothesis of GRS that maximized vortex rings (i.e., just before vortex ring pinch off) are significant for propulsion purposes in the sense that they give the most efficient delivery of thrust in a given amount of time.

An evaluation of the pressure contribution to the total impulse per pulse using the generalized slug flow equations with the impulse and jet velocity measurements elucidates the effect of vortex ring pinch off. The results show that very little nozzle exit overpressure exists once the vortex rings have pinched off from the trailing jet, demonstrating

that the propulsive benefit of starting jets is directly determined by the nozzle exit over-pressure provided during vortex ring formation. A control volume analysis of the fluid in front of the jet relates the pressure contribution to impulse to the reaction force on the jet section provided by the inertia of the accelerated ambient fluid. An alternative description of the origin of the pressure impulse is given by a hydrodynamic analysis of the impulse associated with a completed vortex ring. This analysis demonstrates that the pressure impulse is determined by the acceleration of two classes of ambient fluid by the starting jet: (a) "added mass," which is fluid external to the nozzle that is accelerated out of the way by the initiation of a starting jet and that is accelerated to follow the forming vortex ring as it translates downstream, and (b) entrained mass that is inducted into the body of the ring as the shear layer rolls up and is convected downstream with the ring. Since the relative contribution of these two classes is not determinable from the measurements, the relative importance of the leading vortex ring and the trailing jet for fluid entrainment is not resolved by this experiment.

The result that over-pressure is small during the ejection of a trailing jet also provides a way to extrapolate measurements of the total energy and circulation from PIV measurements of these quantities for the rings alone and measurements of the jet velocity during a pulse. The approximate results for the contribution of nozzle exit over-pressure to circulation, Γ_p, and energy, E_p, show that the contribution is increasingly significant for circulation as L/D decreases and that the contribution to energy as a fraction of the total energy, E_p/E, increases with L/D for $2.0 < L/D < 4.0$. The results for Γ_p suggest this effect is determined primarily by nozzle exit over-pressure at the initiation of a pulse while

the E_p/E results suggest over-pressure due to fluid entrainment also becomes significant later in the pulse ejection where the jet velocity is higher.

A simplified model of the initial stages of a starting jet formed by an impulsive velocity program demonstrates the importance of pressure effects at the initiation of a starting jet. In particular, application of the model to the NS ramps shows that Γ_p for this family of velocity programs is approximately $\frac{U_{max}D}{\pi}$. Pressure effects, therefore, give a nice explanation of the discrepancy between the estimates of ring circulation from the slug model and actual circulation measurements. The deficiencies of the model in predicting I_p, however, illustrate the importance of including entrainment effects to obtain a complete description of vortex ring formation.

As a final consideration, it is important to evaluate the effect of nozzle exit over-pressure on the models for predicting vortex ring pinch off. The results show that over-pressure has a significant effect on the model based on the Kelvin-Benjamin variational principle in that it does not correctly predict the appearance of vortex ring pinch off in the NS and PS cases studied. A more rigorous evaluation of the non-dimensional energy α using the actual values of the dynamic quantities (as determined or approximated from measurements) rather than those estimated from the slug model indicates that the principle of the model is sound, but correct evaluation of α should give α_{piston} *nearly equal to* α_{lim} until vortex ring pinch off occurs, at which point α_{piston} drops below α_{lim}. Consideration of the SG model, on the other hand, suggests that this model is less affected by nozzle exit over-pressure primarily because it is less dependent on the contribution of over-pressure

through Γ and because a proper choice of the non-dimensional core radius ε in the model tends to factor out this issue.

To conclude this discussion, it is emphasized that the differences between starting jets that produce isolated vortex rings and those that produce vortex rings followed by trailing jets can be attributed to the nozzle exit over-pressure exhibited during the formation of vortex rings and the lack thereof during the ejection of a trailing jet. Because of this result it is nearly impossible to draw meaningful conclusions about the development of the individual dynamic quantities I, E, and Γ from the slug model, which ignores pressure effects and, therefore, *does not distinguish* between vortex rings and trailing jets. It is possible to correct the slug model for some special cases (such as the determination of circulation for impulsively started jets), but proper modeling of the mechanisms for accelerating ambient fluid during the formation of a vortex ring at finite L/D is needed to provide a satisfactory substitute for the slug model. The importance of modeling such mechanisms is highlighted by the difference in the propulsive benefit (as indicated by I_p/I) between the NS and PS ramps where the higher value for the relatively impulsive NS ramps suggests utilization of added mass effects at the initiation of a pulse can be an important way to enhance the propulsive output of starting jets. While the data presented here do not resolve all the issues sufficiently well to allow detailed modeling (especially of the relative importance of added mass and entrained mass in determining nozzle exit over-pressure), they do indicate what issues are involved and motivate further investigation.

CHAPTER 4

Investigation of the Time-Averaged Thrust and Vorticity Evolution of a Fully-Pulsed Jet

4.1 Introduction

The previous chapter on the dynamic properties of starting jets illuminated the importance of vortex ring formation and pinch off for the impulse and thrust produced by a single starting jet. For practical applications, such as propulsion or pumping using fluid entrainment, multiple starting jets or pulses in the form of a fully-pulsed jet are of interest in order to generate thrust or pumping indefinitely. In a fully-pulsed jet, however, the ambient fluid is no longer quiescent at the initiation of each pulse since it has been disturbed by preceding pulses. This is a crucial factor that makes the extension of starting jets to fully-pulsed jets non-trivial and raises several specific issues of interest in studying fully-pulsed jets.

First, since it was found that the impulse due to nozzle exit over-pressure is critical to the impulse generated by starting jets, it is important to determine the effect of the proximity of successive pulses in a fully-pulsed jet (i.e., pulsing frequency) on the mechanisms that provided the over-pressure in starting jets (added mass and fluid entrainment effects). Fundamentally, this is an issue of how the proximity of previous pulses affects vortex ring

formation and pinch off since it was determined that the pressure impulse for starting jets is governed by vortex rings and not trailing jets.

Second, the ejection of multiple pulses implies multiple vortex rings in the flow, which allows for the possibility of vortex ring interaction. As discussed in chapter 1, Weihs [39] hypothesized that vortex ring interaction could have significant ramifications for propulsion due to the increased convective velocity of an infinite train of vortex rings over that of individual vortex rings. Thus, the multiplicity of pulses afforded by a fully-pulsed jet may provide propulsive benefits greater than that expected from a simple additive superposition of the results for individual starting jets[1].

Applying Weihs' result to a real fully-pulsed jet, however, is not necessarily straightforward. Specifically, Weihs' analysis is not concerned with the phenomenon of vortex ring pinch off in that it deals only with vortex rings (trailing jets are not considered). It also implicitly embodies several other assumptions:

1. The formation of vortex rings in a fully-pulsed jet is undisturbed by the presence of preceding pulses in that the amount of ambient fluid accelerated by each ring is the same irrespective of the separation of vortex rings;
2. It is possible to reduce the separation of vortex rings generated by a fully-pulsed jet to any arbitrary level (barring collision of vortex rings) by increasing the pulsing frequency; and
3. It is possible to generate an infinite train of vortex rings at any arbitrary pulsing frequency (i.e., the vortex rings remain coherent and co-axial).

While the first assumption deals with the issue of vortex ring formation introduced above, the last two emphasize the importance of understanding how the vorticity associated with individual pulses interacts/evolves to generate the downstream structure of the jet. It is

1. Significantly, any propulsive benefit obtained by the close proximity of successive vortex rings must somehow be related to an increased contribution from nozzle exit over-pressure since the momentum flux of the jet pulses does not change as the pulsing frequency increases and the ring separation decreases.

important, therefore, to determine how evolution of the vorticity associated with individual starting jets is affected by the presence of multiple vortex rings in the flow in order to fully assess the vortex ring interaction effects proposed by Weihs.

The goal of this chapter is to extend the results of the previous chapter by investigating the issues presented above associated with the presence of multiple pulses in a fully-pulsed jet. Of particular interest is determining to what extent the propulsive benefits associated with vortex ring formation in starting jets persist in fully-pulsed jets. The potential for propulsive benefits from vortex ring interaction (implying the possibility of an optimal pulsing frequency) is also of interest. To explore these interests, the time-averaged thrust of several fully-puled jets is measured at different pulsing conditions. The trends in the thrust measurements are related to the effect of previous pulses on vortex ring formation, ring velocity (following Weihs' model), and jet "structure" using PIV measurements of circulation and vorticity evolution within 10 diameters of the nozzle exit plane.

4.2 Experimental Conditions

The velocity programs used to generate the pulses for these experiments were the same as those used to investigate starting jets and are shown in Figure 3.1. To generate a fully-pulsed jet, the pulses were separated by a period T between the beginning of successive pulses, giving a pulsing frequency $f = 1/T$. Since it is the separation between pulses that is of interest in fully-pulsed jets, the appropriate non-dimensional frequency is given by

$$St_L \equiv \frac{fL}{\overline{U}_J} = \frac{t_p}{T}, \tag{4.1}$$

which, by the last equality, corresponds to a duty cycle. In this equation, $\overline{U_J}$ denotes the time average of U_J from 0 to t_p, which is equivalent to L/t_p. Since a fully-pulsed jet returns to zero velocity between each pulse, St_L varies between 0 and 1 for all possible fully-pulsed jets with 1 corresponding to successive pulses being adjacent to each other in time. The fully-pulsed jets studied here were for $0.1 < St_L < 0.85$ for the NS ramps (with St_L up to 0.9 for $L/D = 2.0$). Mechanical difficulties limited the St_L range to $0.1 < St_L < 0.65$ for the $L/D = 3.0$ and 4.0 cases of the PS Ramps and $0.1 < St_L < 0.71$ for the rest of the PS Ramps. Thrust measurements were taken in the indicated St_L ranges in St_L increments of approximately 0.05.

The maximum values of St_L for the NS and PS ramps correspond to frequencies well in excess of 15 Hz for $L/D = 2.0$ of both families of velocity programs and in excess of 14 Hz for the $L/D = 3.0$ case of the NS Ramps. This indicates that the operating range of the $L/D = 2.0$ pulses straddles the broad resonance peak at around 16 Hz in the frequency response of the jet velocity for a steady commanded piston velocity of $U_p = 0.5$ in /s [see Figure 2.8 (b)]. This resonance was observed to affect the results mostly for the $L/D = 2.0$ cases. To avoid this effect as much as possible and achieve higher St_L values, two velocity programs at an Re_m of 9100 were devised and are shown in Figure 4.1. These programs are referred to as the NS2 Ramps for $L/D = 2.0$ and 2.3. The St_L range studied with these velocity programs was 0 to 0.97, which corresponds to a maximum pulsing frequency of 15.7 Hz for $L/D = 2.0$ and 13.8 Hz for $L/D = 2.3$.

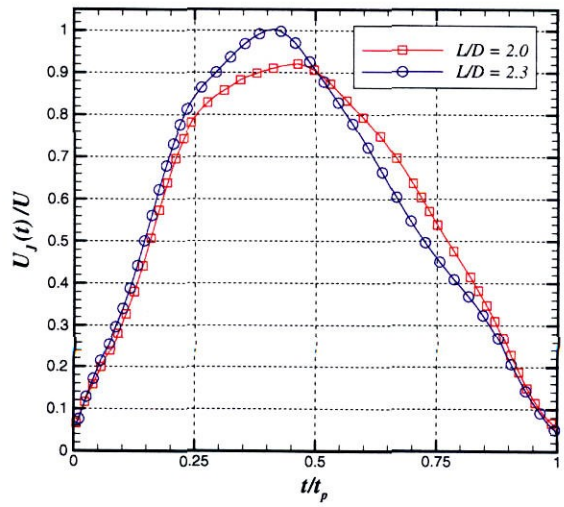

FIGURE 4.1 Velocity Programs for the NS2 Ramps (U = 0.72 m/s).

With regard to the thrust measurements, only the time averaged thrust is considered for reasons discussed in section 2.4.3.1. To avoid initial transients, the first 1.0 seconds of the force measurements were not included in the evaluation of the average thrust. To ensure good convergence of the running average function used to calculate the time averaged thrust [see equation (2.27)], at least 20 pulses were included in the averaging for each test case.

4.3 Definition and Application of the Intermittent Jet Normalized Thrust

As recognized by Weihs [39] and Seikmann [37], to evaluate the thrust performance of a fully-pulsed jet it is necessary to consider some representative jet for comparison. For this investigation, the representative jet considered is one with the same mass flux, pulsing frequency, and velocity program as the fully-pulsed jet, but *all* effects of vortex ring formation and fluid entrainment are ignored. The resulting jet, dubbed an "inter-

mittent jet" by analogy with a steady jet that has been chopped into segments, is shown in Figure 4.2.

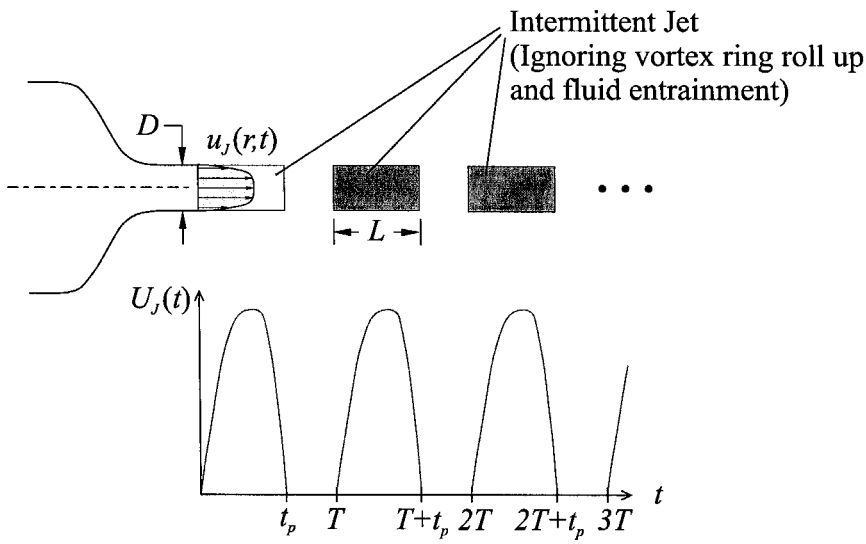

FIGURE 4.2 Representation of the Hypothetical Case of an "Intermittent Jet."

The absence of all effects associated with vortex ring formation and fluid entrainment can be expressed physically by ignoring nozzle exit over-pressure so that the thrust produced by the intermittent jet is due entirely to the momentum flux from the jet velocity. Then the time averaged thrust from this hypothetical jet is given by

$$\overline{F_{IJ}} \equiv \lim_{t\to\infty} \frac{\rho}{t}\int_0^t \int_A u_J^2(r,\tau)\,dA\,d\tau = f I_U \tag{4.2}$$

where the second equality follows because the jet is periodic and u_J is zero from t_p to T for each pulse. Given $\overline{F_{IJ}}$, the intermittent jet normalized thrust, F_{IJ}, is defined as the quotient of the average thrust of the fully pulsed jet (obtained from the force balance measurements) and $\overline{F_{IJ}}$, namely,

$$F_{IJ} \equiv \frac{\overline{F_T}}{\overline{F_{IJ}}}. \tag{4.3}$$

In the limit of zero pulsing frequency, $\overline{F_T} \rightarrow fI$ where I is the total impulse for an individual starting jet. Therefore, $F_{IJ} \rightarrow I/I_U$ as $f \rightarrow 0$, so F_{IJ} is a generalization of the non-dimensional impulse introduced in section 3.4. This also indicates the importance of this normalization for this investigation since it factors out the velocity contribution to thrust and focuses on the pressure contribution.

In order to compare the results of these experiments with the theoretical results of Weihs [39], the relationship between F_{IJ} and the normalized thrust defined by Weihs is considered here. The normalization used by Weihs defines a hypothetical jet whose mean thrust is given by

$$\overline{F_W} \equiv \dot{m} U_s \tag{4.4}$$

where $\dot{m}$ is the time averaged mass flux of the hypothetical jet, which is matched to that of the fully-pulsed jet, and U_s is the jet velocity during the ejection of each pulse. This gives the normalized thrust $F_W = \overline{F_T}/\overline{F_W}$. Since Weihs appears to be considering fully-pulsed jets with constant jet velocity during each pulse, a direct comparison between his normalization and F_{IJ} is not possible. If, however, one makes the reasonable generalization

$$U_s = \overline{U_J} = \frac{L}{t_p} \tag{4.5}$$

and the obvious generalization for $\dot{m}$, Weihs' normalization can be generalized to

$$F_W = \frac{\overline{F_T}}{\rho A L^2 (f/t_p)} = \frac{F_{IJ}}{P} \tag{4.6}$$

where

$$P \equiv \frac{\rho A L^2}{t_p I_U} \tag{4.7}$$

is a shape factor for the velocity programs. For the velocity programs used in this experiment, P is roughly constant at approximately 0.80 (0.77 to 0.82) and is constant to within a few percent for a given L/D, so F_W will be considered equivalent to F_{IJ} in that both normalizations should show the same trends.

As a final consideration, it is noted that I_U should be independent of pulsing frequency because it is determined by the velocity program. Since the pulsing frequencies for a few of the cases overlap a system resonance, as noted earlier, this is not entirely true for these experiments. To circumvent this problem, I_U was determined as a function of frequency for $L/D \leq 5$ so that F_{IJ} could be accurately evaluated over the entire parameter space. (For $L/D > 5$, the pulsing frequencies were low enough that I_U was approximately constant with frequency.) This seemed a reasonable way to factor out the system behavior because the *shape* of the velocity programs was nearly independent of frequency (as evidenced by the fact that P was constant with frequency to within a few percent) even though I_U was not. The validity of this approach will be discussed later.

4.4 Thrust Measurements

Measurements of the intermittent jet normalized thrust for the NS, NS2, and PS ramps are presented and discussed below along with the I/I_U results of section 3.4, which correspond to F_{IJ} at $St_L = 0$. Surface plots of uncorrected F_{IJ} (i.e., F_{IJ} determined by assuming I_U is constant at the value determined at $f = 2$ Hz) along with plots of $\overline{F_p}$ and $\overline{F_p}/(\rho A U_{max}^2)$ for the NS and PS ramps are shown in appendix E.

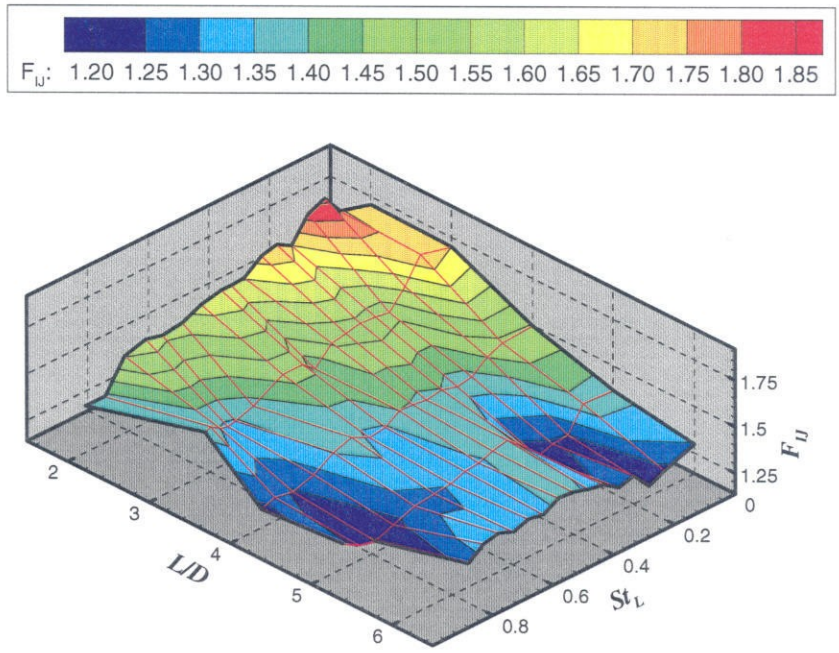

FIGURE 4.3 Intermittent Jet Normalized Thrust for the NS Ramps.

4.4.1 F_{IJ} Results for the NS and NS2 Ramps

The F_{IJ} results for the NS ramps are shown in Figure 4.3. It is apparent from these results that the basic trends observed for $I_{nd} = I/I_U$ at $St_L = 0$ are still present at nonzero St_L, but with some modifications. Specifically, F_{IJ} is greater than 1 for all St_L tested, indi-

cating a benefit from nozzle exit over-pressure (i.e., from vortex ring formation) is *always* obtained by pulsing. Furthermore, F_{IJ} is highest for small L/D and then tapers off for larger L/D as the trailing jet starts to dominate the flow. Indeed, the cross-section at $St_L = 0.1$ is nearly identical to that at $St_L = 0$. For $St_L > 0.1$, however, it is evident that a general trend of F_{IJ} decreasing with St_L appears. The first significant decrease in F_{IJ} with St_L appears rather abruptly for all L/D. This is seen at $St_L = 0.25$ for $L/D = 2.0$, $St_L = 0.1$ for $L/D = 3.0$, and with generally decreasing St_L for the remaining cases until it appears at $St_L = 0$ for $L/D = 6.0$. After this initial decrease, there appears to be a gradual decrease in F_{IJ} with St_L, modified by a few small hills and valleys. The most notable exception is at $L/D = 6.0$ where there appears to be a broad hill in the mid-St_L range. This hill is only around 0.07 high, however, which is comparable to the measurement uncertainty at this location. Another exception appears to exist for $St_L \approx 0.35$ at $L/D = 2$, as shown in the cross section of F_{IJ} at $L/D = 2$ in Figure 4.4. The error bars shown in Figure 4.4, however, indicate that this peak is also comparable to the measurement uncertainty. A larger peak occurs at $St_L < 0.25$ for $L/D = 2$, but again the error bars make its significance questionable. This peak will be addressed again later.

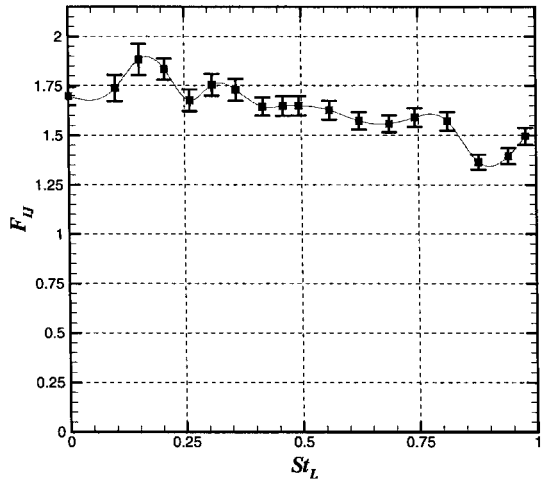

FIGURE 4.4 Cross Section of Figure 4.3 at *L/D* = 2.0.

For comparison with the NS ramp results, the results for the NS2 ramps are shown in Figure 4.5 (a). The basic trend expressed by these results confirm the general observations about the behavior of F_{IJ} with increasing St_L for the NS ramps. That is, the results for both NS2 ramps show an initially high value for F_{IJ} followed by a rather abrupt decrease in F_{IJ} ending around $St_L = 0.25$ to 0.30. This is followed by a gradual decrease in F_{IJ} until $St_L = 1.0$. Comparison of Figure 4.5 (a) with Figure 4.5 (b) also confirms the validity of using the values of I_U determined as a function of frequency to factor out the effect of the system resonance on the force measurements. While the F_{IJ} results in Figure 4.5 (a) nearly collapse, the uncorrected results in Figure 4.5 (b) (determined using a constant value for I_U) do not even follow the same trends for $St_L > 0.4$.

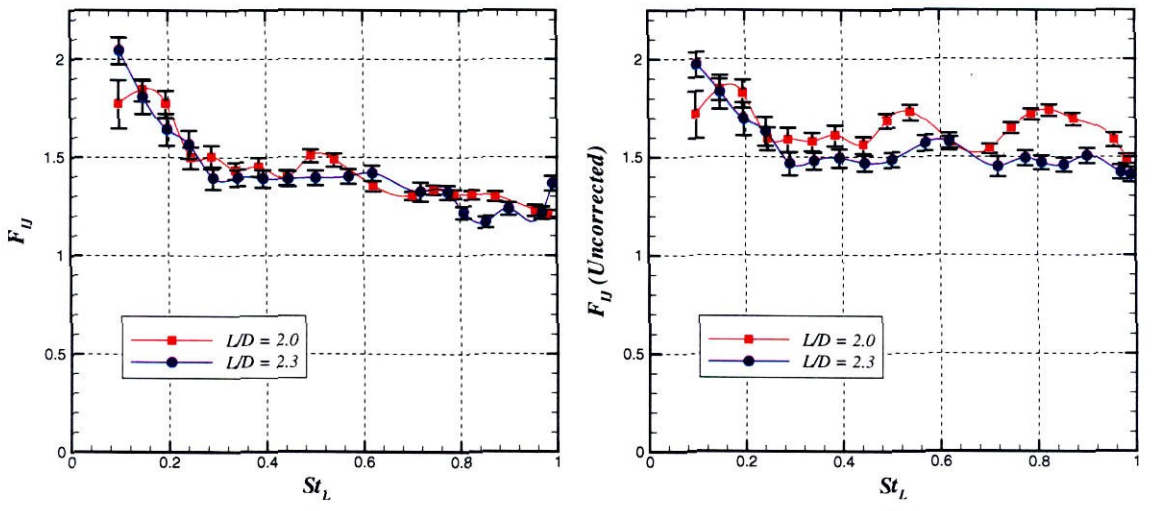

FIGURE 4.5 F_{IJ} Results for the NS2 Ramps: (a) F_{IJ}, (b) Uncorrected F_{IJ}.

The initial, abrupt decrease in F_{IJ} with St_L for the NS and NS2 ramps represents an important interaction of individual pulses with preceding pulses. This is highlighted by the fact that after the completion of the decrease at $St_L = 0.1$ for $L/D = 3.0$ (NS ramp), F_{IJ} for the $L/D = 3.0$ case remains significantly below that for the $L/D = 2.0$ pulses. For $St_L < 0.1$, however, the $L/D = 3.0$ results are comparable to or greater than those for $L/D = 2.0$. It seems reasonable, then, that the phenomenon causing this reduction in thrust is disrupting the formation of the leading vortex ring. The most likely culprit for this reduction in thrust is an interaction of the forming vortex ring with the trailing jet of the previous pulse. For $L/D > 3.0$ this is certainly a possibility because $L/D - F$ is large for these cases, implying a substantial trailing jet. The reason such an interaction could take place at such a low St_L, where the leading vortex rings should be quite disparate, is that the trailing jets for the NS ramps move slowly relative to the leading vortex rings. Thus, they remain relatively close to the nozzle exit plane and can easily interact with

emerging pulses. This also holds for $L/D = 3$ because $L/D - F$ is not identically zero for this case, implying a small, but significant trailing jet exists for this case. A similar situation exists for the NS2 ramps because the longer deceleration times of their velocity programs provide for a small (weak), but significant trailing jets.

Figure 4.6 and Figure 4.7 show the kinematics of this interaction for $L/D = 2.3$ of the NS2 ramps. In Figure 4.6 (a), $St_L = 0.11$, which is low enough that viscosity dissipates the trailing jet remnant before the next pulse emerges in Figure 4.6 (b). In Figure 4.7, $St_L = 0.29$ and the small vorticity small patches associated with the trailing jet remain close to the nozzle as the next pulse is emerging, thereby interacting with the forming vortex ring. The presence of this vorticity so close to a forming vortex ring means that its formation is no longer equivalent to formation in quiescent fluid. It is not clear exactly how this interaction would lead to an initial decrease in F_{IJ} (or more specifically, a decrease in the pressure contribution to thrust), but it is likely related to a reduction in the thrust component from the initial acceleration of ambient fluid by the forming vortex ring due to the non-zero velocity of the this fluid at pulse initiation. That is, some of the ambient fluid already has non-zero velocity, so the emerging jet does not have to accelerate it from rest and the impulse required to move this fluid as the ring is forming is less. For high enough St_L, it is conceivable that the detrimental effects of this interaction are ameliorated by the fact that the forming vortex ring also must accelerate the trailing jet remnant itself [as is beginning to be observed in Figure 4.7 (b)]. This potential shift in the nature of the interaction may account for the sudden leveling in F_{IJ} that appears for $St_L > 0.30$ in Figure 4.5 (a).

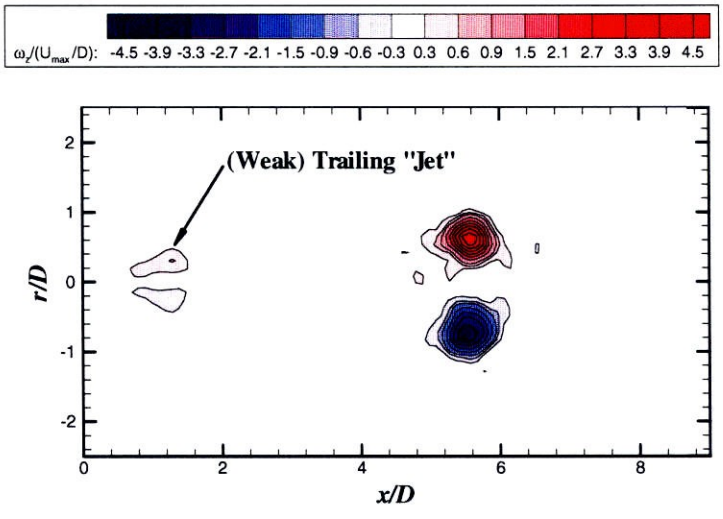

(a)

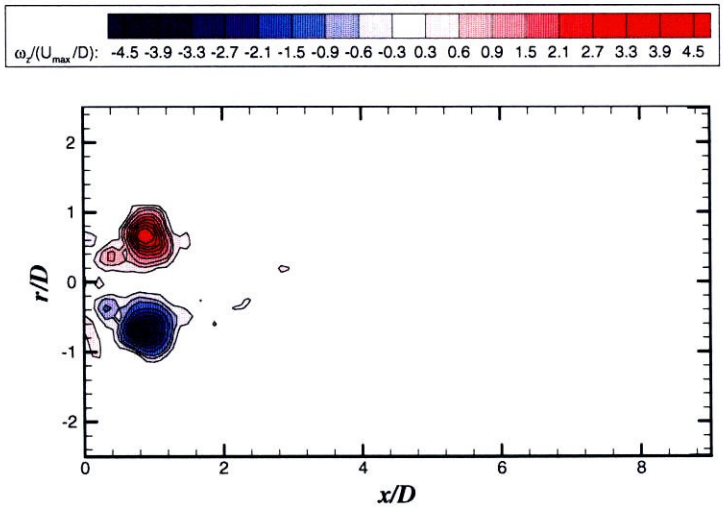

(b)

FIGURE 4.6 Vorticity Contours for Two Instances of the L/D = 2.3, NS2 Ramp Case at St_L = 0.11: (a) $t = t_1$, (b) $t = t_1 + 0.40$ s.

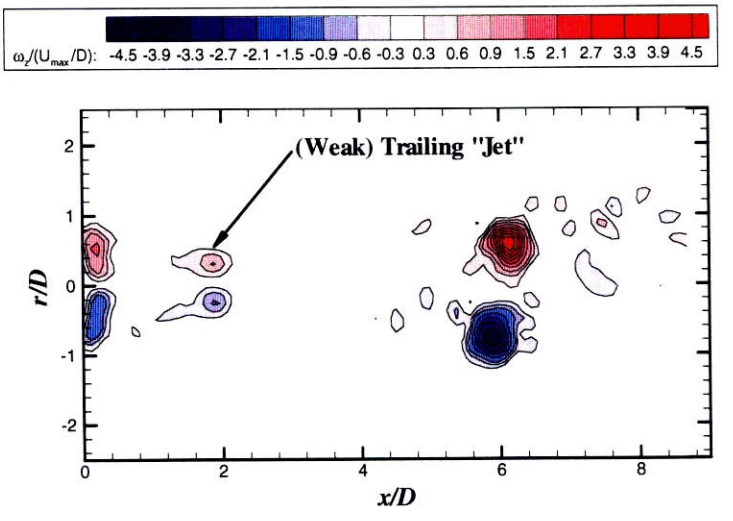

(a)

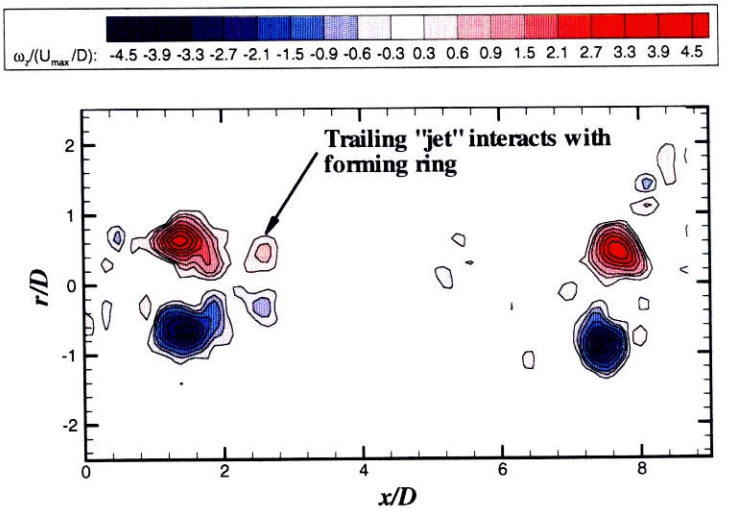

(b)

FIGURE 4.7 Vorticity Contours for Two Instances of the L/D = 2.3, NS2 Ramp Case at St_L = 0.29: (a) $t = t_1$, (b) $t = t_1 + 0.067$ s.

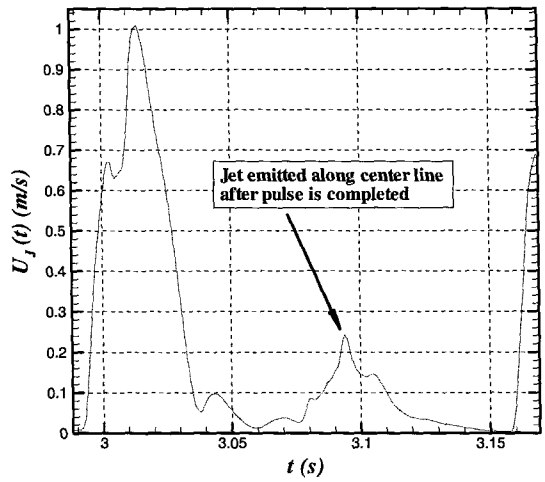

FIGURE 4.8 Velocity for an Entire Pulse Period of L/D = 2.0, NS Ramp, St_L = 0.26.

For the L/D = 2.0 case of the NS ramps, almost no (if any) trailing jet exists, so it is difficult to see how the phenomenon described above could be active in this case to explain the decrease in F_{IJ} at St_L = 0.25. There is, however, a mechanism for producing patches of vorticity in front of emerging pulses associated with the stopping vortex of preceding pulses. Figure 4.8 illustrates this with the velocity time trace measured by the hot-film for $t = t_1$ to $t = t_1 + T$ for the L/D = 2.0, NS ramp at St_L = 0.26. Here it is clear that fluid with significant velocity is ejected along the nozzle center line *after* the pulse is completed. Figure 4.9 shows some PLIF images of this case that indicate the stopping vortex doesn't begin to enter the nozzle until after the piston has stopped. Since the piston is no longer moving and the stopping vortex is bringing ambient (black) fluid into the nozzle, conservation of mass requires that some fluid be ejected from the nozzle after the pulse is completed. This is seen to cause the sharpening of the dye boundary for the small blob of dye in front of the nozzle in last two images of the sequence. The interaction of the vorticity that results from this "stopping vortex jet" with an emerging vortex ring for St_L = 0.25

is shown in Figure 4.10. Thus, is appears that a similar phenomenon accounts for the decrease in F_{IJ} at $St_L = 0.25$ for the $L/D = 2.0$ case of the NS ramps as well[2].

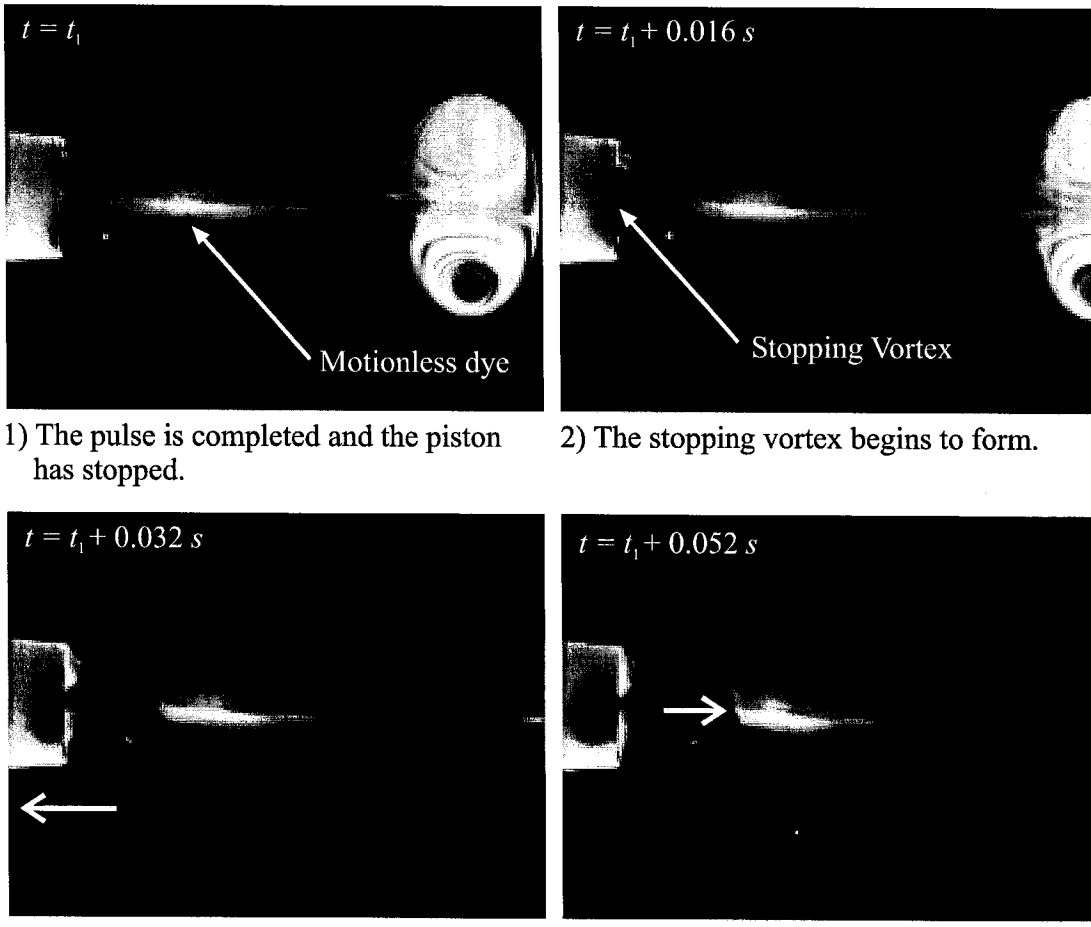

1) The pulse is completed and the piston has stopped.

2) The stopping vortex begins to form.

3) The stopping vortex moves in the direction indicated by the arrow.

4) Evidence of the jet ejected as the stopping vortex moves up the nozzle is given by displacement of the trailing edge of the dye (indicated by the arrow).

FIGURE 4.9 A Sequence of PLIF Images for *L/D* = 2.0, NS Ramp Illustrating the Generation of a Stopping Vortex and Associated Jet.

2. A strong "stopping vortex jet" was not observed in the remaining NS and NS2 ramps because the relatively gradual jet deceleration for these cases provided for a relatively weak stopping vortex.

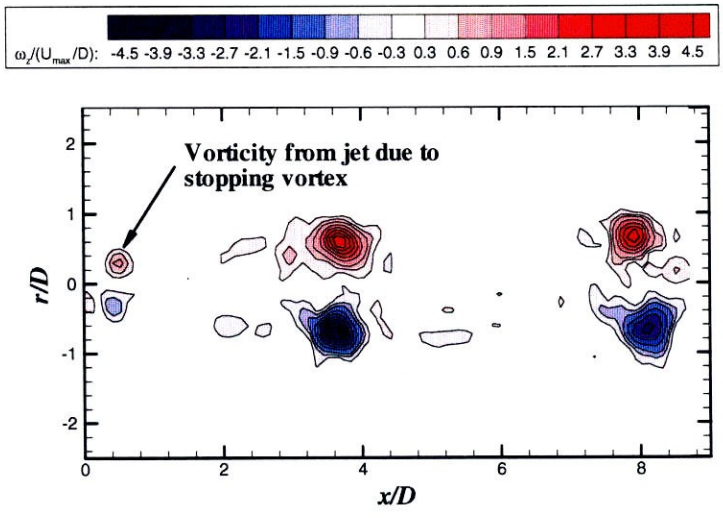

(a)

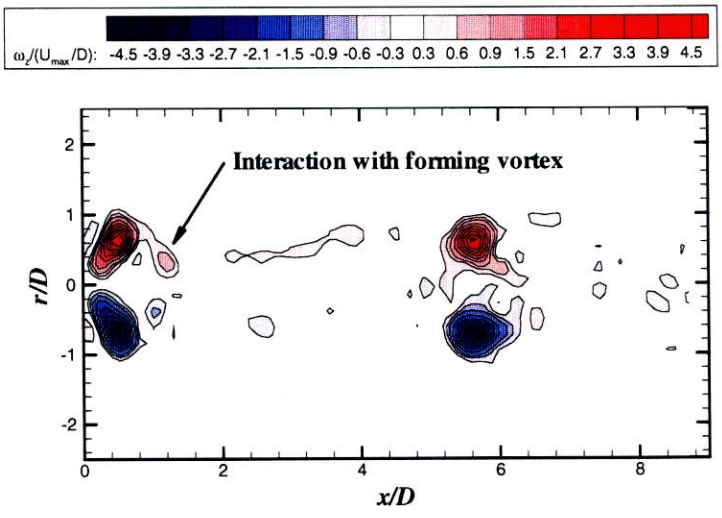

(b)

FIGURE 4.10 Contour Plots for L/D = 2.0, NS Ramp at St_L = 0.25 Illustrating the Interaction of an Emerging Pulse with the Vorticity Produced by the Jet Ejected During the Formation of a Stopping Vortex: (a) $t = t_1$, (b) $t = t_1 + 0.067$ s.

It should also be noted that although the interaction described above for L/D = 2.0 of the NS ramps is used to explain a decrease in F_{IJ} at $St_L = 0.25$, it is also the only legitimate candidate for explaining the peak in F_{IJ} for $St_L < 0.25$ (see Figure 4.4). Since it

is difficult to see how such an interaction could so quickly transition from a positive to a negative effect and the measurement uncertainty for $St_L < 0.20$ is relatively large, further investigation of this peak in F_{IJ} is required to evaluate its significance.

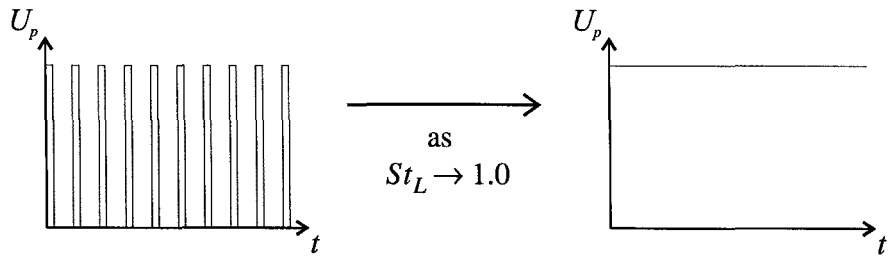

FIGURE 4.11 Illustration of the Piston Velocity for $L/D << 1.0$ in the Limit of St_L Going to 1.0.

While the previous discussion attributes the initial abrupt decrease in F_{IJ} as St_L increases to an (unfavorable) interaction of forming vortex rings with remnants of preceding pulses, the gentle decrease in F_{IJ} with St_L that appears after this is likely due to the slow change in the flow field as the pulses come closer together. This can be illustrated by considering the case for $L/D \ll 1$. In the limit of $St_L \rightarrow 0$, the measurements presented so far show that $F_{IJ} \gg 1$ (i.e., $F_{IJ} > 1.5$) for $L/D = 2.0$, implying that $F_{IJ} \gg 1$ for $L/D \ll 1$ and $St_L \rightarrow 0$ as well. For $St_L \rightarrow 1.0$, however, the piston velocity approaches a steady jet configuration for $L/D \ll 1$, as illustrated in Figure 4.11. Since the nozzle over pressure for a steady jet is negligible, $F_{IJ} \approx 1.0$ in this limit. This reasoning implies an overall decrease in F_{IJ} with St_L for small L/D. That is, F_{IJ} is reduced by the fact that less and less fluid external to the nozzle is accelerated at the initiation of a pulse as the pulses come closer together because the fluid has been accelerated by previous pulses. This reduces the pressure contribution to thrust and forces F_{IJ} toward 1.0. A similar mecha-

nism can be expected for larger L/D since acceleration of ambient fluid at pulse initiation was seen to play a strong role in the impulse produced by individual starting jets in the previous chapter. For the NS (and PS) velocity programs, however, the limit of F_{IJ} as St_L approaches 1.0 should be significantly above 1.0 since the velocity programs are not square, dictating that even in the limit of St_L going to 1.0, the jet is still highly forced. The data confirm this, giving F_{IJ} between 1.2 and 1.5 as St_L approaches 1.0 for the NS and NS2 ramps.

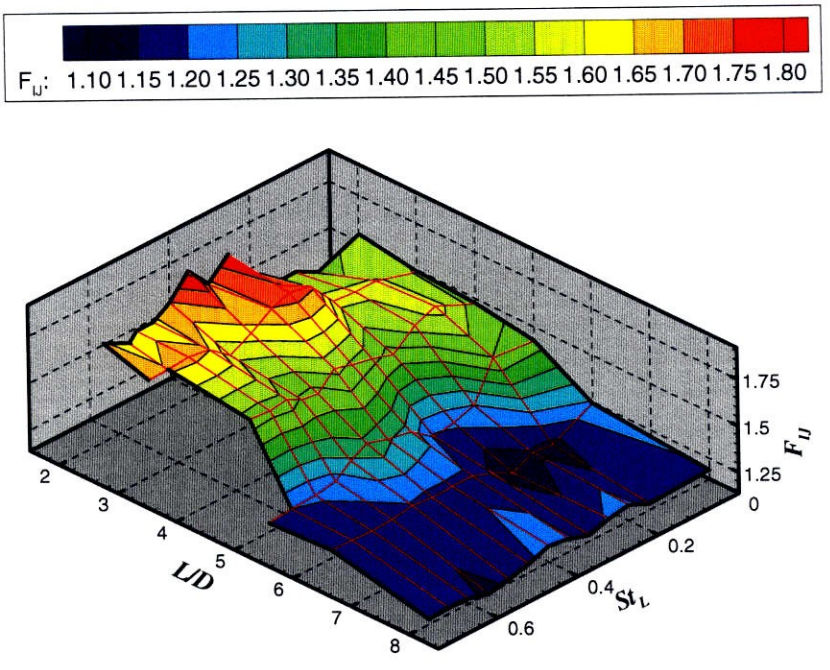

FIGURE 4.12 Intermittent Jet Normalized Thrust for the PS Ramps.

4.4.2 F_{IJ} Results for the PS Ramps

The intermittent jet normalized results for the PS ramps are shown in the surface plot in Figure 4.12. This figure indicates that, as with the NS ramps, the F_{IJ} values are always greater than 1.0, are high for low L/D, and become lower for larger L/D. The

later result suggests, as before, that the presence of a trailing jet significantly affects the thrust for all pulsing frequencies. The results also show an initial, rather abrupt decrease in F_{IJ} for $L/D > 4.0$ at low St_L, but not for small L/D. In fact, for small L/D the largest F_{IJ} appear around $St_L = 0.4$. In this region the results are highly suspect, however, because it was difficult to accurately determine I_U due to the merging of the jets associated with the stopping vortices (which were much stronger for the PS ramps) with the beginning of the next pulses. In other words, it is not possible to determine if the peaks at $St_L = 0.3$ and 0.4 for $L/D = 2.0$ are real phenomena. Thus, the only strong conclusion that can be made for the $L/D < 4.0$ results is that F_{IJ} is larger for these cases than for larger L/D, which is likely due to the lack of strong trailing jets for $L/D < 4.0$.

For the larger L/D results ($L/D \geq 4$), it is interesting to note that the generally decreasing trend in F_{IJ} with St_L for larger St_L observed in the NS and NS2 ramps is not present. This is not entirely unexpected because the PS ramps have a slow startup ramp (especially for large L/D), meaning that the thrust associated with acceleration of ambient fluid during the initiation of a pulse is less significant for these velocity programs, as noted in the previous chapter. Hence, the mechanism described in section 4.4.1 to account for the gradual decrease in F_{IJ} at higher St_L observed in the NS and NS2 ramps should be less important for the PS ramps.

4.5 The Dependence of Vortex Ring Velocity and Separation on St_L

Conspicuously absent from the results presented so far is a dramatic increase in F_{IJ} with St_L, as expected from the analysis of Weihs [39]. That is, the vortex rings generated at smaller L/D (e.g., $L/D = 2.0$) are expected to get closer together as St_L increases toward 1.0. Weihs [39], on the other hand, predicts that F_{IJ} should increase dramatically when vortex ring separation becomes very small. Since no dramatic increase in F_{IJ} is observed as St_L increases (even in the NS2 ramps where St_L increases all the way to 0.97), it is worthwhile to investigate the dependence of vortex ring separation and velocity on St_L for the NS2 ramps.

To determine vortex ring separation and velocity, PIV measurements were used to locate the centroids of vorticity of the upper and lower vortex ring cores for several values of St_L at $L/D = 2.0$ of the NS, NS2, and PS ramps. The locations of these centroids in the r-x plane for all of the cases tested are shown in appendix E. For the purposes of determining ring separation and velocity, only centroids in the range $1 < x/D < 3$ were considered. (This range was selected because the ring separations tended to be constant over this range and the vortex rings began to break down beyond this range for higher St_L, as will be discussed in section 4.6.) The average ring separation a normalized by the average ring radius R_r is shown as a function of St_L in Figure 4.13 (a) for the NS2 ramps. The normalized average ring velocity for the NS2 ramps as a function of a/R_r is shown in Figure 4.13 (b). Only normalized ring velocities are considered in an attempt to factor out any dependence of ring velocity on the system resonance that caused unwanted variations

in the uncorrected measurements of F_{IJ}. The factor used to normalize the ring velocities was chosen to be $\sqrt{\frac{\rho\Gamma^3}{\pi I}}$ since Shusser and Gharib [35] showed that vortex ring velocity, W, for *individual* vortex rings with $L/D > 2.0$ should be approximately proportional to this quantity. For these results, Γ and I were estimated by Γ_U and I_U.

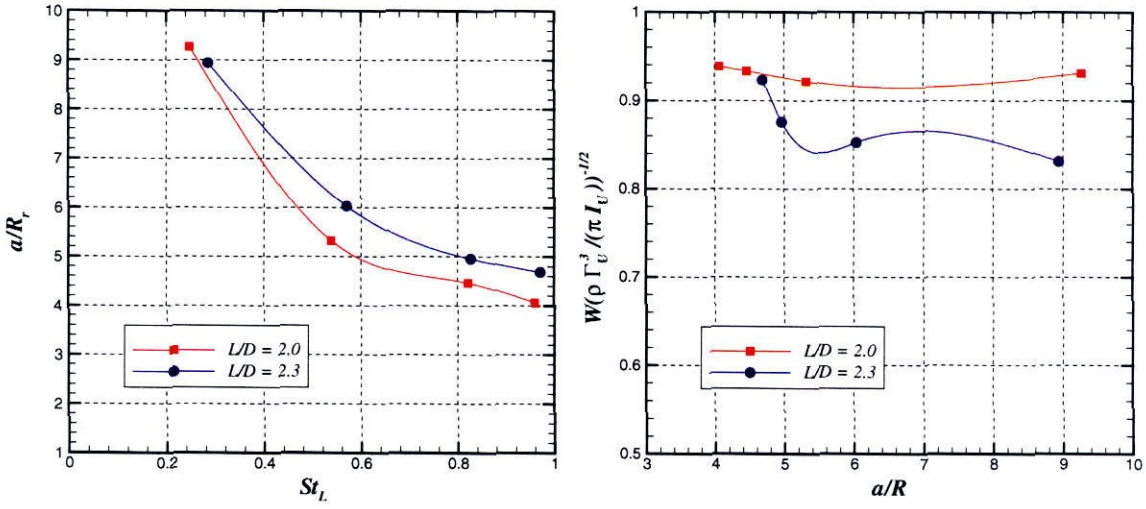

(a) (b)

FIGURE 4.13 Ring Separation and Velocity of Rings in the Range $1 < x/D < 3$ for the NS2 Ramps: (a) Non-dimensional Ring Separation, (b) Non-dimensional Ring Velocity.

The trend for a/R_r shown in Figure 4.13 (a) shows that the ring separation does in fact decrease as St_L increases. The minimum a/R_r achieved, however, is 4.0 for L/D = 2.0. Since this is the value obtained at $St_L = 0.96$, it represents the minimum possible vortex ring separation that can be achieved for a fully-pulsed jet composed of these velocity programs. Moreover, Figure 4.13 (b) demonstrates that the non-dimensional ring velocity is nearly constant with a/R_r (only a slight increase is observed as a/R_r decreases), implying that the vortex ring separation was likely never reduced enough to observe the

expected dramatic increase in ring velocity. Indeed, Figure 1b in Weihs [39] indicates that a significant increase in ring velocity (for rings with small L/D) would not be expected unless a/R_r is reduced below 3.0. It appears, then, that one reason a dramatic increase in F_{IJ} with St_L was never observed is that the conditions under which this increase is expected were never achieved. The results for a/R_r also suggest that it is difficult (if not impossible) to achieve a/R_r sufficiently small to see the thrust benefits predicted by Weihs [39]. The only way to pack vortex rings more densely than was achieved in this experiment is to use pulses with smaller L/D and/or velocity programs with more nearly uniform velocity throughout the pulse duration.

4.6 Vorticity Evolution in a Fully-Pulsed Jet

To provide a more complete picture of the behavior of fully-pulsed jets as well as illuminate additional issues contributing to the lack of an increase in F_{IJ} at high St_L as predicted by Weihs [39], this section briefly considers vorticity evolution with downstream distance for several L/D and St_L values of the NS and NS2 ramps. Of particular interest are the locations and magnitudes of vorticity peaks as well as the circulation and vorticity centroid locations associated with these peaks. Measurements of these quantities were obtained using PIV measurements of the flow for $x/D < 9.0$. For display and analysis purposes, only vorticity peaks greater than 20% of the maximum vorticity in an image are shown. The peak locations were determined to sub-grid accuracy by fitting a Gaussian curve to the local vorticity surrounding each peak. The circulation associated with the

vorticity peaks was determined by finding the vorticity contour around each peak at a level of 20 s^{-1} (which was observed to contain > 95% of the circulation for individual rings in most cases) and calculating the circulation and centroid associated with the vorticity in these contours. Although only a few cases are discussed here, plots of circulation and locations of vorticity centroids and peak vorticity for all cases interrogated with PIV are shown in appendix E.

4.6.1 Evolution of Circulation with Downstream Distance

The evolution of circulation contained in contours at 20 s^{-1} around vorticity peaks for L/D = 2.0 of the NS2 ramps and L/D = 4.0 of the NS ramps are shown in Figure 4.14 and Figure 4.15 respectively. Only a few of the cases tested are shown in order to show the general behavior as St_L is increased. Following Rosenfeld *et al.* [28], the circulation has been normalized by $U_{max}D$.

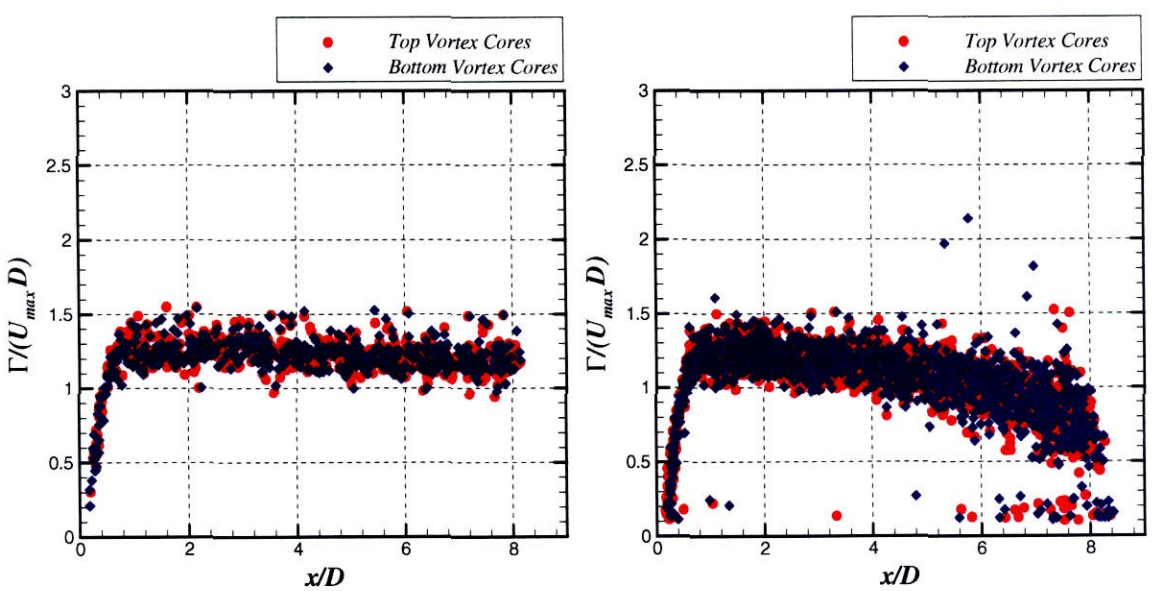

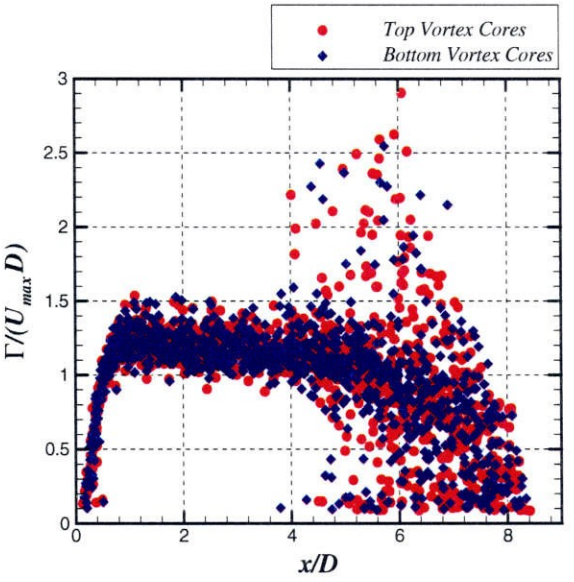

(c)

FIGURE 4.14 Evolution of Circulation for L/D = 2.0, NS2 Ramp: (a) St_L = 0.13, (b) St_L = 0.54, (c) St_L = 0.82.

For the L/D = 2.0, NS2 ramp case, the circulation initially increases nearly linearly for all St_L. At $St_L = 0.13$, the circulation remains nearly constant after the maximum circulation is reached at $x/D \approx 1.0$. For larger St_L, it is seen that the mean circulation begins to decrease with x/D after reaching an initial maximum. For $St_L = 0.82$, the rate of decrease increases with x/D and the mean circulation becomes quite small for x/D near 8.0. Since cancellation of circulation through diffusion across the center line is obviously negligible for $x/D < 8.0$ due to the constancy of circulation for the $St_L = 0.13$ case, this decrease is likely caused by only two effects. First, for higher St_L the vorticity tends to break up into smaller patches, as evidenced by the instances of very small circulation at $x/D > 4$ in the $St_L = 0.82$ and $St_L = 0.54$ cases. (The large values of circulation for $x/D > 4$ in these cases are due to the few instances where large patches of vorticity were close

enough together to be included in the same contour.) Second, the vortex rings tend to wander off of the nozzle axis for larger x/D at high St_L, so the circulation recorded by PIV in the plane of the laser sheet decreases. This "blooming" of multiple vortex rings was reported in passing by Glezer [13] and Saffman [31] for turbulent vortex rings, but no detailed analysis was given. It will presented in more detail for this case in the next section.

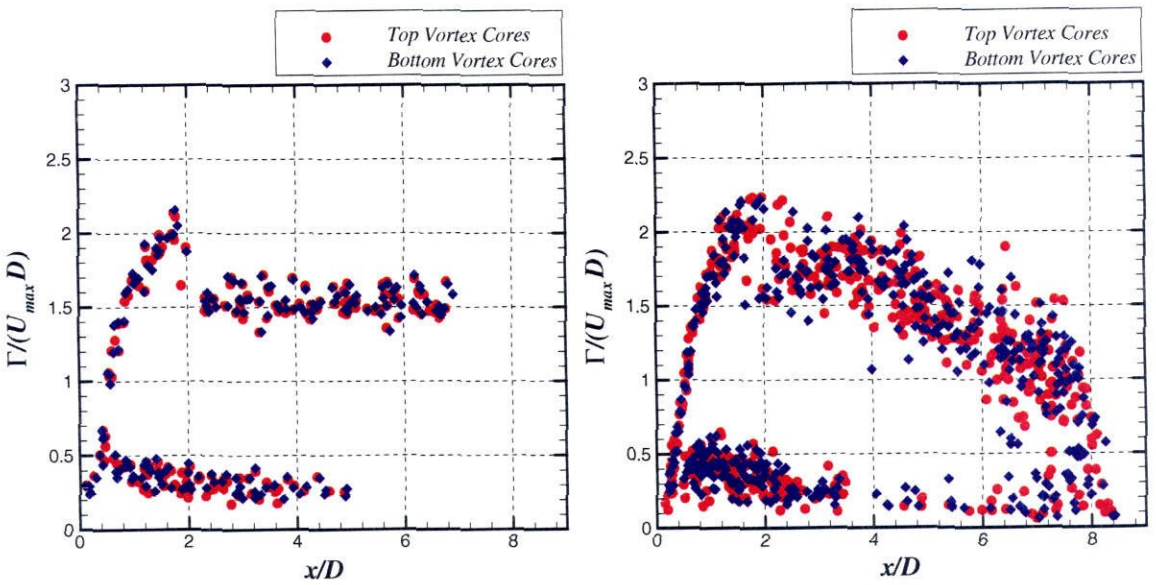

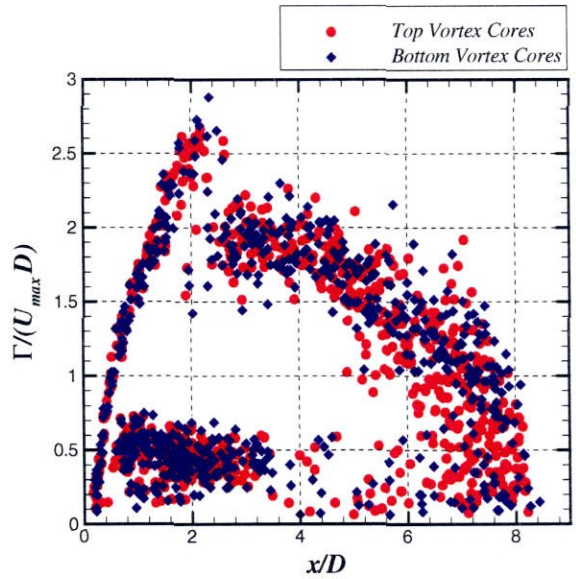

(c)

FIGURE 4.15 Evolution of Circulation for L/D = 4.0, NS Ramp: (a) St_L = 0.06, (b) St_L = 0.51, (c) St_L = 0.76.

The circulation for L/D = 4.0 shows a more interesting evolution. It also increases linearly at first, but it increases to a much higher value than for the L/D = 2.0, NS2 ramp case. After the maximum value is reached it drops down suddenly. This drop occurs when the vortex ring pinches off from the generating jet, at which point the low circulation values (i.e., near 0.5) from the trailing jet appear for $x/D < 5$. The sudden decrease in circulation is observed at high St_L as well, indicating that the presence of a preceding pulse does not eliminate the pinch off phenomenon even when the pulses are very close together (which was implicitly assumed in the discussion of the thrust measurements). It is, however, noted that the pinch off is less dramatic at St_L = 0.51. It is also apparent that the initial circulation of the leading vortex ring after pinch off appears to increase with St_L. The reasons for these two observations is not clear from the data, but it should be noted that St_L = 0.51 corresponds to a slight dip in F_{IJ} for L/D = 4.0 of the NS

ramps. Finally, the circulation associated with the leading vortex ring after pinch off appears to decrease with x/D for higher St_L as with the $L/D = 2.0$ case. This reduction is probably for the same reasons discussed previously.

4.6.2 Evolution of Vorticity and Circulation Structure in the Jet with Downstream Distance

The "structure" of the jet is investigated through the (x,r) coordinates of the vorticity peaks and associated vorticity centroids. In the plots presented in this section, the locations of the vorticity peaks or centroids associated with the peaks are indicated by the symbol location. The normalized peak vorticity $\frac{\omega_\theta}{U_{max}/D}$ associated with each point is indicated by the symbol color for the plots of vorticity peak location while the normalized circulation $\frac{\Gamma}{U_{max}D}$ associated with contour at 20 s^{-1} around each vorticity peak is indicated by the symbol color in the plots of centroid location.

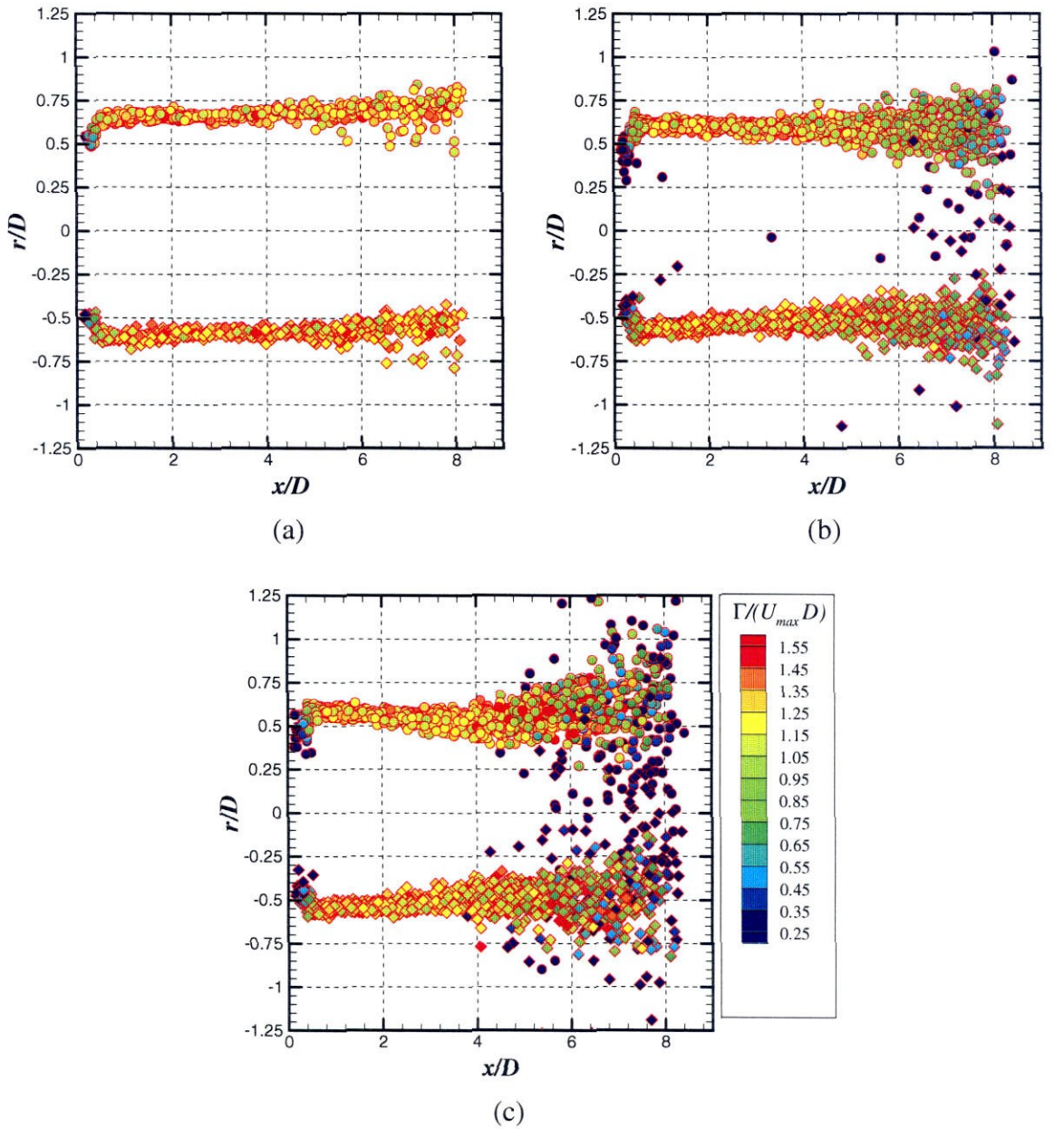

FIGURE 4.16 Centroid Locations for L/D = 2.0, NS2 Ramp: (a) St_L = 0.13, (b) St_L = 0.54, (c) St_L = 0.82.

The centroid locations for the L/D = 2.0, NS2 ramp at several St_L values is shown in Figure 4.16. For St_L = 0.13, the centroid locations initially move out radially and then remain at a constant diameter as the vortex rings move downstream. The symbol colors indicate, as noted previously, that the circulation remains constant with x for $x/D < 8.5$.

It also appears that the centroids drift slightly upward as they move downstream. The source of this drift is uncertain, but it could be due to the small (a few cm/s) convection currents in the tank. For higher St_L it is clear that the centroids do not follow a consistent path for $x/D > 4$, as seen by the wider radial spread of points in this region. This confirms the previous statement regarding the tendency of the vortex rings to wander off of the nozzle center line at larger x/D for high St_L.

The tendency of the vortex rings to wander off axis as they get closer together must be due to interactions with neighboring vortex rings. One candidate for such an interaction is illustrated with a 2D example in Figure 4.17. Here three point-vortex pairs are shown. On the left they are axially aligned and it is indicated that the induced velocity on the center vortex pair by the neighboring vortex paris is in the direction of the axis, tending to increase the velocity of the vortex pair (in accordance with the analysis of Weihs [39] for the 3D case of rings). On the right the vortex pairs are equally separated, but the center pair is displaced vertically. The induced velocity vectors on the center pair in this case show that it will start to tilt in such a way that its own convective velocity will take it *further* from the center line. Due to the symmetry of individual vortex rings, a similar conclusion should hold for the 3D case of a train of vortex rings, indicating that the train is *unstable* to perturbations that shift vortex rings off axis. Since such an interaction would get stronger as vortex rings get closer together, it could easily explain why the centroids don't all follow the same path for large St_L. It also suggests it would be very difficult to generate the long train of *coaxial* vortex rings assumed in Weihs' [39] analysis as the vortex ring separation decreases.

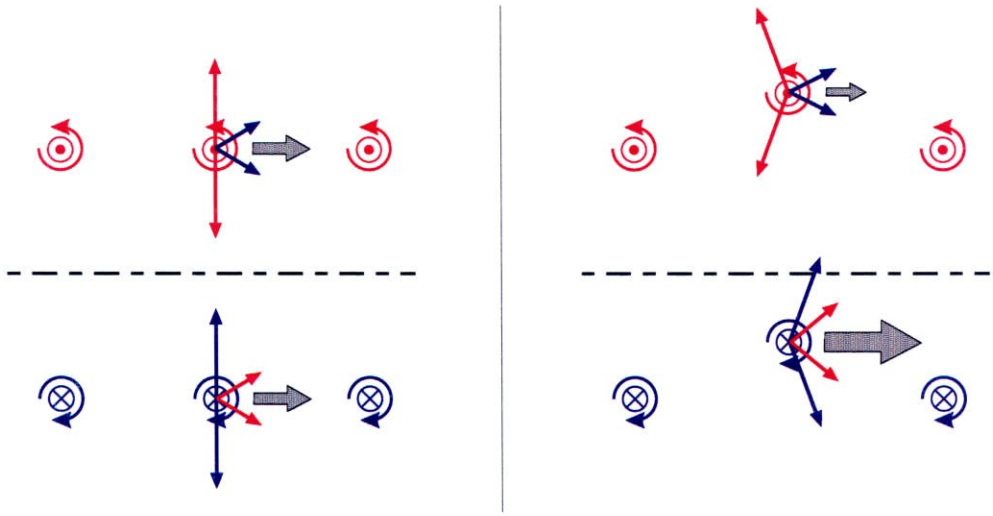

Aligned Vortex Pairs Misaligned Vortex Pairs

FIGURE 4.17 Illustration of a Vortex Interaction That Can Move Perturbed Vortex Pairs Off Axis.

An additional conclusion that follows from Figure 4.16 is that the initial vortex ring diameter decreases by as much as 13% as St_L increases toward 1.0. An explanation for this can be deduced from a straightforward application of the ideas presented in Figure 4.17, as illustrated in Figure 4.18. In this case the flow near the nozzle is of interest, so only two vortex pairs are considered, namely, a leading vortex pair and a trailing vortex pair (representing a vortex ring forming at the nozzle). Then it is clear from Figure 4.18 that the induced velocity of the leading vortex pair on the trailing vortex pair tends to reduce the diameter of the trailing pair. (In this analysis, the image vorticity of the trailing vortex pair associated with the boundary provided by the nozzle has been ignored since the trailing pair represents a forming vortex and is weak relative to the leading vortex pair.) Similarly, the induced velocity of preceding vortex rings on forming vortex rings tends to reduce the diameter of forming rings. This effect becomes stronger as ring separation decreases with increasing St_L, giving the trend in initial ring diameter observed

in Figure 4.16. Because of the potential significance of this result for understanding vortex ring formation and the overall structure of a fully-pulsed jet, further investigation of this phenomenon would be worthwhile.

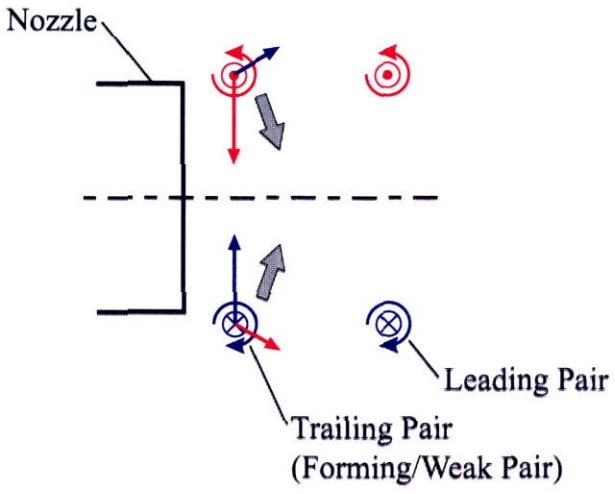

FIGURE 4.18 Illustration of a Vortex Interaction that Can Reduced the Diameter of a Forming Vortex Pair.

While the plots of vorticity centroid location in Figure 4.16 suggest the vorticity remains confined to bands away from $r = 0$ even for St_L approaching 1.0, plots of vorticity peak locations indicate otherwise. The vorticity peak locations for the cases illustrated in Figure 4.16 are shown in Figure 4.19. The main conclusion that follows from these plots is that the vortex cores stay coherent when they are widely separated at low St_L, but begin to break up for $x/D < 8.5$ as St_L is increased past 0.50. This confirms the statement in section 4.6.1 suggesting one reason for decreased circulation with downstream distance is the break up of vortex rings. Indeed, for $St_L = 0.82$, no discernible coherent structure appears beyond $x/D = 4$ as the vorticity peaks are nearly evenly distributed over the jet. The transition at $x/D = 4$ for $St_L = 0.82$ is rather abrupt and might be considered a transition to turbulence. At the very least it is clear the jet diameter begins to grow rapidly after

this point. This result also demonstrates it is difficult to obtain a *coherent* train of vortex rings beyond $x/D > 4$ as St_L approaches 1.0 (for these velocity programs), which suggests another reason the prediction of Weihs [39] was not observed in this experiment.

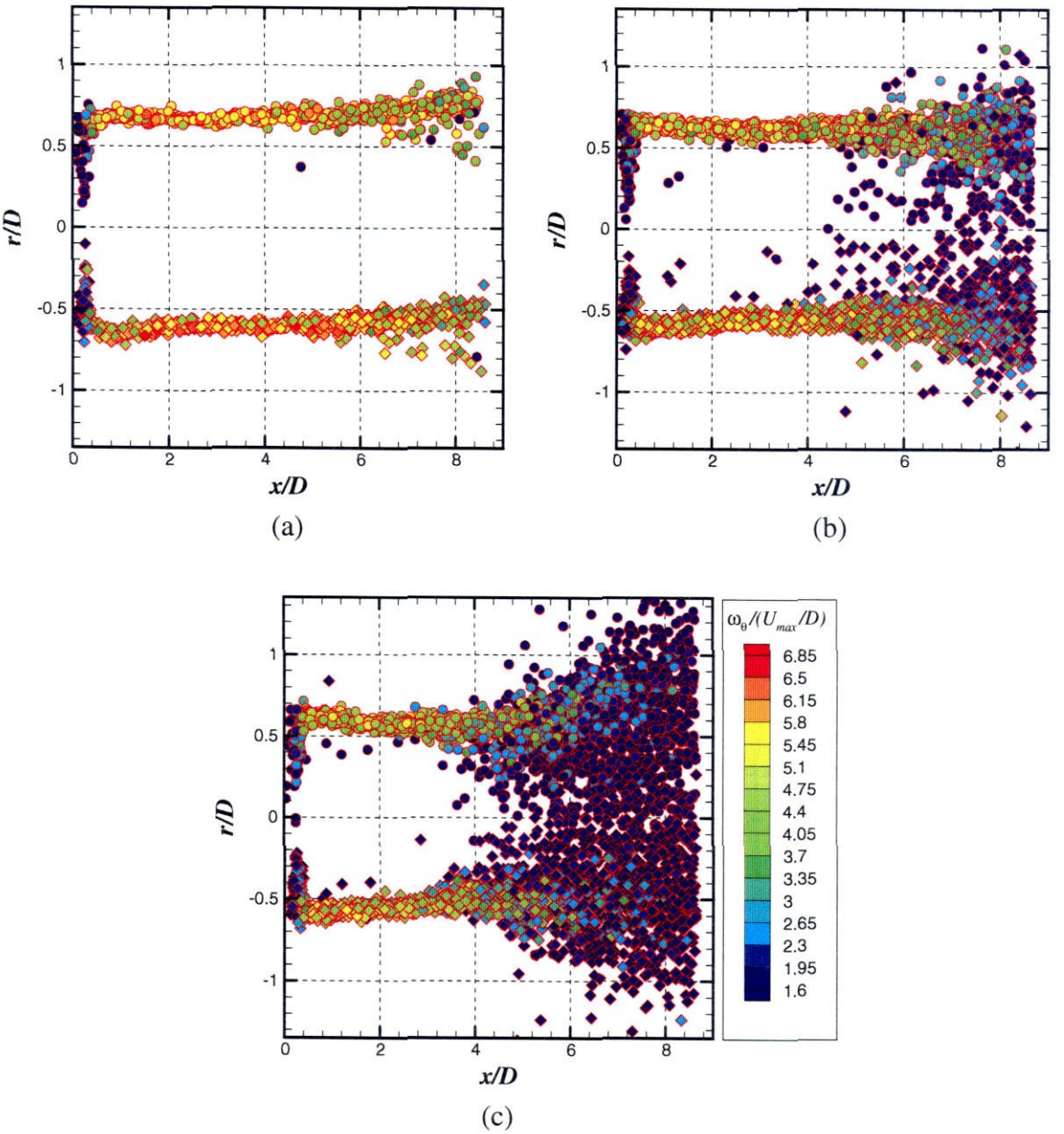

FIGURE 4.19 Vorticity Peak Locations for L/D = 2.0, NS2 Ramp: (a) St_L = 0.13, (b) St_L = 0.54, (c) St_L = 0.82.

For comparison with the $L/D = 2.0$ cases discussed above, plots of centroid and vorticity peak locations for $L/D = 4.0$ of the NS ramp family are shown in Figure 4.20 and Figure 4.21 respectively. In these figures two clusters of points are discernible near the nozzle. The inner cluster (with lower vorticity and circulation) is due to the trailing jet while the outer cluster is from the leading vortex ring. After pinch off occurs (i.e., after the circulation of points associated with the leading vortex ring suddenly drops) the points in the inner cluster stop. This indicates, as noted earlier, that the trailing jet remains near the nozzle for the NS ramps since the convection velocity associated with its vorticity is low. Indeed, the points associated with the trailing jet remain at $x/D < 4.5$ (which is most easily seen in the plots of vorticity centroid locations).

The basic conclusions about the evolution of the vortex rings made for the $L/D = 2.0$ cases above also appear to be generally true for the *leading* vortex rings in this case. The most notable deviations are that the centroids of the leading vortex rings appear to wander a bit more for $x/D > 4$ than in the $L/D = 2.0$ case (i.e., the spread in centroid locations around the mean path is larger). Additionally, for $St_L = 0.76$, the vorticity peak distribution that occurs for $x/D > 4$ is more sparse near $r = 0$ compared to the $L/D = 2.0$ case. These effects are probably due to interaction of the leading vortex rings with the trailing jets of previous pulses, but it is difficult to see the precise nature of this interaction from these plots. Finally, almost no decrease in the diameter of the leading vortex ring with St_L is discernible in Figure 4.21, in contrast to the $L/D = 2.0$ case discussed above. This is to be expected since the leading vortex rings are now separated by a trailing jet, even at high St_L.

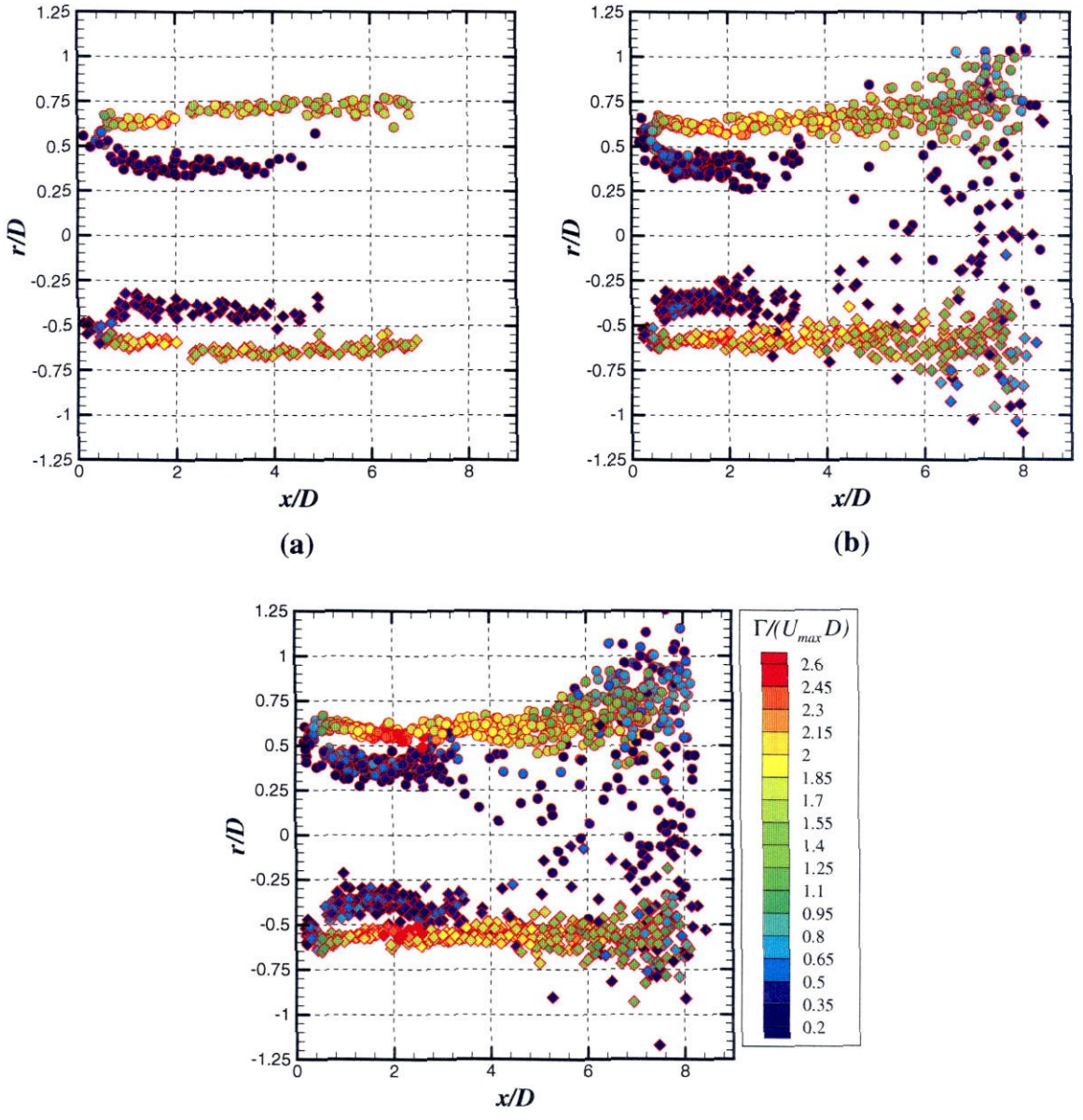

FIGURE 4.20 Centroid Locations for L/D = 4.0, NS Ramp: (a) St_L = 0.06, (b) St_L = 0.51, (c) St_L = 0.76.

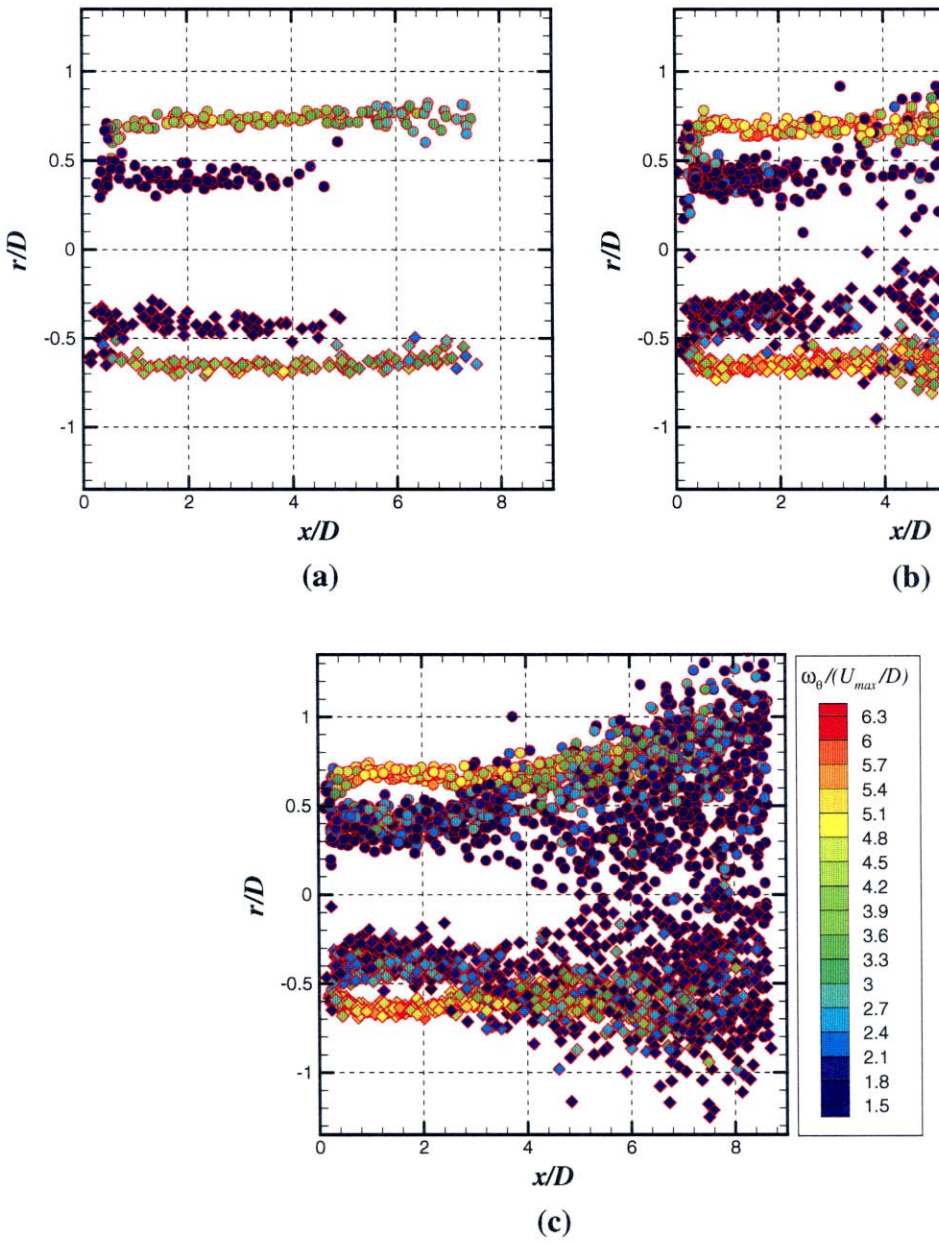

FIGURE 4.21 Vorticity Peak Locations for L/D = 4.0, NS Ramp: (a) St_L = 0.06, (b) St_L = 0.51, (c) St_L = 0.76.

In summary, the main conclusions of this subsection are as follows:

1. A significant decrease in vortex ring circulation with x/D at high St_L occurs due to break up of vorticity and a tendency of the vortex rings to move off axis;
2. The vortex ring pinch off phenomenon described for single pulses at L/D = 4.0 of the NS ramps appears to be present for high St_L of the fully-pulsed jet (up to 0.87 if the plots in appendix E are consulted);

3. The vorticity distribution of the fully-pulsed jet examples presented appears to be compact and confined to the vortex rings and trailing jets for small St_L, but as St_L increases the vorticity breaks up and spreads out for $x/D > 4$;
4. The initial ring diameter decreases with St_L for small L/D, but remains constant at L/D large enough to generate a significant trailing jet; and
5. The wandering and break-up of vortex rings as St_L increases past 0.50 suggest additional reasons why the prediction of Weihs [39] was not observed for the F_{IJ} measurements at $L/D < 3.0$.

4.7 Conclusions

The results of chapter 3 for individual starting jets are extended to fully-pulsed jets by measuring the time averaged thrust for a periodic series of pulses in each velocity program family for non-dimensional frequencies, St_L, in the range 0.1 to 0.85 for the NS ramps and 0.1 to 0.7 for the PS ramps. A non-dimensional thrust, F_{IJ}, is introduced as a generalization of the non-dimensional impulse defined in chapter 3 to interpret the results. While effects of a system resonance make the results for the PS ramps unreliable for $L/D < 4.0$, the NS ramp results are useful in extending the $St_L = 0$ result of chapter 3.

The overall trend in F_{IJ} with increasing L/D follows the results for $St_L = 0$ in that it decreases with L/D for L/D sufficiently large while always remaining above 1. The decrease with L/D seems to be associated with the pinch off of vortex rings from the generating jet even for non-zero St_L. Based on PIV measurements of circulation, this phenomenon persists up to $St_L = 0.76$ for $L/D = 4.0$ (and up to $St_L = 0.87$ by the plots in appendix E). For the NS ramps, some new trends are also seen to appear for non-zero St_L. First, there is an abrupt decrease in F_{IJ} at a value of St_L that decreases with L/D. This is attributed to an interaction of the forming vortex ring in each pulse with the remnants of

the previous pulse (be it a trailing jet or an effect due to a stopping vortex, as in the $L/D = 2.0$ case). Second, after the initial drop there is a gradual decrease in F_{IJ} with St_L for most cases, especially $L/D = 2.0$. This is attributed to a decrease in the requirement of forming pulses to accelerate ambient fluid as the pulses are closer together due to the fact that this has already been done by preceding pulses.

The basic results for the NS ramps are confirmed by the NS2 ramps (a new family of velocity programs at a lower Re_m). These velocity programs also extend the results up to $St_L = 0.97$. The F_{IJ} results at St_L approaching 1.0 for the NS2 ramps do not show the increase in F_{IJ} with St_L predicted by Weihs [39]. Analysis of the vortex ring separation and velocity for these cases shows that no significant increase in ring velocity is achieved with increasing St_L and that it is not possible to pack the rings close enough together to observe such an increase with these velocity programs. Analysis of the vorticity evolution of the jet also shows that the vortex rings begin to wander off axis for increasing St_L due to interactions with neighboring vortex rings and that they break down for $x/D > 4$ (NS2 ramps) as St_L approaches 1.0. This suggests another reason that the thrust benefit predicted by Weihs at high St_L is not observed is that a large train of *coherent, coaxial* vortex rings cannot be generated by these velocity programs as the vortex rings are packed closer together.

A final observation revealed by the analysis of the vorticity evolution of the jet is that the initial ring diameter decreases with St_L for sufficiently small L/D. This effect is attributed to the induced velocity or preceding rings on forming vortex rings. The poten-

tial significance of this result for understanding vortex ring formation and the overall structure of a fully-pulsed jet dictates that it warrants further investigation.

CHAPTER 5

Summary and Recommendations

5.1 Summary of Results

Two families of velocity programs (the NS and PS ramps) defined for a range of stroke ratios were used to generate starting and fully-pulsed jets to elucidate the importance of vortex ring formation for pulsatile jet propulsion. The phenomenon of vortex ring pinch off was observed for both the NS ramps and the PS ramps, with pinch off occurring at higher L/D for the PS ramps.

The experiments on starting jets clearly illustrated the existence of a maximization principle for average thrust during a pulse, $\bar{F}_p$, and its non-dimensional equivalent, $\bar{F}_p/(\rho A U_{max}^2)$. This maximization principle is driven by vortex ring pinch off since $\bar{F}_p$ and $\bar{F}_p/(\rho A U_{max}^2)$ were maximized at stroke ratios very near the point where the vortex rings were just beginning to pinch off from the generating jet for *both* the NS and PS ramps. Interestingly, $\bar{F}_p/(\rho A U_{max}^2)$ was typically lower for the PS ramps at equivalent stroke ratios below the point where pinch off was observed. Although a maximum in the average thrust during a pulse was not expected at the outset, its existence demonstrates

that the procedure for optimizing the average thrust produced in a finite amount of time is to form isolated vortex rings of maximal circulation since a trailing jet contributes proportionally less to the total impulse than the formation of a vortex ring.

The thrust and impulse benefit provided by vortex ring formation was attributed to the nozzle exit over-pressure present during the formation of a vortex ring, which could be as much as 41% of the total impulse and appeared to be nearly absent during the ejection of a trailing jet. A control volume analysis of the fluid in front of the nozzle was used to show that this pressure can be viewed as a reaction force related to the acceleration of ambient fluid by the forming ring. A hydrodynamic analysis of a completed vortex ring confirmed this result and showed that the nature of the accelerated ambient fluid could conceptually be divided into two components: (a) fluid entrained into the body or "bubble" of the vortex ring during roll-up of the shear layer, and (b) additional fluid outside the bubble given a non-zero velocity by the motion of the ring (added mass). Measurements of impulse alone, however, did not allow the relative contributions of these effects to pressure to be determined.

The apparent absence of nozzle exit over-pressure during the ejection of a trailing jet allowed the pressure contribution to circulation, Γ_p, and the pressure work, E_p, to be determined from PIV measurements of the pinched-off vortex rings and measurements of the jet velocity. The pressure work was observed to be a significant fraction of the total energy for both velocity programs, but was more significant for the NS ramps. Curiously, E_p/E increased with L/D for both velocity programs until reaching an apparent maximum significantly after pinch off was observed. Based on this observation it was hypothesized that entrained mass effects give a large contribution to nozzle exit over-pressure

late in a pulse ejection (i.e., when the shear-layer roll-up is more advanced) where the jet velocity is highest. Entrained mass effects were the primary candidate here because the added mass contribution to pressure was assumed to be significant primarily at pulse initiation, where the average jet velocity tends to be lower (especially for the PS ramps). The ratio Γ_p/Γ, on the other hand, was found to steadily decrease with L/D, suggesting that the pressure contribution to circulation is contributed primarily by added mass effects at pulse initiation since a longer pulse does not add to Γ_p.

A model for the initiation of an impulsive velocity program was proposed to illuminate the contribution of added mass effects to nozzle exit over-pressure near the beginning of a pulse. The model was applied for $X/D \ll 1$ so that the flow could be approximated as a cylindrical slug and entrainment effects could be ignored. Since the NS ramps are relatively impulsive and Γ_p appeared to be governed by effects at pulse initiation, this model was used to estimate Γ_p for the NS ramps, giving good agreement with the measured results. Pressure effects, therefore, provided a nice explanation for the known discrepancy between measured ring circulation and the standard slug model estimates of circulation. Application of the model to pressure impulse for the NS ramps proved less useful since the model ignores the growth of the ring and its concomitant fluid entrainment, but it illustrated that nozzle exit over-pressure at pulse initiation can be a significant fraction of I_p. This suggested that the thrust benefit provided by the NS ramps over the PS ramps [in terms of I_p/I or $\bar{F}_p/(\rho A U_{max}^2)$] may be due to the initially impulsive nature of the NS ramps, providing an initially larger nozzle exit over-pressure.

Given the central role played by nozzle exit over-pressure in these results, it was noted that *none* of the conclusions for the starting jet study could have been obtained from the slug model since it ignores nozzle exit over-pressure and, therefore, does not distinguish between a vortex ring and a trailing jet[1]. This observation is immensely important given the tacit acceptance of the validity of the slug model in much of the literature on vortex rings. In particular, the model of vortex ring pinch off based on the Kelvin-Benjamin variational principle proposed by GRS was re-evaluated. The results showed that the model proposed by GRS is accurate, but that the slug model overestimates the non-dimensional energy α, especially at small L/D.

In the investigations of the fully-pulsed jets, mechanical difficulties undermined the reliability of results for the PS ramps at low L/D, but interesting information was obtained for the NS ramps and a new family of velocity programs at a lower Re_m: the NS2 ramps. Overall the results for the NS and NS2 ramps indicated a propulsive benefit from nozzle exit over-pressure was always obtained by pulsing since F_{IJ} was significantly greater than one for all cases tested. The results also justified the level of detail used in the analysis of individual starting jets in that many of the features observed in the pulsed-jet case appeared to be related to a persistence or degradation of the flow features found in the starting jets. Such was the case for the general decrease in F_{IJ} with L/D observed for sufficiently high L/D, which was attributed to the persistence of vortex ring pinch off even at high St_L, as confirmed by PIV measurements of circulation. Decreases in F_{IJ} with St_L were also observed; the first being a relatively sudden decrease at low St_L that leveled

1. Ironically, the only point where the slug model appears to be reasonable is during the ejection of a trailing jet.

off in favor of the second, relatively shallow decrease with St_L that persisted all the way to $St_L \approx 1$. Both decreases were ascribed to a reduction in the pressure impulse required to initially accelerate fluid in front of the nozzle during vortex ring formation. In the case at low St_L this was apparently affected by the tails of preceding pulses remaining near the nozzle exit while the later, gradual decrease with St_L was attributed to the flow becoming more like a steady jet (i.e., less intermittent) as the pulses were moved closer together.

An investigation of the propulsive benefits predicted by Weihs [39] was also conducted using the NS2 ramps. The results did not show the expected significant increase in F_{IJ} with St_L, even for St_L approaching 1.0 (the limit for a fully-pulsed jet). This result was due to a violation of the assumptions of Weihs' model in two areas:

1. The vortex ring separation could not be reduced below $a/R_r = 4$ with the NS2 velocity programs; and
2. A coherent train of coaxial vortex rings could not be maintained at large St_L because (a) the vortex rings tended to wander off axis as St_L was increased (probably because of interactions with neighboring vortex rings), and (b) the vortex rings would break up beyond $x/D = 4.0$ for St_L above about 0.75.

Therefore, no significant propulsive benefit was observed from the interaction of successive pulses, so the optimal pulsing conditions in terms of maximal F_{IJ} occurred at $St_L = 0$ (except for an anomalous peak for $L/D = 2.0$ of the NS ramps at $St_L = 0.17$ whose significance was questionable due to measurement uncertainty).

Finally, a phenomenon of potential interest was observed for fully-pulsed jets of small enough stroke ratio to avoid vortex ring pinch off. Namely, the initial vortex ring diameter was observed to decrease with St_L. This was attributed to the induced velocity of preceding vortex rings on forming rings.

5.2 Recommendations for Future Work

Given the obvious importance of nozzle exit over-pressure to starting jets, it seems worthwhile to pursue a detailed investigation of the entrained and added mass effects to which this pressure has been ascribed. The data presented here have strongly implied the existence of these mechanisms, but the literature in this area is sparse. A strong understanding of the mechanics associated with accelerating these mass components could suggest ways to optimize velocity programs for performance (since much of the difference in impulse between the NS and PS ramps is likely due to differences in the entrained and added mass contributions for these programs). It could also suggest simple ways to correct the slug model and provide deeper insight to the behavior of fully-pulsed jets. This is not a trivial endeavor, however, because this investigation has noted the importance of determining the contributions of these effects during vortex ring development, but under these circumstances they are not as easily defined as for a developed ring.

The quality of the results for the fully-pulsed jets, on the other hand, could be substantially improved if modifications to the design of the experimental apparatus were made to eliminate or attenuate the mechanical resonance that plagued these results. If such modifications could be made, some of the potentially interesting peaks in F_{IJ} for the PS ramps could be studied with more confidence and in more detail. A mechanically improved system would also prove useful for considering cases with smaller L/D in an attempt to achieve conditions satisfying the assumptions of Weihs' analysis and thereby investigate the possibility of optimal pulsing conditions at non-zero St_L for lower L/D. Finally, the study of the structure of the fully-pulsed jets presented in chapter 4 was rather

brief, but it revealed some interesting behavior worthy of more detailed study with better time resolution not only by parties investigating pulsatile propulsion, but also by those interested in transition to turbulence.

APPENDIX A

A Simple Model for A Piston Moving Against Friction in a Cylinder

The simplest model that embodies the basic physics of a piston moving against friction in a cylinder is a mass attached to a spring sliding against friction on a surface. For the experimental apparatus presented in chapter 2, the mass being moved is the driver piston, the surface is the driver cylinder, and the flexible element is (probably) the connection between the actuator and the driver piston. In this scenario, oscillations in the angular alignment of the piston with the cylinder can occur if a (small) gap exists between the piston and cylinder on one side of the piston, allowing for angular misalignment between the piston and cylinder and causing the friction between the piston and cylinder to be localized opposite of the gap, as illustrated in Figure A.1. That the piston in the apparatus used for this investigation was slightly under-sized, allowing for the possibility of such a gap, was noted in section 2.2.1.

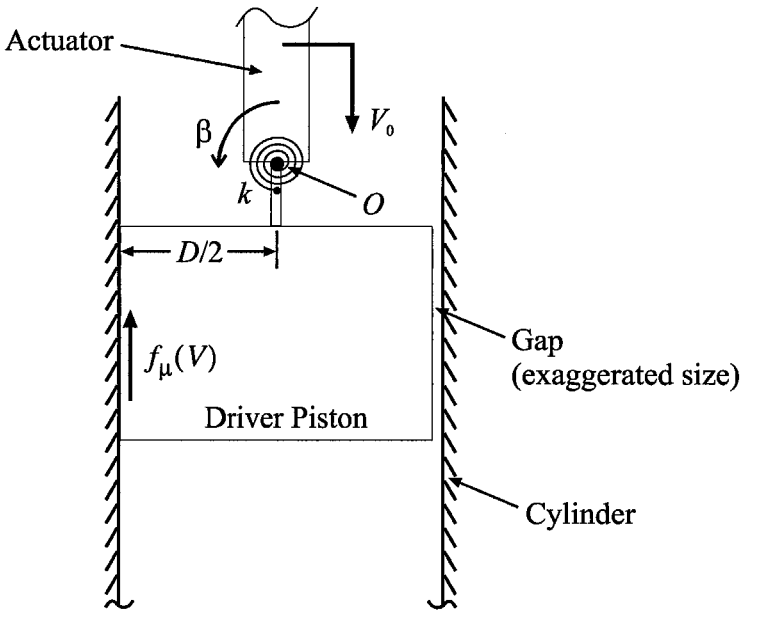

FIGURE A.1 Model of Frictional Effects Between a Moving Piston and a Cylinder.

Using the coordinate system defined in Figure A.1, a simple balance of moments around point O gives the equation of motion for oscillations of the piston (to first order) as

$$I_O\ddot{\beta} = -k\beta - f_\mu(V)\left(\frac{D}{2}\right) \tag{A.1}$$

where I_O is the moment of inertia of the piston about point O, k is the torsional stiffness, f_μ is the frictional force, V is the relative velocity between the piston and cylinder defined by

$$V = V_0 + \dot{\beta}\left(\frac{D}{2}\right), \tag{A.2}$$

and V_0 is the commanded piston velocity (constant for this analysis). Taylor expanding f_μ about V_0 gives

$$f_\mu(V) = f_\mu(V_0) + f'_\mu(V_0)\left(\dot{\beta}\left(\frac{D}{2}\right)\right) + \frac{1}{2}f''_\mu(V_0)\left(\dot{\beta}\left(\frac{D}{2}\right)\right)^2 + \frac{1}{6}f'''_\mu(V_0)\left(\dot{\beta}\left(\frac{D}{2}\right)\right)^2 + hot. \tag{A.3}$$

Assuming f_μ has the form shown in Figure A.2, neglecting higher order terms, and substituting the result into the equation of motion gives

$$\ddot{\beta} = -\frac{k}{I_O}\beta - \frac{f_0}{I_O}\left(\frac{D}{2}\right) + \frac{f_1}{I_O}\left(\frac{D}{2}\right)^2\dot{\beta} - \frac{f_3}{I_O}\left(\frac{D}{2}\right)^4\dot{\beta}^3 \tag{A.4}$$

where $f_i = \left|\frac{1}{i!}f_\mu^{(i)}(V_0)\right|$, and $f_2 \approx 0$. Finally, defining η as β - β_0 where $\beta_0 \equiv -\frac{f_0}{k}\left(\frac{D}{2}\right)$ is the equilibrium value for β reduces the equation of motion to

$$\ddot{\eta} - \frac{1}{I_O}\left(\frac{D}{2}\right)^2\left(f_1 - f_3\left(\frac{D}{2}\right)^2\dot{\eta}^2\right)\dot{\eta} + \frac{k}{I_O}\eta = 0. \tag{A.5}$$

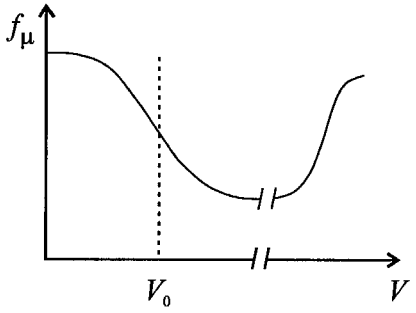

FIGURE A.2 Assumed Form of $f_\mu(V)$.

Equation (A.5) is the result for a damped harmonic oscillator with the damping given by a quadratic function of $\dot{\eta}$. For $\dot{\eta} \approx 0$ the damping is negative, implying that the fixed point at $\eta = 0$ is unstable. This is confirmed by the eigenvalues of the linear part of equation (A.5) when it is written in matrix form, namely,

$$\lambda_{1,2} = \frac{f_1}{2I_O}\left(\frac{D}{2}\right)^2 \pm \frac{1}{2}\sqrt{\left(\frac{f_1}{I_O}\left(\frac{D}{2}\right)^2\right)^2 - \frac{4k}{I_O}}, \tag{A.6}$$

which both have positive real part indicating the system will diverge from $\beta = \beta_0$. As $\dot{\eta}$ becomes large, however, the damping in equation (A.5) eventually becomes positive (stabilizing), so the system reaches a stable limit cycle for sufficiently large $\dot{\eta}$. Indeed, taking the time derivative of equation (A.5) yields the Van der Pol equation for $\dot{\eta}$, the solution of which contains a stable limit cycle around the origin in phase space. Hence, the system will oscillate about $\beta = \beta_0$. Since β_0 is not zero, these oscillations change the volume in front of the driver piston and, therefore, impose oscillations on the jet velocity. This could partially explain the jet velocity oscillations in Figure 2.8 (a) for constant commanded piston velocities.

For a proper evaluation of the model it is desirable to estimate the values of the model parameters for the physical system and compare the predicted and measured velocity oscillations. Such an analysis depends knowledge of the first and third derivatives of f_μ, which requires a more detailed knowledge of f_μ than can be extrapolated from the available data. Nevertheless, a few qualitative observations can be made. Specifically, based on Figure A.2, f_1 initially increases with V_0 and then decreases. Assuming a relatively constant f_3, this implies the value of $\dot{\eta}$ at which the damping becomes positive initially increases and then decreases with V_0, suggesting the amplitude of the oscillations in the jet velocity should initially increase with $V_0 = U_p$ and then decrease. Similar behavior is seen in Figure 2.8, especially Figure 2.8 (b) where the dominant peak (which is related to this model by hypothesis) initially grows in amplitude with increasing U_p and then tapers off. The tendency for this peak to increase frequency with U_p, however, is not easily explained by this model unless a mechanism is introduced that allows k to change with

V_0. It is also clear that this model also does not explain all of the dynamics observed in Figure 2.8 (b) since it does not account for the peaks in this figure that appear below 20 Hz for U_p approaching 0.5 in/s. Despite the deficiencies noted by these last two points, the model does provide a starting point for improvements to the design of the system.

APPENDIX B

Details of the Analysis of Unsteady Entrance Pipe Flow by Atabek and Chang

This appendix presents a brief overview of the analysis of Atabek and Chang [1] for unsteady entrance pipe flow that was used in section 2.4.2.3 to extend the hotfilm measurements to the unsteady cases studied in chapters 3 and 4. The notation follows that of Atabek and Chang, which is different from the notation used elsewhere in the text.

B.1 Problem Formulation

The analysis concerns entrance flow in a circular pipe of radius a, where the flow enters at $x = 0$ (in contrast to the coordinate system used in the main text where $x = 0$ corresponds to the nozzle exit plane). The flow at $x = 0$ is assumed to be parallel, uniform in r, and periodic in time, namely,

$$u(x = 0, r, t) = u_0 \left[1 + \sum_{k=1}^{n} (a_k \cos k\omega t + b_k \sin k\omega t) \right]. \qquad \text{(B.1)}$$

To simplify the governing equations, the standard boundary layer approximations are imposed. The resulting equations are still non-linear due to the convective term. This

term is linearized by assuming the convective velocity is $\mathbf{u} = [u(x = 0, r, t), 0, 0]$ throughout the flow. The justification given by Atabek and Chang is that this substitution is valid without error at $x = 0$ and far downstream where the flow is fully developed. The governing equations then reduce to

$$\frac{\partial u}{\partial t} + u_0\left[1 + \sum_{k=1}^{n}(a_k \cos k\omega t + b_k \sin k\omega t)\right]\frac{\partial u}{\partial x} = -\frac{1}{\rho}\frac{\partial p}{\partial x} + \frac{\nu}{r}\frac{\partial}{\partial r}\left(r\frac{\partial u}{\partial r}\right) \tag{B.2}$$

$$\frac{\partial u}{\partial x} + \frac{1}{r}\frac{\partial (rv)}{\partial r} = 0$$

with boundary conditions given by (a) equation (B.1) and $v = 0$ at $x = 0$, $0 \le r < a$, and (b) $\mathbf{u} = 0$ at $r = a$ and $x > 0$.

B.2 Solution

Atabek and Chang give a lengthy but straightforward derivation of the solution to the problem formulated in section B.1. The result for u is

$$\frac{u(x, r, t)}{u_0} = U_P(r) + U_{PT}(r, t) + U_E(x, r, t) \tag{B.3}$$

and the results for v can be obtained by integrating the continuity equation [equation (B.2) (b)]. In equation (B.3), U_P is the solution for steady, fully-developed Poiseuille flow, U_{PT} is the correction to U_P for periodic, time-dependent mass flux through the pipe, and U_E is the entrance region correction for $x < \infty$. The mathematical expressions for these terms are

$$U_P(r) = 2\left(1 - \frac{r^2}{a^2}\right), \tag{B.4}$$

$$U_{PT}(r,t) = \mathrm{Re}\left\{\sum_{k=1}^{n}(a_k - ib_k)\left[\frac{J_0(i^{3/2}\sqrt{k}\alpha(r/a)) - J_0(i^{3/2}\sqrt{k}\alpha)}{J_2(i^{3/2}\sqrt{k}\alpha)}\right]e^{ik\omega t}\right\}, \tag{B.5}$$

and

$$U_E(x,r,t) = -4\sum_{j=1}^{\infty}\frac{1}{\gamma_j^2}\left\{1 + \sum_{k=1}^{n} M_{kj}[a_k\cos(k(\omega t - A) - \theta_{kj}) + b_k\sin(k(\omega t - A) - \theta_{kj})]\right\} \times\left[1 - \frac{J_0(\gamma_j(r/a))}{J_0(\gamma_j)}\right]\exp\left[-\frac{\gamma_j^2}{\alpha^2}A\right] \tag{B.6}$$

In these equations, J_n are Bessel functions of the first kind of order n, γ_j are the zeros of J_2, and the following definitions are made:

$$\alpha \equiv a\sqrt{\frac{\omega}{\nu}}, \tag{B.7}$$

which is the Wormersley number,

$$M_{jk} \equiv \frac{1}{\sqrt{1 + k^2(\alpha/\gamma_j)^4}}, \tag{B.8}$$

and

$$\theta_{jk} \equiv \mathrm{atan}k\left(\frac{\alpha}{\gamma_j}\right)^2. \tag{B.9}$$

The parameter A is given by

$$A = \omega t - F(s - \Delta) \tag{B.10}$$

where s is defined by

$$s = \omega t + \sum_{k=1}^{n} \frac{1}{k}(a_k \sin k\omega t - b_k \cos k\omega t), \tag{B.11}$$

$\omega t = F(s)$ is the solution of equation (B.11) for ωt, and Δ is defined by

$$\Delta \equiv \frac{x\alpha^2}{a \cdot Re_0}. \tag{B.12}$$

The Reynolds number, Re_0, used here is $\frac{u_0 a}{\nu}$. To apply this result, equation (B.11) must be invertible, which is true if $\frac{ds}{d(\omega t)} > 0$, i.e., if $u(x = 0, r, t) > 0$ throughout the oscillation period. Provided this condition holds, Atabek and Chang provide a convenient, graphical method for finding A. For $x \to \infty$, $A \to \infty$ and $U_E \to 0$, so the solution corresponds to the fully-developed flow solution for $x \to \infty$ as advertised.

APPENDIX C

Details of the Model for Vortex Ring Pinch Off Proposed by Shusser and Gharib (the SG Model)

C.1 Description of the Model

A detailed description of the kinematic model for vortex ring formation and pinch off proposed by Shusser and Gharib is given in their recent papers [34] and [35] and extended to time varying piston velocity programs in Shusser *et al.* [36]. The key assumptions of the model are as follows:

1. The values of the circulation (Γ), impulse (I), and energy (E) supplied to the flow by a piston-cylinder mechanism can be approximated by the slug model, namely,

$$\Gamma(t) \approx \Gamma_{sm}(t) = \frac{1}{2}\int_0^t U_J^2(\tau)\,d\tau\,, \tag{C.1}$$

$$I(t) \approx I_{sm}(t) = \rho A \int_0^t U_J^2(\tau)\,d\tau\,, \tag{C.2}$$

and

$$E(t) \approx E_{sm}(t) = \frac{\rho A}{2}\int_0^t U_J^3(\tau)\,d\tau\,; \tag{C.3}$$

2. Key kinematic quantities of a forming vortex ring near pinch off (such as its radius, R_r, and velocity, W) can be approximated by Fraenkel's second-order formulae for rings in the Norbury family (see Fraenkel, [11]), namely

$$R_r = b(\varepsilon)\sqrt{\frac{2I}{\rho\pi\Gamma}}, \tag{C.4}$$

and

$$W = B(\varepsilon)\sqrt{\frac{\rho\Gamma^3}{\pi I}} \tag{C.5}$$

where ε is the ratio of the (mean) core radius to R_r, and B and b are given by

$$B(\varepsilon) = \frac{1}{4}\sqrt{1+\frac{3}{4}\varepsilon^2}\left[\ln\frac{8}{\varepsilon} - \frac{1}{4} + \frac{3\varepsilon^2}{8}\left(\frac{5}{4} - \ln\frac{8}{\varepsilon}\right)\right] \tag{C.6}$$

and

$$b(\varepsilon) = \left[2\left(1+\frac{3}{4}\varepsilon^2\right)\right]^{-1/2}; \tag{C.7}$$

3. The velocity of the generating jet in the immediate vicinity of the ring can be approximated by a one-dimensional expansion of the jet from the nozzle diameter (D) to the diameter of the ring ($2R_r$), as shown in Figure C.1; and
4. The forming vortex ring pinches off from the generating jet when the monotonically increasing ring velocity, W, reaches the jet velocity in the vicinity of the ring [approximated from assumption (3)]. That is, vortex ring pinch off occurs at the instant when

$$W = \left(\frac{2R_r}{D}\right)^2 U_J \tag{C.8}$$

and the vortex ring stops gaining energy and circulation at this point.

The basic idea in assumption (4) is that vortex ring formation is completed once the ring velocity exceeds the velocity of the jet in the immediate vicinity of the ring, preventing additional vorticity in the shear layer of the jet from being entrained into the ring.

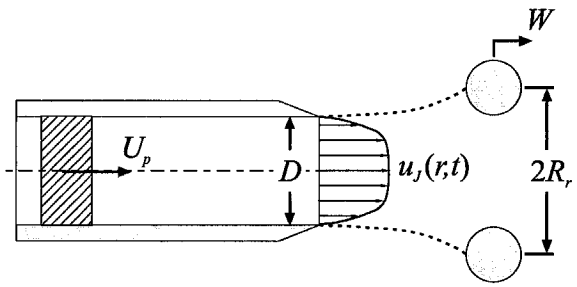

FIGURE C.1 Vortex Ring Formation from a Piston-Cylinder Mechanism as Modeled by Shusser and Gharib, [35].

Given the model assumptions and a specified velocity program $U_J(t)$, the model still has one free parameter: ε. In the extension of the model to time varying velocity programs, Shusser *et al.* [36] assume that at pinch off, ε is constant at $\varepsilon = \varepsilon_F \approx 0.4$, which corresponds to $B(\varepsilon_F) = 0.6987$ and $b(\varepsilon_F) = 0.6682$. This value for ε was chosen to provide the best overall match of the calculated vortex ring velocity *and* non-dimensional energy at pinch off with the actual values obtained from experiments. The problem is now closed and the model predicts vortex ring pinch off at the instant t_F, defined implicitly by[1]

$$\frac{D^2\sqrt{\rho\pi^3}}{8b^2(\varepsilon_F)B(\varepsilon_F)} = \sqrt{\frac{I(t_F)\,\Gamma(t_F)}{U_J^2(t_F)}}. \tag{C.9}$$

The formation number F is then given by

$$F = \frac{1}{D}\int_0^{t_F} U_J(\tau)\,d\tau. \tag{C.10}$$

1. It may take some amount of time beyond t_F for the pinch off to be completed, but the model predicts that only the impulse, energy, and circulation ejected by the piston-cylinder mechanism up to time t_F is entrained into the ring.

An important feature of this model is that it generalizes the concept of the formation number. As expressed in GRS, the formation number corresponds to the non-dimensional time $[tU_J(t)]/D = X(t)/D$ when the total circulation ejected corresponds to the circulation in the pinched-off vortex ring, so it requires a large enough L/D for pinch off to be observed in order to define the formation number. In the SG model, on the other hand, F is defined for all L/D. For sufficiently short L/D the model returns $t_F \approx t_p$ and hence, $F \approx L/D$, indicating that no pinch off has occurred and an isolated vortex ring is produced by the pulse. For large enough L/D, the model indicates that $L/D \gg F$, implying that the leading vortex ring has pinched off from the generating jet. This motivates the definition of a non-dimensional trailing jet length as $L/D - F$ where vortex ring pinch off has occurred for values of $L/D - F$ significantly different from zero.

C.2 Confirmation of the Model for Time-Varying Velocity Programs

In the extension of the SG model to time-varying velocity programs given in Shusser *et al.* [36] it is shown that the model predicts the formation number for the time varying programs in Rosenfeld *et al.* [28] to within 4%. The applicability of the model to velocity programs similar to those used in chapters 3 and 4 is investigated here in an attempt to extend the results to an Re_m over four times larger than that used in Rosenfeld *et al.* and substantiate its use for this investigation.

To provide a reasonable test of the model on velocity programs similar to those in Figure 3.1, it was necessary to surmount the insufficient time resolution afforded by DPIV as noted in section 3.3. This was accomplished using PLIF flow visualization of the jet

recorded at 250 frames per second with a Kodak high-speed video camera. Quantitative information was obtained by tracking various flow features in the frame sequence. In the spirit of the SG model, the features tracked were the vortex ring cores and the crests of the instability waves in the trailing jet, as indicated in Figure C.2. This procedure gave an indication of the position and velocity of the ring and the shear layer of the trailing jet.

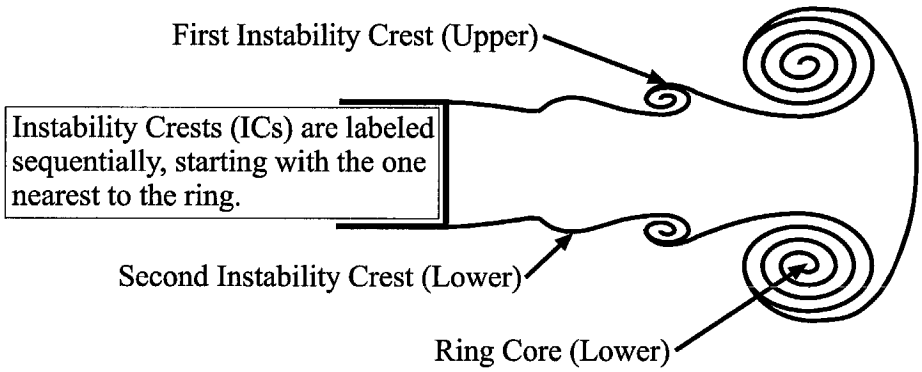

FIGURE C.2 Flow Features Tracked in the PLIF Images.

The actual velocity programs used for these tests are shown in Figure C.3, which are designated the NS' and PS' ramps and are very similar to the NS and PS ramps shown in Figure 3.1. Tracking the vortex ring velocity for the NS' ramps shows an initial increase in the ring velocity which then levels off, as illustrated for $L/D = 5.0$ in Figure C.4 (a). In fact, for the NS' ramps with $L/D > 2$, the ring velocity saturates *before* the pulse is completed. The instant where the ring velocity first saturates, t_s, is taken as the point where entrainment of circulation has ceased, i.e., pinch off has occurred (for $L/D > 2$). Although this definition of pinch off is not the same as used by GRS, it is in accord with figure 11 of their paper where it is shown that the vortex ring velocity saturates at $X(t)/D \approx F$. Furthermore, Figure C.4 (a) illustrates that the velocity of the first instability crest (IC) drops below the ring velocity at t_s, as expected from the SG model.

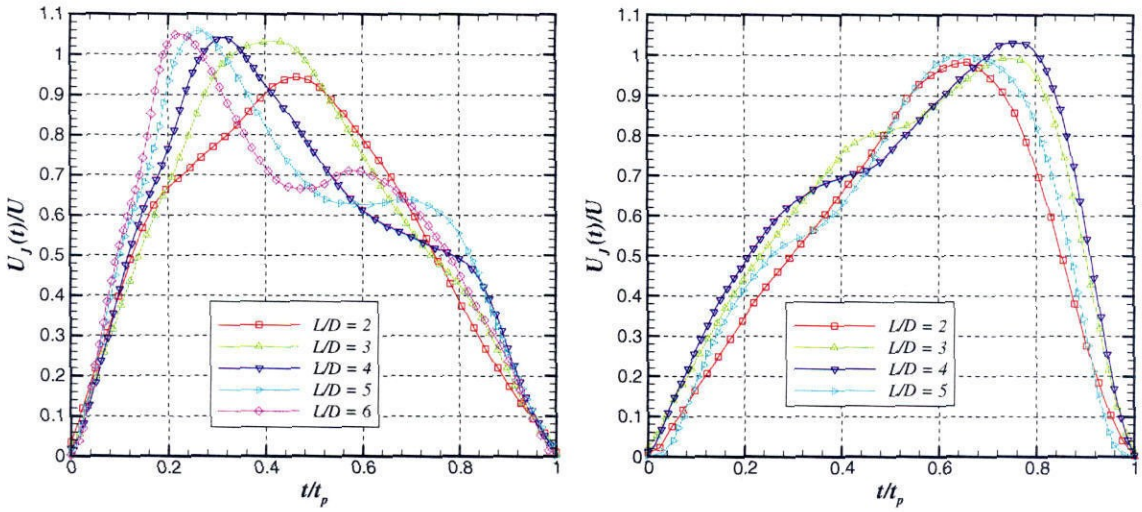

FIGURE C.3 Velocity Programs Used in the Flow Visualization Study: (a) NS' Ramps, (b) PS' Ramps.

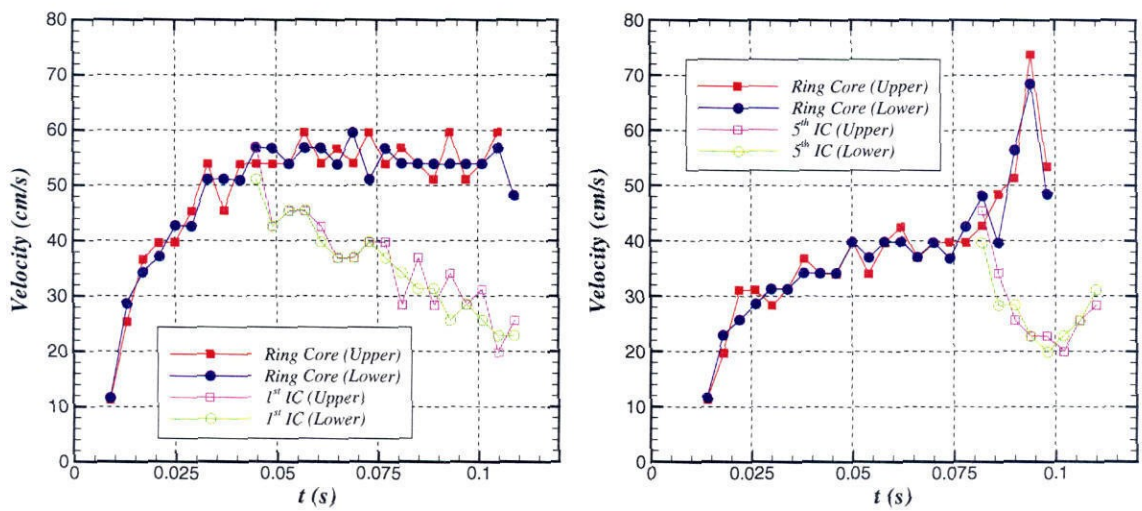

FIGURE C.4 Velocities of Specific Flow Features Obtained from Flow Visualization: (a) *L/D* = 5.0, NS' Ramp, (b) *L/D* = 5.0, PS' Ramp.

For the PS' ramps the situation is more complicated because the ICs overtake and merge with the leading vortex ring so that the ring velocity never truly saturates and the ring cores eventually become impossible to track. So, for these velocity programs, pinch off is hypothesized at the instant (also designated t_s) where the velocity of an IC first

drops below that of the ring. This is illustrated in Figure C.4 (b) for L/D = 5 of the PS' ramps where the 5th IC is the first to slow below the ring velocity. The figure also shows that the ring velocity appears to increase sharply after t_s, which is caused by the merging of the ring with a previous IC and marks the point where it became impossible to track the vortex ring core.

Having determined t_s from the flow visualization images for the NS' and PS' ramps, the formation number based on these observations is given by

$$F_s \equiv \frac{1}{D}\int_0^{t_s} U_J(\tau)d\tau \qquad \text{(C.11)}$$

where U_J is determined from separate hotfilm measurements and synchronized with the video by determining the jet velocity from the leading edge of the jet in the first few frames after a pulse is initiated. Using the U_J measurements to determine the formation number predicted by the SG model, F_{SG}, allows the "direct" measurements of F from the flow visualization to be compared with the model results. The results are compared in Table C.1, which shows that F_s agrees with F_{SG} to within experimental error for the cases where F_s could be determined. In the case of L/D = 2.0 of the NS' ramps, no pinch off is observed in the flow visualization, but $F_{SG} \approx (L/D)_{measured}$ for this case, so no trailing jet is expected. [$(L/D)_{measured}$ is determined by equation (C.11) using the pulse duration as the upper limit of integration instead of t_s.] For L/D < 5.0 of the PS' ramps, no non-merging IC is observed, so t_s could not be defined. It was noted however, that some fluid

was not entrained into the ring for $L/D = 4.0$, consistent with the model prediction that $F_{SG} < (L/D)_{measured}$.

The agreement between F_s and F_{SG} for the velocity programs tested along with the results of Shusser *et al.* [36] substantiates the use of the SG model in this investigation.

TABLE C.1 Comparison of the Formation Number Determined From the SG Model and PLIF Flow Visualization.

L/D (nominal)[a]	NS' Ramps			PS' Ramps		
	$(L/D)_{meas}$ [b]	F_{SG}	F_s	$(L/D)_{meas}$ [b]	F_{SG}	F_s
2.0	1.90 ± 0.05	1.80 ± 0.05	NPO[c]	1.80 ± 0.05	1.75 ± 0.03	NPO[c]
3.0	2.81 ± 0.10	2.42 ± 0.10	2.50 ± 0.08	2.81 ± 0.10	2.72 ± 0.08	NPO[c]
4.0	3.81 ± 0.10	2.73 ± 0.10	2.57 ± 0.10	3.75 ± 0.15	3.48 ± 0.10	NIC[d]
5.0	4.83 ± 0.10	2.84 ± 0.10	2.67 ± 0.10	4.70 ± 0.20	4.00 ± 0.15	4.10 ± 0.10
6.0	5.75 ± 0.10	2.95 ± 0.10	2.73 ± 0.10			

a. Based on commanded piston displacement

b. $(L/D)_{measured}$, as determined from the time integral of U_J over the pulse duration.

c. No Pinch Off: no pinch off observed in the flow visualization

d. No Instability Crest: all ICs merged with the leading vortex ring, but some fluid was left behind after the ring formation was complete.

APPENDIX D

Derivation of the Generalized Slug-Flow Equations

D.1 Introduction

The slug-flow equations give an analytical description of a piston cylinder mechanism with nozzle diameter D and piston velocity $U_p(t)$ that injects the dynamic quantities impulse, energy, and circulation (I, E, and Γ, respectively) into the fluid external to the nozzle. The common practice in vortex ring research has been to model this process as quasi-steady and ignore terms associated with the nozzle pressure, resulting in the so-called slug-model equations for vortex ring formation. This practice is highly questionable since the process of vortex ring formation from a piston-cylinder mechanism is fundamentally unsteady in that it involves *starting* jets. Ignoring the pressure terms can obscure important physics and lead to incorrect conclusions. For this reason, a derivation of the complete or generalized slug-flow equations[1] is given here. The equations for energy and impulse reveal additional pressure terms that are commonly understood, but the derivation of the equation for circulation leads to a pressure term that has not previously been mentioned in the literature.

---

1. The equations are dubbed "generalized" because they include terms that are neglected in the slug model.

D.2 Derivation of the Impulse and Energy Equations

Since the slug-flow equations are concerned with the energy and impulse injected into the fluid *external* to a piston-cylinder mechanism, the equations related to these quantities are derived by considering the control volume equations for the fluid external to the flow generating device. The top view of an axisymmetric control volume suitable for this purpose is illustrated in Figure D.1.

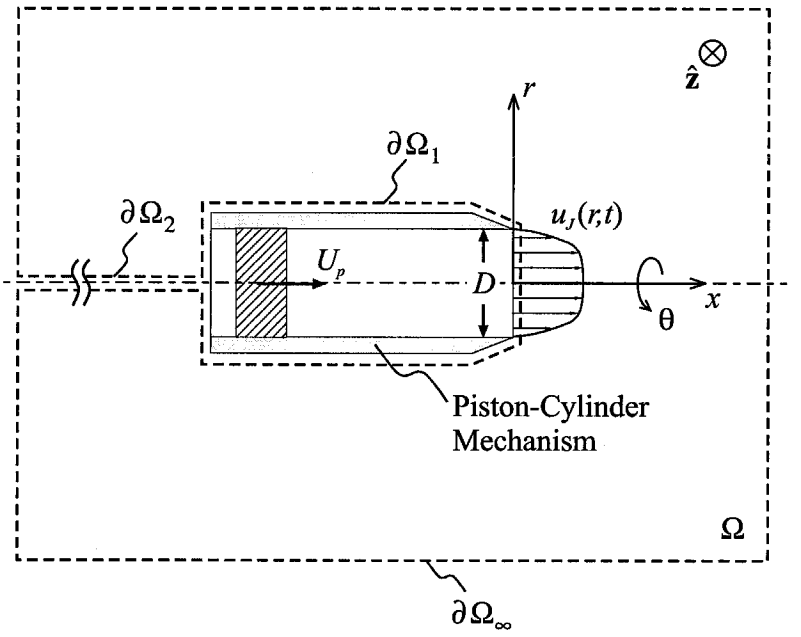

FIGURE D.1 Top View of an Axisymmetric Control Volume of the Fluid External to the Piston-Cylinder Vortex Generator.

D.2.1 The Impulse Equation

The momentum equation for an incompressible fluid in a fixed control volume Ω acted on by a constant gravitational field is given by

$$\rho\frac{\partial}{\partial t}\int_{\Omega}\mathbf{u}dV+\rho\int_{\partial\Omega}\mathbf{u}(\mathbf{u}\cdot\hat{\mathbf{n}})dS=-\int_{\partial\Omega}p\hat{\mathbf{n}}dS-\int_{\partial\Omega}\phi_g\hat{\mathbf{n}}dS+\int_{\partial\Omega}\tau\hat{\mathbf{n}}dS+\mathbf{F}_{ext} \tag{D.1}$$

where $\hat{\mathbf{n}}$ is the unit outward normal, τ is the shear stress tensor, ϕ_g is the gravitational potential (per unit volume), and $\mathbf{F}_{ext}$ is the vector sum of the external forces (besides shear and pressure forces) applied to the surface of the control volume. In this case, $\mathbf{F}_{ext}$ is zero. The contribution from shear stress is also negligible since there is no flow on $\partial\Omega_\infty$, the flow from the nozzle is axisymmetric (eliminating the $\tau_{\theta x}$ and τ_{rx} terms of $\tau\hat{\mathbf{n}}$), $\frac{\partial u}{\partial x}\approx 0$ for sufficiently high Reynolds number (eliminating the τ_{xx} term of $\tau\hat{\mathbf{n}}$), and any shear stress exerted on the external portion of the nozzle is small and only exists during the initial roll-up of the vortex ring (Didden, [10]). Additionally, the gravitational potential for a uniform gravitational field oriented in the $-\hat{\mathbf{z}}$ direction can be expressed as

$$\phi_g = \rho g h - p_\infty \equiv -p_h \tag{D.2}$$

where g is the gravitational constant, h is the vertical distance from the nozzle center line, and p_∞ is the ambient fluid pressure at the level of the nozzle center line [i.e., the pressure at $(x, r)\rightarrow(\infty, 0)$]. Finally, integrals over $\partial\Omega_2$ are zero in the limit that the radius of this surface goes to zero. Given these considerations, equation (D.1) reduces to

$$\rho\frac{\partial}{\partial t}\int_{\Omega}\mathbf{u}dV+\int_{\partial\Omega_\infty}(p-p_h)\hat{\mathbf{n}}dS=-\int_{\partial\Omega_1}(p-p_h)\hat{\mathbf{n}}dS-\rho\int_{\partial\Omega_1}\mathbf{u}(\mathbf{u}\cdot\hat{\mathbf{n}})dS. \tag{D.3}$$

Cantwell [8] showed that for an incompressible, Newtonian flow with finite regions of vorticity,

$$\rho\frac{\partial}{\partial t}\int_{\Omega}\mathbf{u}dV + \int_{\partial\Omega_\infty}(p-p_h)\hat{\mathbf{n}}dS = \frac{\partial}{\partial t}\int_0^t\int_{\Omega}\mathbf{F}(\mathbf{x},\tau)dVd\tau \tag{D.4}$$

where **F** is the total force (per unit volume) applied to the fluid in $\Omega^{(2)}$. For unbounded flows,

$$\mathbf{I}(t) \equiv \frac{\rho}{2}\int_{\Omega}\mathbf{x}\times\omega(\mathbf{x},t)dV = \int_0^t\int_{\Omega}\mathbf{F}(\mathbf{x},\tau)dVd\tau \tag{D.5}$$

where **I** is the hydrodynamic impulse and ω is the vorticity vector defined as

$$\omega \equiv \nabla\times\mathbf{u}\,. \tag{D.6}$$

Proof of equation (D.5) is given in Saffman [32] and Lamb [15]. Using these results, the right-hand side of equation (D.3) is identical to the time rate of change of the impulse of the flow, giving

$$\frac{\partial\mathbf{I}}{\partial t} = -\int_{\partial\Omega_1}(p-p_h)\hat{\mathbf{n}}dS - \rho\int_{\partial\Omega_1}\mathbf{u}(\mathbf{u}\cdot\hat{\mathbf{n}})dS. \tag{D.7}$$

---

2. Under the stated assumption of finite regions of vorticity, $p-p_h\to 0$ as $|\mathbf{x}|\to\infty$, but $\int_{\partial\Omega_\infty}(p-p_h)\hat{\mathbf{n}}dS$ remains finite (non-zero). For the special case where $\partial\Omega_\infty$ is spherical, Cantwell [8] and Saffman [32] show that $\int_{\partial\Omega_\infty}(p-p_h)\hat{\mathbf{n}}dS = \frac{1}{3}\frac{\partial\mathbf{I}}{\partial t}$ and $\rho\frac{\partial}{\partial t}\int_{\Omega}\mathbf{u}dV = \frac{2}{3}\frac{\partial\mathbf{I}}{\partial t}$ where **I** is defined in equation (D.5). Saffman [32], however, notes that the fraction of $\frac{\partial\mathbf{I}}{\partial t}$ associated with $\rho\frac{\partial}{\partial t}\int_{\Omega}\mathbf{u}dV$ (and hence, with $\int_{\partial\Omega_\infty}(p-p_h)\hat{\mathbf{n}}dS$) depends on the assumed shape of $\partial\Omega_\infty$, implying that $\rho\int_{\Omega}\mathbf{u}dV$ (the real momentum) is not well defined for unbounded flows. The hydrodynamic impulse, **I**, on the other hand, is well defined for unbounded flows, as indicated by equation (D.5).

Equation (D.7) represents the general result for the impulse applied to the external flow by a piston cylinder mechanism involving minimal assumptions. If the assumption of parallel flow at the nozzle exit is explicitly invoked for sufficiently high Reynolds number, then $\mathbf{u} = u_J(r,t)\hat{\mathbf{x}}$ over the nozzle area A and $\mathbf{u} = 0$ elsewhere on $\partial\Omega_1$. The additional assumption of negligible flow over the surface of the device external to the nozzle diameter D implies that the pressure over $\partial\Omega_1$ is p_h everywhere except over the nozzle area. Using these ideas and taking account of the fact that $\hat{\mathbf{n}}$ is the unit outward normal to the surface, equation (D.7) becomes

$$\frac{\partial \mathbf{I}}{\partial t} = \rho\int_A u_J^2(r,t)\hat{\mathbf{x}}dS + \int_A [p(r,t) - p_h]\hat{\mathbf{x}}dS. \tag{D.8}$$

Integrating with respect to time gives

$$I(t) = I_U(t) + I_p(t) \tag{D.9}$$

where

$$I_U(t) \equiv \rho\int_0^t \int_A u_J^2(r,\tau)dSd\tau, \tag{D.10}$$

$$I_p(t) \equiv \int_0^t \int_A [p(r,\tau) - p_\infty]dSd\tau, \tag{D.11}$$

I is the magnitude of $\mathbf{I}$ (which is equal to the x-component of $\mathbf{I}$ in this case), and p_∞ is defined as the (constant) ambient pressure at the depth of the nozzle center line[3]. Equa-

3. Since the variation in p_h with depth h is linear and the nozzle is circular, the integral of p_h over the nozzle area is just Ap_∞.

tion (D.9) is referred to here as the generalized impulse equation for slug flow, equation (D.10) defines the "velocity impulse," and equation (D.11) defines the "pressure impulse."

D.2.2 The Energy Equation

Conservation of energy for the control volume Ω in Figure D.1 can be written as

$$\frac{\partial}{\partial t}\int_{\Omega}\rho\left(e+\frac{u^2}{2}\right)d\Omega+\int_{\partial\Omega}\rho\left(e+\frac{u^2}{2}\right)(\mathbf{u}\cdot\hat{\mathbf{n}})dS = \tag{D.12}$$
$$\int_{\partial\Omega}(p-p_h)(\mathbf{u}\cdot\hat{\mathbf{n}})dS+\int_{\partial\Omega}\tau\mathbf{u}\cdot\hat{\mathbf{n}}dS-\int_{\partial\Omega}\mathbf{q}\cdot\hat{\mathbf{n}}dS-\int_{\Omega}\rho Q dV$$

where e is the internal energy of the fluid and p_h accounts for the gravitational potential as defined in equation (D.2). For this problem, heat flux out of the control volume, $\mathbf{q}$, and volume heating, Q, are zero, so these terms can be ignored. The ρgh term in p_h can also be eliminated since $\mathbf{u}$ is axisymmetric and, therefore, the surface integral of $\rho gh(\mathbf{u}\cdot\hat{\mathbf{n}})$ is zero. Finally, the velocity field decays like $|\mathbf{x}|^{-3}$ for a vorticity field of finite extent (Cantwell [8]) and $\mathbf{u}$ is zero on solid boundaries due to the no slip condition, so the surface integrals are non-zero only over the nozzle area A. Equation (D.12) therefore reduces to

$$\frac{\partial}{\partial t}\int_{\Omega}\rho\left(e+\frac{u^2}{2}\right)d\Omega=\int_{A}\rho\left(e+\frac{(p-p_\infty)}{\rho}+\frac{u_J^2(r,t)}{2}\right)u_J(r,t)\,dS+\int_{A}\tau\mathbf{u}\cdot\hat{\mathbf{n}}dS \tag{D.13}$$

where the parallel flow assumption has been invoked to give $u^2\approx u_J^2$ over the nozzle area.

If it is further assumed (as in section D.2.1) that the flow is of sufficiently high Reynolds number, the last term on the right-hand side of equation (D.13) is negligible.

This also implies that the flow is conservative with no mechanism for changing the internal energy e (assuming that the fluid ejected from the nozzle and the quiescent fluid are the same fluid at the same temperature). Therefore, e is a constant and, for a constant density fluid,

$$\frac{\partial}{\partial t}\int_{\Omega} \rho e \, d\Omega = \rho e \frac{\partial}{\partial t}\int_{\Omega} d\Omega = 0. \tag{D.14}$$

Since e is a constant state variable, its value is arbitrary. For simplicity, it will be taken to be zero. Then equation (D.13) becomes

$$\frac{\partial E}{\partial t} = \frac{\rho}{2}\int_{A} u_J^3(r, t)\, dS + \int_{A} [p(r, t) - p_\infty] u_J(r, t)\, dS \tag{D.15}$$

where

$$E \equiv \frac{\rho}{2}\int_{\Omega} u^2 d\Omega \tag{D.16}$$

is the (kinetic) energy of the flow. Integrating with respect to time gives

$$E(t) = E_U(t) + E_p(t) \tag{D.17}$$

where

$$E_U(t) \equiv \frac{\rho}{2}\int_0^t \int_A u_J^3(r, \tau)\, dS d\tau \tag{D.18}$$

and

$$E_p(t) \equiv \int_0^t \int_A [p(r,t) - p_\infty] u_J(r,t)\, dS d\tau . \tag{D.19}$$

Equation (D.17) is referred to here as the generalized energy equation for slug flow and gives the amount of energy added to the flow by the piston-cylinder mechanism. Equation (D.18) indicates the amount of energy added due to the flux of kinetic energy through the nozzle and is called the "kinetic energy term." Equation (D.19) gives the amount of energy added due to the work done on the fluid by the nozzle (over)pressure and is called the "pressure work term."

D.3 Derivation of the Equation for Total Circulation

The equation for circulation in slug flow concerns the rate of change of circulation in the fluid external to the piston-cylinder mechanism (which is typically assumed to roll up into a vortex ring). From Stokes' Theorem,

$$\Gamma \equiv \oint_C \mathbf{u} \cdot d\mathbf{s} = \int_S \omega \cdot \hat{\mathbf{n}} dS \tag{D.20}$$

where S is an open surface in 3D space, C is its bounding curve, $\hat{\mathbf{n}}$ is the unit normal to the surface, and $d\mathbf{s}$ is a length element oriented tangent to C. This relation indicates that it is an *area* integral of the flow external to the nozzle that is of interest for determining the circulation injected into the flow. An appropriate control surface for the integration is a flat surface that intersects the axis of symmetry of the nozzle and extends over all $r > 0$ and

$x > 0$, as shown in Figure D.2. The goal then is to determine $\frac{\partial \Gamma}{\partial t}$ for this surface, which will be pursued by first deriving two general equations for $\frac{\partial}{\partial t}\int_S \omega \cdot \hat{\mathbf{n}} dS$ where S is arbitrary.

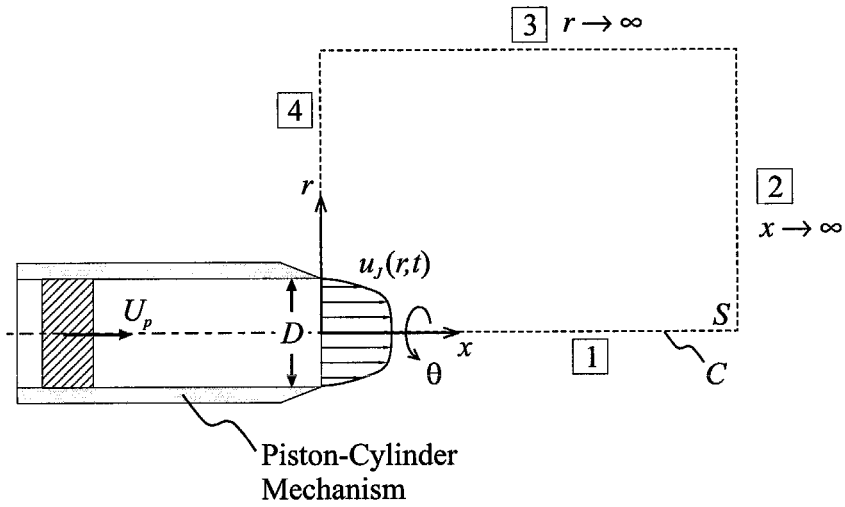

FIGURE D.2 A Surface *S* and Bounding Contour *C* for Determining the Rate at Which Circulation is Injected into the Fluid by a Piston Cylinder Mechanism.

D.3.1 General Equations for the Rate of Change of Vorticity in an Open Surface

The governing equations for this flow are the continuity and momentum equations for an incompressible, Newtonian flow:

$$\nabla \bullet \mathbf{u} = 0 \tag{D.21}$$

and

$$\frac{D\mathbf{u}}{Dt} = -\frac{\nabla p}{\rho} + \nu \nabla^2 \mathbf{u} \tag{D.22}$$

where the effect of gravity has been ignored and it is implicitly assumed that the static pressure field p_h has been subtracted from p so that $p \to 0$ as $|\mathbf{x}| \to \infty$. The curl of the momentum equation then leads to the vorticity transport equation, namely,

$$\frac{\partial \omega}{\partial t} + \nabla \times (\omega \times \mathbf{u}) = \nu \nabla^2 \omega . \tag{D.23}$$

Using the vector identity

$$\nabla^2 \mathbf{a} = \nabla(\nabla \bullet \mathbf{a}) - \nabla \times (\nabla \times \mathbf{a}) , \tag{D.24}$$

the vorticity transport and momentum equations can be written as

$$\frac{\partial \omega}{\partial t} + \nabla \times (\omega \times \mathbf{u}) = -\nu \nabla \times (\nabla \times \omega) \tag{D.25}$$

and

$$\frac{D\mathbf{u}}{Dt} + \frac{\nabla p}{\rho} = -\nu \nabla \times \omega \tag{D.26}$$

respectively. Integrating equation (D.25) over a general surface S (not necessarily the one shown in Figure D.2) with bounding contour C and applying Stokes' Theorem gives

$$\frac{\partial}{\partial t} \int_S \omega \cdot \hat{\mathbf{n}} \, dS = -\oint_C (\omega \times \mathbf{u} + \nu \nabla \times \omega) \cdot d\mathbf{s} . \tag{D.27}$$

Substituting equation (D.26) into this result yields

$$\frac{\partial}{\partial t} \int_S \omega \cdot \hat{\mathbf{n}} \, dS = -\oint_C \left[\omega \times \mathbf{u} - \left(\frac{D\mathbf{u}}{Dt} + \frac{\nabla p}{\rho} \right) \right] \cdot d\mathbf{s} . \tag{D.28}$$

Equations (D.27) and (D.28) allow determination of the rate of change of circulation in an open area using flow quantities on the perimeter of the area. The $\omega \times \mathbf{u}$ term represents a flux of (pre-existing) vorticity across C, but the $\frac{D\mathbf{u}}{Dt}$ and $\frac{\nabla p}{\rho}$ terms are vorticity "sources."

D.3.2 Applying the General Equations to the Slug-Flow Example

Equations (D.27) and (D.28) are now applied to the special case depicted in Figure D.2. From the results of Cantwell [8], the terms in the contour integrals (for either equation) decay like $|\mathbf{x}|^{-n}$, $n > 2$, for large $|\mathbf{x}|$. The contribution from the integral along paths 2 and 3 are therefore zero. Along 1, equation (D.27) gives the contribution to the contour integral as

$$\int_1 (\ldots) = -\int_0^\infty \frac{1}{r}\frac{\partial(r\omega_\theta)}{\partial r}\bigg|_{r\to 0} dx \tag{D.29}$$

since the flux term is zero along $r = 0$ due to axisymmetry. The integrand in this expression, however, is related to the diffusion of vorticity across the center line since

$$[\nabla^2\omega]_\theta\big|_{r\to 0} = \left[\frac{\partial}{\partial r}\left(\frac{1}{r}\frac{\partial(r\omega_\theta)}{\partial r}\right) + \frac{\partial^2\omega_\theta}{\partial x^2}\right]\bigg|_{r\to 0} = \frac{\partial}{\partial r}\left(\frac{1}{r}\frac{\partial(r\omega_\theta)}{\partial r}\right)\bigg|_{r\to 0} \tag{D.30}$$

for this axisymmetric case. If the duration of the starting jet is sufficiently short (e.g., low L/D or high Reynolds number), this term has a negligible effect (as noted by Didden

[10]). The integral along 1 is therefore negligible and the time rate of change of vorticity in the fluid for $x > 0$ is completely determined by the integral along 4.

Integrating the right-hand side of equation (D.28) along 4 and identifying the area integral of ω with Γ in accordance with equation (D.20) gives

$$\frac{\partial \Gamma}{\partial t} = \int_0^{\infty} \left(\omega_\theta u - \left(\frac{\partial v}{\partial t} + \frac{1}{2}\frac{\partial v^2}{\partial r} + u\frac{\partial v}{\partial x} + \frac{1}{\rho}\frac{\partial p}{\partial r} \right) \right) \Bigg|_{x=0} dr . \tag{D.31}$$

This result can be simplified by noting that $u = 0$ at $r \to \infty$, $v = 0$ at $r = 0$ (axisymmetry) and $r \to \infty$, and by making the substitution $\omega_\theta = \frac{\partial v}{\partial x} - \frac{\partial u}{\partial r}$. After integrating the terms that are perfect differentials and recasting pressure in terms of absolute pressure (i.e., $p \to p - p_h$), equation (D.31) reduces to

$$\frac{\partial \Gamma}{\partial t} = \frac{1}{2}u_{cl}^2(t) + \frac{1}{\rho}[p_{cl}(t) - p_\infty] - \frac{\partial}{\partial t}\int_0^{\infty} v|_{x=0} dr \tag{D.32}$$

where u_{cl} and p_{cl} are the velocity and absolute pressure (respectively) at $x = 0$, $r = 0$. The last term in this expression has no significance since $v = 0$ initially and after the piston motion is completed (i.e., after the ejected fluid has convected downstream), making its time integral over the duration of the piston motion zero. Since it has no *net* effect on Γ, it will be ignored, giving

$$\Gamma(t) = \frac{1}{2}\int_0^t u_{cl}^2(\tau) d\tau + \frac{1}{\rho}\int_0^t [p_{cl}(\tau) - p_\infty] d\tau \equiv \Gamma_U(t) + \Gamma_p(t) . \tag{D.33}$$

This expression is referred to here as the generalized equation for total circulation with the associated velocity (Γ_U) and pressure (Γ_p) terms as in the previous sections. Note that this

result makes no assumptions about the nature of the flow through the nozzle (i.e., no parallel flow assumption) or the flow outside the nozzle.

APPENDIX E

Additional Figures of Fully-Pulsed Jet Results

E.1 Thrust Measurements

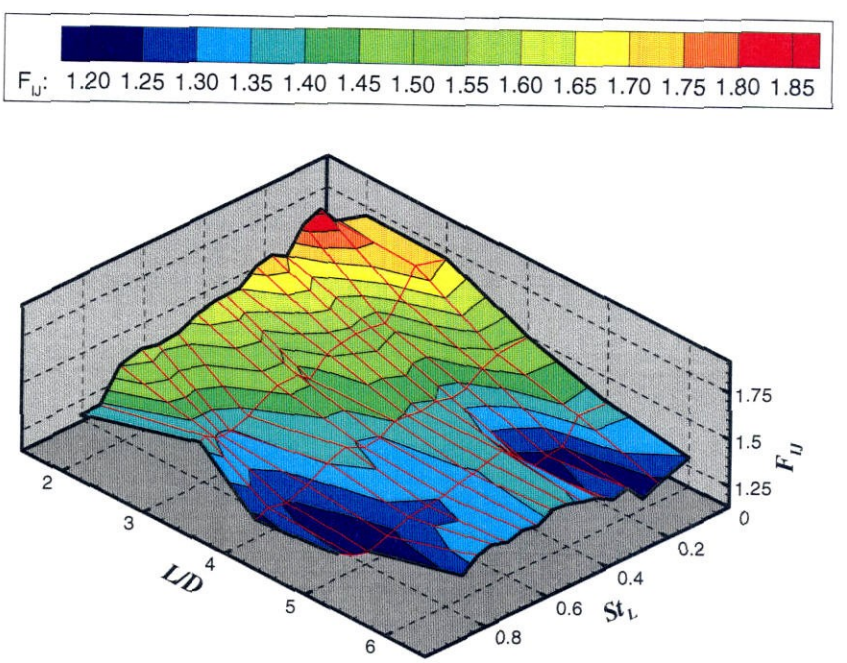

FIGURE E.1 F_{IJ} Results for the NS Ramps.

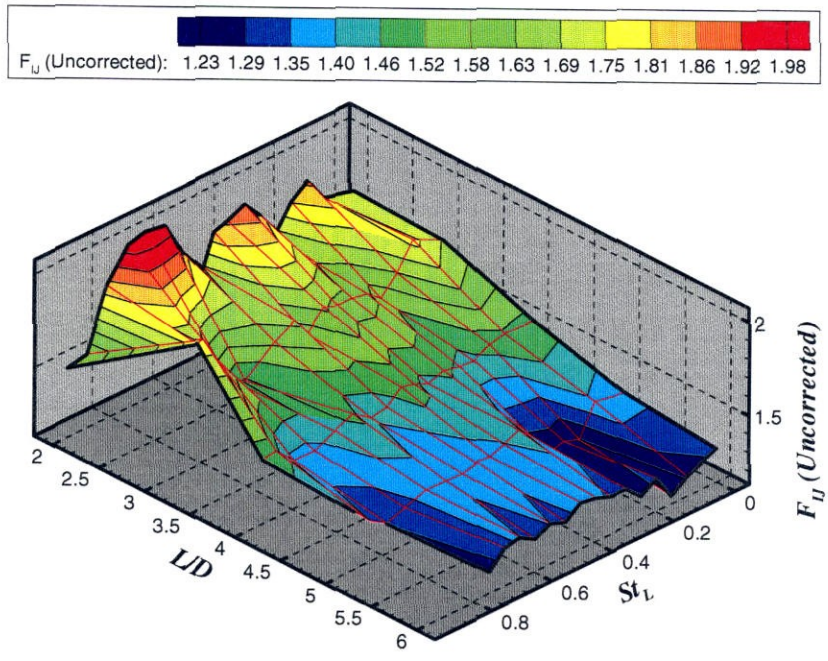

FIGURE E.2 Uncorrected F_{IJ} Results (Using a Constant I_U) for the NS Ramps.

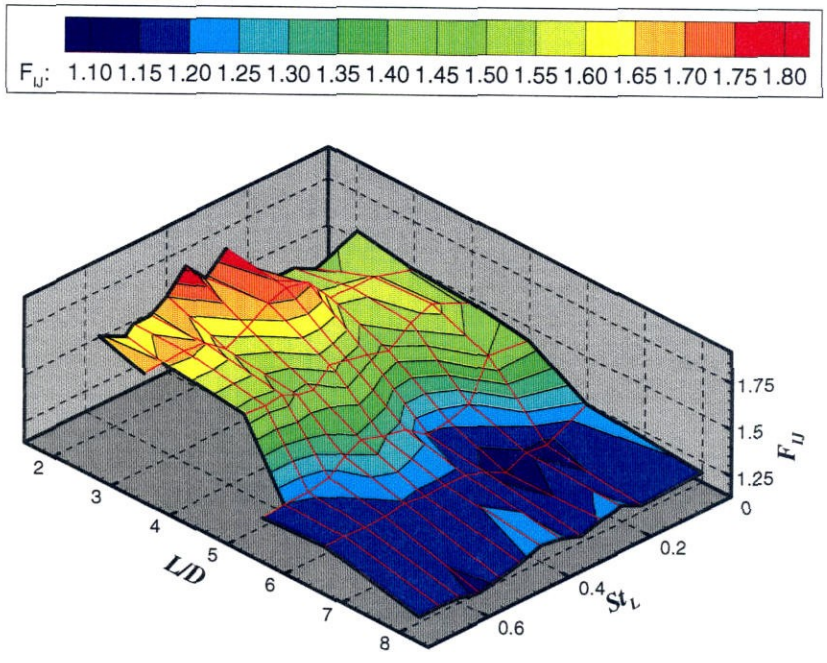

FIGURE E.3 F_{IJ} Results for the PS Ramps.

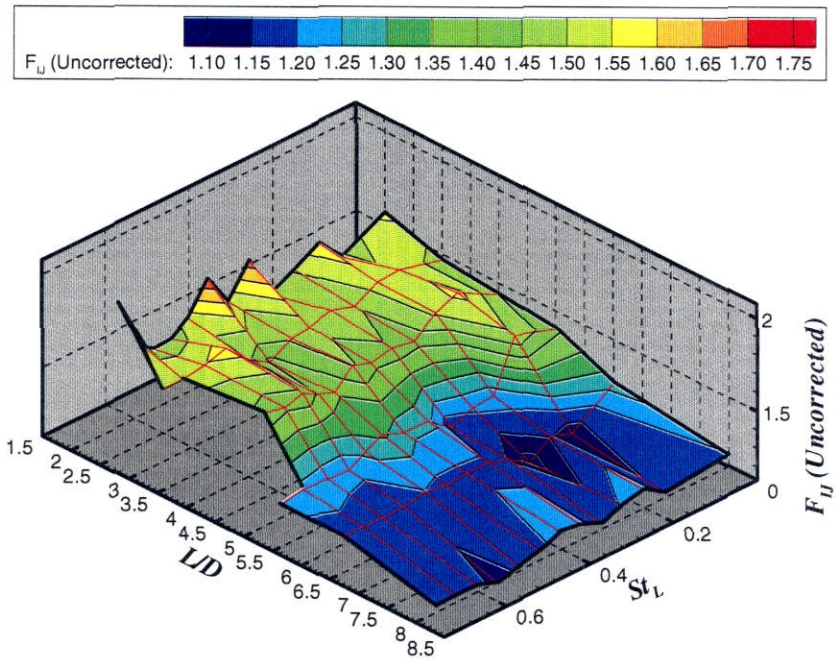

FIGURE E.4 Uncorrected F_{IJ} Results (Using a Constant I_U) for the PS Ramps.

Note: For a fully pulsed jet, the average thrust during a pulse is defined as $\bar{F}_p \equiv \frac{T}{t_p}\bar{F}_T$.

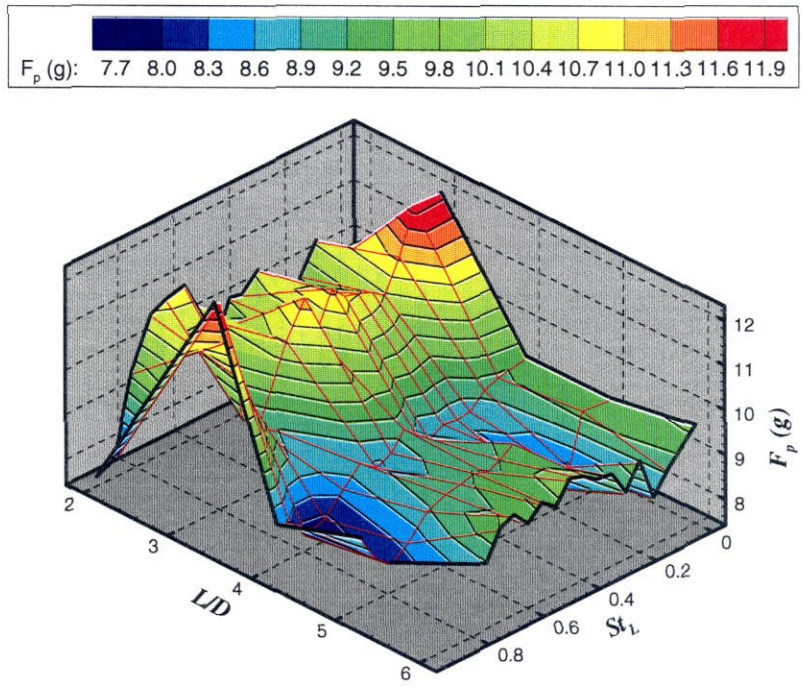

FIGURE E.5 Average Thrust During a Pulse for the NS Ramps.

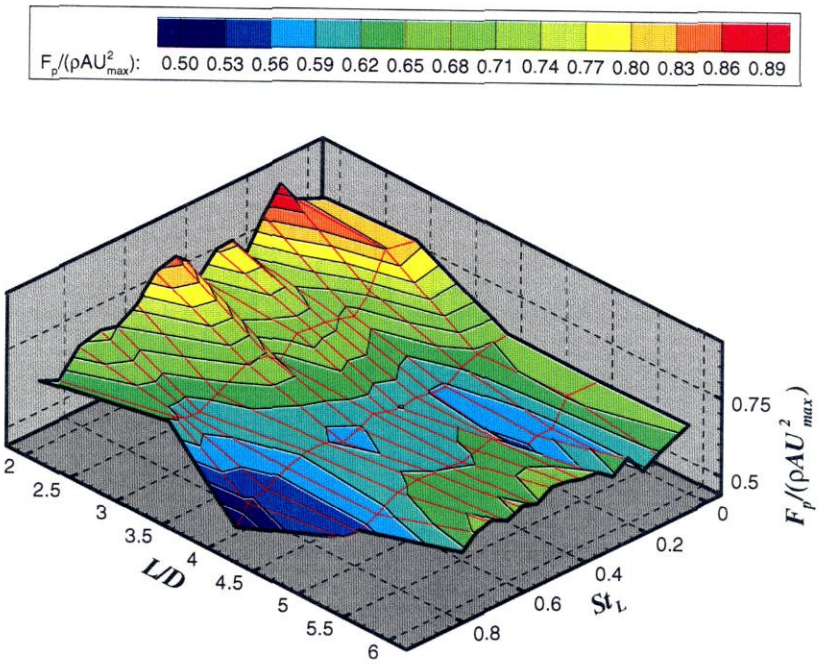

FIGURE E.6 Non-Dimensional Average Thrust During a Pulse for the NS Ramps.

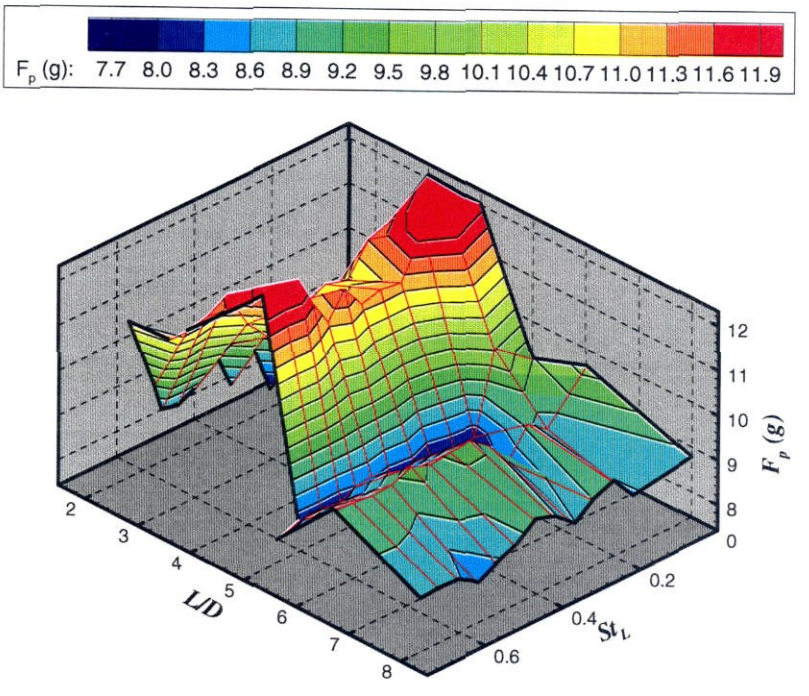

FIGURE E.7 Average Thrust During a Pulse for the PS Ramps.

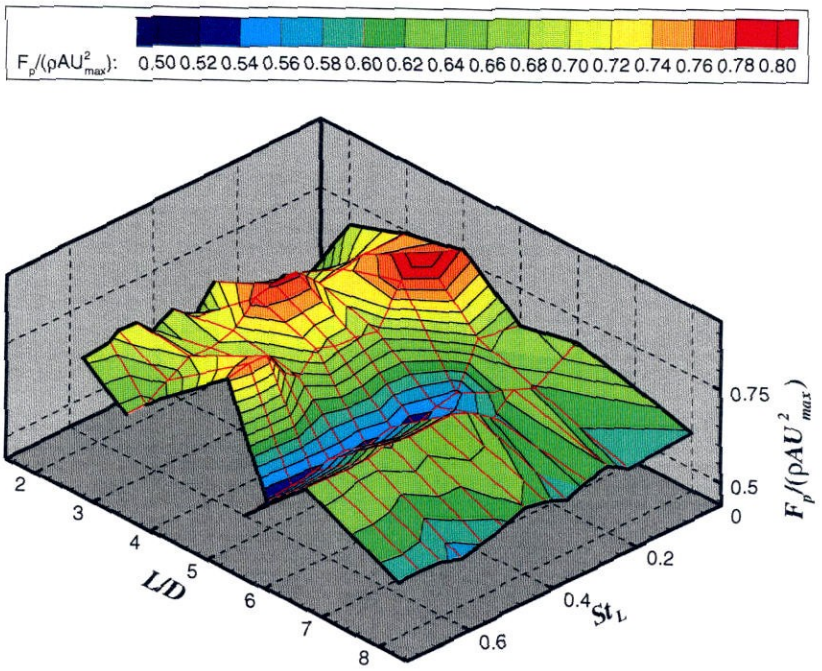

FIGURE E.8 Non-Dimensional Average Thrust During a Pulse for the PS Ramps.

E.2 Evolution of Circulation with Down-Stream Distance

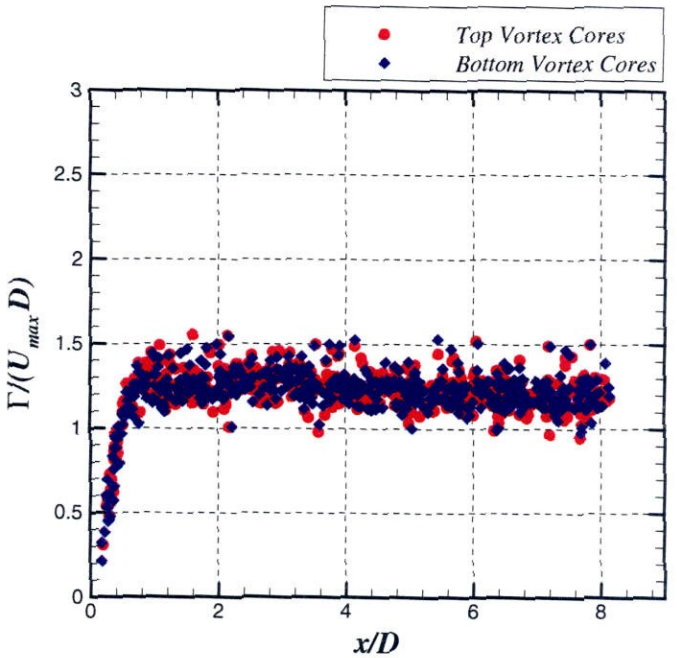

(a) $St_L = 0.13$

FIGURE E.9 Evolution of Circulation for *L/D* = 2.0, NS2 Ramps.

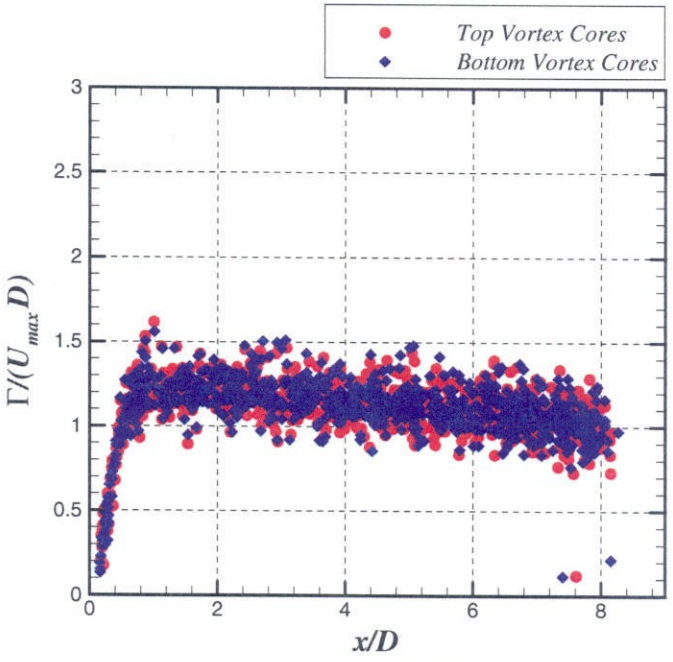

(b) $St_L = 0.25$

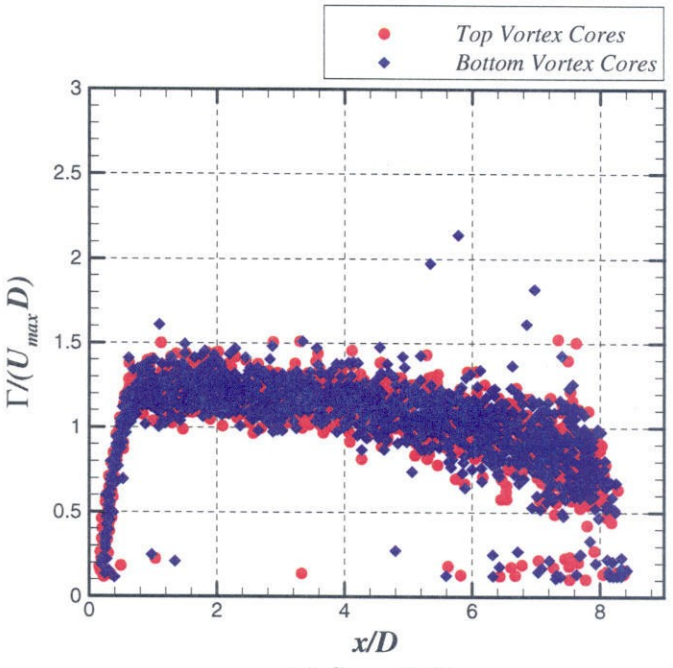

(c) $St_L = 0.54$

Figure E.9 Continued.

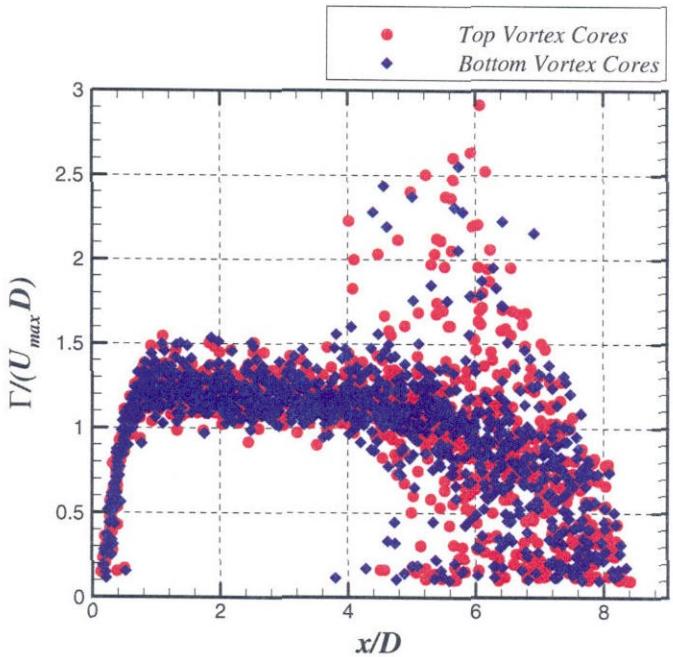

(d) $St_L = 0.82$

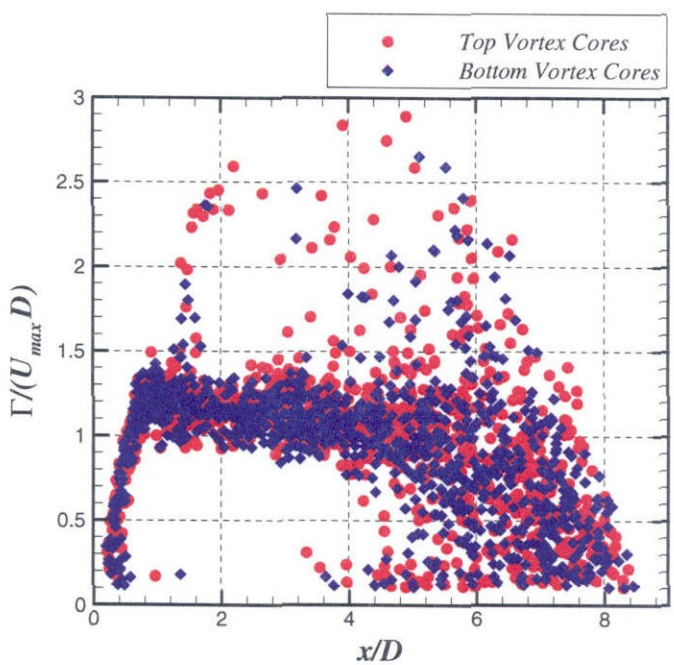

(e) $St_L = 0.96$

Figure E.9 Continued.

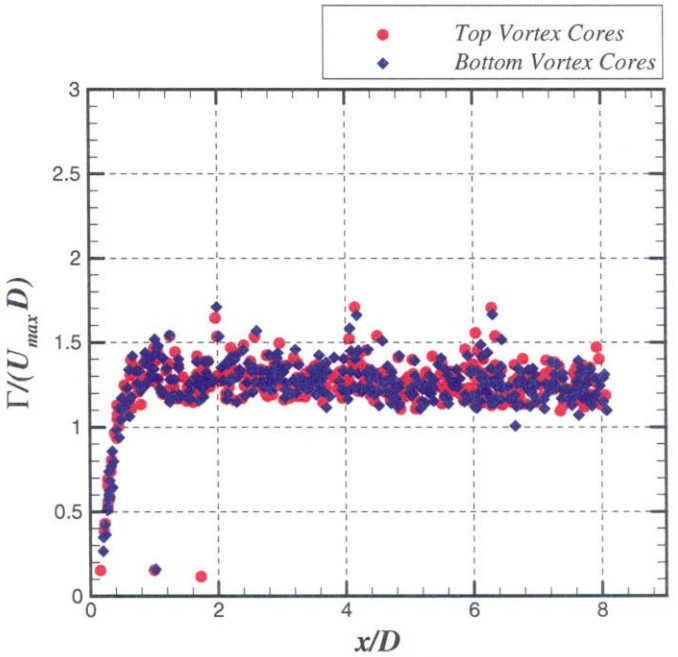

(a) $St_L = 0.11$

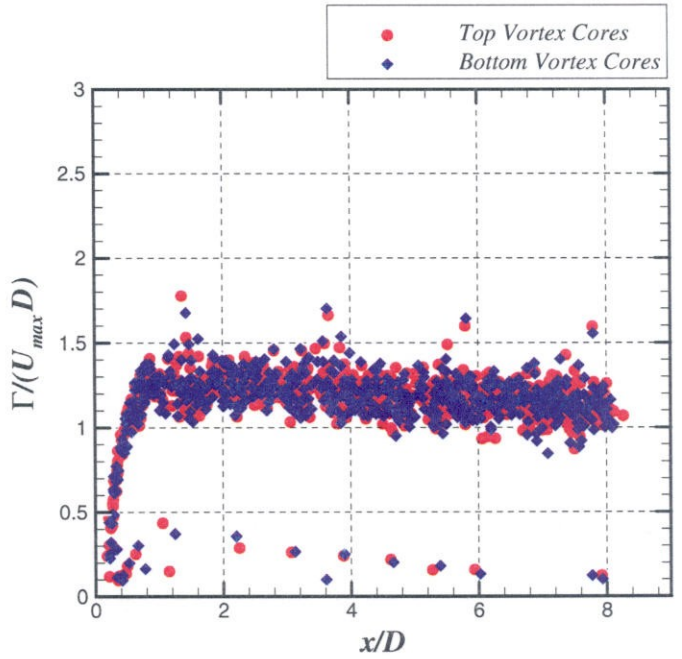

(b) $St_L = 0.18$

FIGURE E.10 Evolution of Circulation for L/D = 2.3, NS2 Ramps.

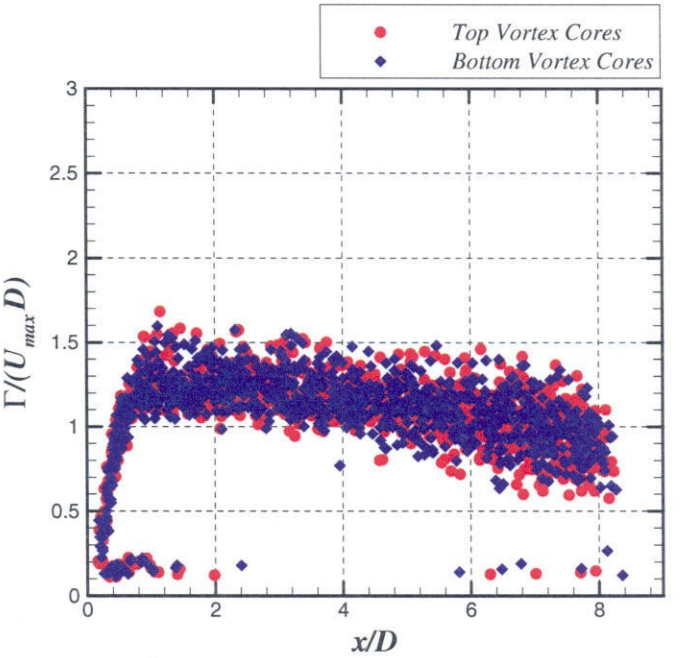

(c) $St_L = 0.29$

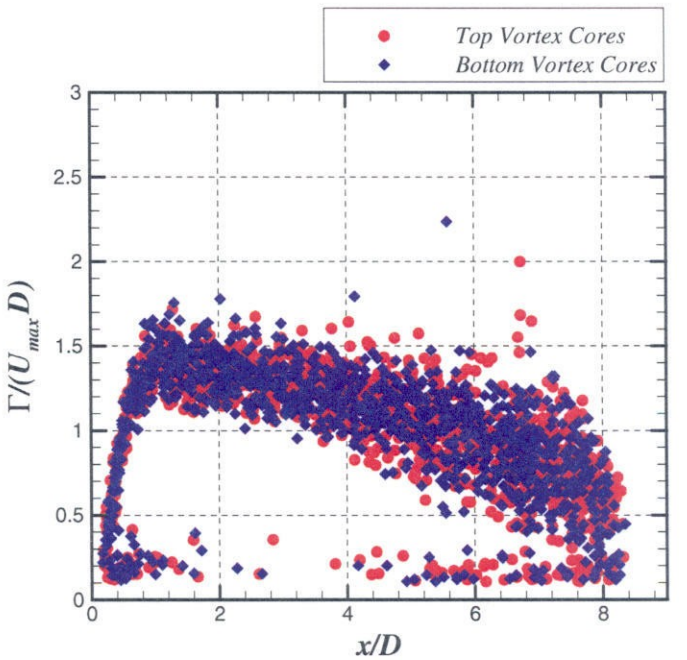

(d) $St_L = 0.57$

Figure E.10 Continued.

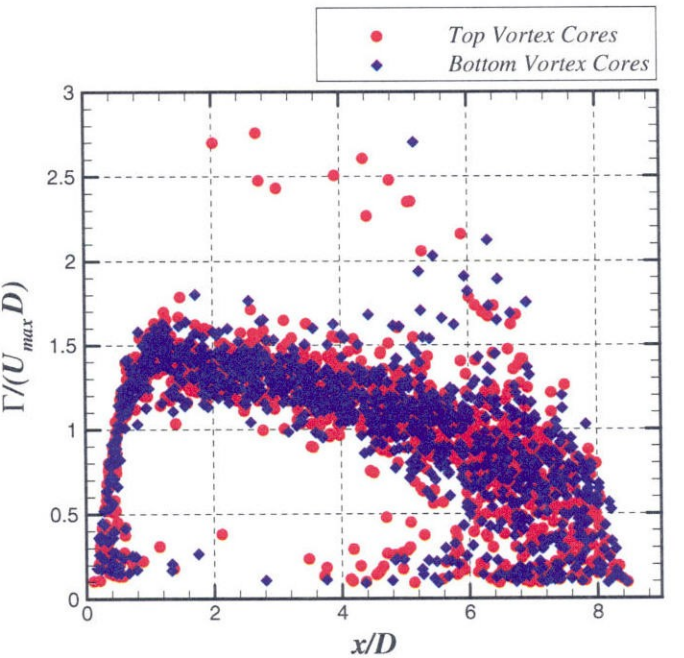

(e) $St_L = 0.82$

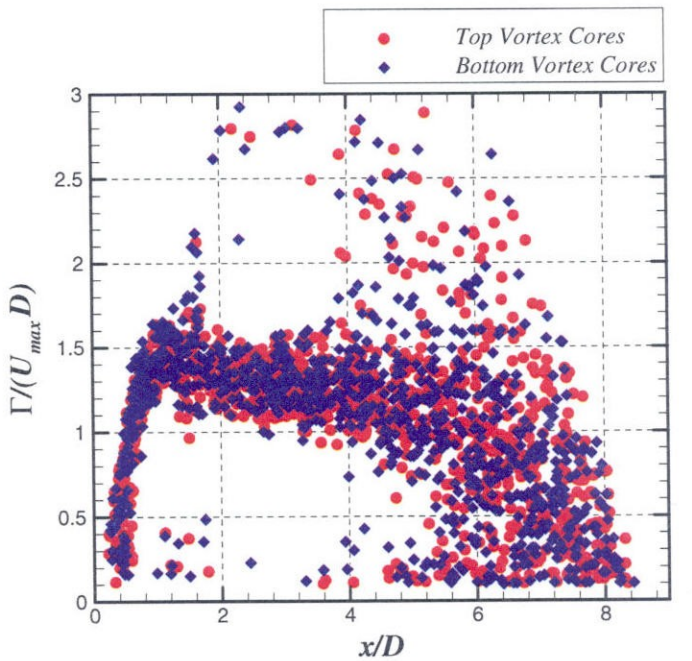

(f) $St_L = 0.97$

Figure E.10 Continued.

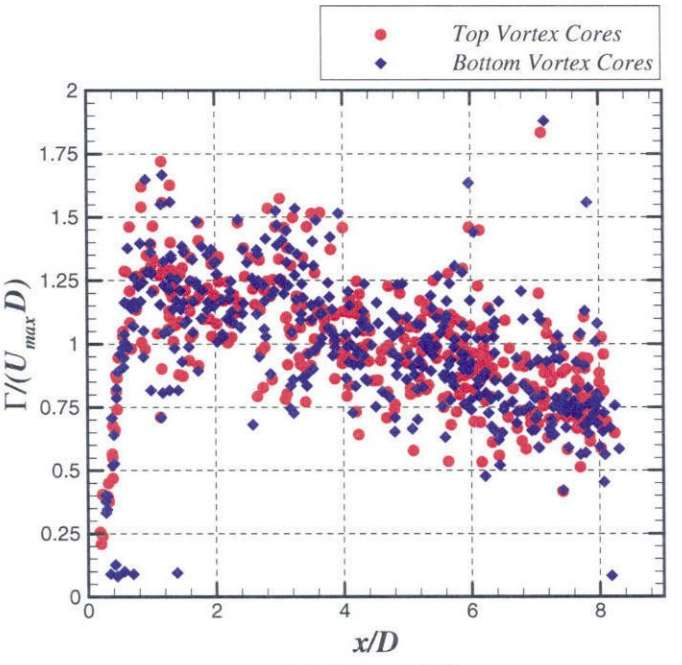

(a) $St_L = 0.26$

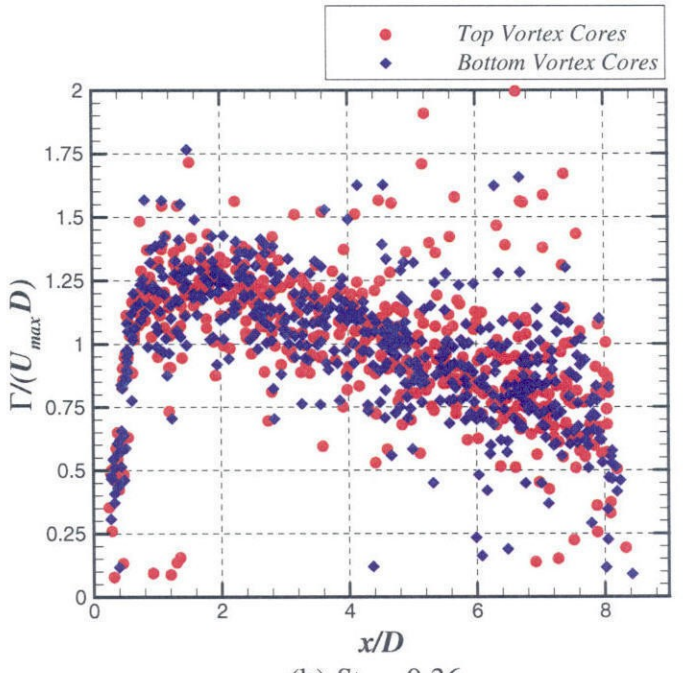

(b) $St_L = 0.36$

FIGURE E.11 Evolution of Circulation for L/D = 2.0, NS Ramps.

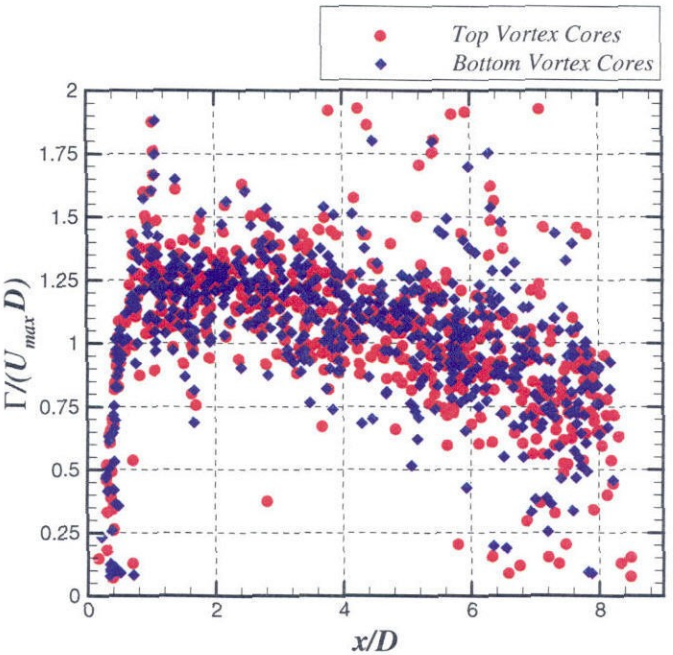

(c) $St_L = 0.46$

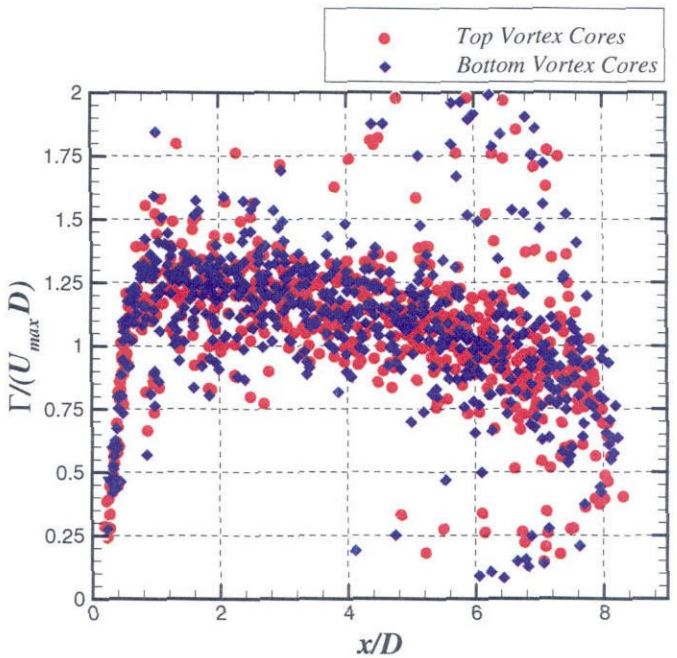

(d) $St_L = 0.50$

Figure E.11 Continued.

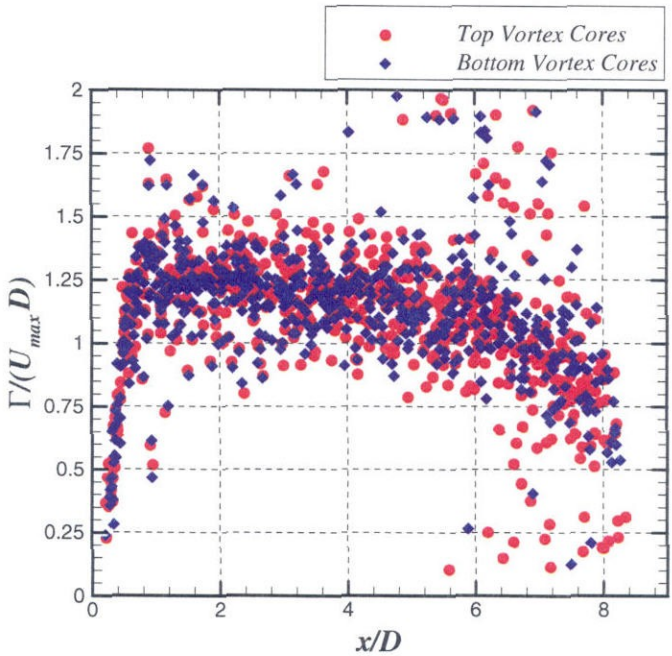

(e) $St_L = 0.56$

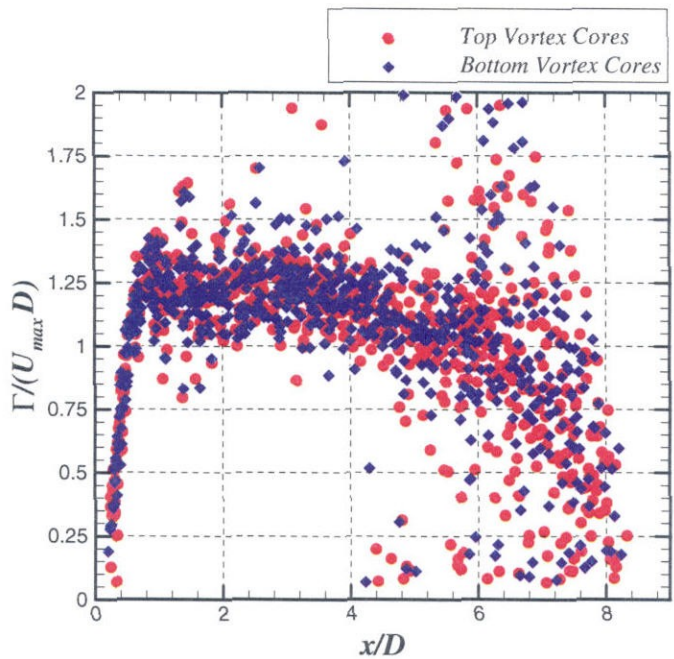

(f) $St_L = 0.69$

Figure E.11 Continued.

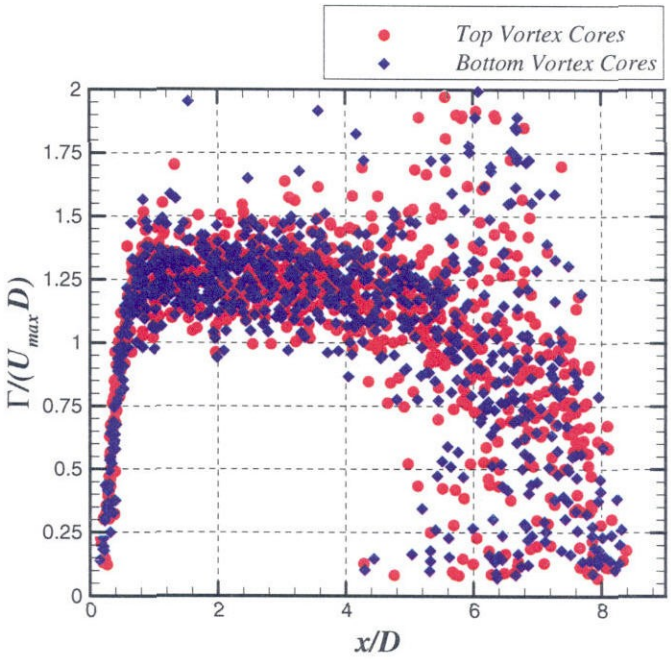

(g) $St_L = 0.85$

Figure E.11 Continued.

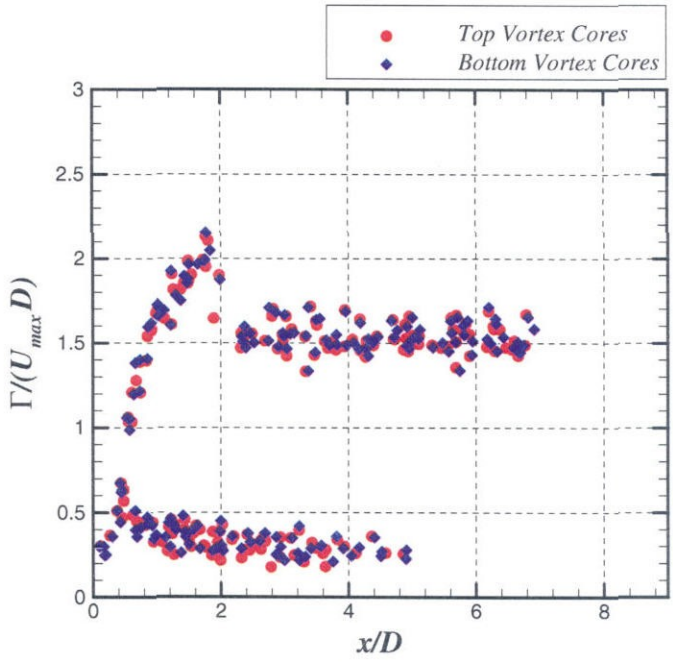

(a) $St_L = 0.06$

FIGURE E.12 Evolution of Circulation for L/D = 4.0, NS Ramps.

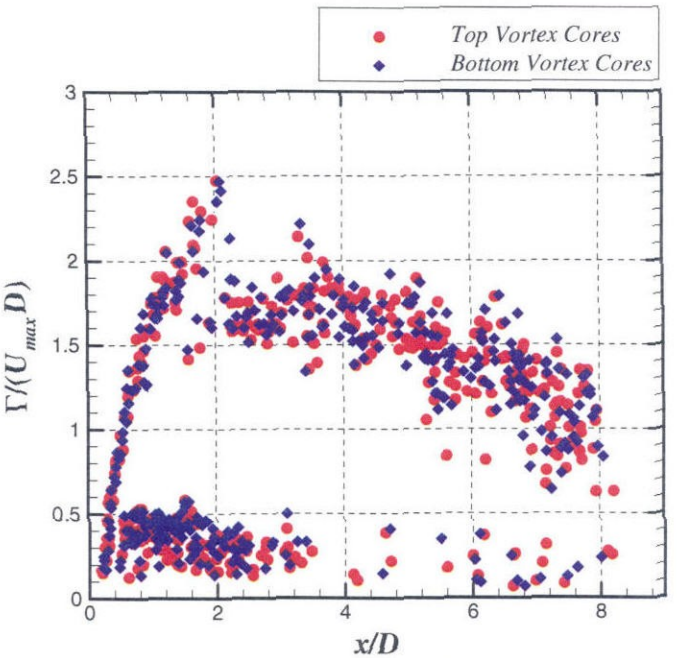

(b) $St_L = 0.42$

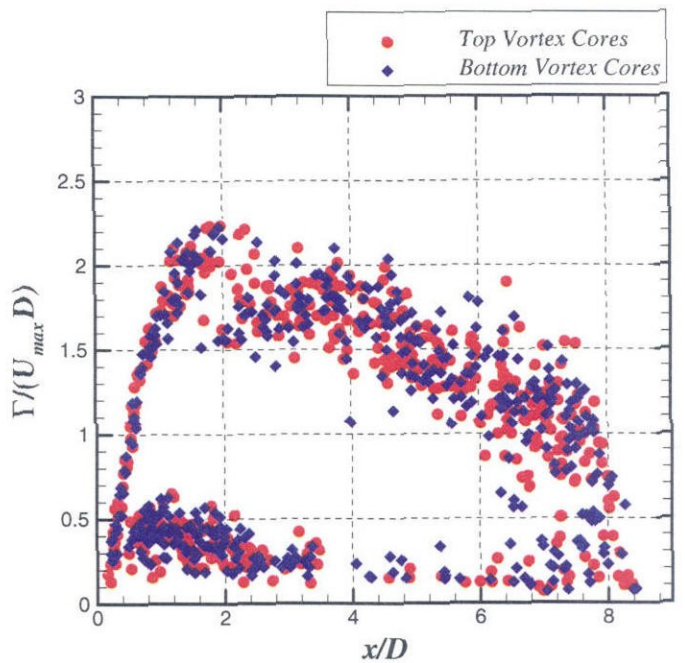

(c) $St_L = 0.51$

Figure E.12 Continued.

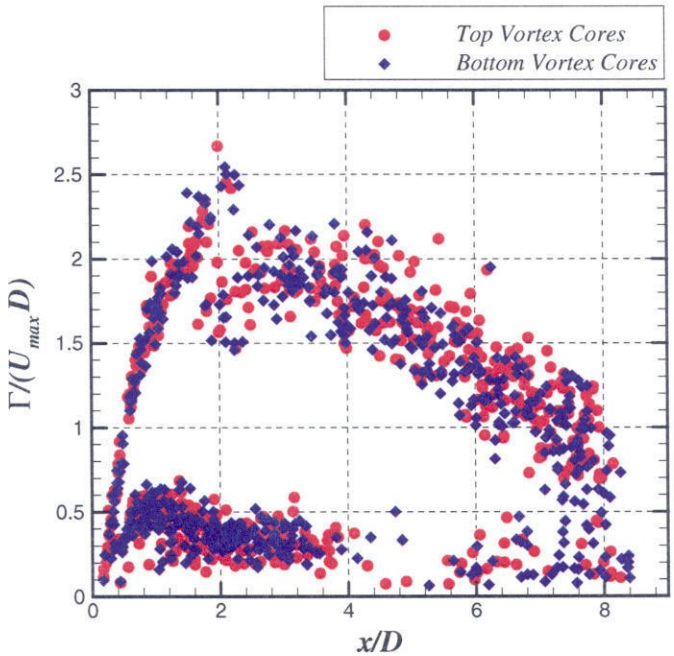

(d) $St_L = 0.60$

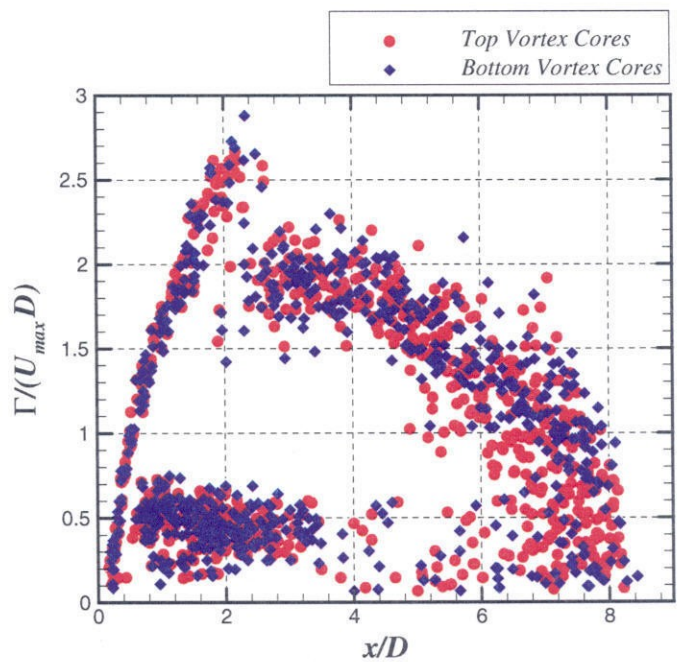

(e) $St_L = 0.76$

Figure E.12 Continued.

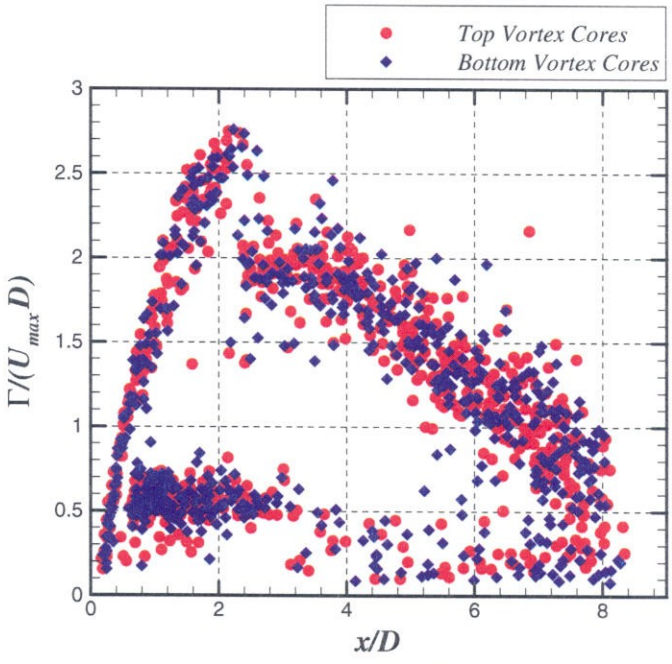

(f) $St_L = 0.87$

Figure E.12 Continued.

E.3 Evolution of Vorticity Centroid Positions

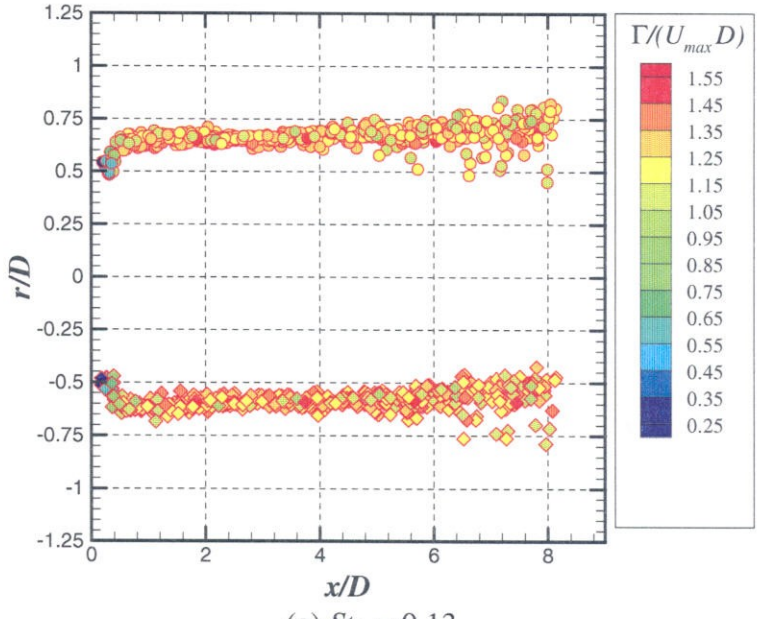

(a) $St_L = 0.13$

FIGURE E.13 Evolution of Vorticity Centroid Positions for L/D = 2.0, NS2 Ramps.

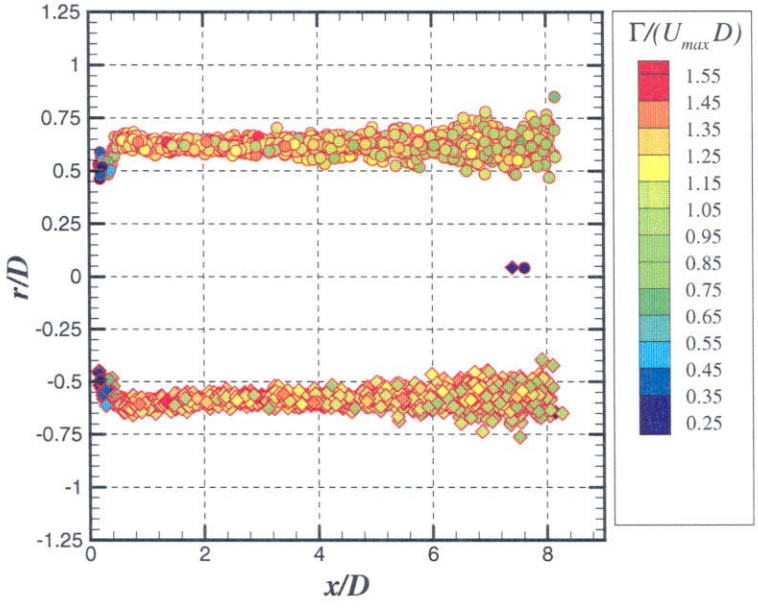

(b) $St_L = 0.25$

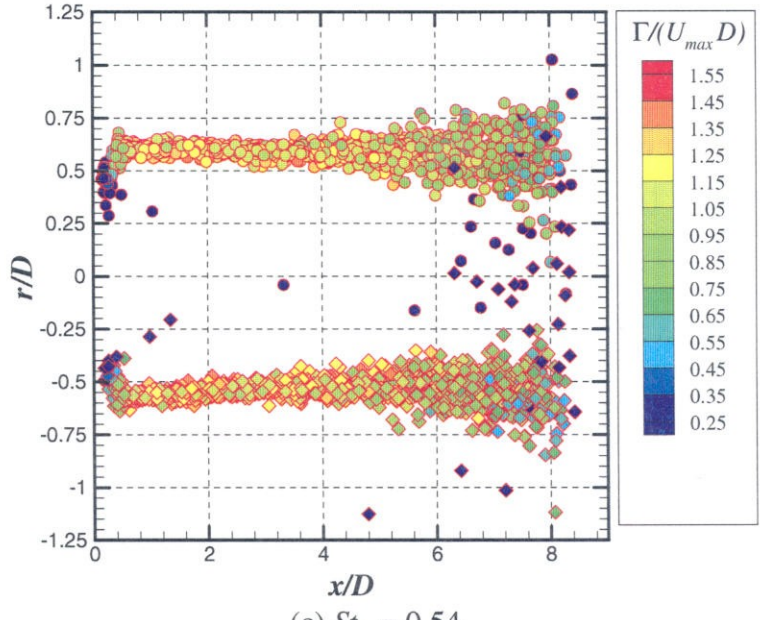

(c) $St_L = 0.54$

Figure E.13 Continued.

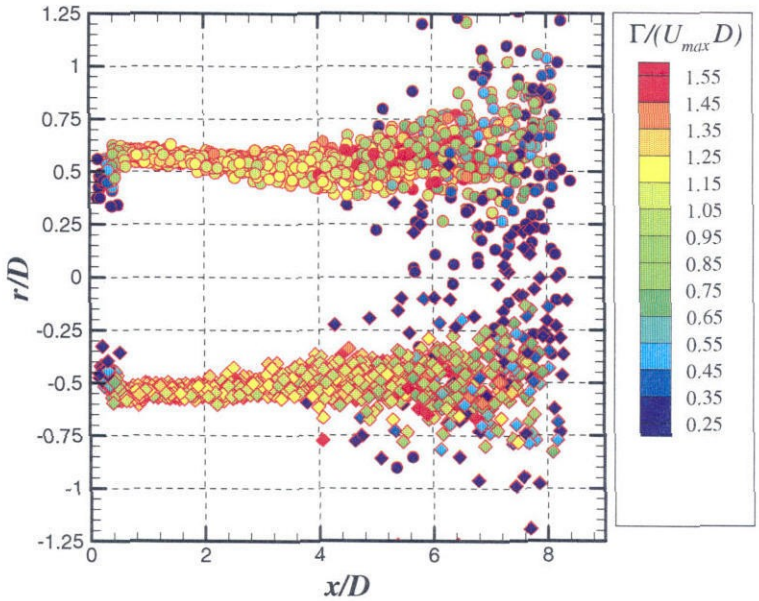

(d) $St_L = 0.82$

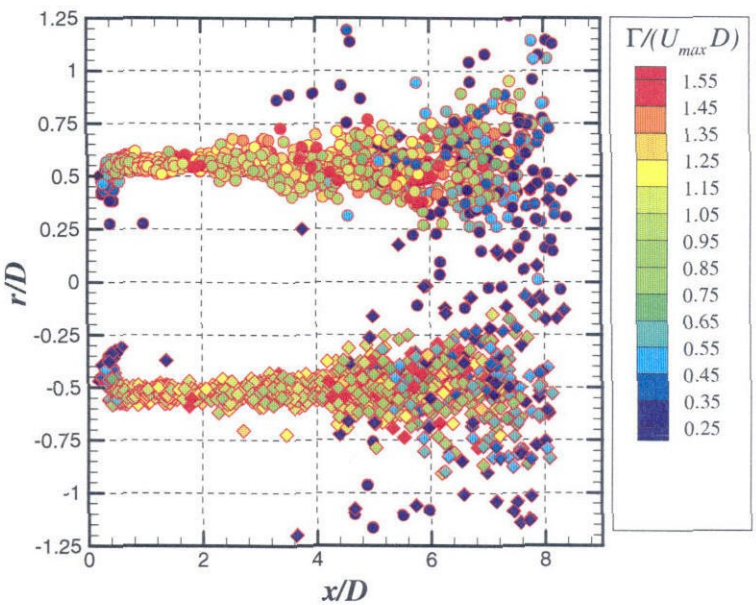

(e) $St_L = 0.96$

Figure E.13 Continued.

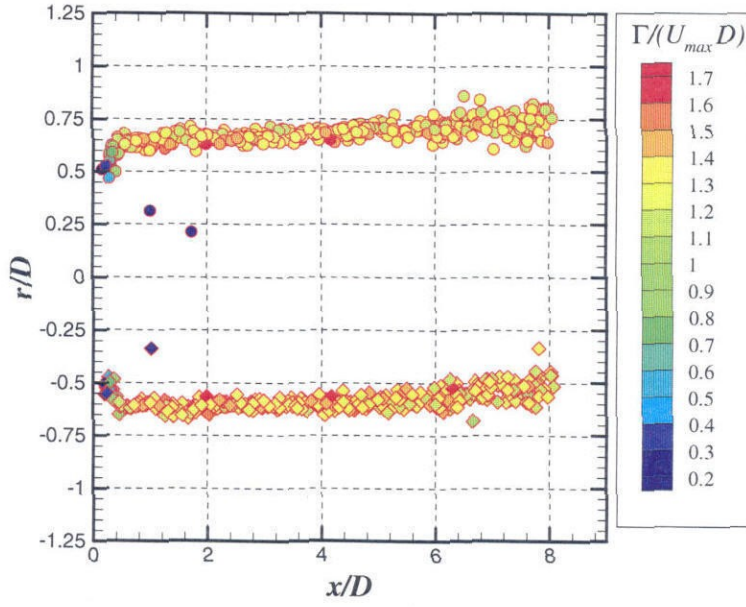

(a) $St_L = 0.11$

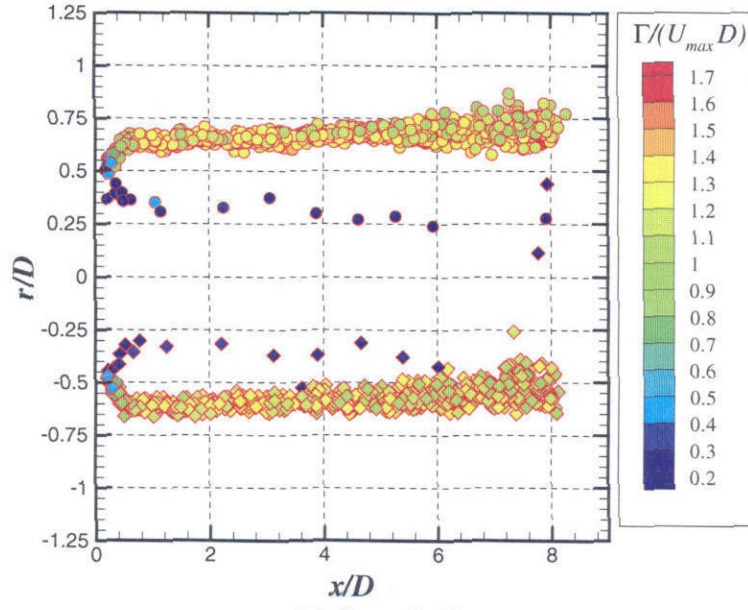

(b) $St_L = 0.18$

FIGURE E.14 Evolution of Vorticity Centroid Positions for L/D = 2.3, NS2 Ramps.

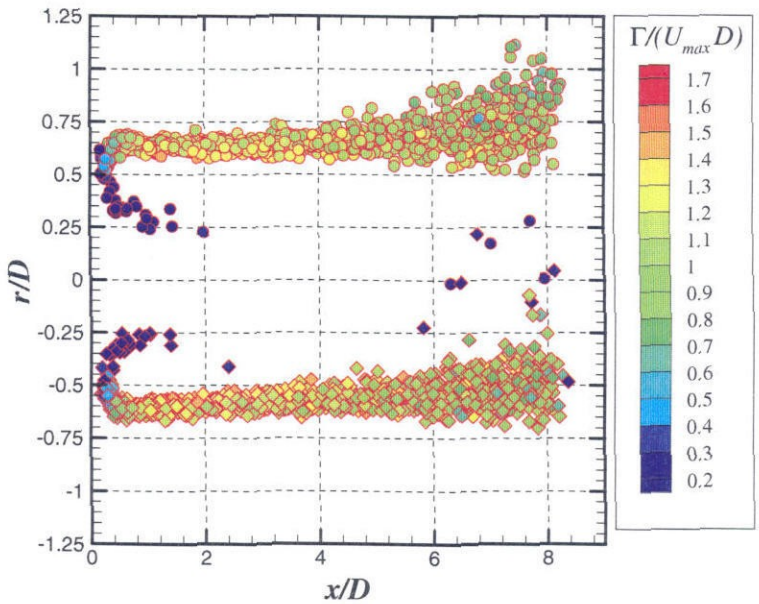

(c) $St_L = 0.29$

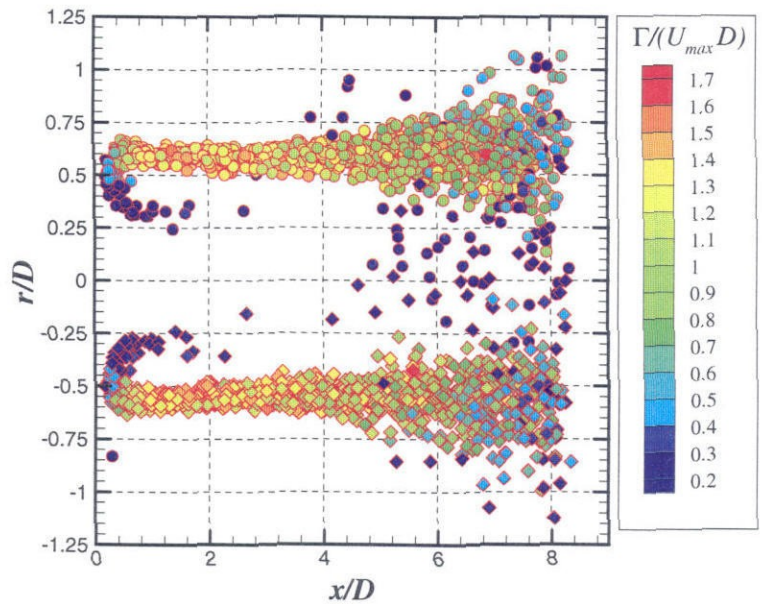

(d) $St_L = 0.57$

Figure E.14 Continued.

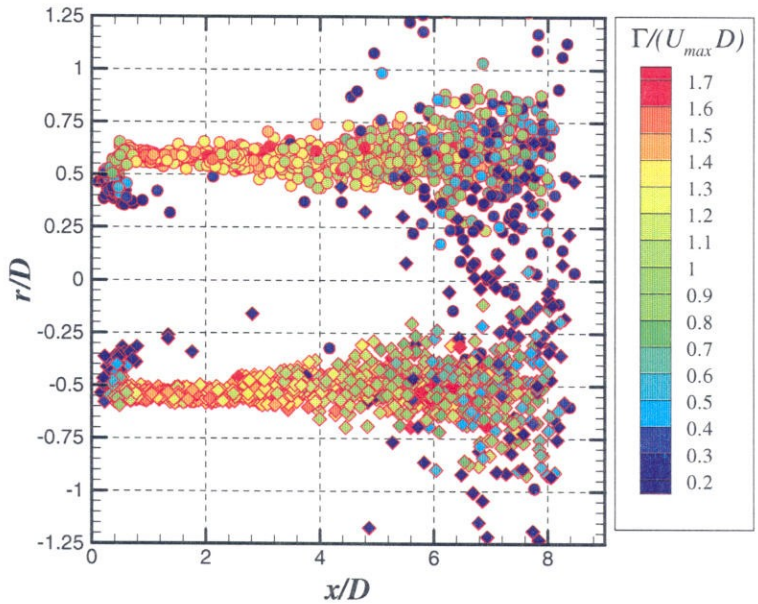

(e) $St_L = 0.82$

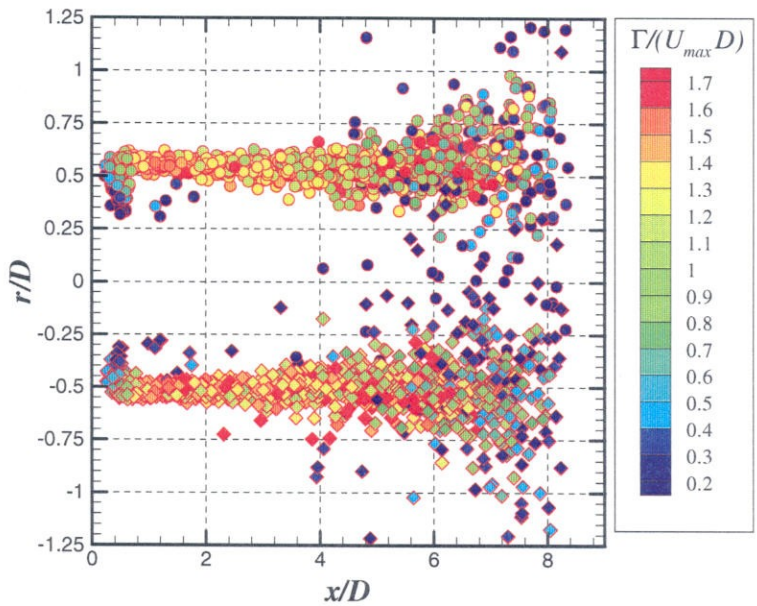

(f) $St_L = 0.97$

Figure E.14 Continued.

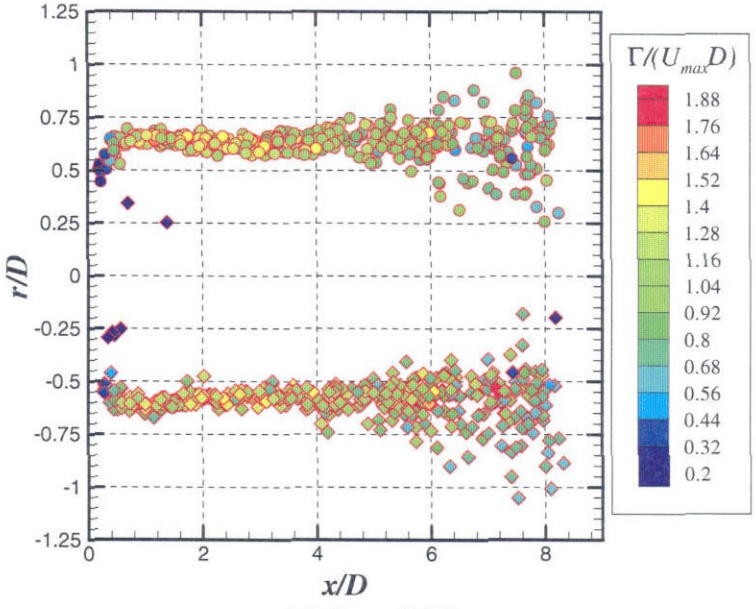

(a) $St_L = 0.26$

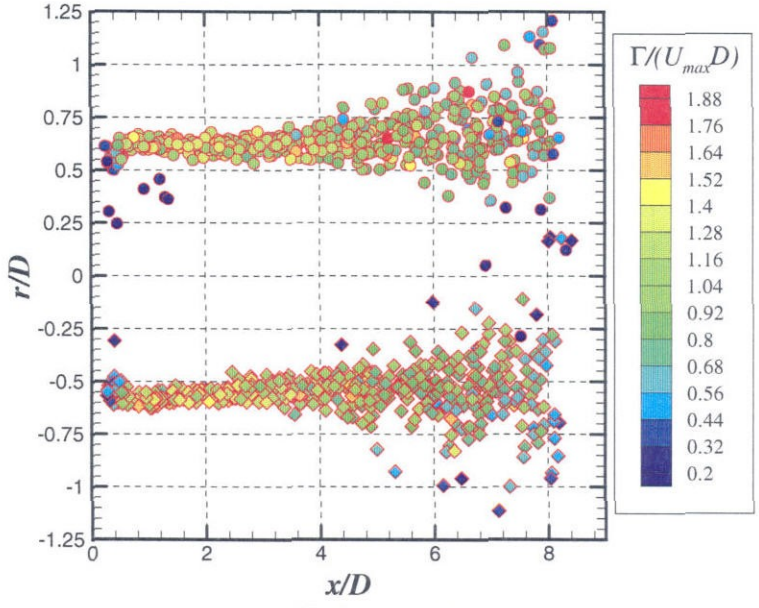

(b) $St_L = 0.36$

FIGURE E.15 Evolution of Vorticity Centroid Positions for L/D = 2.0, NS Ramps.

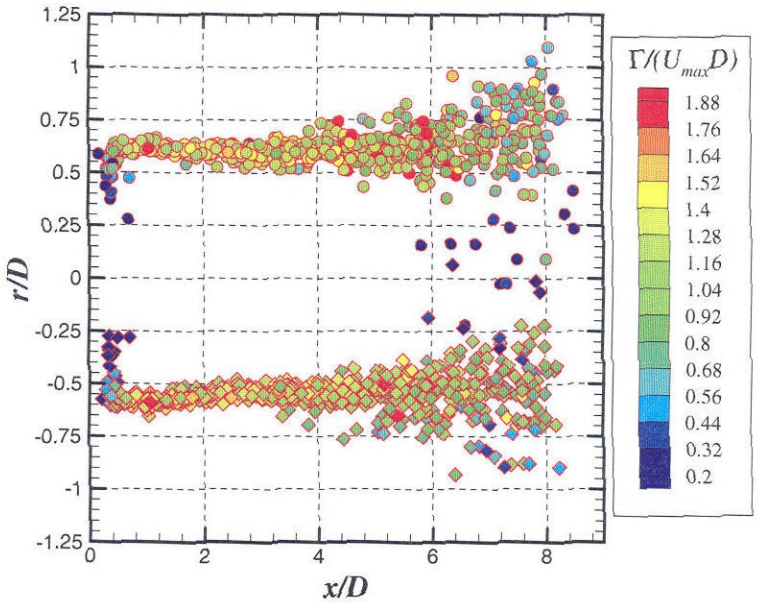

(c) $St_L = 0.46$

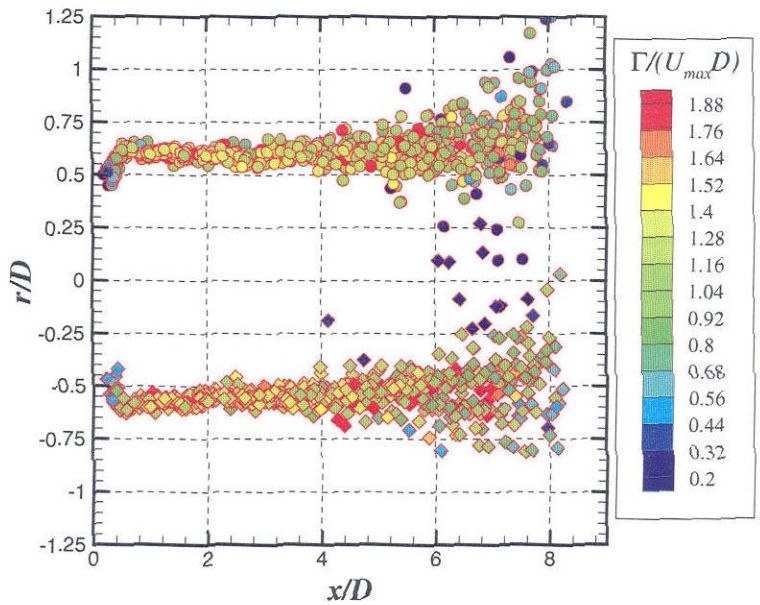

(d) $St_L = 0.50$

Figure E.15 Continued.

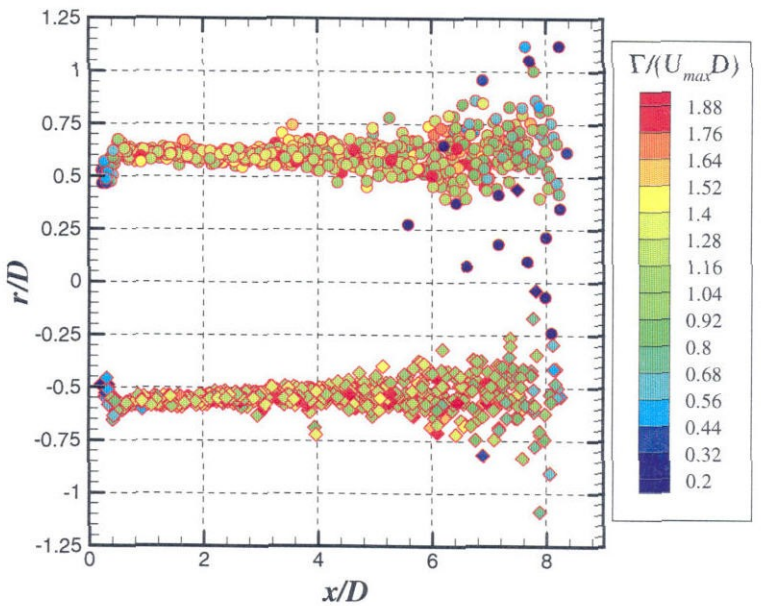

(e) $St_L = 0.56$

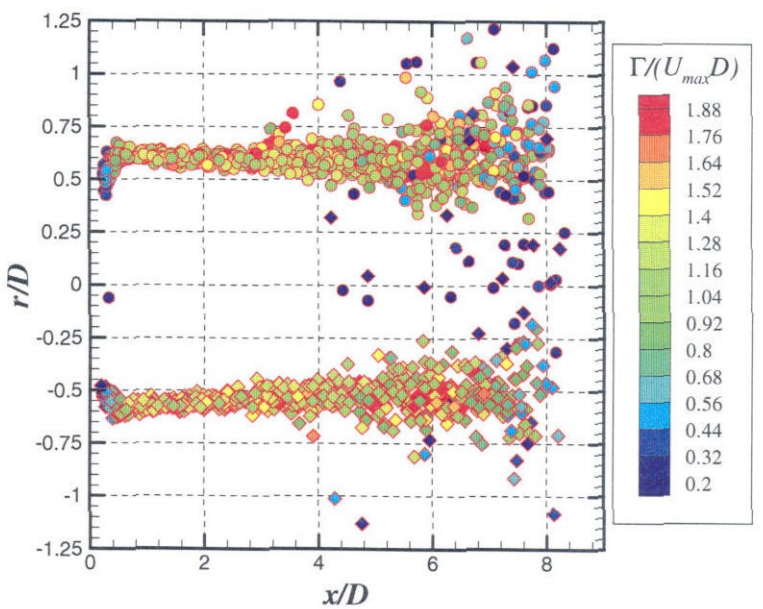

(f) $St_L = 0.69$

Figure E.15 Continued.

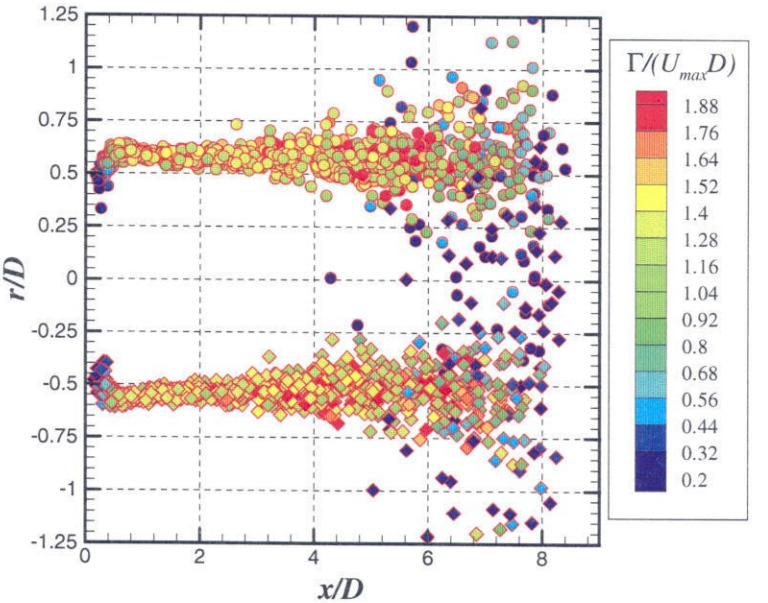

(g) $St_L = 0.85$

Figure E.15 Continued.

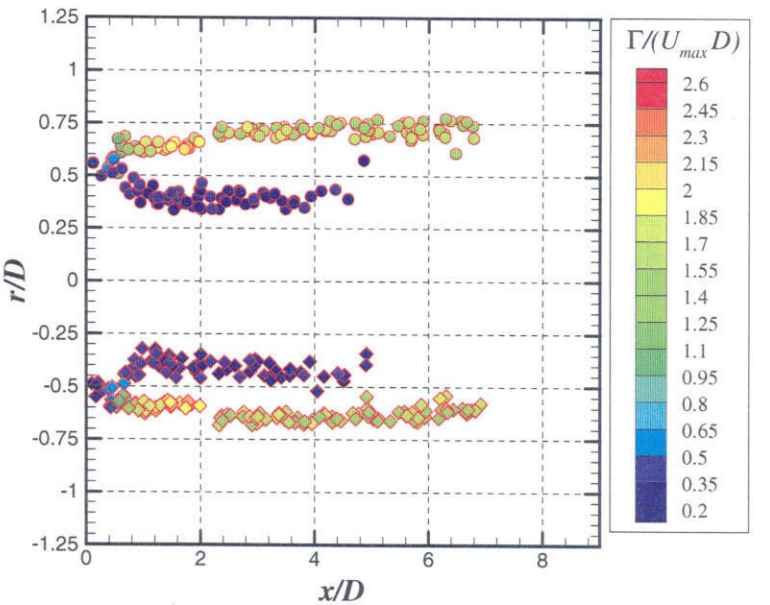

(a) $St_L = 0.06$

FIGURE E.16 Evolution of Vorticity Centroid Positions for L/D = 4.0, NS Ramps.

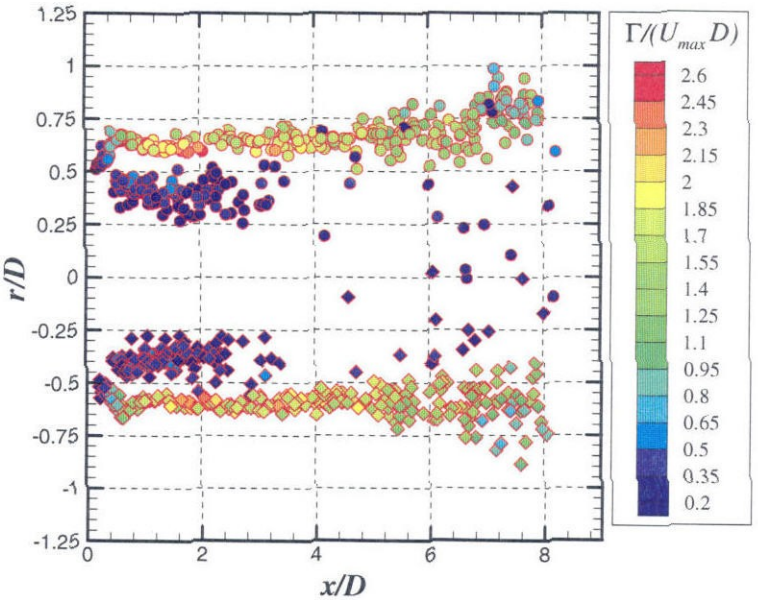

(b) $St_L = 0.42$

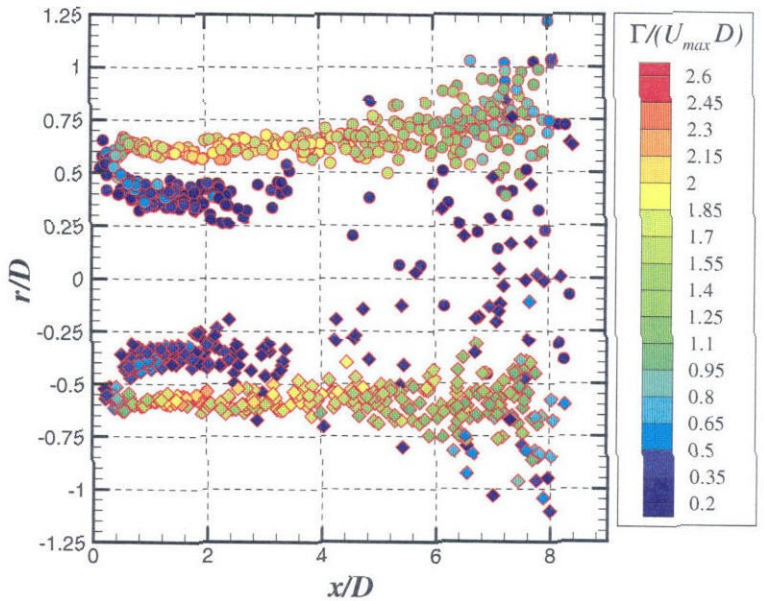

(c) $St_L = 0.51$

Figure E.16 Continued.

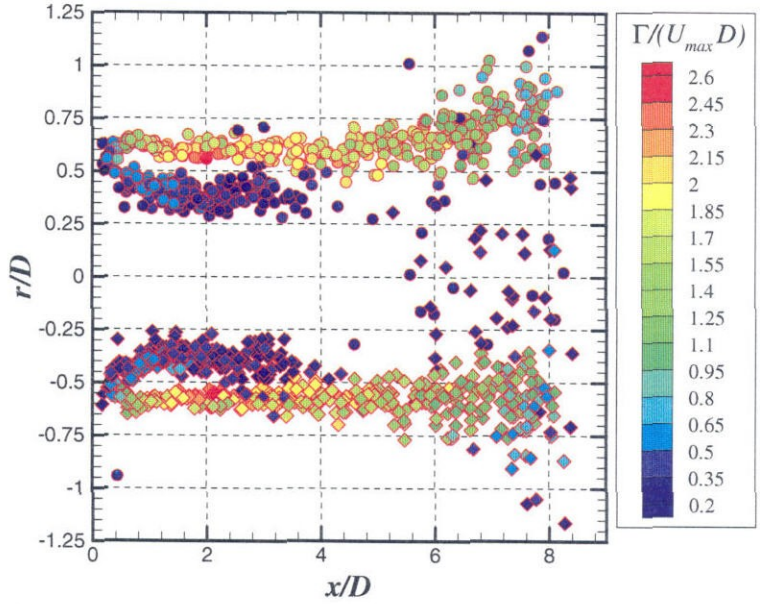

(d) $St_L = 0.60$

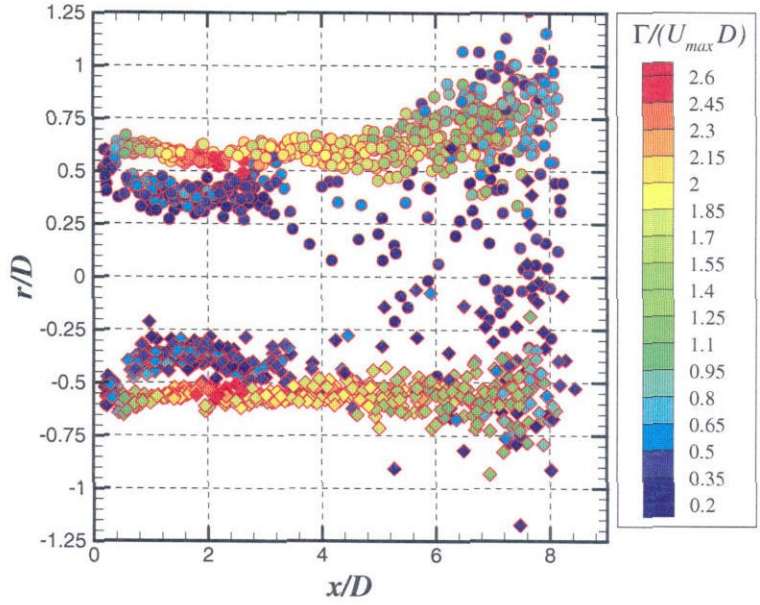

(e) $St_L = 0.76$

Figure E.16 Continued.

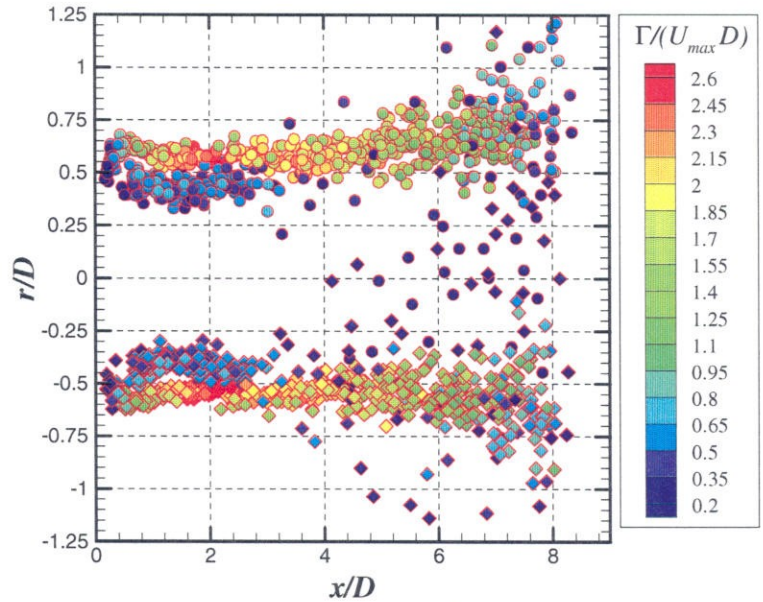

(f) $St_L = 0.87$

Figure E.16 Continued.

E.4 Evolution of Vorticity Peak Positions

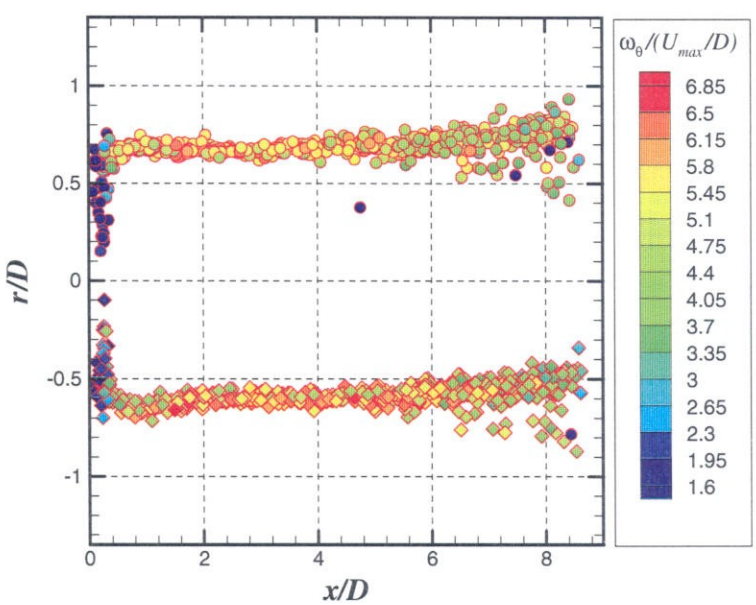

(a) $St_L = 0.13$

FIGURE E.17 Evolution of Vorticity Peak Positions for L/D = 2.0, NS2 Ramps.

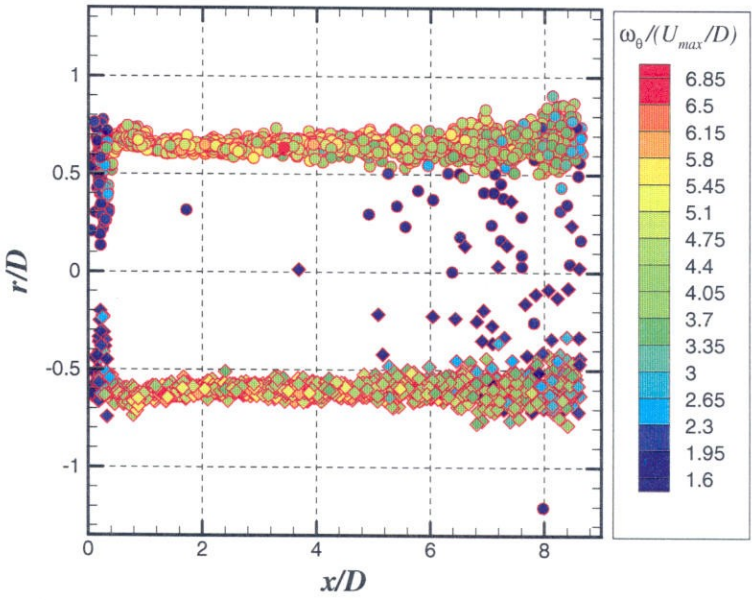

(b) $St_L = 0.25$

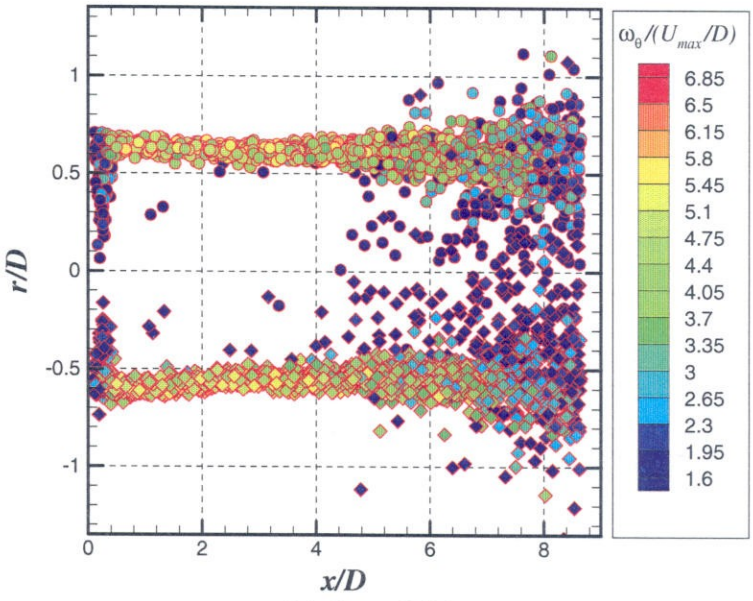

(c) $St_L = 0.54$

Figure E.17 Continued.

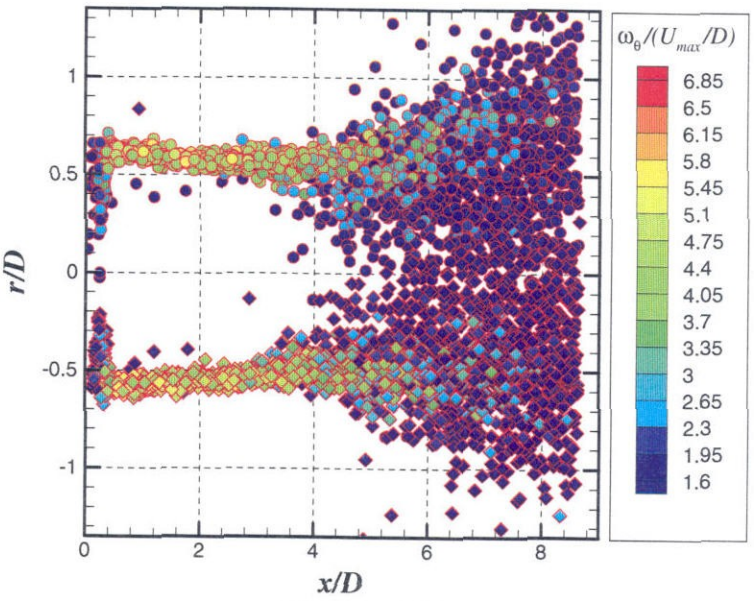

(d) $St_L = 0.82$

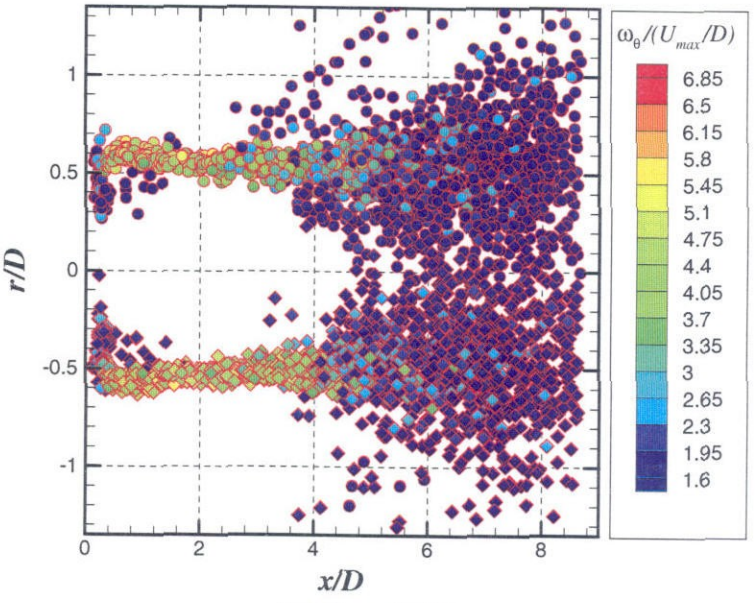

(e) $St_L = 0.96$

Figure E.17 Continued.

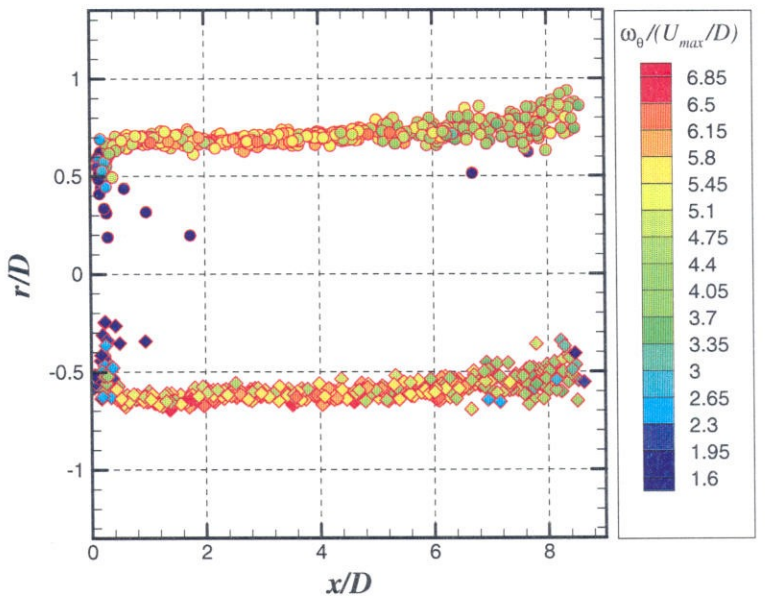

(a) $St_L = 0.11$

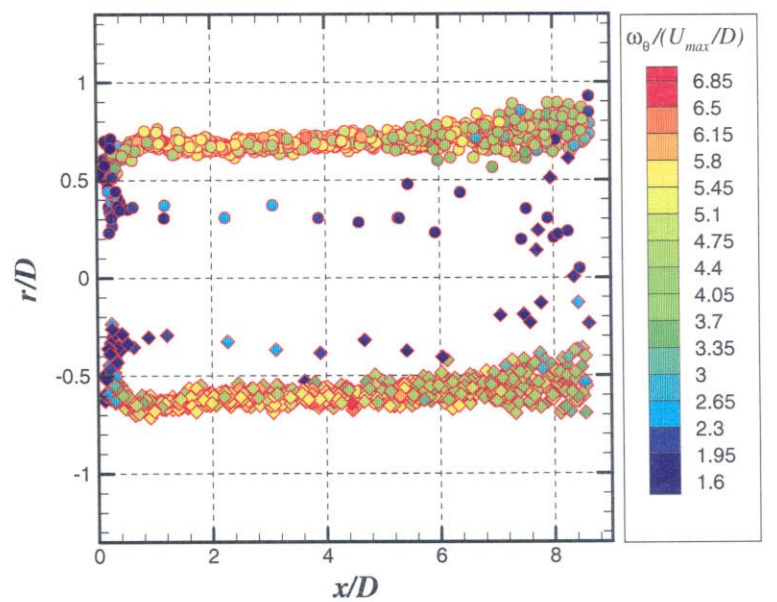

(b) $St_L = 0.18$

FIGURE E.18 Evolution of Vorticity Peak Positions for L/D = 2.3, NS2 Ramps.

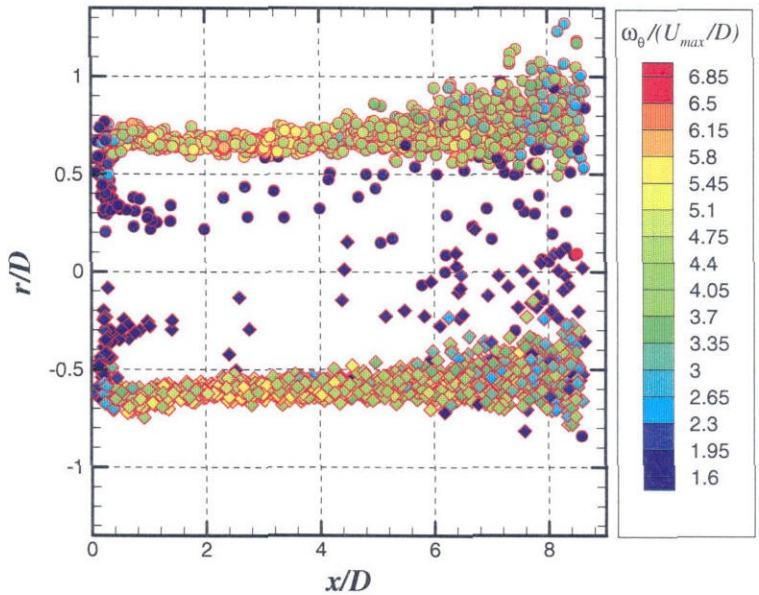

(c) $St_L = 0.29$

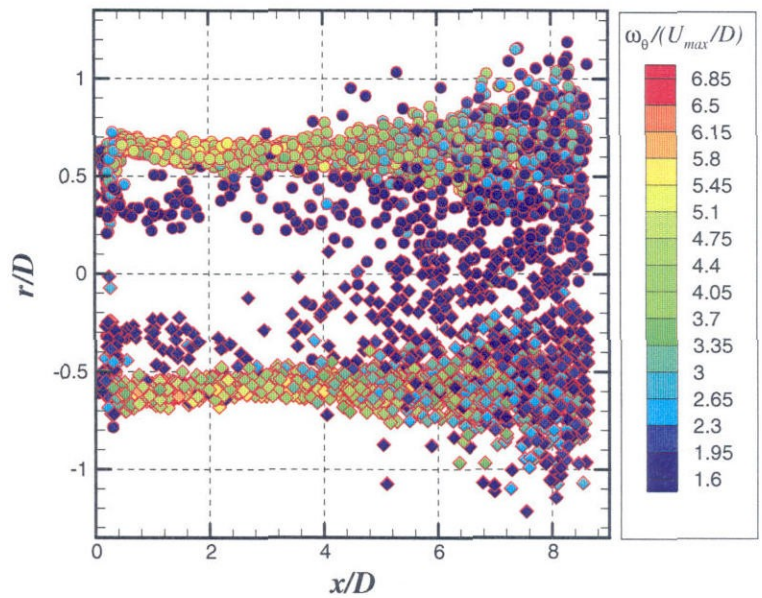

(d) $St_L = 0.57$

Figure E.18 Continued.

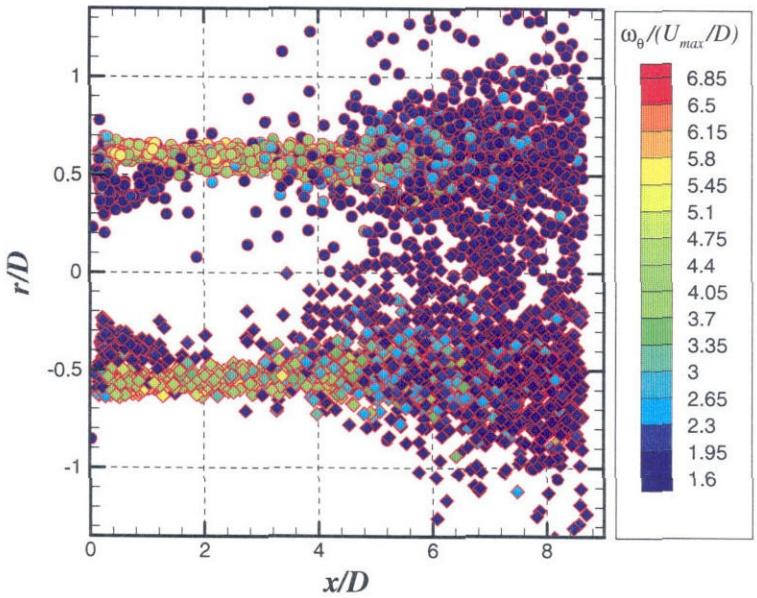

(e) $St_L = 0.82$

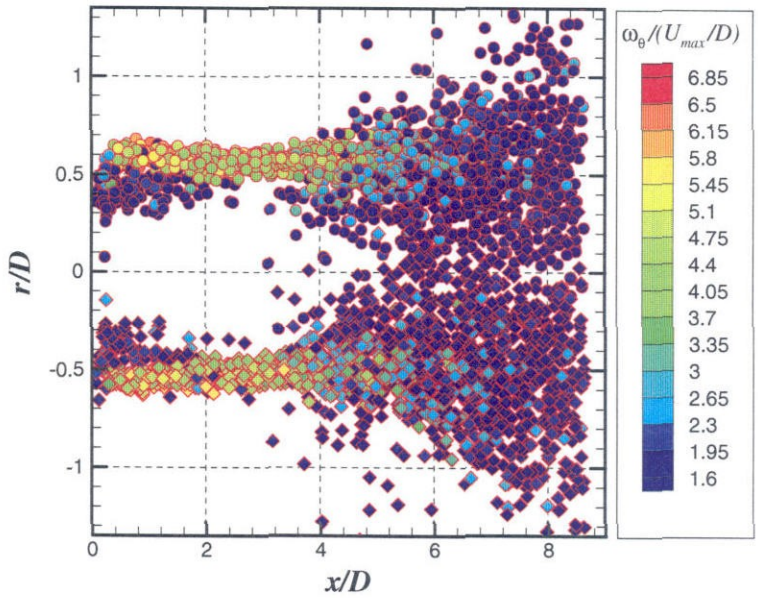

(f) $St_L = 0.97$

Figure E.18 Continued.

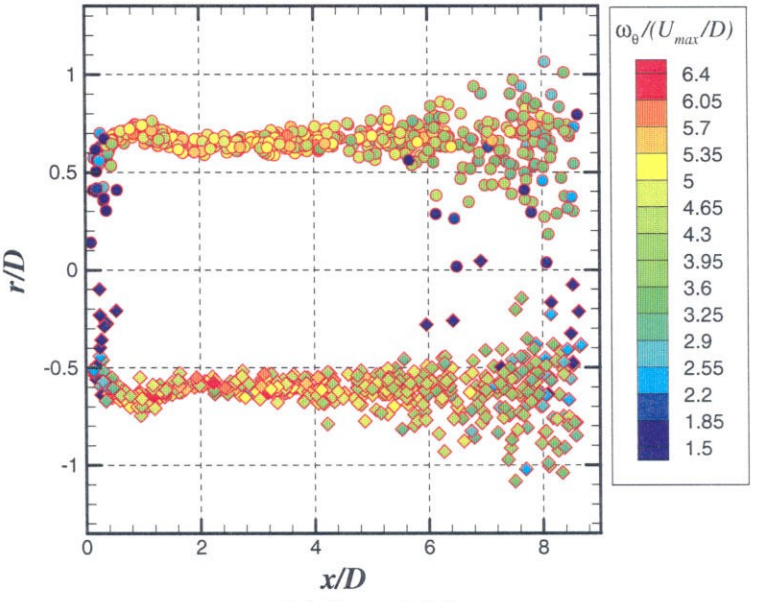

(a) $St_L = 0.26$

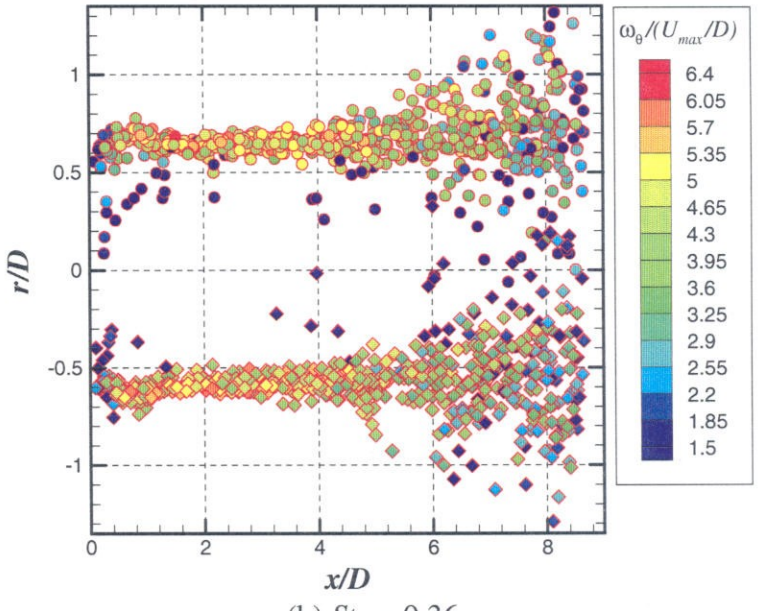

(b) $St_L = 0.36$

FIGURE E.19 Evolution of Vorticity Peak Positions for L/D = 2.0, NS Ramps.

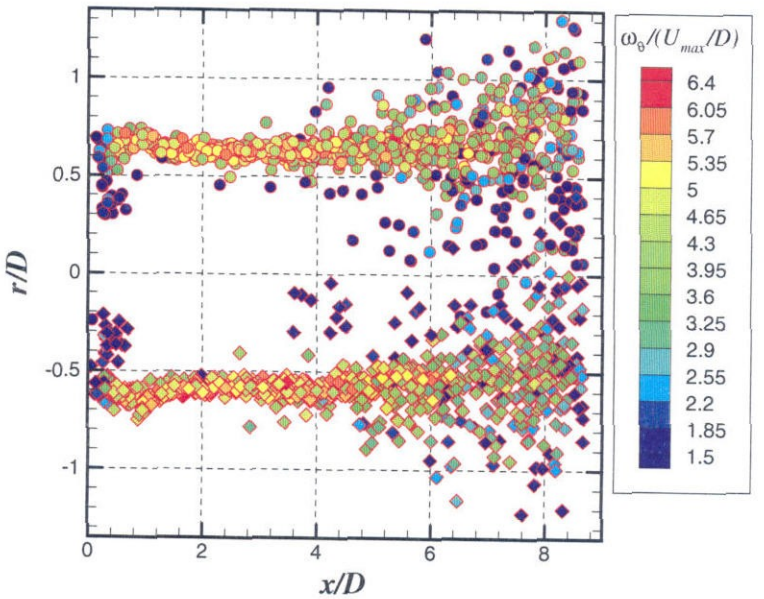

(c) $St_L = 0.46$

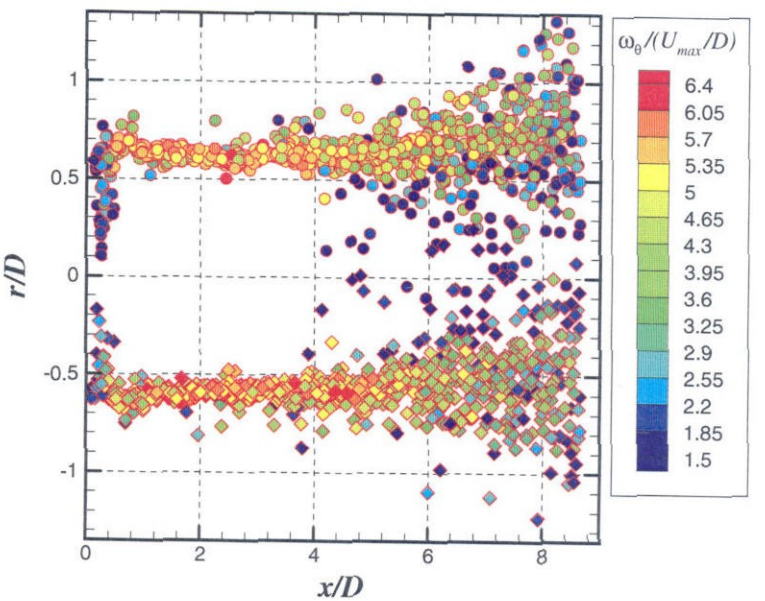

(d) $St_L = 0.50$

Figure E.19 Continued.

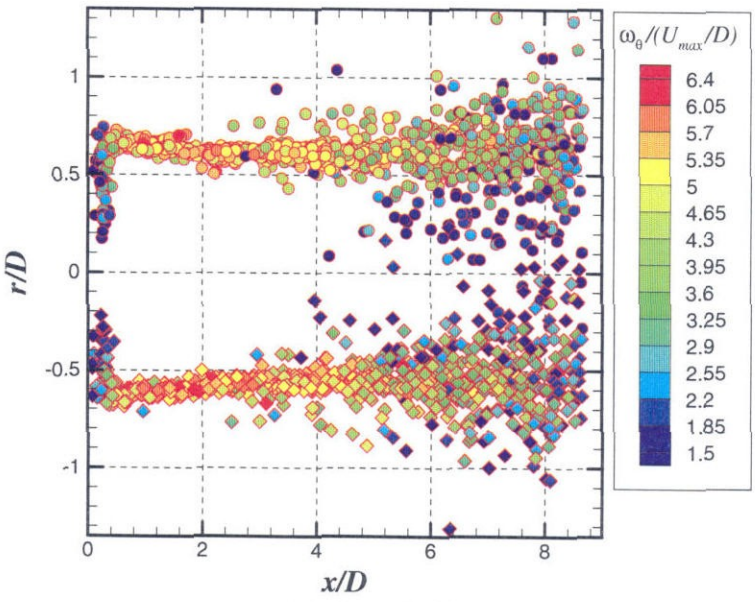

(e) $St_L = 0.56$

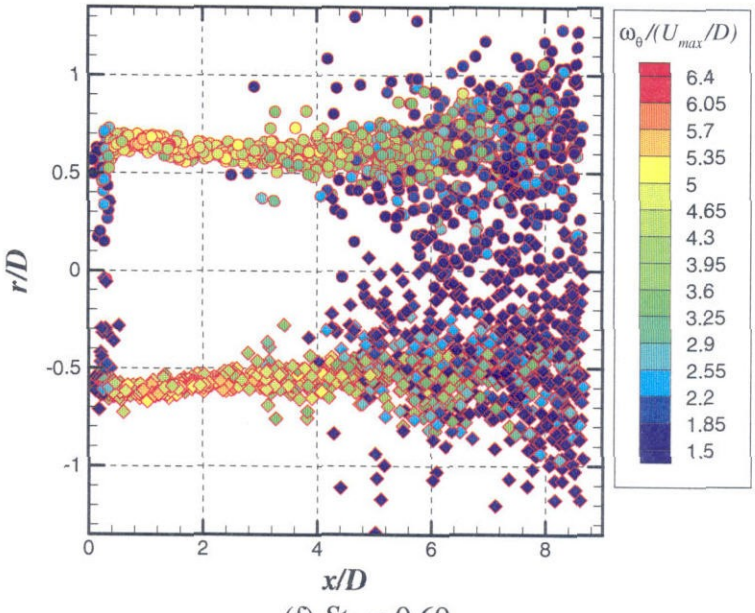

(f) $St_L = 0.69$

Figure E.19 Continued.

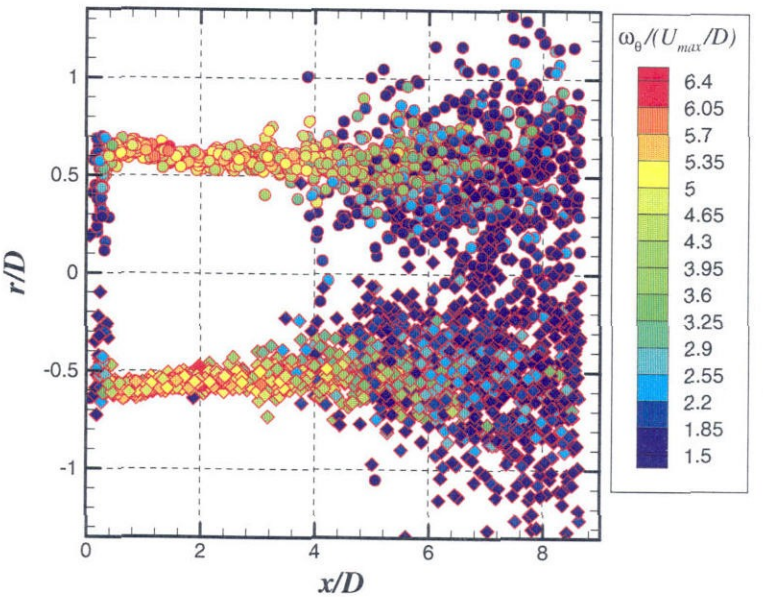

(g) $St_L = 0.85$

Figure E.19 Continued.

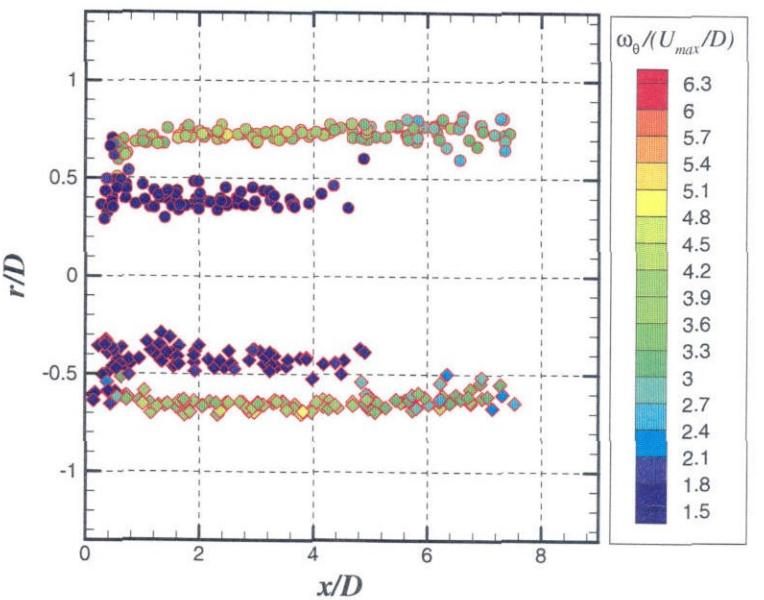

(a) $St_L = 0.06$

FIGURE E.20 Evolution of Vorticity Peak Positions for L/D = 4.0, NS Ramps.

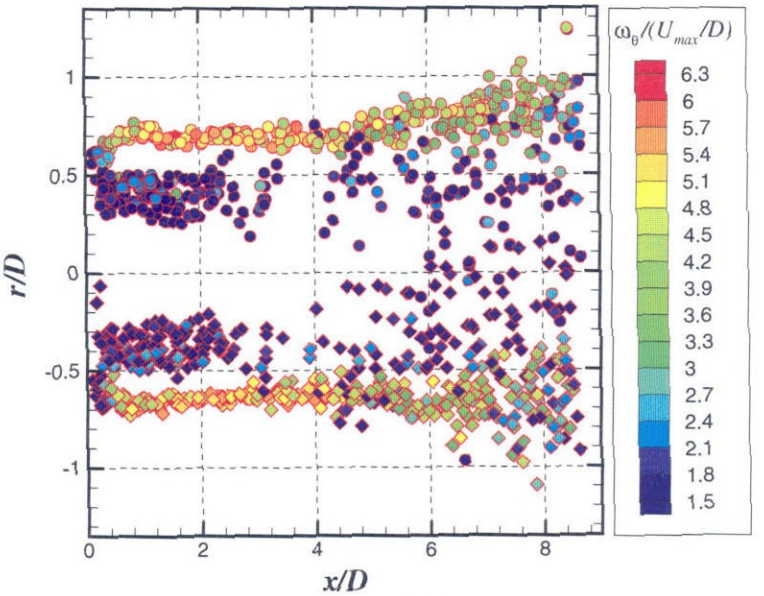

(b) $St_L = 0.42$

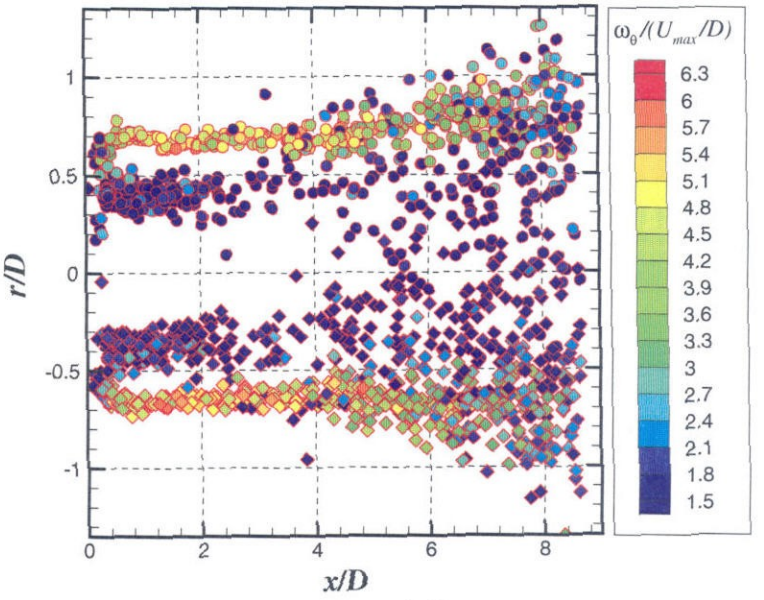

(c) $St_L = 0.51$

Figure E.20 Continued.

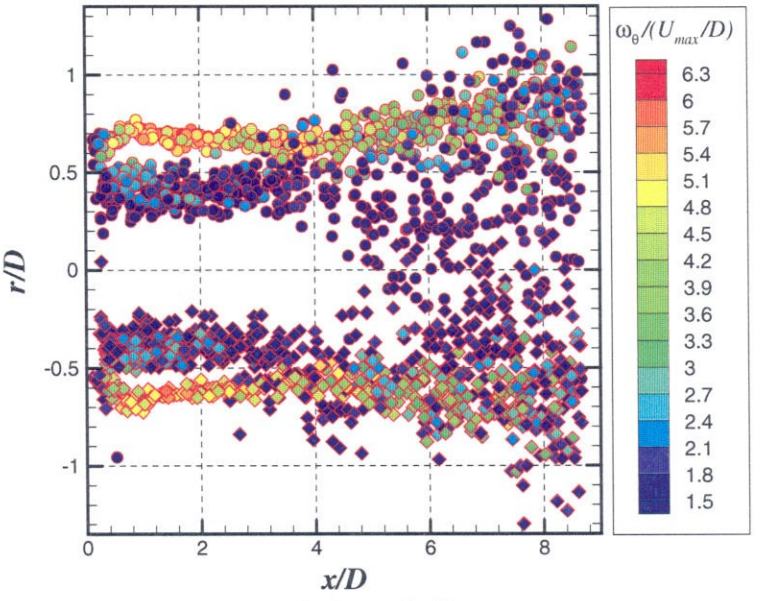

(d) $St_L = 0.60$

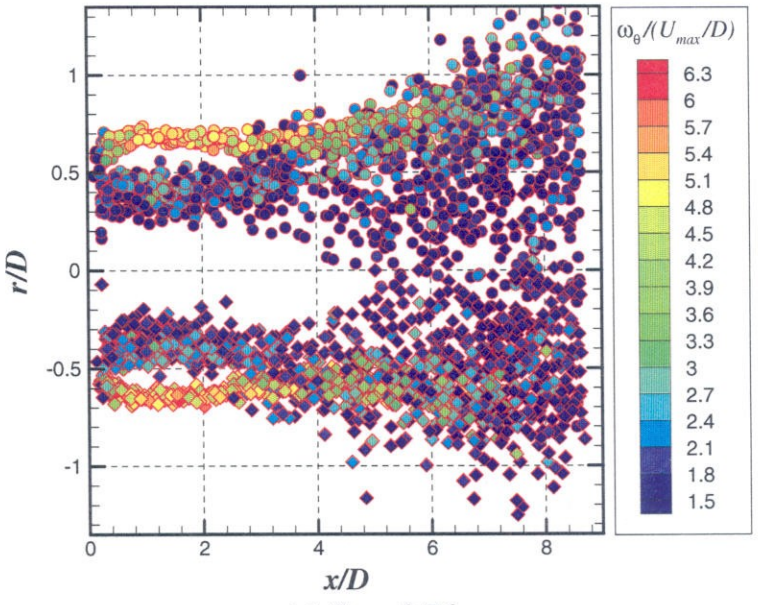

(e) $St_L = 0.76$

Figure E.20 Continued.

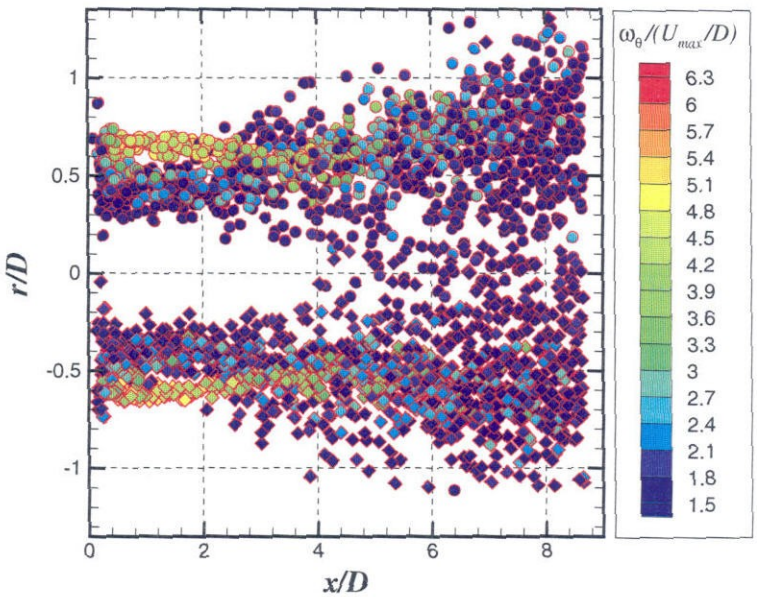

(f) $St_L = 0.87$

Figure E.20 Continued.

References

1. Atabek, H. B., and Chang, C.C. 1961. Oscillatory Flow Near the Entry of a Circular Tube. *A. F. Angew. Math. and Phys. (ZAMP)* **12**, 185-201.
2. Bartol, I. 1999. *Distribution, Swimming Physiology, and Swimming Mechanics of Brief Squid* Lolliguncula Brevis. Ph.D. Dissertation, The College of William and Mary in Virginia.
3. Batchelor, G. K. 1967. *An Introduction to Fluid Dynamics*. Cambridge.
4. Bremhorst, K. and Hollis, P.G. 1990. Velocity Field of an Axisymmetric Pulsed, Subsonic Air Jet. *AIAA J.* **28**, 12, 2043 - 2049.
5. Bremhorst, K. and Gehrke, P.J. 2000. Measured Reynolds Stress Distributions and Energy Budgets of a Fully Pulsed Round Air Jet. *Exp. Fluids* **28**, 519 - 531.
6. Broze, G. and Hussain, F. 1994. Nonlinear Dynamics of Forced Transitional Jets: Periodic and Chaotic Attractors. *J. Fluid Mech.* **263**, 93-132.
7. Broze, G. and Hussain, F. 1996. Transitions to Chaos in a Forced Jet: Intermittency, Tangent Bifurcations and Hysteresis. *J. Fluid Mech.* **311**, 37-71.
8. Cantwell, B. 1986. Viscous Starting Jets. *J. Fluid Mech.* **173**, 159-189.
9. Crow, S.C. and Champagne, F.H. 1971. Orderly Structure in Jet Turbulence. *J. Fluid Mech.* **48**, 547-591.
10. Didden, N. 1979. On the Formation of Vortex Rings: Rolling-up and Production of Circulation. *A. F. Angew. Math. and Phys. (ZAMP)* **30**, 101-116.
11. Fraenkel, L.E. 1972. Examples of Steady Vortex Rings of Small Cross-Section in an Ideal Fluid. *J. Fluid Mech.* **51**, 119-135.
12. Gharib, M., Rambod, E., and Shariff, K. 1998. A Universal Time Scale for Vortex Ring Formation. *J. Fluid Mech.* **360**, 121-140.
13. Glezer, A. 1981. *An Experimental Study of a Turbulent Vortex Ring.* Ph.D. Thesis, California Institute of Technology.
14. Glezer, A. 1988. The Formation of Vortex Rings. *Phys. of Fluids* **31**, 12, 3532 - 3542.
15. Lamb, H. 1932. *Hydrodynamics*. Dover.
16. Lim, T.T. and Nickels, T.B. 1995. Vortex Rings. In *Vortices in Fluid Flows* (ed. by S. I. Green). Kluwer.
17. Linden, P.F. and Turner, J.S. 2000. The Formation of "Optimal" Vortex Rings, and the Efficiency of Propulsion Devices. *J. Fluid Mech.* (in press).
18. Maxworthy, T. 1977. Some Experimental Studies of Vortex Rings. *J. Fluid Mech.* **81**, 465-495.
19. Miloh, T., Waisman, G., and Weihs, D. 1978. The Added-Mass Coefficients of a Torus. *J. of Eng. Math.* **12**, 1-13.

20. Mohseni, K. and Gharib, M. 1998. A Model for Universal Time Scale of Vortex Ring Formation. *Phys. of Fluids* **10**, 10, 2436 - 2438.
21. Mohseni, K., Ran, H., and Colonius, T. Numerical Experiments on Vortex Ring Formation. *J. Fluid Mech.*, (to be published).
22. Nitsche, M. and Krasny, R. 1994. A Numerical Study of Vortex Ring Formation at the Edge of a Circular Tube. *J. Fluid Mech.* **276**, 139-161.
23. Nitsche, M. 1996. Scaling Properties of Vortex Ring Formation at a Circular Tube Opening. *Phys. of Fluids* **8**, 1848-1855.
24. Norbury, J. 1973. A Family of Steady Vortex Rings. *J. Fluid Mech.* **57**, 417 - 431.
25. Prandtl, L. and Tietjens, O.G. 1934. *Applied Hydro- and Aeromechanics*. Dover.
26. Pullin, D.I. 1979. Vortex Ring Formation at Tube and Orifice Openings. *Phys. of Fluids* **22**, 401-403.
27. Raffel, M., Willert, C.E., and Kompenhans, J. 1998. *Particle Image Velocimetry: A Practical Guide*. Springer-Verlag.
28. Rosenfeld, M., Rambod, E., and Gharib, M. 1998. Circulation and Formation Number of Laminar Vortex Rings. *J. Fluid Mech.* **376**, 297-318.
29. Saffman, P.G. 1975. On the Formation of Vortex Rings. *Stud. Appl. Math.* **54**, 3, 261-268.
30. Saffman, P. 1978. The Number of Waves on Unstable Vortex Rings. *J. Fluid Mech.* **84**, 625-639.
31. Saffman, P. 1981. Dynamics of Vorticity. *J. Fluid Mech.* **106**, 49-58.
32. Saffman, P. 1992. *Vortex Dynamics*. Cambridge.
33. Shariff, K. and Leonard, A. 1992. Vortex Rings. *Ann. Rev. Fluid Mech.* **24**, 235-279.
34. Shusser, M. and Gharib, M. 1999. A New Model for Inviscid Vortex Ring Formation. *30th AIAA Fluid Dynamics Conference*, Norfolk, June 28 - July 1.
35. Shusser, M. and Gharib, M. 2000. Energy and Velocity of a Forming Vortex Ring. *Phys. of Fluids* **12**, 3, 618 - 621.
36. Shusser, M., Rosenfeld, M., Mohseni, K., and Gharib, M. Vortex Ring Formation in a Piston/Cylinder Arrangement for Time-Dependent Velocity Programs. (*to be published*).
37. Siekmann, J. 1963. On a Pulsating Jet From the End of a Tube, With Application to the Propulsion of Certain Aquatic Animals. *J. Fluid Mech.* **15**, 399-418.
38. Vermeulen, P.J., Ramesh, V., and Yu, W.K. 1986. Measurements of Entrainment by Acoustically Pulsed Axisymmetric Air Jets. *ASME J. Eng. Gas Turb. and Power*, **108**, 479-484.
39. Weihs, D. 1977. Periodic Jet Propulsion of Aquatic Creatures. *Fortschr. Zool.* **24**, 171-175.
40. Westerweel, J., Dabiri, D., and Gharib, M. 1997. The Effect of a Discrete Window Offset on the Accuracy of Cross-Correlation Analysis of Digital PIV Recordings. *Exp. Fluids* **23**, 20-28.
41. Willert, C.E. and Gharib, M. 1991. Digital Particle Image Velocimetry. *Exp. Fluids* **10**, 181-193.